Synthesis and Characterisation of Epitaxial 2D Nanocrystals



Peiyu Chen

St. Catherine's College

University of Oxford

A thesis submitted for the degree of

Doctor of Philosophy

Trinity Term 2019

Synthesis and Characterisation of Epitaxial 2D Nanocrystals

Peiyu Chen

St. Catherine's College, University of Oxford

A thesis submitted for the degree of *Doctor of Philosophy*, Trinity Term 2019

Abstract

This thesis focuses on the synthesis and characterisation of two materials, monolayer molybdenum disulphide (MoS_2) crystals and gold nanocrystals/monolayers, supported on single crystal strontium titanate ($SrTiO_3$) substrates.

On three terminations of $SrTiO_3$ substrates, (111), (110), and (001), monolayer MoS_2 crystals are found to preferentially align their $<2\bar{1}\bar{1}0>$-type directions (i.e., the sulphur-terminated edge directions) with the $<1\bar{1}0>$-type directions on $SrTiO_3$. These arrangements allow near-perfect coincidence epitaxy between seven MoS_2 unit cells and four $SrTiO_3$ unit cells. This maximises the interfacial van der Waals bonding between MoS_2 monolayers and $SrTiO_3$.

When $SrTiO_3$-supported MoS_2 monolayers are annealed in ultrahigh vacuum, the sulphur loss begins at 700 °C. The sulphur vacancies can be filled by annealing the crystals in a hot sulphur atmosphere, and the optical properties of monolayer MoS_2 can nearly be fully recovered. The sulphur annealing no longer takes effect when all the Mo has been oxidised into MoO_2 and MoO_3 at 800–900 °C. The MoS_2 crystal shapes are stable upon annealing until the residual MoO_3 particles evaporate at above 1000 °C.

Gold nucleates as monolayers on $SrTiO_3(001)$-(2×1) and as multiply twinned particles on $SrTiO_3(001)$-$c(4 \times 2)$ and $SrTiO_3(111)$-(4×4)+(6×6). In scanning tunnelling microscopy, a square pattern of bright spots with a periodicity of 1.54 ± 0.06 nm is frequently observed. The monolayers are thought to adopt mixed hexagonal and square packing of atoms because of their observed internal angles of 60°/120° and 90°/135°.

The shapes of gold nanocrystals deviate from the equilibrium Wulff shape due to the influence of the $SrTiO_3$ single crystal substrates. On any $SrTiO_3$ substrate, the height-to-width ratio of gold crystals is not a constant but rather increases the crystal height. The ratio between the {111} and {001} surface areas of the gold crystals is found to differ on three different $SrTiO_3$ substrates. The reentrant facets of the Wulff shapes are not observed.

These findings extend our understanding of epitaxial crystals and nanomaterials grown on $SrTiO_3$. This yields a platform for the growth of tailored nanomaterials for electronic and catalytic applications.

Preface

The work presented in this thesis was carried out by the author from January 2016 to August 2019 at the Department of Materials, University of Oxford, under the supervision of Professor M. R. Castell. No part of this thesis has been previously submitted for a degree at this or any other university. Some of the work has been published in peer-reviewed scientific publications and presented at scientific conferences:

Publications:

- Chen, P.; Castell, M. R. Wetting behavior of Li-metal, as part of "2020 Solid-State Battery Roadmap". Invited review paper by *J. Phys. Energy* **2020**, submitted.
- Chen, P.; Murugappan K.; Castell, M. R. Shapes of Epitaxial Gold Nanocrystals on $SrTiO_3$ Substrates. *Phys. Chem. Chem. Phys.* **2020**, in press (DOI: 10.1039/c9cp06801e).
- Chen, P.; Xu, W.; Gao, Y.; Holdway, P.; Warner, J. H.; Castell, M. R. Thermal Degradation of Monolayer MoS_2 on $SrTiO_3$ Supports. *J. Phys. Chem. C* **2019**, *123*, 3876−3885.
- Chen, P.; Xu, W.; Gao, Y.; Warner, J. H.; Castell, M. R. Epitaxial Growth of Monolayer MoS_2 on $SrTiO_3$ Single Crystal Substrates for Applications in Nanoelectronics. *ACS Appl. Nano Mater.* **2018**, *1*, 6976−6988.

Conference presentations:

- AVS 66th International Symposium & Exhibition, Columbus, USA (2019). *Won the Dorothy M. and Earl S. Hoffman Award.*
- 34th European Conference on Surface Science (ECOSS-34), Aarhus, Denmark (2018). *Won the Carlsberg Foundation Award.*
- Surface Science Day, Liverpool, UK (2017).
- 13th European Conference on Surface Crystallography and Dynamics (ECSCD-13), San Sebastián, Spain (2017).
- nanoScience@Surfaces, Cambridge, UK (2016).

Acknowledgements

This thesis has been completed with the kind support and help from a network of generous people around me. I would like to take this opportunity to express my sincere thanks to all of them.

First and foremost, I would like to thank my supervisor, Professor Martin Castell, for offering valuable guidance at every stage of my doctorate. During the past 3½ years, his passion for science and rigorous attitude have shaped my understanding of scientific research and have (I hope) made me a better scientist. I am particularly grateful for his time dedicated to discussing the details of my experimental results and patiently revising my papers. I also appreciate the conference opportunities that Martin facilitated and encouraged me to pursue.

My thanks also go to my colleagues in our research group. Dr. Yakun Gao has been a very helpful senior colleague, who trained me on the STM and took me under her wing during the first two years when we worked on the MoS_2 projects. Dr. Xiao Hu imparted her knowledge of the STM and other aspects of science to me, and created a lively atmosphere in our office. Shuqiu Wang is thanked especially for introducing me to the image processing tool *SmartAlign* and the good times we shared in the office. I also truly appreciate the hours that Dr. Krish Murugappan spent on imaging my gold nanocrystals on the Zeiss Merlin SEM. I should thank Dr. Merel Lefferts for teaching me to set up the K-cell and Fubiao Gu for sharing his excellent understanding of science and our instruments. Other group members during my time at Oxford – Ben Armitage, Aatif Rasheed, Tabitha Jones, Yuhan Zhu, are heartily thanked for their friendly advice and support.

I had a very pleasant time working with Dr. Wenshuo Xu for over two years on the MoS_2 projects, along the way having inspiring scientific discussions and writing up the papers

together. Dr. Philip Holdway was helpful in generating and interpreting XPS data for my MoS_2 project. My gratitude also goes to Jiawei Jiang, who helped to image my MoS_2 crystals on the Zeiss Merlin SEM and did some EDX trials for me. I am also deeply indebted to Chris Spencer, the JEOL engineer, who has been amazing – he fixed the STM and rescued us many times when all hope was lost. Peter Flaxman in the department workshop helped to maintain my sample holders, and his help has been much appreciated. Without him I would have overheated and damaged a lot more samples. Many thanks to Professor Pat Roche, for his advice and encouragement when I felt unsure about which way to go.

I am grateful to a few funding bodies that partially sponsored my DPhil: the China Oxford Scholarship Fund, St. Catherine's College, and the Great Britain-China Educational Trust. There are also many organisations that made my conference trips possible by offering generous travel grants. These include Armourers and Brasiers', IOP, IOM3, the Keith Prout Crystallography Fund, Carlsberg Foundation, Hertford College, St. Catherine's College, and Oxford University Department of Materials.

Finally, I would like to give my most profound gratitude to my parents for their love, emotional support, and financial assistance. They have dedicated their life to my well-being and development, and without them, I would not have the opportunity to pursue higher education in this country for eight years. My special thanks to my husband, Dr. Yi-Ge Huang, who designed a stepper motor for my sample heating experiments, which saved me thousands of hours of manual work. He has also been incredibly supportive in many other aspects, e.g., proofreading the whole of this thesis, my papers, and my job applications. I thank him for his love, care, and company, which have been the best part of my life in Oxford.

Contents

1 Introduction 1

1.1 Surface science and substrate engineering 1

1.2 Outline of the thesis 3

2 Literature Review 5

2.1 $SrTiO_3$ single crystal substrates 5

2.1.1 Introduction 5

2.1.2 (111) surface reconstructions 7

2.1.3 (110) surface reconstructions 10

2.1.4 (001) surface reconstructions 11

2.2 Monolayer MoS_2 14

2.2.1 Introduction 14

2.2.2 Crystal structures and shapes 16

2.2.3 Photoluminescence (PL) and Raman studies 19

2.2.4 Van der Waals epitaxy 24

2.2.5 Thermal degradation 26

2.3 Gold nanostructures 28

2.3.1 Introduction 28

2.3.2 Wulff and Winterbottom constructions for fcc crystals 29

2.3.3 Influence of substrate on nanocrystals 30

2.3.4 Influence of environment on gold nanocrystals 33

2.3.5 Gold monolayers 37

2.4 Summary and outlook 41

3 Experimental Techniques 42

3.1 The main instrument 42

3.2 Substrate preparation 44

3.2.1 Purpose of preparation 44

3.2.2 Degassing and annealing 45

3.2.3 Sputtering 46

3.2.4 Prepared surfaces 47

3.3 Crystal and nanostructure growth 49

3.3.1 MoS_2 crystals 49
3.3.2 Gold nanostructures 51
3.4 Scanning tunnelling microscopy (STM) 52
3.5 X-ray photoelectron spectroscopy (XPS) 55
3.6 Scanning electron microscopy (SEM) 57
3.7 Raman spectroscopy and photoluminescence (PL) 58
3.8 Summary 60

4 Epitaxial Growth of Monolayer MoS_2 on $SrTiO_3$ Single Crystal Substrates 61
4.1 Introduction 62
4.2 Results 62
4.2.1 MoS_2 on $SrTiO_3$(111) 65
4.2.2 MoS_2 on $SrTiO_3$(110) 69
4.2.3 MoS_2 on $SrTiO_3$(001) 72
4.2.4 Raman spectroscopy and PL 74
4.3 Discussion 79
4.4 Conclusions 83

5 Thermal Degradation of Monolayer MoS_2 on $SrTiO_3$ Supports 84
5.1 Introduction 84
5.2 Results 85
5.2.1 SEM and STM experiments 86
5.2.2 XPS analysis 89
5.2.3 PL and Raman spectroscopy 93
5.2.4 Optical microscopy (OM) 95
5.2.5 Sulphur annealing 96
5.3 Discussion 98
5.4 Conclusions 101

6 Gold Particle Nucleation Behaviour on $SrTiO_3$ Substrates 102
6.1 Introduction 102
6.2 Results 103
6.2.1 Single crystals, monolayers, and multiply twinned particles 103
6.2.2 Monolayer structure 106
6.2.3 Dewetting of monolayers 109
6.3 Discussion 111

6.4 Conclusions and future work 115
6.4.1 Atomic structure: STM and/or DFT 116
6.4.2 Electronic structure: ARPES or XPS 117

7 Shapes of Epitaxial Gold Nanocrystals on $SrTiO_3$ Substrates 119
7.1 Introduction 119
7.2 Results and discussion 120
7.2.1 Crystal epitaxy 120
7.2.2 Height-to-width ratio (h/l) 124
7.2.3 A_{111}/A_{001} or s/l ratio 130
7.2.4 Wulff and growth shapes 135
7.3 Conclusions 141

8 Conclusions 143
8.1 Overview 143
8.2 Monolayer MoS_2 crystals on $SrTiO_3$ 144
8.3 Gold monolayers and nanocrystals on $SrTiO_3$ 145
8.4 Future work 147

Appendix A: Reported surface reconstructions of $SrTiO_3$ (Chapter 2) 149

Appendix B: Derivations of equations in Chapters 6 and 7 153
B.1 Gold monolayers 153
B.2 (111)-based gold crystals 154
B.2.1 Wulff construction 154
B.2.2 Hexagon Wulff 155
B.2.3 Hexagon growth 159
B.2.4 Fixed-h hexagon 160
B.2.5 Triangle Wulff 162
B.2.6 Triangle growth 165
B.3 (001)-based gold crystals 166
B.3.1 Pyramid Wulff 166
B.3.2 Pyramid growth 170
B.4 (110)-based gold crystals (hut Wulff) 171

References 174

Chapter 1

Introduction

1.1 Surface science and substrate engineering

The outermost atomic layers in a solid are referred to as its surface.[1] The broken symmetry at the surface brings about abrupt changes in the electronic structure compared with its bulk.[2] Upon creation of the surface, the surface bonds tend to rearrange themselves to minimise the energy increase as a result of the deficit of neighbouring atoms.[3] The process could be **'relaxation'** where atoms are displaced from their bulk positions with no disturbance of periodicity. Alternatively it could also be '**reconstruction**' where atoms are relocated, possibly with the loss or addition of atoms such that a new periodicity is reached. For example, reconstruction tends to saturate dangling bonds formed upon cleavage, which otherwise make the surface unstable and are responsible for an increase in the surface energy.[4] The new periodicity as a result of the atomic rearrangements is expressed in terms of a surface unit cell as a multiple of the two-dimensional (2D) bulk terminated unit cell. A classic example is the (7 × 7) reconstruction of the Si(111) surface. It was first observed in 1959 by Schlier and

Farnsworth[5] and comprehensively explained in 1985 by Takayanagi *et al.* using a model referred to as the dimer-adatom stacking-fault (DAS) model.[6]

Therefore a surface can exhibit drastically different structural or electronic properties,[7] which is the origin of **'surface science'** – the study of the physical and chemical properties of surfaces. Surface science encompasses a wide range of applications including heterogeneous catalysis[2,8] and semiconductor device fabrication.[9,10] In 2D materials science, surface structures have a critical influence on all surface processes, e.g., growth of 2D materials and nanostructures. The morphologies and structures of 2D materials can be heavily influenced by their interface with the substrate. A good knowledge of the substrate surface effect on the growth or adsorption process is very important in the field of materials science from fundamental and applied points of view. Therefore, **substrate engineering** has become an attractive research topic, which will eventually lead to the controllable modification of the chemistry and functional properties of 2D materials, thin films, and nanostructures.[11,12]

In this thesis, all work is concerned with surface science and substrate engineering. Two nanomaterials, monolayer molybdenum disulphide (MoS_2) and nanosized gold, are investigated, which are supported on various terminations and reconstructed surfaces of the single crystal substrate, strontium titanate ($SrTiO_3$). $SrTiO_3$ was chosen as the substrate material because it has several surface terminations with different symmetries that have been extensively studied: (111), (110), and (001). All these terminations exhibit a variety of surface reconstructions with different compositions and surface chemistry. Throughout the thesis, Wood's notation is used to describe the reconstructed surfaces of $SrTiO_3$, with the general form $SrTiO_3(hkl)$-$(m \times n)R\varphi$. It refers to the (hkl) surface of $SrTiO_3$ with a reconstructed surface unit cell that is m times the bulk unit cell in direction $\boldsymbol{a}$ and n times the bulk unit cell in direction $\boldsymbol{b}$, where $\boldsymbol{a}$ and $\boldsymbol{b}$ are a pair of in-plane lattice parameters of the bulk crystal. Wood's notation is followed by '$R\varphi$' if the surface unit cell is rotated with respect to the bulk by an angle of φ (in degrees).

The first supported material studied in this thesis is monolayer MoS_2, which is a 2D semiconductor with a direct bandgap of 1.8–1.9 eV.[13,14] It is viewed as a promising candidate in optoelectronics and low-power digital electronics.[15,16] The second supported material is gold nanostructures, which have attracted intense research interest because of its exceptional catalytic activity and interesting optical behaviour.[17–21]

1.2 Outline of the thesis

In many previous studies, the two nanomaterials (MoS_2 and gold) were grown and characterised on oxide substrates, which simply served as inert supports. The aim of the work presented in this thesis is to contribute knowledge to the area of substrate engineering by elucidating the interesting role of $SrTiO_3$ substrates. The morphologies and hence the functional properties of the supported materials (MoS_2 and gold) are found to be highly dependent on their interaction with the $SrTiO_3$ substrates. An outline of the thesis follows below.

Chapter 2 reviews the previous research on the three materials studied or used in this thesis. This includes the surface reconstructions on $SrTiO_3$, crystal structures and optical properties of monolayer MoS_2, and shapes of gold nanostructures. An emphasis is placed on the discussion of substrate influence on the two supported materials.

Chapter 3 is a general introduction to the growth and characterisation techniques used to generate the results in this thesis. Most techniques are surface sensitive, e.g., scanning tunnelling microscopy (STM), scanning electron microscopy (SEM), and X-ray photoelectron spectroscopy (XPS).

Chapters 4–7 present the original experimental work carried out by the author. Chapter 4 is concerned with the epitaxial relationship between MoS_2 monolayers and the three terminations of $SrTiO_3$ substrates, (111), (110), and (001). The interaction between MoS_2 and $SrTiO_3$ is found to influence the orientations, shapes, and optical properties of MoS_2 monolayers.

In Chapter 5, the thermal degradation of MoS_2 monolayers is studied in terms of their structural, compositional, and optical behavioural changes, from 700 °C to above 1000 °C. Their degraded optical properties can be partially healed by annealing in a sulphur atmosphere, unless oxides of Mo have formed because of the oxygen supplied by the $SrTiO_3$ substrates.

Chapters 6 and 7 present the work on gold nanostructures grown on three different surfaces on $SrTiO_3$(001) and (111), including monolayers, multiply twinned particles (MTPs), and nanocrystals. $SrTiO_3$(001)-(2 × 1) is the only surface of $SrTiO_3$ found to be capable of stabilising gold monolayers. In Chapter 6, STM work demonstrates the quasi-rectangular shapes of the monolayers, the square pattern of bright spots on them, and their dewetting behaviour. The possible origin of monolayer formation in relation to the substrate is also discussed.

The investigation of the gold nanocrystals is presented in Chapter 7. The three $SrTiO_3$ substrate surfaces are found to modify the gold crystal shapes through interfacial strain, by promoting the growth of {111} and {001} crystal facets differently, and by encouraging reentrant facets to grow out.

A summary and concluding remarks of the experimental work are presented in Chapter 8, along with comments on possible future research. The work within this thesis establishes the influence of substrates on 2D and nanomaterials, and promisingly demonstrates that the latter can be functionalised in a controllable manner.

Chapter 2

Literature Review

In this thesis, 2D materials, nanomaterials, and their interactions with the substrates are investigated. The background of each material studied or used in this thesis is introduced in this chapter: the substrate material $SrTiO_3$ (section 2.1), monolayer MoS_2 (section 2.2), and gold nanostructures (section 2.3). For each of these, the review describes their brief histories and the most relevant past research results. A summary of the review is presented in section 2.4, with an outlook on how this review of the fields forms the foundation for my own research.

2.1 $SrTiO_3$ single crystal substrates

2.1.1 Introduction

$SrTiO_3$ has attracted substantial interest since the 1970s mostly because of its versatile crystal surfaces.[22–24] The intense interest in this material stems from the diversity of its applications: in photoelectrolysis,[25,26] in oxygen gas sensing,[27] and as a substrate for the growth of high-T_c

superconductors,[28] catalytic nanoparticles,[29,30] and thin films.[31,32] Since the chemical properties of surfaces strongly depend on their atomic surface structures, chemical compositions, and electronic distributions, it is important to understand these properties of $SrTiO_3$ surfaces.

$SrTiO_3$ is a clear colourless crystal with a high refractive index in its pure form. Stoichiometric $SrTiO_3$ is an insulator with a bandgap of 3.2 eV at room temperature.[33] This large bandgap makes it an inefficient absorber of visible light and limits its potential applications.[34] However, it can be made semiconducting[35] or even superconducting[36,37] by reduction or doping. It can be doped to be both *n*-type and *p*-type, e.g., with niobium (Nb)[38,39] and indium (In),[40] respectively. $SrTiO_3$ adopts a cubic perovskite structure, which refers to a class of compounds with the same type of crystal structure as $CaTiO_3$.[41] Bulk $SrTiO_3$ possesses a simple cubic lattice above 105 K (a = 3.905 Å),[42] and its unit cell is shown in Figure 2.1. The Ti^{4+} ions are octahedrally coordinated with respect to the O^{2-} ions, and the Sr^{2+} ions are in a site that is 12-fold-coordinated by O^{2-} ions.

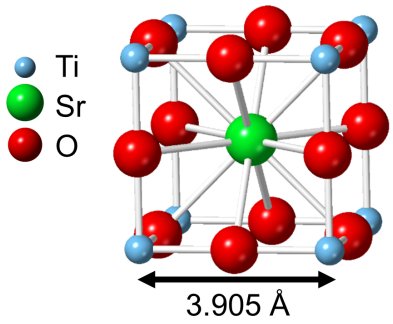

Figure 2.1: $SrTiO_3$ unit cell with a lattice parameter of 0.3905 nm.

$SrTiO_3$ is able to accommodate a large range of surface stoichiometries, and hence it exhibits a variety of surface reconstructions with different compositions and surface chemistry. Its three surface terminations are discussed in more detail below, mainly in terms of their surface reconstructions.

2.1.2 (111) surface reconstructions

As shown in Figure 2.2a, (111) planes of $SrTiO_3$ can be described as alternating layers of Ti^{4+} and SrO_3^{4-}, with a distance of ½ d_{111} between neighbouring layers. The d_{111} spacing is the distance between similar adjacent (111) planes, e.g., adjacent SrO_3^{4-} planes, with a magnitude of 0.225 nm.[43] A top view of the (111) plane is shown in Figure 2.2b, which has a rhombic surface unit cell. The fact that the (111) planes are alternatingly positive and negative results in a non-zero macroscopic dipole moment along the [111] direction. This induces $SrTiO_3$(111) to be an electrostatically polar surface.[44,45] Therefore, it would have to reconstruct itself in order to remove the dipole moment and reduce the resulting large surface energy.[43,46] The (1 × 1) structure of $SrTiO_3$(111) was reported in some early studies, which was based on the results of reflection high-energy electron diffraction (RHEED) and low-energy electron diffraction (LEED).[35,47–49] However, $SrTiO_3$(111) is unlikely to be unreconstructed, so the (1 × 1) RHEED and LEED signals simply come from the bulk with a disordered surface.

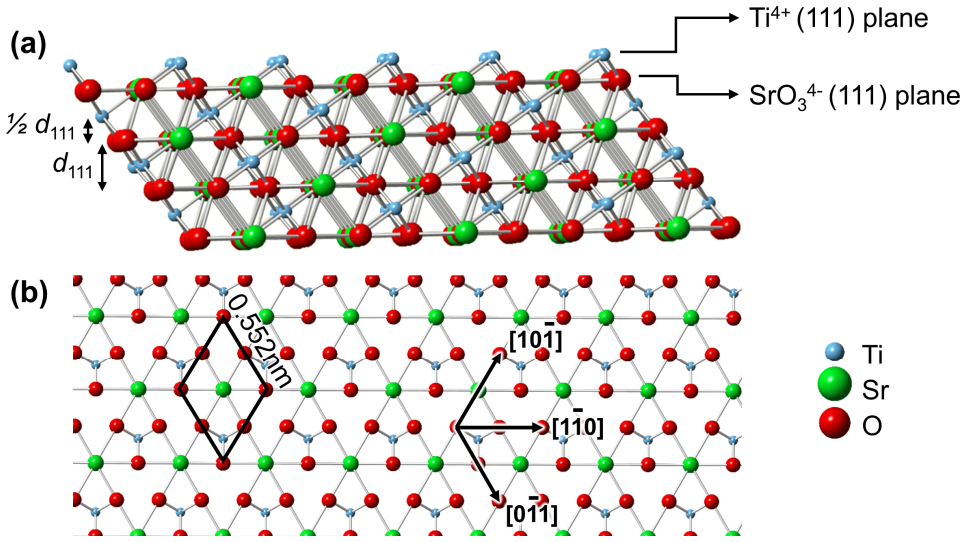

Figure 2.2: (a) Side view and (b) top view of bulk-terminated $SrTiO_3$(111) planes. In (b), a surface unit cell is indicated by the rhombus and the lattice directions are labelled. Only two layers of atoms are shown in (b) for clarity.

The investigation of the (111) surface started in the 1970s, mainly on its terminating structure, using surface sensitive techniques such as XPS, ultraviolet photoelectron spectroscopy (UPS),

LEED, and STM. For about two decades, the focus was primarily on the changes in its surface ionic species and electronic properties.[35,44,48–53] In 1998, Haruyama *et al.* first confirmed a (4 × 4) reconstruction.[47] Up to now, a wide range of surface reconstructions have been observed: (9/5 × 9/5),[43,45,54] (2 × 2),[55,56] (√7 × √7)R19.1°,[38] (3 × 3),[43,45,54–56] (√13 × √13)R13.9°,[38] (4 × 4),[43,47,54–57] (5 × 5),[43,57] and (6 × 6)[43,45,54,55,57] reconstructions, as well as a TiO(111)-(2 × 2) nanophase under highly reducing conditions.[43]

These surface reconstructions form under different preparation conditions including the annealing temperature and time, oxygen partial pressure, and whether an ion beam is sputtered on the specimen. The different surface processing gives rise to different mechanisms of stabilising the surface polarity.[43] An important example is that sputtering the sample surface with argon ions (Ar^+) makes the near surface region Sr deficient,[35,58] creates structural defects such as oxygen vacancies, and renders it amorphous or severely disordered.[54] These affect the surface stoichiometry, and the degree of disorder depends on the sputtering energy and time.[59,60]

Despite the large number of reconstructions reported, some of them are observed to coexist on the same surface, particularly those with similar preparation conditions. Coexistence and similar treatments suggest similar surface energies and compositions. For example, (√7 × √7)R19.1° and (√13 × √13)R13.9° are generated together by an ultrahigh vacuum (UHV) anneal at 850 °C without prior Ar^+-ion sputtering.[38] Once the $SrTiO_3$(111) surface is Ar^+-ion sputtered and annealed at higher temperatures (usually above 1000 °C), it forms a family of (n × n) type surfaces where n = 9/5, 2, 3, 4, 5, 6.[43,45,47,54–57] Extended UHV annealing at even higher temperatures (e.g., 1400 °C) may cause more severe oxygen loss from the surface, and under such highly reducing conditions, a TiO(111)-(2 × 2) nanophase is observed.[43] Table A.1 in Appendix A lists the detailed preparation conditions for the reported reconstructions on $SrTiO_3$(111) from 1998 to 2015.

The most complete morphologies of the reconstructed surfaces on $SrTiO_3$(111) were reported by Russell and Castell.[38,43] A selection of the highest-resolution STM images is put together in Figure 2.3: each reconstruction has a unique surface morphology, and surface unit cells are clearly identified.

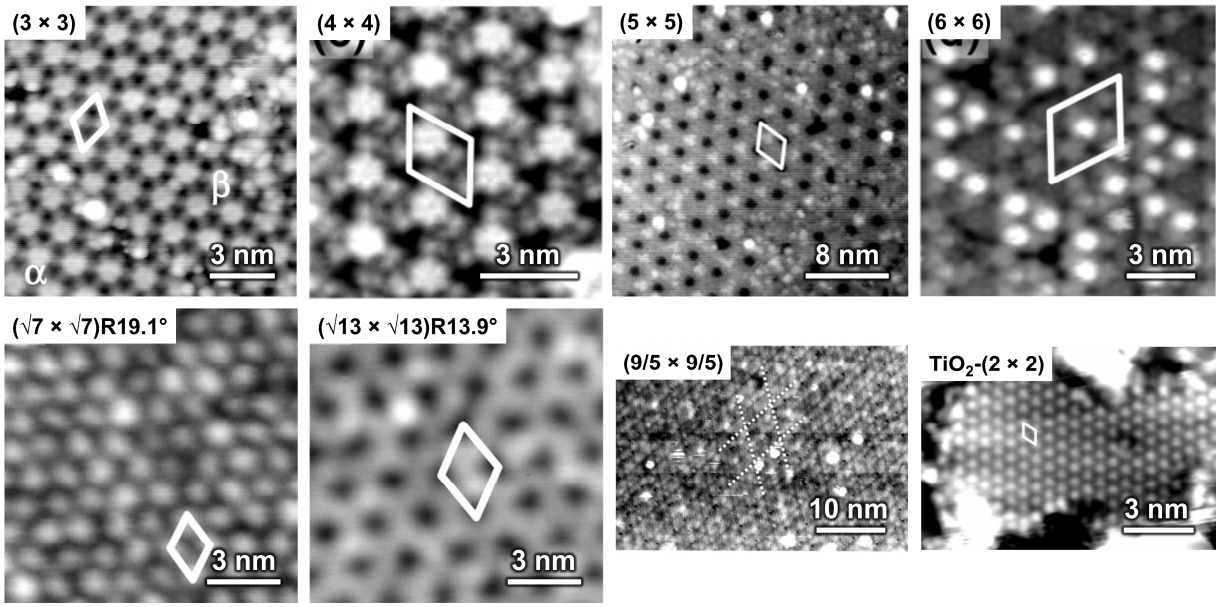

Figure 2.3: STM images of a selection of reconstructed $SrTiO_3$(111) surfaces, as labelled in their top-left corners. Each white rhombus indicates a reconstructed surface unit cell, and the dotted lines in (9/5 × 9/5) represent trenches separated by a distance equivalent to five times the reconstructed unit cells. Adapted from Russell and Castell, 2007,[38] 2008.[43]

Atomic-level structural solutions have been proposed for some of the reconstructions shown above by density functional theory (DFT) calculations.[56,61] For example, the surfaces of (√7 × √7)R19.1° and (√13 × √13)R13.9° consist of a single layer of edge-sharing TiO_6 and TiO_5[] (where [] is a vacant octahedral site) octahedra.[61] The ($n \times n$) surfaces ($2 \leq n \leq 4$) contain a layer of tetrahedral TiO_4 units sitting on top of octahedral TiO_5[] and TiO_6 units in the second layer, e.g., the brightest spots in (3 × 3) and (4 × 4) are TiO_4 tetrahedra.[56] The compositional difference in these two families of surfaces is consistent with Russell and Castell's conclusion: higher concentrations of Ti at the surface are observed when oxygen is more depleted, and this can be achieved by longer Ar^+-ion sputtering and higher annealing temperatures.[43]

2.1.3 (110) surface reconstructions

The $SrTiO_3$ crystal viewed in the <110> directions is made up of a stack of alternating $SrTiO^{4+}$ and O_2^{4-} layers (Figure 2.4a).[62] The d_{110} spacing is 0.28 nm.[63] The (110) plane has a rectangular unit cell as shown in Figure 2.4b. Again, any bulk-terminated $SrTiO_3$(110) would have a polar surface, which has to reconstruct to reduce the surface energy.

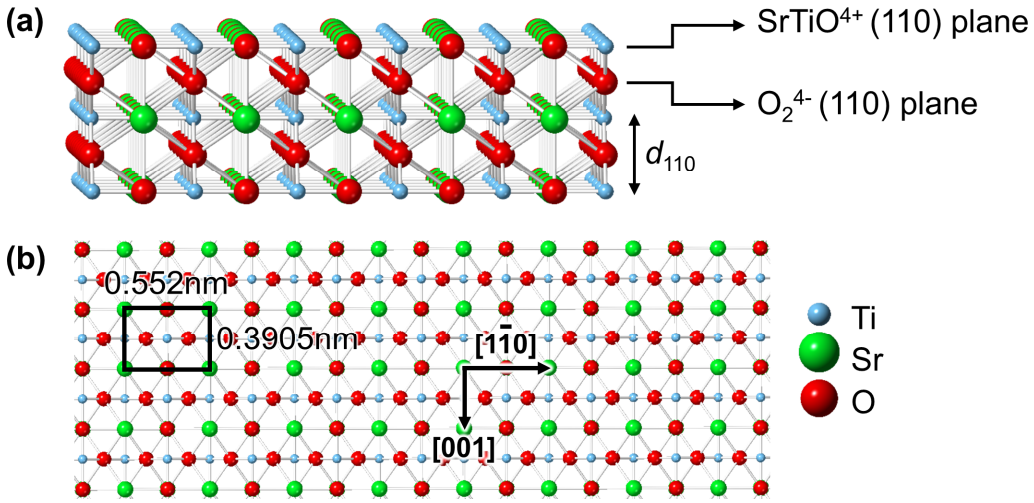

Figure 2.4: (a) Side view and (b) top view of bulk-terminated $SrTiO_3$(110) planes. In (b), a surface unit cell is indicated by the rectangle and the lattice directions are labelled.

Similar to (111), the (110) surface only started to be researched a few decades ago, e.g., as a substrate for the growth of films of cuprate superconductors.[64] A large number of (110) reconstructions were reported and some key and mature ones from 1994 to 2008 are listed in Table A.2 in Appendix A. On $SrTiO_3$(110), most surface reconstructions do not require Ar^+-ion sputtering and are generated in UHV at 800–1200 °C.

The clearest STM images of the (110) reconstructions reported so far are summarised in Figure 2.5. The white rectangles indicate the reconstructed unit cells. For the series of (n × 1) structures, where n = 3, 4, 5, 6, the bright spots in their STM images are TiO_4 tetrahedra, as proposed by DFT calculations in a few studies.[65,66]

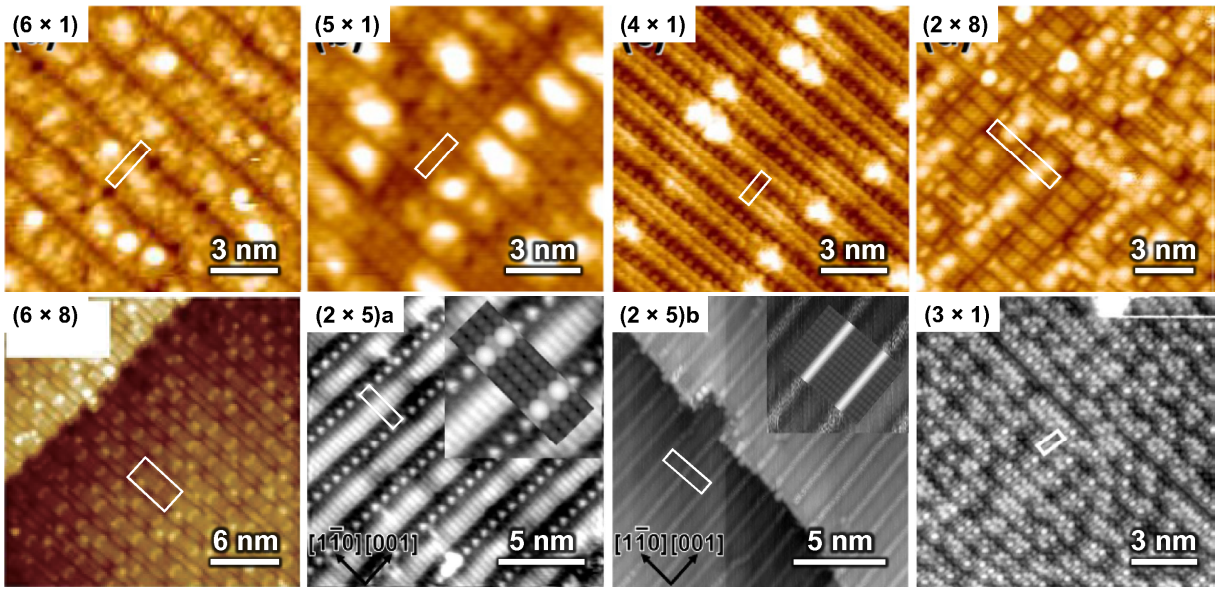

Figure 2.5: STM images of a selection of reconstructed $SrTiO_3$(110) surfaces, as labelled in their top-left corners. The white rectangles indicate reconstructed surface unit cells. The insets in the two types of (2 × 5) reconstructions are magnified views superimposed with simulated STM images. Adapted from Russell and Castell, 2008,[63] Wang *et al.*, 2012,[67] Wang *et al.*, 2016,[66] and Yang *et al.*, 2018.[68]

2.1.4 (001) surface reconstructions

(001) planes of $SrTiO_3$ are illustrated in Figure 2.6a, as alternating layers of TiO_2 and SrO.[69] Most STM studies show unit-cell-high steps (0.3905 nm),[69,70] corresponding to the d_{001} spacing in Figure 2.6a. The (001) plane has a square unit cell (Figure 2.6b).

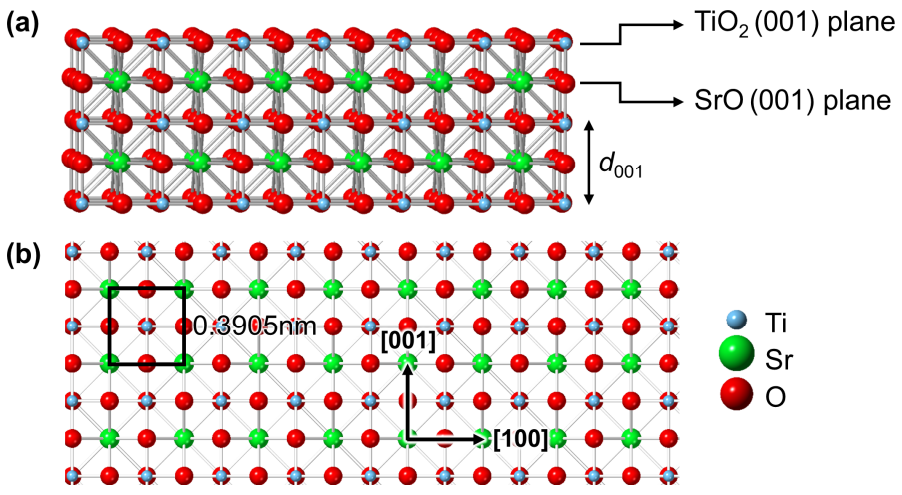

Figure 2.6: (a) Side view and (b) top view of bulk-terminated $SrTiO_3$(001) planes. In (b), a surface unit cell is indicated by the square and the lattice directions are labelled.

The research history of $SrTiO_3$(001) can be traced back the furthest among all surface terminations of $SrTiO_3$, and its character became very well understood more than ten years ago. This history from 1990 to 2007 is listed in Table A.3 in Appendix A. To summarise, before 2002, the (1 × 1) structure of $SrTiO_3$(001) was frequently reported, mainly based on RHEED and LEED results.[69,71–78] The bulk termination is more likely to survive than those of $SrTiO_3$(111) and $SrTiO_3$(110) because the TiO_2 and SrO (001) planes are non-polar.

To produce well reconstructed $SrTiO_3$(001) surfaces, a buffered NH_4F–HF (BHF) solution of pH ~4.5 is frequently used. This acidic solution can selectively dissolve the SrO atomic plane to leave a smooth TiO_2 atomic plane, as the former is a basic oxide and the latter is acidic.[79] Among the reconstructed (001) surfaces, (2 × 1) and (2 × 2) are the earliest discoveries, which are usually generated by UHV annealing at up to 950 °C without Ar^+-ion sputtering.[69,72,74–76,80–84] After 2002, many more reconstructed $SrTiO_3$(001) surfaces were reported with clear STM images. Among these, the most commonly observed family of reconstructions are produced by Ar^+-ion sputtering followed by high-temperature UHV anneals (750–1000 °C). This procedure gives rise to the *c*(4 × 2) reconstructed surface and a series of self-assembled nanostructures described as nanolines and nanodots: (6 × 2), (9 × 2), (12 × 2), (6 × 8), and (7 × 4).[84–86] Figure 2.7 shows a selection of the best-quality STM images reported of the $SrTiO_3$(001) surfaces. According to DFT calculations, their structures are based on Ti-centred polyhedral building blocks (TiO_4, TiO_5, and TiO_6) in the top few layers.[87,88]

It is interesting to note that among all surface reconstructions on all three terminations of $SrTiO_3$ that have been structurally resolved, $SrTiO_3$(001)-(2 × 1) is special. This is because (i) it is the only known hydroxylated surface and (ii) it has a much higher surface energy than other reconstructions,[89] e.g., higher than *c*(4 × 2) by 0.4–0.6 J m^{-2}, determined experimentally and theoretically.[90,91] Its surface also consists of interconnected TiO_x polyhedra (Figure 2.8a),

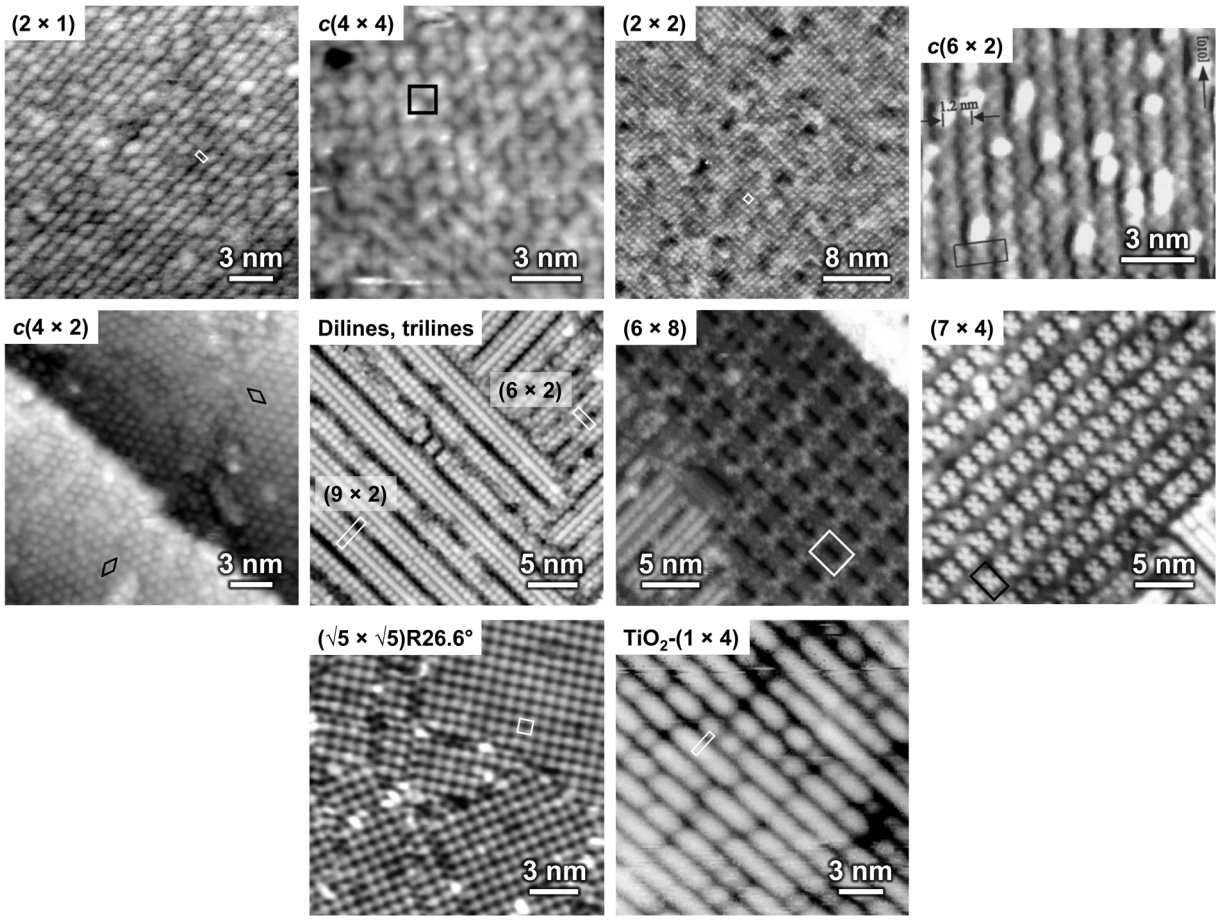

Figure 2.7: STM images of a selection of reconstructed $SrTiO_3$(001) surfaces, as labelled in their top-left corners and in the image. White/black squares and rectangles indicate reconstructed surface unit cells. Adapted from Jiang and Zegenhagen, 1999,[76] Castell, 2002,[69] Silly and Castell, 2004,[92] Deak *et al.*, 2006,[84] Silly *et al.*, 2006,[83] Marsh *et al.*, 2006,[86] and Newell *et al.*, 2007.[93]

but in the lowest-energy model each unit cell (indicated by the black rectangle) has a H_2O molecule adsorbed (Figure 2.8b). In the bottom panel of Figure 2.8b the additions are circled in red: a lone H atom attached to an O atom which is otherwise in single coordination, and an –OH group bonded to the most undercoordinated surface Ti.[89] This is consistent with the preparation conditions for (2 × 1) in most studies: annealing at up to 950 °C in UHV without sputtering.[69,74,76,80] Also, the (2 × 2) surface is possibly structurally related to (2 × 1) as it is often generated under similar conditions and observed to co-exist with (2 × 1).[72,74,75,81–83] Sputtering and/or higher-temperature thermal treatments are likely to remove the surface-adsorbed water, which is hard to recover in a UHV environment. Such treatments would lead to the *c*(4 × 2) surface and the related nanostructures.[84–86]

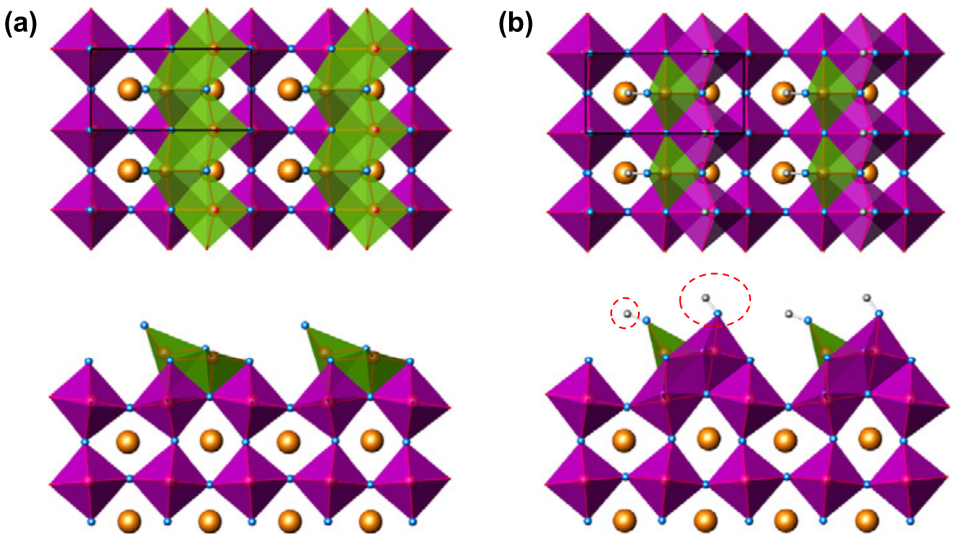

Figure 2.8: Polyhedral models of (a) the bare and (b) the hydrated $SrTiO_3$(001)-(2 × 1) surface: top views (top) and side views (bottom). Sr = large orange, Ti = red, O = blue, and H = grey. Purple polyhedra = TiO_6 and green polyhedra = TiO_5. The surface unit cell is outlined in the top views by the black rectangles and the adsorbed water (H and –OH) is circled in red in the side view of the hydrated version. Adapted from Becerra-Toledo *et al.*, 2012.[89]

2.2 Monolayer MoS_2

2.2.1 Introduction

Since the discovery of graphene, atomically thin 2D materials have been attracting growing interest.[94–96] Among these, transition metal dichalcogenides (TMDCs) have been widely studied for their great potential in the fields of nanoelectronics, optoelectronics,[15,97] and valleytronics.[98,99] It was discovered that the electronic properties of TMDCs are drastically affected by dimensionality: they are indirect-bandgap materials in their bulk form, and exhibit an indirect-to-direct transition in the monolayer limit (i.e., from 3D to 2D).[13,14] They also possess metallic edge states (i.e., in the regime of the monolayer bandgap 0–1.8 eV) in both 1D and 2D forms due to the shape finiteness.[100–103]

Amongst all TMDCs, MoS_2 and WS_2 (particularly the former) have been most extensively studied as the prototypical materials.[104] They have bandgap energies that span the visible and

near-infrared range of the electromagnetic spectrum, and therefore stand out as the most promising candidates for electronic and optoelectronic applications.[16,97,105] MoS_2 in its bulk form is a semiconductor with an indirect bandgap of 1.2–1.3 eV, which transforms into a direct bandgap of 1.8–1.9 eV when the material is as thin as a monolayer.[13,14] Figure 2.9a illustrates such a transition: the four panels are the DFT-calculated band structures of bulk, quadrilayer, bilayer, and monolayer MoS_2, respectively. The bandgap becomes direct and at the same time increases in size as the material is thinned down.[14,104] The relevant Brillouin zone points are sketched in Figure 2.9b.[106]

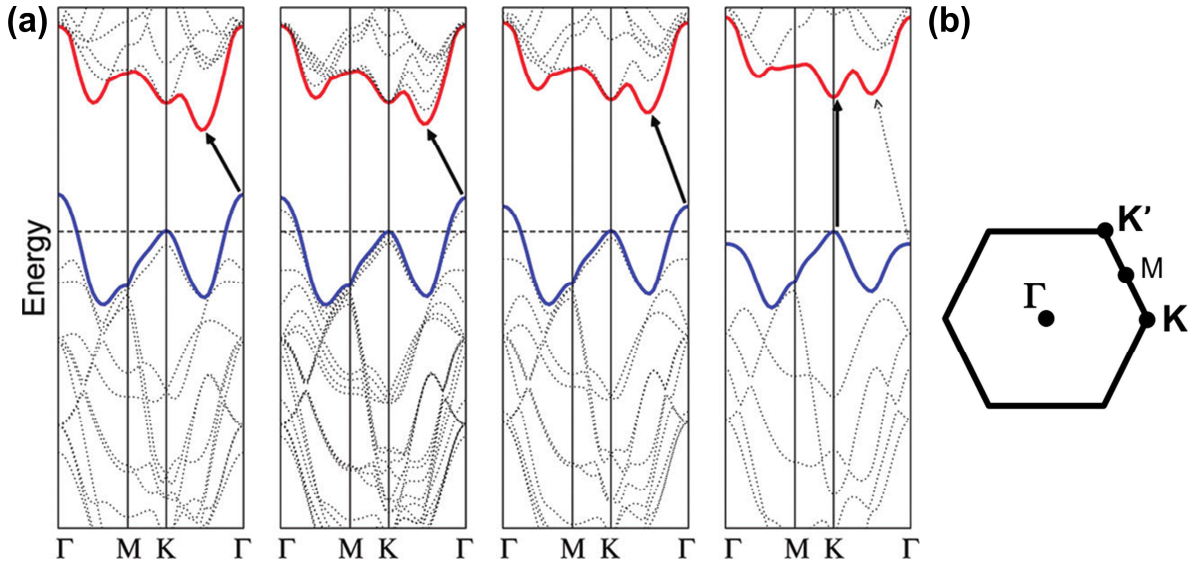

Figure 2.9: Electronic structures of MoS_2. (a) DFT-calculated band structures of MoS_2, from left to right: bulk, quadrilayer, bilayer, and monolayer, showing a transition from an indirect to a direct bandgap. The lowest-energy transitions are indicated by solid arrows. For a monolayer, the direct excitonic transition occurs at the K point. Reprinted from Splendiani *et al.*, 2010.[14] (b) Brillouin zone for a reduced dimensional hexagonal lattice with the relevant high symmetry points labelled. Reprinted from Kioseoglou *et al.*, 2016.[106]

Monolayer MoS_2 is also viewed as a 2D semiconductor with great potential because of its high charge mobility,[107] optical transparency, and extreme mechanical flexibility.[108] For example, the in-plane charge mobility was measured to be greater than 200 $cm^2 V^{-1} s^{-1}$ (having increased by two orders of magnitude in recent years), with an on/off current ratio of up to ~10^8 (where a ratio of 10^4–10^7 is generally required for use as switches).[109,110] These properties make it competitive with graphene for use in novel low-power digital electronics, e.g., field-effect

transistors (FETs).[15,97,105] It mechanical flexibility, in addition, holds a promise for better performance than graphene in flexible electronics.[108,111,112]

For a 2D material like MoS_2, the growth technique chemical vapour deposition (CVD) has the advantage over exfoliation in that it allows the substrate to influence the chemistry and properties of the MoS_2 monolayers. This is important from a technological point of view because the properties of a 2D material can be highly sensitive to its interfaces.[104] CVD growth on a well-prepared substrate results in a collection of large MoS_2 domains that have controllable morphology.[113,114] A schematic illustration of the MoS_2 CVD system is shown in Figure 3.6 (Chapter 3) using the precursors MoO_3 and S in an argon gas flow.[115]

2.2.2 Crystal structures and shapes

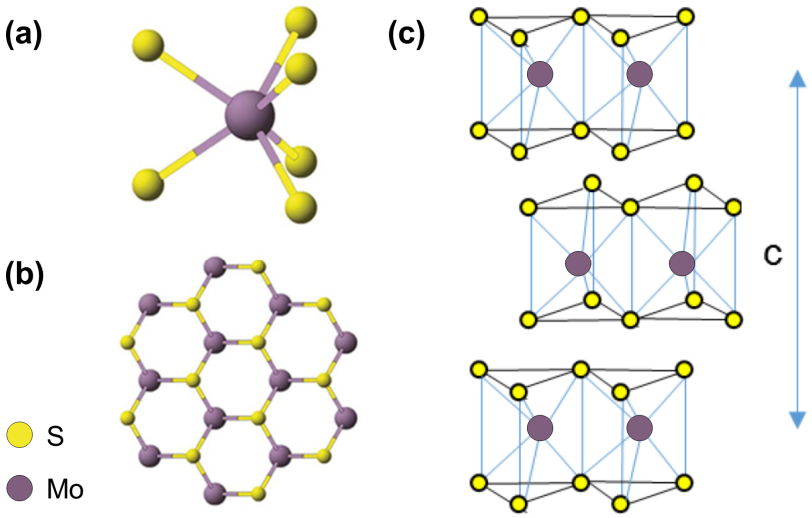

Figure 2.10: Crystal structure of 2H-MoS_2: (a) trigonal prismatic coordination of S atoms around a Mo atom, (b) top view, and (c) a unit cell. In 2H-MoS_2 the repeating unit consists of two layers of S–Mo–S ('c' = repeating unit). Adapted from Kappera *et al.*, 2014[116] and Ye *et al.*, 2015.[117]

In their 2D form, TMDCs (with the general formula MX_2) are present in a single layer of an X–M–X covalently bonded sandwich structure.[13,14] MoS_2 crystals have three main phases with different structures: 2H-, 1T-, and 3R-MoS_2.[104,116–118] Among them, 2H-MoS_2 is the

thermodynamically stable phase in which a Mo atom is prismatically coordinated by six surrounding S atoms (Figure 2.10a) and its top view is shown in Figure 2.10b.[116,117] The unit cell of 2H-MoS_2 consists of two displaced S–Mo–S layers and the unit cell height is indicated by 'c', equal to a length of 12.3 Å (Figure 2.10c).[119] Equivalently, each layer occupies a thickness of 6.15 Å in bulk MoS_2. Any two layers of S–Mo–S are weakly bonded by van der Waals (vdW) forces, but within each layer the atoms are covalently bonded.

Disulphide crystals fabricated by CVD show various domain shapes: triangles, hexagons, truncated triangles, three-pointed stars, and six-pointed stars.[120,121] Figure 2.11 summarises the reasons for the formation of different shapes by illustrating the possible growth scenarios.[122] It is assumed that all domains start growing from a hexagonal nucleus with three sides of Mo zigzag (Mo-zz) terminations and the other three sides of S zigzag (S-zz) terminations. Mo-zz and S-zz are the most energetically stable edge structures of MoS_2 domains.[120] In Figure 2.11, the shape evolution is divided into three cases: Mo:S > 1:2, Mo:S = 1:2, and Mo:S < 1:2. The exact ratio would influence the energetic stability of the Mo-zz and S-zz terminations, leading to different crystal shapes. In brief, if Mo and S atoms are present according to the exact

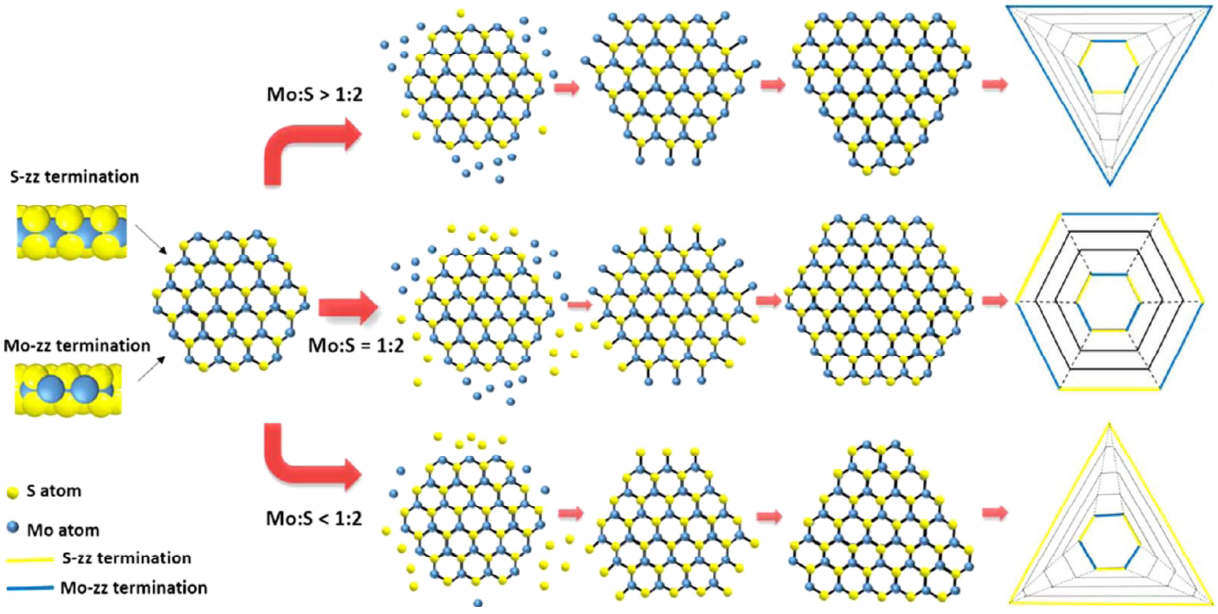

Figure 2.11: Schematic illustration of how different domain shapes of MoS_2 crystals evolve from a hexagonal starting point, with different ratios of Mo:S. Adapted from Wang *et al.*, 2014.[122]

stoichiometry, i.e., Mo:S = 1:2, then the final domain is a hexagon. Otherwise they would grow into triangles. An intermediate case is when the Mo:S ratio is only slightly above or below 1:2 – in this case the energy difference between the two types of terminations is small, resulting in truncated triangles, e.g., the shape before the last triangle in Figure 2.11. These arguments are also supported by experimental evidence.[120,121,123]

Example SEM images of (a) hexagons and truncated triangles and (b) triangles of MoS_2 crystals are shown in Figure 2.12.[122] When the Mo:S ratio deviates too much from 1:2, e.g., if Mo or S is very insufficient, a three-pointed star will form. It is also likely to transform into several-pointed stars because of the imperfect S-zz edges (Figure 2.12c). In practice, in the CVD setup for MoS_2 growth, the factors affecting the Mo:S ratio mainly include the amounts of precursors used and the temperature distribution, the latter of which influences the amount of MoO_3 evaporated.

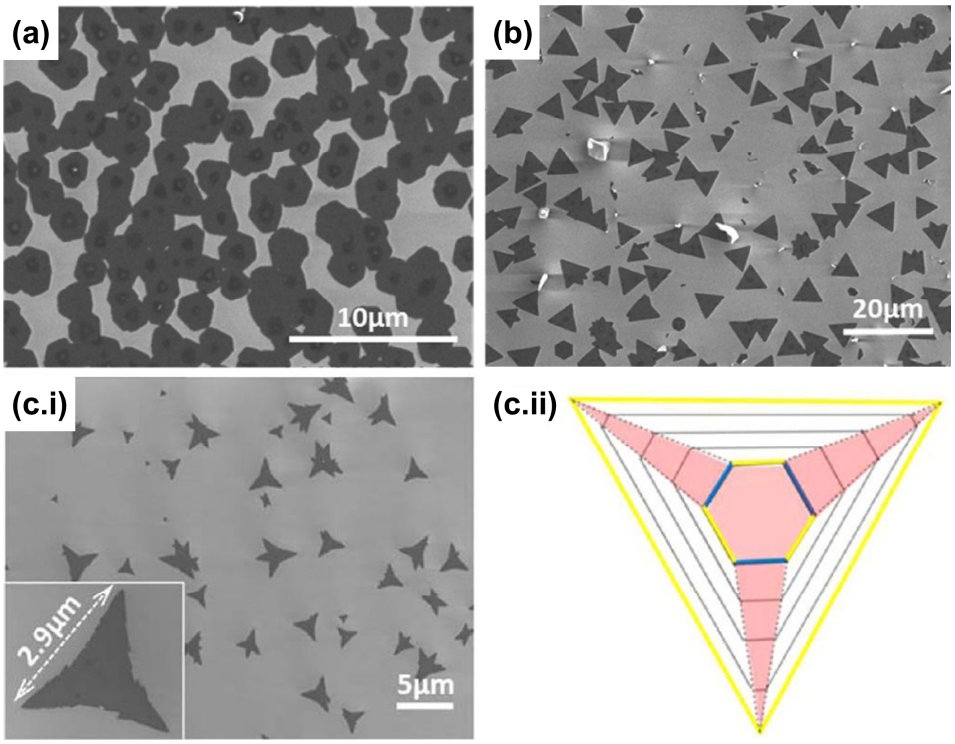

Figure 2.12: SEM images of MoS_2 crystals grown on a SiO_2/Si substrate: (a) hexagons and truncated triangles, (b) triangles, and (c.i) several-pointed stars, with an inset of an enlarged three-pointed star. (c.ii) Schematic drawing showing the formation of a three-pointed star. Reprinted from Wang *et al*., 2014.[122]

2.2.3 Photoluminescence (PL) and Raman studies

Because of the interesting optical properties of monolayer MoS_2, this material is most frequently characterised by Raman spectroscopy and PL. These techniques can provide information on the layer thickness, strain, doping level, lattice defects, and crystal texture of MoS_2 crystals.

The main PL peak of monolayer MoS_2 occurs at a wavelength corresponding to a photon energy of 1.8–1.9 eV,[13,14,124–126] consistent with the value of the direct bandgap. Figure 2.13a shows a typical PL spectrum of monolayer MoS_2 grown on SiO_2 by CVD.[127] In this case, it consists of four sub-peaks: A, B, A^-, and LS. Both A and B peaks arise from neutral exciton (i.e., an electron and a hole) emissions from direct optical transitions. These transitions occur from the conduction band to the split valence bands at the K point (K→K), as shown in the electronic band structure of monolayer MoS_2 in Figure 2.13b.[128] The B emission occurs at a higher photon energy as it originates from a transition towards a lower-lying valence band.[129] In Figure 2.13a, there are also two small sharp peaks at the B position, which possibly result from core-level transitions. The A^- peak arises from the recombination of negative trions, each

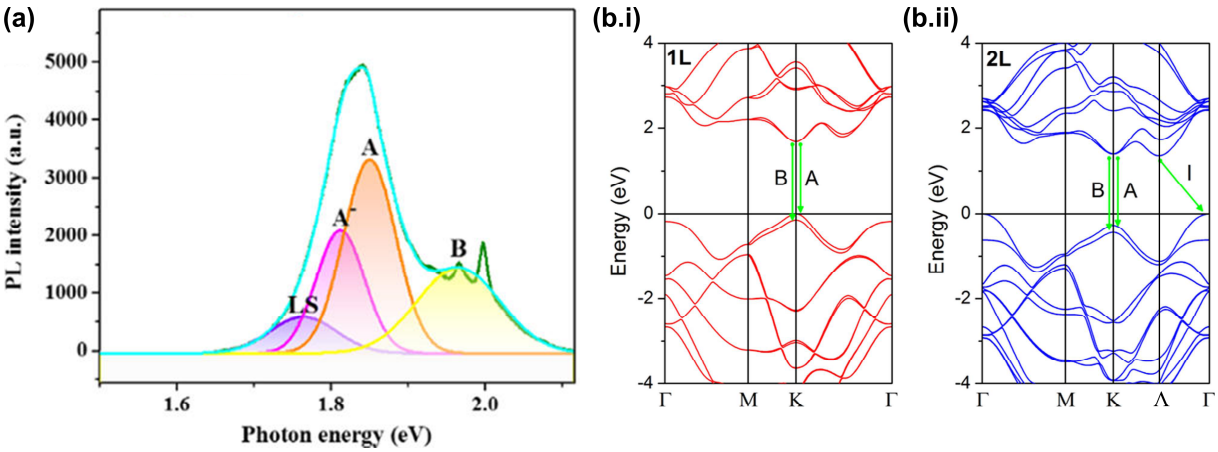

Figure 2.13: PL of MoS_2. (a) Deconvoluted PL spectrum of monolayer MoS_2 with four Gaussian peaks fitted: B excitons, A excitons, A^- trions, and localised states (LSs). Adapted from Xu *et al.*, 2018.[127] (b) DFT-calculated electron band structures of (b.i) monolayer and (b.ii) bilayer MoS_2 showing the A, B, and I optical transitions. Adapted from Kim *et al.*, 2016.[128]

of which is composed of two electrons and a hole. They emit at a slightly lower energy than the A excitons by ~20 meV because of the large binding energy of the second electron.[130,131] The fourth PL peak labelled 'LS' is due to localised states (LSs) correlated with the lattice defects in MoS_2.[132] In bilayer (and thicker) MoS_2 crystals, indirect optical transition ($\Lambda \rightarrow \Gamma$) can also occur, as indicated by the arrow 'I' in Figure 2.13b.ii.[128] An example of the resulting PL peak will be shown using my own results in Chapter 4 (Figure 4.7f).

On the other hand, a typical Raman spectrum of MoS_2 crystals shows two active modes: in-plane E^1_{2g} and out-of-plane A_{1g} peaks (Figure 2.14).[133] Example Raman spectra are demonstrated in Figure 2.15b in relation to the MoS_2 crystal thickness.

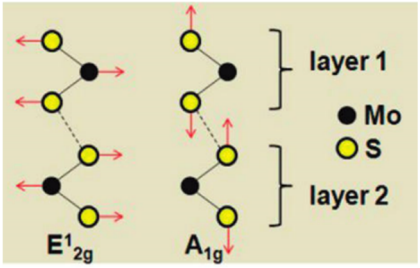

Figure 2.14: Atomic displacements in the two Raman modes. Adapted from Lee *et al.*, 2010.[133]

Below is a discussion of various factors that can cause changes in the peak intensities and positions in the PL and Raman spectra.

Effects of layer thickness

As MoS_2 crystals exhibit a crossover from an indirect to a direct bandgap semiconductor when thinned to a monolayer, the **PL signals** show a dramatic enhancement by a factor of more than 10^4.[13] Figure 2.15a shows the averaged PL spectra of *n*-layer (*n*L, where FL = few-layer) MoS_2 crystals.[124] The PL intensity decreases with increasing crystal thickness, where the main drop occurs upon the transition from a monolayer to a bilayer.[134] Also, both the A and B peaks

soften/red-shift upon increased thickness of the MoS_2 crystals.[13,124] Note that Figure 2.13a and Figure 2.15a present two different common ways of plotting PL spectra, in which the PL intensity is plotted against either photon energy or wavelength, and the resulting spectra are horizontally flipped with respect to each other.

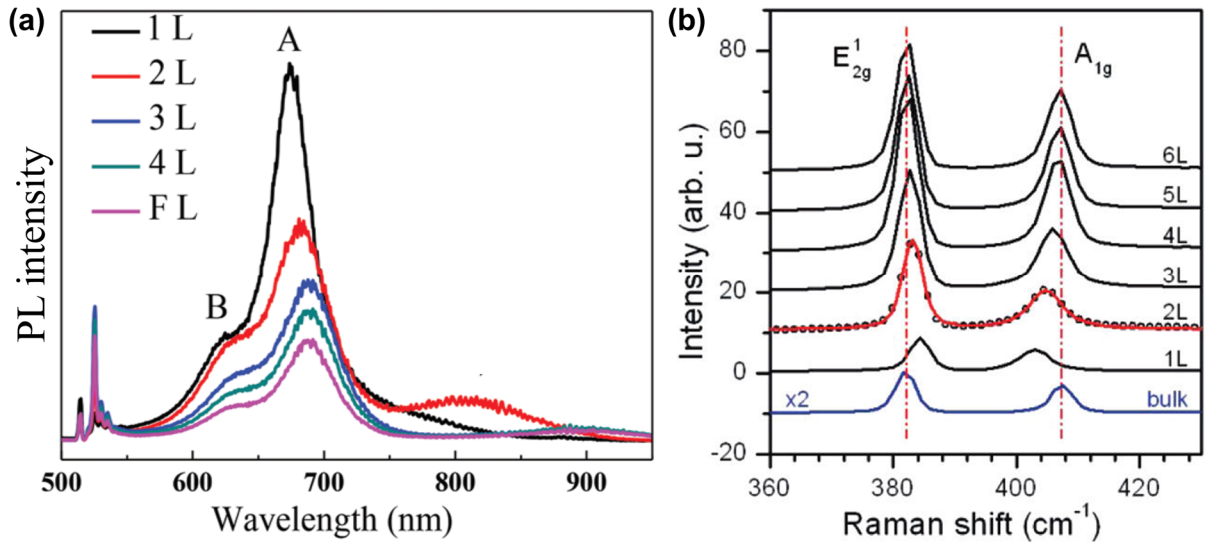

Figure 2.15: (a) Averaged PL spectra of various thicknesses of MoS_2 crystals, where *n*L = *n* layer(s), FL = few layers. The PL intensity drops substantially from 1L to 2L upon the transition from a direct to an indirect bandgap and it gradually decreases further for thicker samples. Adapted from Dhakal *et al.*, 2014.[124] (b) Raman spectra of thin (*n*L) and bulk MoS_2 crystals, showing the E^1_{2g} and A_{1g} peaks. Reprinted from Lee *et al.*, 2010.[133]

Lee *et al.* presented the first and very representative report of **Raman scattering** studies of monolayer and few-layer MoS_2 samples: in Figure 2.15b, the E^1_{2g} and A_{1g} Raman peaks shift away from each other in frequency with increasing thickness.[133] This and many later works all concluded that the difference between their frequencies (often denoted Δk) can be used as an excellent tool to unambiguously pinpoint the number of layers in MoS_2 crystals.[118,122,123] The value of Δk is ~20 cm^{-1} for monolayers and is experimentally verified to be very close regardless of the growth mechanism as long as good crystallinity is obtained.[121,122,126,134] However, in practice the actual value of Δk is affected by many other factors, typically the strain and the doping level in the MoS_2 crystal.

Effects of strain

The lattice mismatch between a thin MoS_2 crystal and its substrate can modify the strain in MoS_2.[11] A common cause of inbuilt strains is the different thermal expansion coefficients (TECs) of MoS_2 and the underlying substrate. This gives rise to a dimension mismatch at the interface during cooling after CVD growth.[135] Strain can also develop as a result of the epitaxial growth of MoS_2 on a lattice-mismatched substrate.[136]

Strains in MoS_2 monolayers can modulate the band structure of the material because the strain modifies the lattice constant and hence the reciprocal lattice constant, which in turn, changes the shape of the electronic bands. Tensile strain results in a reduced bandgap, which is reflected as a redshift in the **PL signal**.[137] The bandgap of monolayer MoS_2 was found to decrease by 50–75 meV per 1% tensile strain,[138] consistent with simulations[139] and optical experiments.[140] On the other hand, compressive strain in MoS_2 crystals is found to blue-shift the PL peak, increase its intensity, and reduce the full width at half maximum (FWHM) of the peak.[141]

In **Raman spectra**, the in-plane mode E^1_{2g} can be much affected by the strain, which has been observed to stiffen upon a compressive strain and soften upon tension. On the other hand, the corresponding out-of-plane A_{1g} peak shows weaker strain dependence.[137,141–145] For monolayer MoS_2, the redshift in the E^1_{2g} peak was reported to be 2.1 cm^{-1} per % of uniaxial tensile strain, but it was only 0.4 cm^{-1} in A_{1g}.[142] For trilayer MoS_2, the blueshift per % of biaxial compression was found to be 4.7 cm^{-1} in the E^1_{2g} peak and 1.8 cm^{-1} in A_{1g}.[141]

Effects of doping level

In a **PL spectrum**, as mentioned above, the A^- peak resulting from negative excitons locates at a slightly lower energy than the A peak resulting from neutral excitons.[130] Therefore, if the monolayer MoS_2 is *n*-doped, e.g., from its substrate, its overall PL peak will red-shift. A possible source of the extra electrons is charged impurities, e.g., at the SiO_2/MoS_2 interface.[146,147] Another possible source is conducting substrates. Theory states that conducting substrates (e.g., gold, graphene) should quench the PL intensity via charge transfer from MoS_2 crystals to the substrates.[148–150] This provides an additional non-radiative path for exciton recombination and hinders the recombination of electron-hole pairs created by the photoexcitation.[148–150] However, this is not consistently found in past literature, where in many cases conducting substrates boost the PL intensity.[126,146,148] Hence the way in which the substrate conductivity impacts the PL intensity remains a controversial subject.

Raman spectroscopy is also influenced by the sample doping level or charge carrier concentration.[151–155] As the A_{1g} mode originates from the out-of-plane vibrations of the charged Mo and S atoms, it stiffens with a decreasing electron density in the MoS_2 layer. This can sometimes be due to a reduced level of doping from the substrate.[146]

Effects of structural defects

Poorer crystallinity of MoS_2 monolayers is found to result in weaker **PL** intensity, e.g., when MoS_2 crystals are grown on SiO_2 substrates, which usually have a higher level of roughness and impurities compared with crystalline substrates.[134,148,156] Also, structural defects in MoS_2 crystals can lead to an increase in the localised states,[132] and this causes a redshift of the PL peak, as shown in Figure 2.13a.[127]

Effects of crystal texture

Finally, in a **Raman spectrum**, the relative integrated intensities of E^1_{2g} and A_{1g} can provide information on the texture of the MoS_2 crystals. Two general types of surface sites are present on these crystals: terrace sites on the basal planes and edge sites on the side surfaces.[157,158] The E^1_{2g} mode corresponds to the in-plane Mo−S phonon and is preferentially excited for terrace terminations, whereas the A_{1g} mode corresponds to the out-of-plane Mo−S phonon and is preferentially excited for edge terminations.[127,157,159] It follows that a larger integrated intensity ratio of A_{1g}/E^1_{2g} reflects a larger proportion of edge sites, e.g., in vertically grown MoS_2 sheets, which are important for catalytic applications in the hydrogen evolution reaction (HER).[127,158]

2.2.4 Van der Waals epitaxy

For MoS_2 monolayers with controllable morphology (e.g., grown by techniques like CVD), epitaxy has been shown to effectively control MoS_2 crystal orientations, which is required to minimise the concentration of grain boundaries in the MoS_2 layer.[114,160] Figure 2.16a shows the

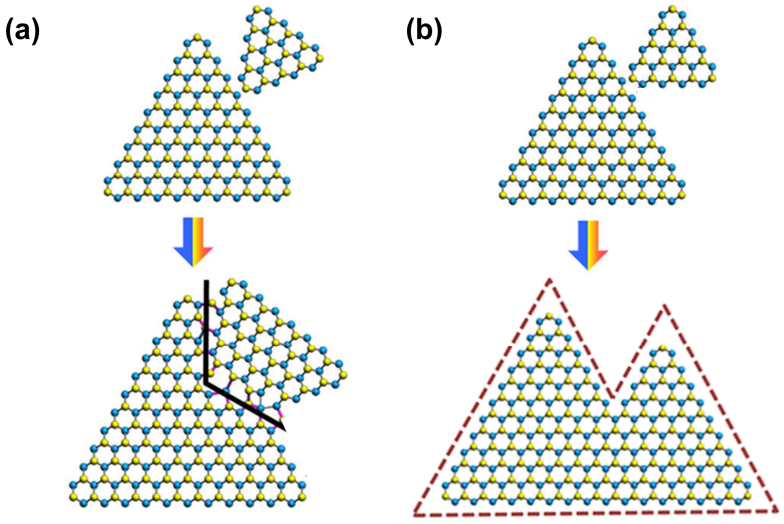

Figure 2.16: Atomic models showing (a) two misoriented MoS_2 crystals joining and creating a grain boundary and (b) a boundary-free domain formed by two MoS_2 crystals with the same orientation. Adapted from Ji *et al.*, 2015.[114]

creation of a grain boundary when two misoriented MoS_2 crystals merge to form a larger domain. In contrast, the grain boundary can be avoided if the component crystals are nucleated with the same orientation (Figure 2.16b).[114] This is especially important in the large-area synthesis of MoS_2 because grain boundaries are detrimental to the electrical properties (e.g., charge mobility) of polycrystalline films.[120,161,162]

By its nature, epitaxial growth cannot occur on amorphous substrates like SiO_2.[122] On crystalline substrates, the main mechanism that allows epitaxy to occur is generally believed to be due to vdW forces on both metallic and nonmetallic substrates,[114,160,163–165] e.g., *c*-plane sapphire[114,160] and Au(111).[165] Figure 2.17a shows some MoS_2 crystals on sapphire grown by CVD and their size is of the order of microns.[160] The triangular crystals are mainly oriented in two ways: pointing upwards and downwards ($\theta = 0°$ and 60° in Figure 2.17b). A minority of them also point left or right ($\theta = 30°$ and $\theta = 90°$ in Figure 2.17b).[160] It should be commented that the MoS_2 atomic models in Figure 2.17b have edge terminations that are unrealistic: the edge atoms have too many dangling bonds and a more realistic type of termination is shown in Figure 2.16. In comparison, the MoS_2 crystals on Au(111) are nanosized (Figure 2.17c) as they were grown by a much slower method than CVD, which involves depositing Mo in a H_2S atmosphere.[166] The STM image also shows the herringbone structure of the Au(111) substrate,

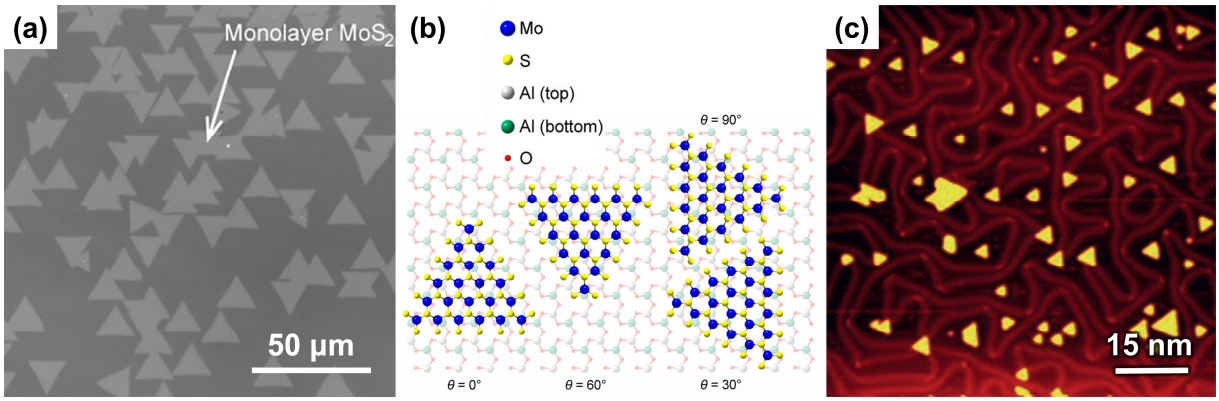

Figure 2.17: Epitaxial MoS_2 crystals. (a) Optical microscopy image of monolayer MoS_2 crystals on *c*-plane sapphire. (b) Schematic drawing of the four crystal orientations in (a). Reprinted from Dumcenco *et al.*, 2015.[160] (c) STM image of MoS_2 crystals on Au(111). Reprinted from Walton *et al.*, 2013.[166]

in which each ridge separates alternating hexagonal-close-packed (hcp) and face-centred-cubic (fcc) regimes.[167] If we consider only the top two atomic layers in hcp and fcc structures, they have the same atomic arrangement but are rotated by 180° with respect to each other. Since the MoS_2 crystals 'flip' their directions by 180° across each ridge, they are in fact exclusively oriented in the same way with respect to the substrate.

Although the vdW interaction is relatively weak compared to in-plane covalent bonding, it still provides a significant force between two 2D sheets. It has been confirmed to powerfully control the interlayer epitaxy of MoS_2 bilayers, where the AA and AB stacking configurations (0° and 60° relative layer rotation) are overwhelmingly favoured compared to others.[168] Furthermore, the indirect-to-direct transition of the MoS_2 bandgap in the monolayer limit is a direct consequence of the absence of neighbouring layers, which only interact via vdW forces. This means that the interlayer forces perturb each other's electronic band structures. Therefore, the importance of vdW bonding should not be overlooked with respect to interfacial bonding between MoS_2 and its substrate. Nevertheless, other possible interfacial bonding mechanisms have also been reported, including electrostatic attraction between MoS_2 and sapphire[114] and chemical bonding between sulphur and various metals.[169–172] The nature of the Au–S bond is particularly controversial; it is claimed to perturb the electronic structure very little in some studies[165,170] and have a covalent nature in others.[169]

2.2.5 Thermal degradation

Many transistors, circuits, and sensors require electronic materials that can operate at high temperatures.[173] Wide-bandgap semiconductors have been found to function effectively at elevated temperatures,[174] and increasing attention is being directed towards the use of

monolayer MoS_2 in high-temperature applications.[173] It is therefore important to understand the effects of high-temperature processing on the structure and optical properties of monolayer MoS_2.

Previous studies in this area were mostly carried out as part of the synthesis of MoS_2 or immediately after its growth. They were used to enhance the crystallinity,[127,175–178] optical properties,[127,175–177] or electronic properties of the MoS_2 crystals.[179,180] A few studies also explored the thermally accelerated oxidation of MoS_2 into MoO_3 under ambient conditions, starting from 100 °C until complete transformation into MoO_3 at up to 550 °C.[181–186] In these studies, the MoS_2 samples were either monolayer/few-layered (supported on SiO_2) or powdered. In the absence of oxygen, MoS_2 is much more stable: the atomic structure of monolayer MoS_2 crystals on Au(111) was seen to be unperturbed at up to 630 °C.[187] On FL MoS_2 crystals on oxide/nitride substrates, thermal decomposition did not occur until 850 °C in the absence of oxygen.[175] In a bulk MoS_2 crystal, sulphur was not completely removed until above 1203 °C in vacuum.[188] Atomic force microscopy (AFM) was used to determine that the oxidation of MoS_2 monolayers started with triangular pits in air (Figure 2.18a).[184,185] The triangular pits reflect the three-fold symmetric lattice structure of monolayer MoS_2 (Figure 2.18b).[185] The etching in Figure 2.18a was predominantly activated by native defects in the crystal and the degradation

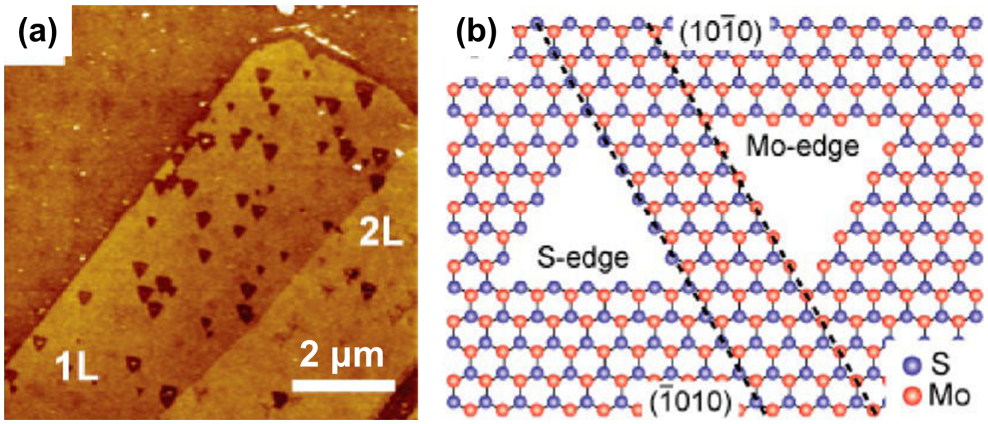

Figure 2.18: Thermal degradation of MoS_2 crystals. (a) AFM image of 1L and 2L MoS_2 on SiO_2 after oxidation at 320 °C for 3 h, showing triangular pits. (b) Schematic drawing of the MoS_2 lattice structure with triangular pits. Reprinted from Yamamoto *et al.*, 2013.[185]

product MoO_3 had not formed yet at this stage. Nevertheless, to date, there has not been a systematic report on the morphology of thermally degraded MoS_2 monolayers in vacuum. Additionally, any methods to recover the properties of degraded MoS_2 are also of significant interest.[127]

2.3 Gold nanostructures

2.3.1 Introduction

In contrast to the inertness of bulk gold, nanosized gold has been a focus of research since the 1980s because of its exceptional catalytic activity.[17] A well-known example is that gold nanoparticles below 5 nm are a highly efficient catalyst for CO oxidation at room temperature.[17,189–191] Their catalytic activity is due to the high fraction of edge/corner atoms, which are the most catalytically active sites.[192] Different facets of metal nanoparticles also exhibit distinct catalytic properties because of their different atomic arrangements and energies.[193,194] For example, high-index facets such as {730} and {210} of platinum (Pt) nanocrystals were found to exhibit enhanced catalytic activity (by up to 400%) for the electro-oxidation of formic acid and ethanol, which are alternatives for direct fuel cells.[193] Hence the catalytic activity of gold nanoparticles is a shape-dependent property. In addition, nanogold exhibits interesting optical behaviour and it has been extensively studied for its application in surface plasmon resonance (SPR) sensors.[18–21] Again, the optical properties of gold nanostructures are highly dependent on morphological factors such as size and shape.[21,195–199] For example, gold nanocubes, tetrahedra, icosahedra, decahedra, octahedra, and nanospheres all display different SPRs because they possess different proportions of sharp edges.[21,195,197] Another example is that among the cubic, cuboctahedral, and octahedral nanocrystals of silver

(Ag), the octahedral nanocrystals display the highest Raman scattering enhancement factor and the best sensitivity for trace amounts of arsenic (As) in contaminated water.[200] Therefore, shape control of gold nanoparticles is a critical area of research that can lead to the rational design of their catalytic and optical properties.[201]

2.3.2 Wulff and Winterbottom constructions for fcc crystals

The thermodynamically stable shape of a free-standing metal crystal is predicted by the Wulff construction.[202] In the Wulff construction, the perpendicular distance of a crystal surface from the origin of the 'Wulff point' (h_{hkl}) is proportional to the surface energy per unit area of that surface (γ_{hkl}). This is illustrated in Figure 2.19b, which shows a Wulff crystal with an fcc structure.[203] The intersection point of the arrows in the middle is the Wulff point. The 3D version of this crystal is shown in Figure 2.19a.[204] On the surface of this example crystal, {111}, {001}, and {110} facets are exposed, which are the three lowest-energy crystallographic planes of an fcc crystal in the order of $\gamma_{111} < \gamma_{001} < \gamma_{110}$. The reason for $\gamma_{111} < \gamma_{001} < \gamma_{110}$ is that a lower-energy surface has a higher atomic density and its atoms have a higher coordination number with neighbouring atoms in the surface plane.[205] Therefore, higher-index crystallographic planes like {211} are rarely seen and in many cases even {110} and {001} facets do not appear. These will be shown in a few examples later in this section.

In Figure 2.19c the Wulff crystal is supported on a substrate. It has a (111) top facet and a height of h. The energy γ^* is defined as $\gamma^* = \gamma_{interface} - \gamma_{substrate}$ (or $\gamma_i - \gamma_s$),[203] i.e., it is the net energy change at the interface when the crystal is attached to the substrate. The crystal height h, or where the substrate truncates the crystal, is predicted by the Winterbottom construction,[206] also known as the Wulff–Kaishew theorem,[207] which modifies the Wulff construction by including

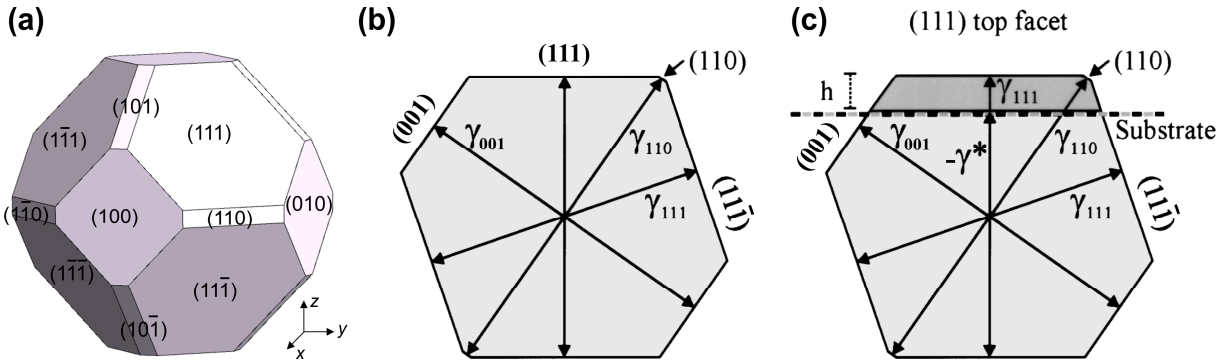

Figure 2.19: Wulff shape of an fcc crystal with {111}, {001}, and {110} facets: (a) 3D model (generated using Wulffmaker),[204] (b) cross section, and (c) cross section of the crystal supported on a substrate (darker grey). In (c), the crystal has a (111) top facet and a height of *h*. Adapted from Hansen *et al.*, 2002.[203]

the crystal–substrate interfacial energy (γ_i) or γ^*. Figure 2.20 shows five different degrees of wetting of a supported Pt crystal, from no wetting (first crystal) to partial wetting (middle three) to complete wetting (last crystal).[29] The energy condition for each degree of wetting is written below the corresponding crystal, determined by the relative values of γ^* (= $\gamma_i - \gamma_s$) and γ_{Pt}. Lower values of γ^* and higher values of γ_{Pt} encourage the crystal to wet.

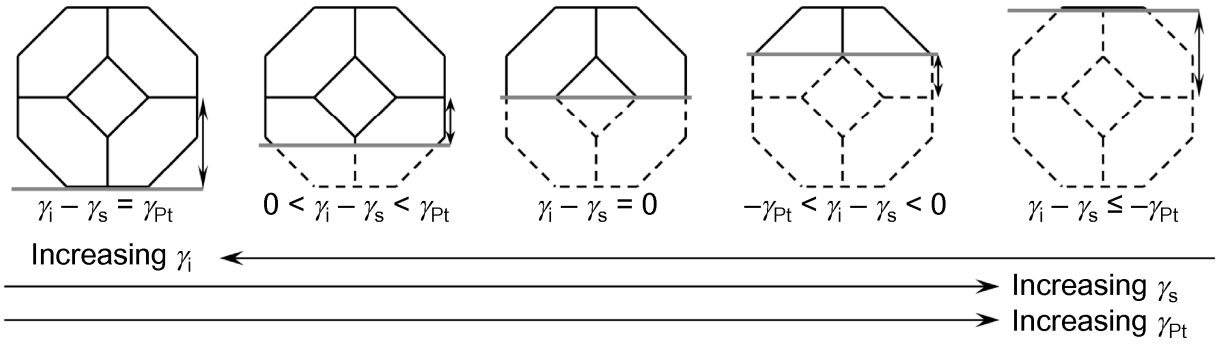

Figure 2.20: Winterbottom construction for a supported Pt crystal with a (001) base and various degrees of wetting. The grey line represents the substrate. Higher γ_i leads to less wetting; higher γ_s and γ_{Pt} lead to more wetting. Adapted from Enterkin *et al.*, 2011.[29]

2.3.3 Influence of substrate on nanocrystals

According to the Winterbottom construction, the substrate plays an important role in determining the aspect ratio of a crystal via γ_i and γ_s. An example is shown in Figure 2.21, in

which gold crystals supported on CeO_2(001) are imaged by aberration-corrected high angle annular dark field (HAADF) scanning transmission electron microscopy (STEM) before and after a water–gas shift (WGS) reaction.[208] Before the reaction there were extended gold atomic layers at the interface, labelled as the Stranski−Krastanov (SK) layer in Figure 2.21a and also shown in the atomic model below the HAADF image. After the reaction, the SK layer vanished and the gold crystal became taller (i.e., a higher height-to-width ratio) as additional {111} reentrant facets were observed (Figure 2.21b). According to Lin *et al.*, the WGS reaction changes the atmosphere from oxidative to reductive, and this environmental change increases the value of γ^* (= $\gamma_i - \gamma_s$) between the gold crystals and the substrate.[208] In many studies the experimental aspect ratio of nanocrystals were used to calculate γ^* and the energies associated with it, e.g., γ_i, γ_s, and the adhesion energy γ_{adh}.[90,203,209–212]

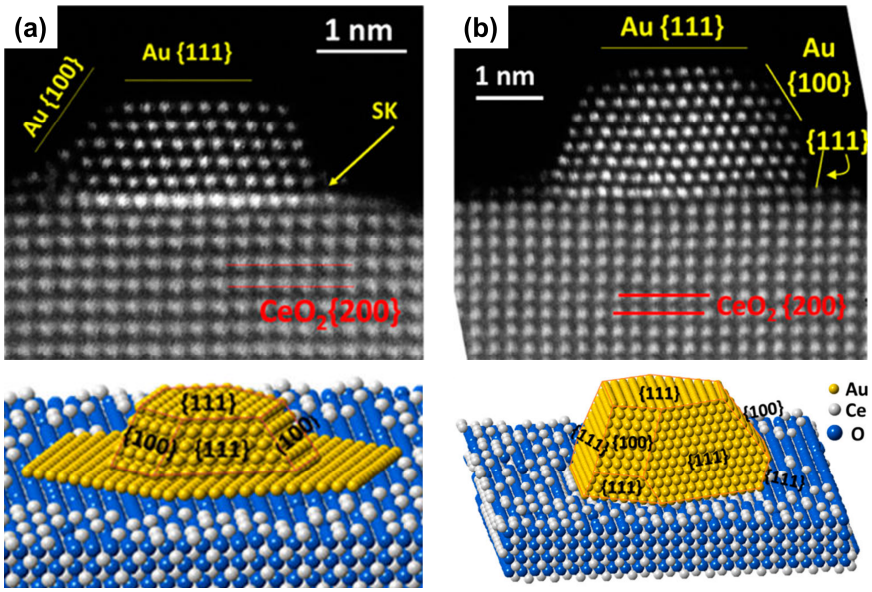

Figure 2.21: Atomically resolved HAADF images of gold crystals on a CeO_2(001) substrate (a) before and (b) after a water–gas shift (WGS) reaction. Below the images are the corresponding atomic models. Reprinted from Lin *et al.*, 2015.[208]

Apart from the aspect ratio of nanocrystals, γ^* also influences the relative energies of different crystal orientations, which have different interfaces with the substrate. For example, the low-energy interfaces of supported fcc crystals include {111}, {001}, and {110}. Gold crystals have not been studied in this respect but Figure 2.22a–c shows some STM images of palladium

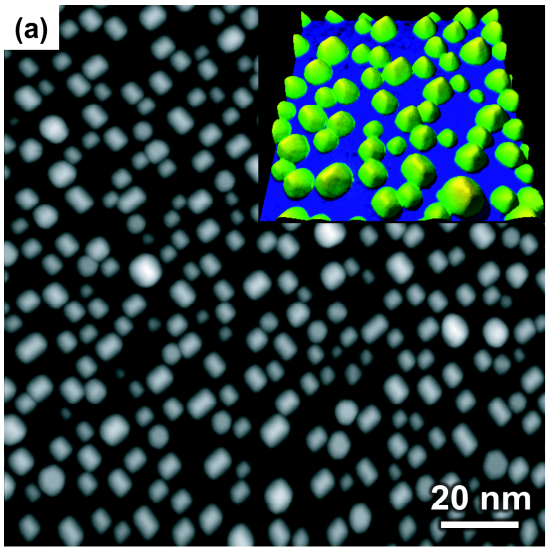

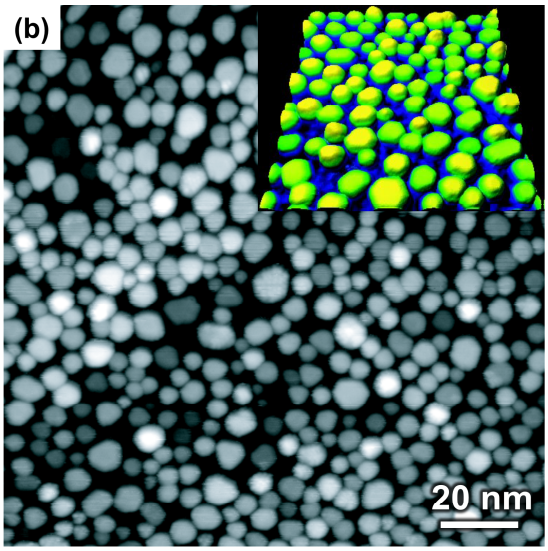

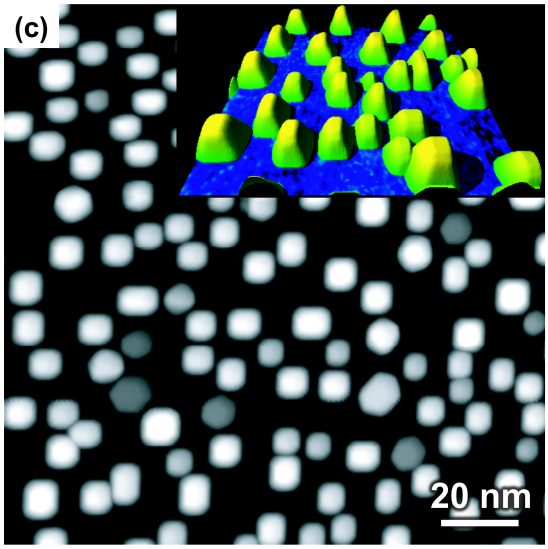

(d)	Wulff shape	Substrate	Substrate temp.	Post anneal-ing
a	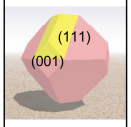	$SrTiO_3$(001) -(2 × 1)	Room temp.	650 °C, 45 min
b	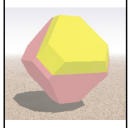	$SrTiO_3$(001) -*c*(4 × 2)	Room temp.	650 °C, 45 min
c	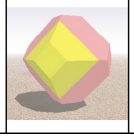	$SrTiO_3$(001) -*c*(4 × 2)	460 °C	650 °C, 45 min

Figure 2.22: (a–c) STM images of Pd crystals on $SrTiO_3$(001) substrates and (d) their Wulff models and preparation conditions. The crystals were deposited onto differently reconstructed $SrTiO_3$(001) surfaces in UHV and the substrates were held at different temperatures during deposition. All three samples were post-annealed. Reprinted from Silly and Castell, 2005.[90]

(Pd) crystals grown on $SrTiO_3$(001) substrates in UHV.[90] The crystals have distinct shapes in panels (a–c) but they are all produced by different orientations of the Wulff shape of Pd, as shown by the 3D models in Figure 2.22d. The Wulff shape of Pd crystals is a truncated octahedron (pink), i.e., it has {111} and {001} facets exposed. The Wulff shape can be cut in different orientations (yellow) to give the three shapes observed in Figure 2.22a–c, named 'huts', 'hexagons', and 'truncated pyramids', respectively. Their crystallographic interfaces with the substrates are (110), (111), and (001), respectively. Silly and Castell explained that the lowest energy shape depends on $\gamma^* = \gamma_i - \gamma_s$.[90] The value of γ^* is therefore dependent on the substrate

reconstruction, i.e., (2 × 1) or *c*(4 × 2), as listed in Figure 2.22d. The other influencing factor is the substrate temperature during deposition (Figure 2.22d), which is a kinetic factor. On $SrTiO_3$(001)-*c*(4 × 2), the truncated pyramid was found to be the stable structure and the hexagon to be metastable. The latter was the favoured growth shape when the substrate was held at room temperature and the crystals were then not able to overcome the energetic barrier to transform into pyramids.[90,213]

Silly and Castell also reported that larger Pd crystals deviate from their equilibrium shapes.[90,213] The huts have elongated {111} side facets and become longer than their equilibrium form. The hexagons grow by increasing their width rather than height and hence become flatter than equilibrium. The pyramids evolve in such a way that their base becomes rectangular rather than square. The authors explained that it is more difficult for a larger crystal to reach its equilibrium shape because atoms have to diffuse longer distances.[213] This explanation does apply to hexagons being flatter, but does not fully address why huts and pyramids are laterally elongated in certain directions.

2.3.4 Influence of environment on gold nanocrystals

As we have seen, a Wulff crystal of gold has {111} and {001} facets only (Figure 2.21). Its shape is defined by two geometric ratios, one of which is the height-to-width ratio determined by the substrate, as discussed above. The other one is the ratio between the {111} and {001} surface areas (A_{111}/A_{001}), which depends on the ratio of γ_{111} and γ_{001}.[214] In other words, it should be a constant in UHV. In reality, the ratio A_{111}/A_{001} is very much influenced by the local environment, which, when outside UHV, can involve hydrocarbons in air, CO gas, and other adsorbates,[215] and these will be discussed later in this section.

There have been only a few UHV investigations of gold crystals, one of which is already demonstrated in Figure 2.21.[208] Another example is shown in Figure 2.23,[212] in which gold nanocrystals were grown on $SrTiO_3$(001) in UHV and most of them have the 'hexagon' shape (Figure 2.23b). However, in these studies the A_{111}/A_{001} ratio was not specifically analysed.

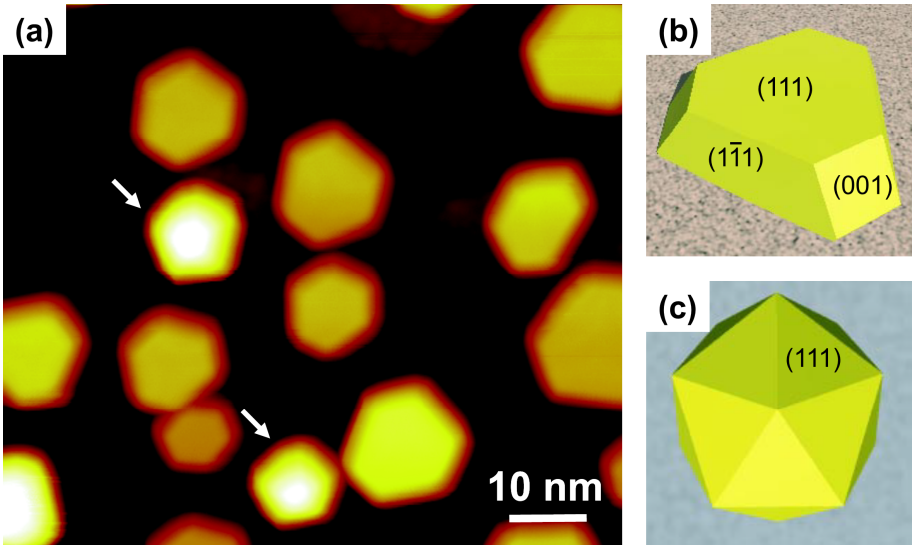

Figure 2.23: (a) STM image of gold particles on $SrTiO_3$(001)-(2 × 1) and (b,c) their models. The gold particles in (a) are a mixture of single crystals (hexagons) and multiply twinned particles (MTPs) (pentagons), the latter of which are indicated by white arrows. A single crystal and an MTP are modelled in (b,c), respectively. Adapted from Silly and Castell, 2006.[212]

In Figure 2.23a, a minority of the gold islands adopt an icosahedral shape (indicated by white arrows) and they are referred to as multiply twinned particles (MTPs). In this orientation, they have pentagon symmetry and a model is shown in Figure 2.23c. A free-standing icosahedron is composed of 20 regular tetrahedra meeting at one point (middle of the icosahedron) and exposing 20 faces which are all equilateral triangles. The individual tetrahedra only have {111} facets (the lowest-energy termination) but together they introduce many twin boundaries. Therefore, the MTPs are a particle form with a reduced surface energy at the cost of strain and twinning energies.[196,216,217] MTPs also exist in other shapes and they have been comprehensively studied as 'modified Wulff shapes' in the past decades.[218–222] MTPs are calculated to be the more stable morphologies at small sizes than their single-crystal

counterparts,[220,223–225] though they often retain their nucleation shapes even when they grow beyond the critical size.[226]

Previous reports on gold crystal shapes are mostly from crystals grown in solution, e.g., using the polyol synthetic method.[21,195–198] Solvent-based growth gives rise to free-standing gold crystals that are a mixture of single crystals and MTPs. The commonly observed shapes are summarised in Figure 2.24.[195–198,205] Figure 2.24a,b shows two MTP morphologies: decahedron and icosahedron. Similar to the icosahedron discussed above, the decahedron is a collection of five regular tetrahedra sharing a common edge, exposing ten {111} facets which are equilateral triangles. Figure 2.24c–g shows five types of single crystals. The truncated tetrahedron (Figure 2.24c) is terminated with {111} planes only. If such a crystal grew into a full tetrahedron, geometrically it would be the constituent part of both the decahedron and the icosahedron (though these structures are not 'built up' by the tetrahedra, but rather form by twinning). It is interesting to note that the tetrahedron is the only non-Wulff single crystal shape observed. The

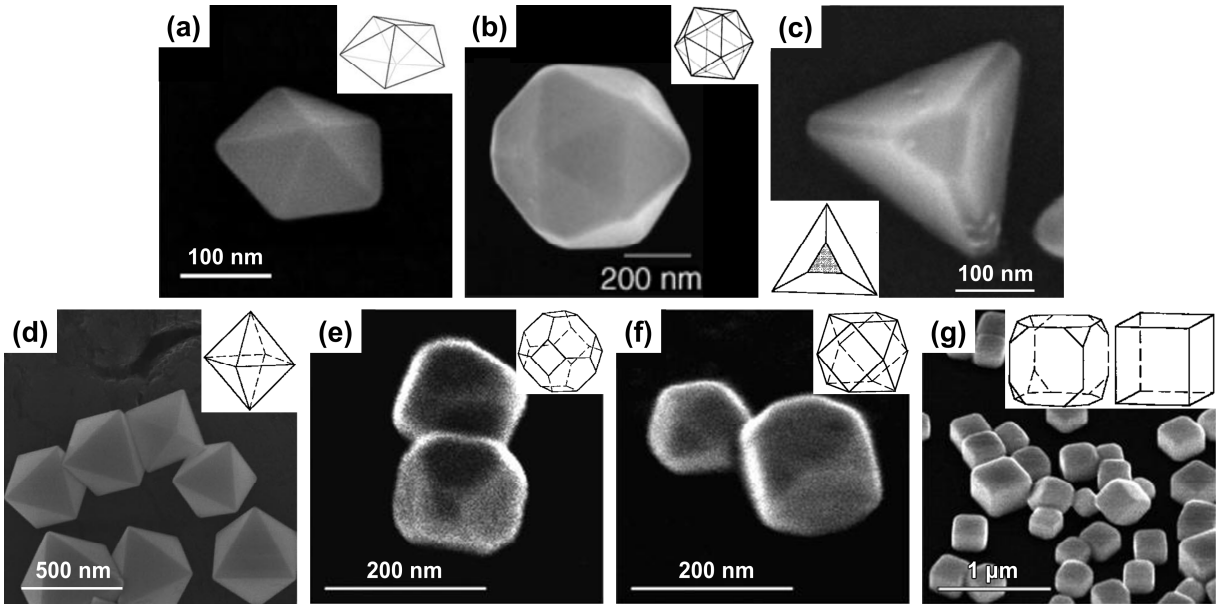

Figure 2.24: SEM images of gold particles with various shapes. (a,b) MTPs: (a) decahedron, (b) icosahedron; (c–g) single crystals: (c) truncated tetrahedron, (d) octahedron, (e) truncated octahedron, (f) cuboctahedron, and (g) (truncated) cube. The insets in the individual panels contain the models of the corresponding shapes. Adapted from Wang, 2000,[205] Kim *et al.*, 2004,[195] Seo *et al.*, 2006,[198] Seo *et al.*, 2008,[196] and Li *et al.*, 2008.[197]

remaining four (Figure 2.24d–g) demonstrate the shape evolution of a Wulff crystal with an increasing proportion of {001} facets. The octahedron (Figure 2.24d) has {111} facets only; the truncated octahedron (Figure 2.24e) is the same shape with the truncated surfaces being {001}. An even higher proportion of {001} facets gives rise to the cuboctahedron (Figure 2.24f). Finally, the (truncated) cube (Figure 2.24g) is dominated by {001} facets and some small {111} facets may be visible at the cube corners. These different shapes are optically different,[21,196,199] which makes it vital to understand the mechanisms underlying the selective formation of nanoparticle shapes.

The crystal shapes, or more specifically, the A_{111}/A_{001} ratio is influenced by the growth rates along <111> and <001> directions, in addition to the values of γ_{111} and γ_{001}.[195,197,205,222,227] For example, a much higher growth rate along <001> leads to a perfect octahedron (Figure 2.24d), and the other way round results in a cube (Figure 2.24g). The differentiated growth velocities are achieved by the selective interaction or adsorption of surfactants (e.g., polymers, foreign ions) on certain crystallographic surface planes. These have been extensively studied for silver[228–230] and gold[195–199,231] nanocrystals. In the case of gold, higher concentrations of poly(vinyl pyrrolidone) (PVP) and poly(diallyldimethylammonium) chloride (PDDA) encourage the formation of a higher proportion of {111} facets.[195–197] It was discovered that increasingly higher concentrations of PVP are required to achieve the crystal shapes of octahedron → truncated tetrahedron → icosahedron → decahedron.[196] The decahedral and the icosahedral structures involve internal strains, which call for higher concentrations of PVP to stabilise their shapes. The icosahedron is comparatively less strained because the shape is more spherical and hence it requires a lower PVP concentration.[196] For the single crystal shapes, the truncated tetrahedron seems to be less thermodynamically favourable than the octahedron, since it is stabilised by a higher PVP concentration and it is not a Wulff shape. However, the latter point is not addressed by the authors or in other literature. On the other hand, {001} facets of

gold crystals were reported to be stabilised by silver ions and cetyltrimethylammonium bromide (CTAB), which enhance the growth rate along <111>.[195,198,199,231] For example, the shape evolution in Figure 2.24d–g, from octahedron to cube, was achieved by incremental increases in the silver ion concentration in the polyol reaction mixture.[198]

2.3.5 Gold monolayers

An unusual form of gold, monolayers (MLs) or 2D wetted islands, was reported to coexist with crystals on various oxide substrates including FeO,[232,233] MgO,[233–239] CaO,[239–241], CeO_2,[242] TiO_2,[243,244] and $SrTiO_3$.[212] With the exception of $SrTiO_3$ and TiO_2 which are bulk single crystals, other oxide substrates are thin films supported on metallic substrates. The gold MLs are of great interest because 2D and 3D isomers of the same metal can exhibit drastically different mechanical, chemical, magnetic, and thermal properties.[236] 2D islands of gold are expected to be more reactive than their 3D counterparts because they have a higher number of undercoordinated surface atoms, which are the most active reaction sites, e.g., during the catalysis of CO oxidation.[238,245–247]

An oxide substrate wetted by a metal is uncommon because in a metal-on-oxide system, Volmer–Weber growth is expected. Metal clusters usually adopt 3D structures on wide-bandgap materials because of the low adhesion with the inert oxide support.[248,249] More interestingly, 2D islands of gold are almost always seen to co-exist with 3D clusters, i.e., Volmer–Weber growth and Frank–van der Merwe growth occur at the same time. Nevertheless, their 2D islands observed to date are limited in size, e.g., up to 500 atoms on CaO and MgO films.[237,241] Due to the size limit, they are only found at low coverages of gold and under kinetically-limited conditions.[212,232,233,235,243,244] These findings suggest that the MLs are likely

to be the energetically favourable form of gold in the small-size regime as opposed to 3D crystals. The 2D islands were seen to transform into 3D crystals by dewetting the vicinal gold atoms upon a 500 °C anneal on $SrTiO_3$.[212]

Figure 2.25a is an STM image of hexagonal gold MLs on a CaO film.[239] A close-up image (Figure 2.25b) shows a moiré structure: the stripes arise from the superposition of the hexagonal

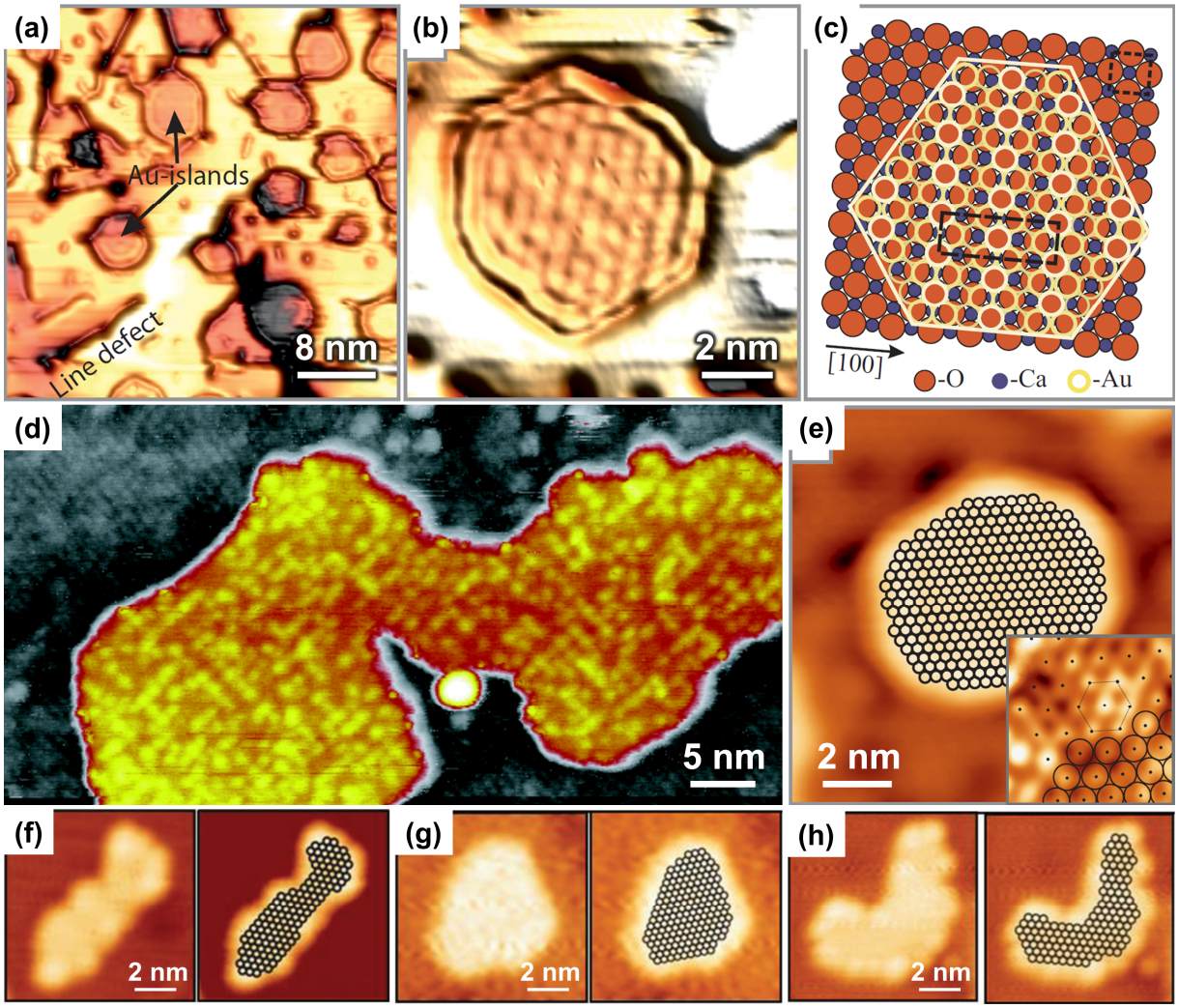

Figure 2.25: STM images and models of gold MLs on oxide substrates. (a) Gold MLs on a 25-ML-thick, Mo-doped CaO film. (b) One of the hexagonal islands in (a), showing stripes ascribed to a hexagonal-on-square moiré structure depicted in (c). The superstructure has a rectangular unit cell marked by a dashed box. (d) An irregularly shaped gold ML island on $SrTiO_3$(001)-(2 × 1) showing an inhomogeneous moiré pattern (bright spots). (e) A gold ML island on a 2-ML-MgO/Ag(001) film filled with a hexagonal lattice with a 2.89 Å periodicity. The inset (2 × 2 nm^2) is an atomically resolved image of the gold island. (f–h) Various shapes of gold MLs on a MgO/Ag(001) thin film and their structural models, termed as 'quasi-rectangular', 'quasi-triangular', and 'quasilinear', respectively. Reprinted from Cui *et al.*, 2015,[239] Silly and Castell, 2006,[212] and Stiehler *et al.*, 2013.[237]

Au(111) and the square CaO(001) lattices (Figure 2.25c).[239] A different moiré pattern was reported for gold MLs on $SrTiO_3$(001)-(2 × 1) (Figure 2.25d), which is a semi-periodic arrangement of bright spots. It was interpreted as a result of the semi-disordered structure of the gold ML and the frustrated commensurate epitaxy between gold and the substrate.[212] On MgO (Figure 2.25e) and FeO substrates, the atomic structure of gold MLs was resolved by STM to be a hexagonal Au(111) structure with a periodicity of 2.89 Å, as in bulk gold.[232,239] This result was assumed in a few other studies because the ML islands were usually hexagonally shaped.[237,238,240] Nevertheless, other shapes have also been reported: quasi-rectangular, quasi-triangular, and quasilinear, and the bulk (111) parameter of 2.89 Å was assumed in all three (Figure 2.25f–h).[237]

Under STM, an interesting phenomenon was consistently reported for gold MLs: the ML height appears to decrease with increasing imaging bias (V_s).[212,234,239,241] As shown in Figure 2.26, at imaging biases of (a) 1.5 V, (b) 2.5 V, and (c) 6.5 V, the 2D islands appear as protrusions, the same elevation as the substrate, and faint depressions, respectively. This is because the apparent height of gold depends on the relative surface local density of states (LDOS) of the gold and the oxide substrate, and different parts of their LDOS energy spectra are accessed at

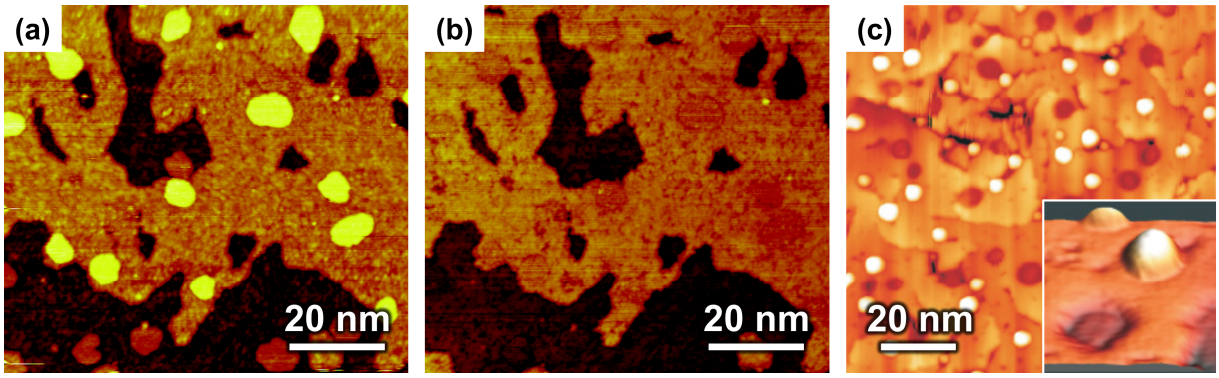

Figure 2.26: STM images of gold MLs on oxide substrates obtained with different imaging biases. (a,b) The same area of gold islands on $SrTiO_3$(001)-(2 × 1), where the islands appear as protrusions in (a) (V_s = 1.5 V) and cannot be seen in (b) (V_s = 2.5 V). Reprinted from Silly and Castell, 2006.[212] (c) 2D and 3D gold islands on a 30-ML-CaO/Mo(001) film, where the 2D islands appear as faint depressions (V_s = 6.5 V). The depression is visualised in the 3D inset (10 × 10 nm^2). Reprinted from Shao *et al.*, 2012.[241]

different imaging biases.[212] Accordingly, the imaging bias of the contrast reversal, i.e., the voltage at which the gold islands adopt the same contrast as the surrounding oxide, is different on different oxides, e.g., 2.5 V on $SrTiO_3$ (Figure 2.26b) and 3.5 V on CaO and MgO.[212,239,241]

The wetting of gold on oxide supports has been explained by two mechanisms: charge transfer and a low interfacial energy with the substrate. Electron transfer from the oxide substrate into the gold islands induces a polarisation effect and improves the electrostatic attraction between them. This stabilises the planar arrangement of gold islands because the enhanced metal–oxide adhesion encourages gold islands to maximise their contact area with the oxide support.[239–241] Charge transfer can be achieved via three routes: (1) electron tunnelling through an ultrathin oxide film supported on an underlying metal substrate,[232,233,238,239,241,250–253] (2) charge donation from dopants in the oxide matrix,[236,239,240] and (3) introduction of an electric field (~1 V nm^{-1}).[254] These three routes were confirmed either experimentally or by DFT calculations to stabilise the wetting growth of gold over 3D growth. Nevertheless, gold clusters in DFT calculations are very small – only up to 20 atoms.[236,250–252,254] As an example of the first route, on Mo-supported CaO films, gold wetted any CaO film thinner than 25 MLs and grew into 3D shapes if the CaO film was thicker than 40 MLs.[241] Figure 2.26c is an example image showing a mixture of 2D and 3D gold islands on a 30-ML-CaO/Mo(001) film. On another substrate, an Ag-supported MgO film, the threshold thickness for the 2D/3D growth transition of gold was 5–8 MLs of the MgO film.[253] It was also noted that charge transfer is possible with gold because of its high electronegativity, and other metals with lower electron affinities such as Pd do not exhibit any charge transfer.[233]

In another explanation for the ML formation, it was argued that the MLs have a lower interfacial energy with the substrate than 3D crystals.[212] It was speculated that as the ML structure is not constrained by additional atomic layers above it, it is allowed to relax and develop some local commensurate epitaxy with the substrate.[212] Both arguments above (charge transfer and a

lower-energy interface) are plausible, but the limited sizes of the 2D islands and their coexistence with crystals are yet to be explained.

2.4 Summary and outlook

This chapter has provided an overview of the relevant published work on the substrate material used in my research, $SrTiO_3$, and the two materials grown on it, monolayer MoS_2 crystals and gold nanostructures. Single crystalline $SrTiO_3$ has three surface terminations that have been extensively studied: (111), (110), and (001). They all exhibit a wide range of surface reconstructions that have been investigated experimentally and theoretically to work out their compositions and surface chemistry. For MoS_2 crystals and gold nanostructures, a strong emphasis has been placed on their relationship with substrates, i.e., how crystalline substrates play a role in manipulating their epitaxy, morphology, and physical properties.

In Chapter 4, MoS_2 monolayers are grown on the three terminations of $SrTiO_3$; how their orientations, shapes, and optical properties are regulated by the substrate is established. In Chapter 5, the thermal stability of $SrTiO_3$-supported monolayer MoS_2 is investigated in UHV. This allows us to assess the suitability of MoS_2 crystals for use in high-temperature electronics. In Chapter 6, STM images of gold MLs on $SrTiO_3$(001)-(2 × 1) are presented, including their shapes and a moiré structure. Their formation and transition into the 3D form are explained in terms of surface/interface energetics. Finally, in Chapter 7, gold nanocrystals are studied on various $SrTiO_3$ surfaces. Their shapes are shown to be controlled by the substrate structure and energy, which are critical to their catalytic and optical properties.

Chapter 3

Experimental Techniques

Most of the results presented in this thesis were obtained in a custom-built three-chamber UHV system located in the Department of Materials at the University of Oxford. This instrument allows most of the sample preparation and characterisation processes to be carried out within UHV, protecting the samples from water, hydrocarbons, and other contaminants and reactive species. This maintains their atomically clean surfaces without substantial contaminant build-up for the duration of the experiments.[255] The UHV system is mainly used for STM. Other techniques used in thesis include molecular beam epitaxy (MBE), XPS, SEM, Raman spectroscopy, and PL.

3.1 The main instrument

As shown in Figure 3.1, the three connected chambers contain an STM (JEOL JSTM 4500s), an SEM (JEOL TM Z9043T), and a treatment chamber for sample preparation. The STM and treatment chambers operate at a base pressure of 10^{-8} Pa, and the SEM chamber at 10^{-7} Pa, all

achieved by the operation of ion pumps as well as titanium sublimation pumps (TSP) when required.

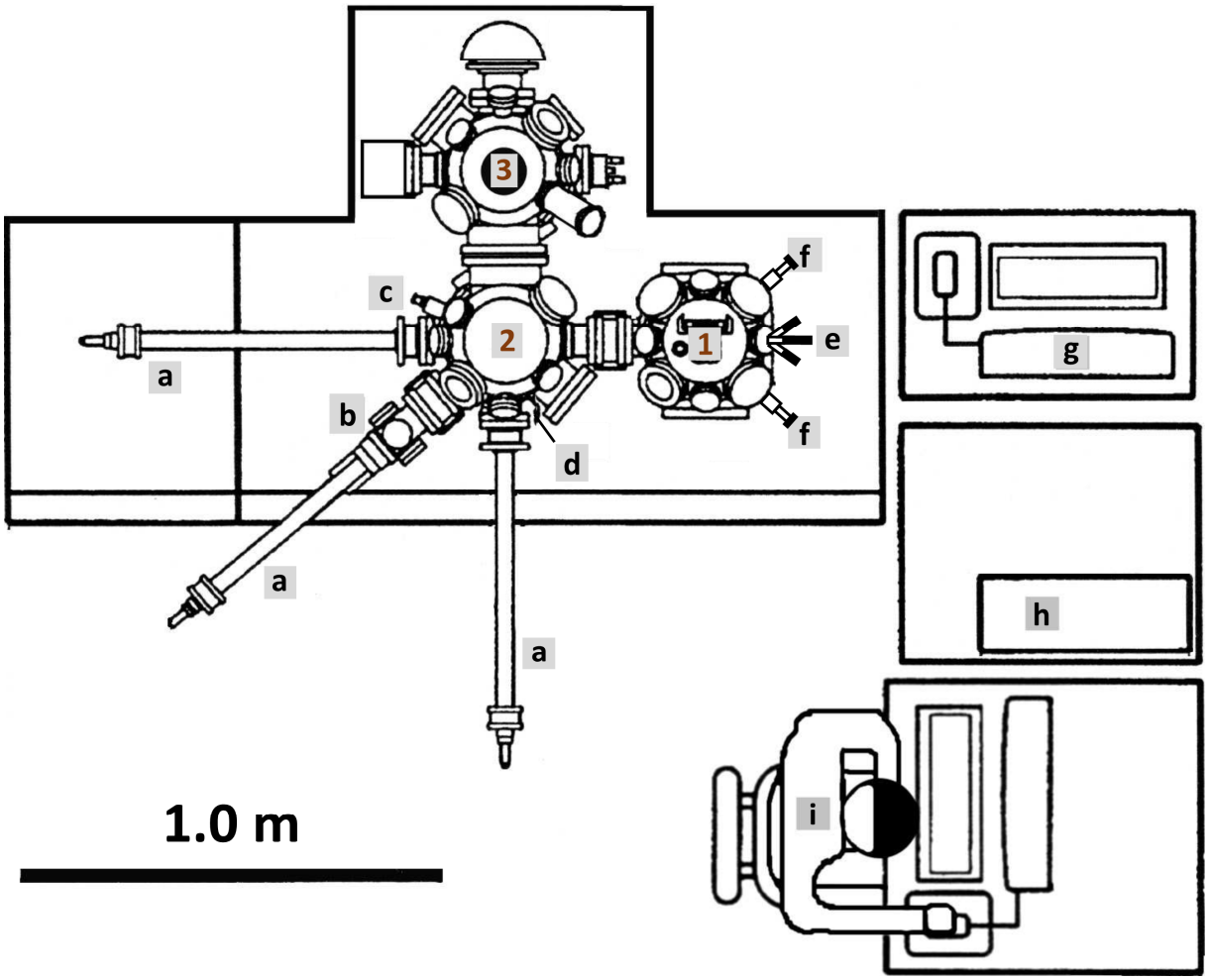

Figure 3.1: Schematic plan of the custom-built three-chamber UHV system, showing (1) the STM chamber (JEOL JSTM 4500s), (2) the treatment chamber, and (3) the SEM chamber (JEOL TM Z9043T). A selection of the facilities is labelled: (a) transfer arms, (b) load-lock vacuum entry, (c) sputtering gun, (d) oxygen valve, (e) electron-beam evaporator, (f) Knudsen cells, (g) SEM computer, (h) STM computer, and (i) operator. Adapted from Marshall, 2009.[256]

Samples and tips are introduced into the UHV system via the load lock, which can be open to air and pumped down to a pressure around 10^{-6} Pa with a turbo molecular pump (TMP). After a period of more than six hours in the load lock, they can be transferred into the treatment chamber. Within the UHV system, neighbouring chambers are separated by gate valves, which are opened when sample transfers are required.

3.2 Substrate preparation

3.2.1 Purpose of preparation

The substrates used in this thesis are $SrTiO_3$ single crystals doped with niobium (Nb) at 0.5% by weight ($7 \times 2 \times 0.5$ mm^3). They were supplied by PI-KEM, U.K., with epi-polished (111), (110), and (001) surfaces. $SrTiO_3$ is an insulator with a bandgap of 3.2 eV at 25 °C.[33] The Nb dopant was included to generate sufficient electrical conductivity at room temperature for STM imaging. The sample was mounted on a JEOL-built sample holder (Figure 3.2a). The tip used for STM imaging was prepared by electrochemically etching a tungsten (W) wire (0.3 mm in diameter) in a solution of 2.0 M NaOH, mounted on a JEOL-built tip holder (Figure 3.2b).

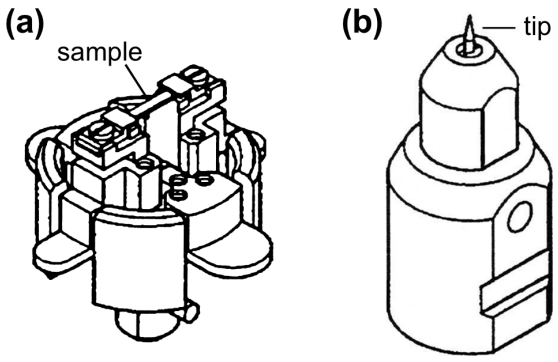

Figure 3.2: JEOL-built (a) sample and (b) tip holders. Adapted from JEOL Ltd., 2000.[257]

Although the as-supplied $SrTiO_3$ samples were epi-polished on the top surface by the manufacturer to a mirror finish, a small depth of disordered polishing damage would remain. Therefore, it had to be ensured that the crystallinity of the sample extended to the top atomic layer before any structure (MoS_2 crystals and gold nanostructures in this thesis) was grown on top. This was done by processing all the samples through UHV annealing and/or Ar^+-ion sputtering. This preparation process eliminates the polishing damage and allows the surface to become crystalline, atomically flat, and relatively free of contaminants. In the case of gold nanostructure growth, the surface energy of the reconstructed substrate surface also matters.

3.2.2 Degassing and annealing

After being introduced into the treatment chamber, samples were degassed first to remove adsorbates and contaminants. This was done by heating them up by resistively passing a direct current through them to the glowing temperature (~600 °C). Further heating caused atomic reconstructions to occur and these high-temperature anneals were used to generate atomically flat surfaces of the $SrTiO_3$ substrates. The samples were annealed in either UHV or partial pressures of oxygen. Oxygen was supplied from an oxygen cylinder attached to the treatment chamber with a valve.

The sample temperature was measured through a viewport with an optical pyrometer. This is possible when the radiation emitted by the hot sample lies within the visible spectrum, corresponding to a minimum measurable temperature of ~850 °C. Below ~850 °C, temperatures were estimated via a temperature (T) calibration curve as a function of the power supplied (P). Shown in Figure 3.3 is an example of such an empirical curve: a room-T point was fixed at P = 0 W, T = 23 °C and another point was available with the knowledge that the sample just starts to glow at ~600 °C. The remaining data points were pyrometer measurements with errors of the order of 15–25 °C. A cubic polynomial trendline (red) is then fitted as the calibration curve. Later in this thesis, all temperatures reported, either measured or estimated, are associated with errors of the magnitude of ~20 °C. Usually higher temperatures have smaller errors because a hotter and hence brighter sample makes the pyrometer measurement easier and more accurate. In Figure 3.3, T increases with P at a lower rate at higher temperatures because the sample loses a disproportionately greater amount of heat by radiation at higher temperatures (radiation power $\propto T^4$ according to the Stefan–Boltzmann law). Note that the calibration curve is slightly different for each sample because of (i) the small variations in the sample holder or sample stage conductivity and (ii) how tightly the samples were mounted. Therefore, such a cubic function was individually calibrated for each sample when possible.

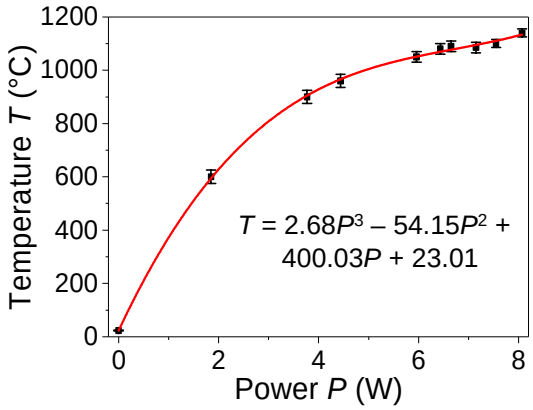

Figure 3.3: Calibration curve of a $SrTiO_3$ sample temperature against the power dissipated by the sample. Apart from the two data points at T = 23 °C (room temperature) and 600 °C (initial sample glowing temperature), all other dots are experimentally measured data with error bars. The curve is fitted to estimate sample temperatures below ~850 °C.

3.2.3 Sputtering

Certain surface reconstructions on $SrTiO_3$ require room-temperature Ar^+-ion sputtering prior to annealing. Sputtering the sample surface introduces structural defects and the degree of disorder depends on the sputtering energy and time.[59,60] It was also used to clean off crystals and deposited metals, to allow the substrates to be re-used.

In this work, a VG Microtech EX03 ion gun was used,[258] mounted onto the treatment chamber. A beam of electrons was generated by heating up a filament by passing a current of 2.95 A through it. The emitted electrons were then accelerated with an energy of 120 eV towards the argon gas passed into the ion gun, where Ar atoms were ionised by collisions with the energetic electrons. This process is schematically illustrated in Figure 3.4. Next, the Ar^+ ions were accelerated through an extractor lens and focused onto the sample with an energy of 500 eV, for both defect introduction and surface cleaning in this work. This corresponds to an ion current of 2.5 μA towards the sample. The Ar^+ ion pressure in the chamber was adjusted to 4.5×10^{-4} Pa during sputtering. Only the sputtering duration varied for different purposes in this thesis, and these will be stated individually for the relevant results.

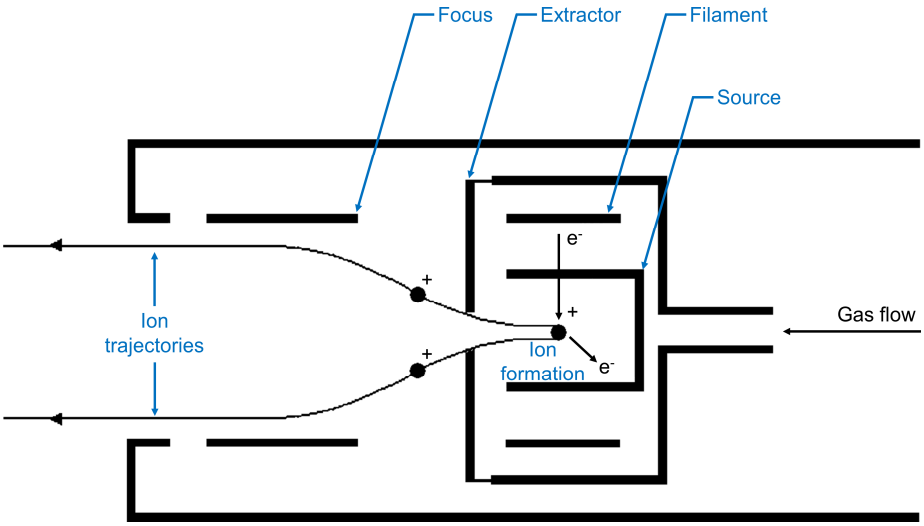

Figure 3.4: Argon flow and ionisation in the VG Microtech EX03 ion gun. Adapted from VG Microtech, 2000.[258]

3.2.4 Prepared surfaces

Table 3.1 below summarises the preparation conditions for the surface reconstructions on $SrTiO_3$(111), (110), and (001) used in this thesis, which are similar to the conditions used in previous studies.[38,43,63,69]

Table 3.1: Summary of preparation conditions for $SrTiO_3$ surface reconstructions.

$SrTiO_3$ surface	Reconstruction	Ar^+-ion sputtering conditions	Annealing temp. (°C)	Annealing time (h)	Environment
(111)	(3 × 3)	500 eV, 8 min	1160	5.0	4.5×10^{-4} Pa O_2
	(4 × 4)	500 eV, 8 min	1140	3.0	4.5×10^{-4} Pa O_2
	(4 × 4) + disordered	500 eV, 2–8 min	1000–1080	1.5	UHV
	(4 × 4) + (6 × 6)	500 eV, 6 min	1090	1.5	UHV
	(5 × 5)	500 eV, 8 min	1090	1.5	UHV
	(5 × 5) + (6 × 6)	500 eV, 6 min	1020	1.5	UHV
	(√7 × √7)R19.1° + (√13 × √13)R13.9°	/	850	1.0	UHV
(110)	(3 × 1)	/	890–960	2.0	UHV
	(4 × 1)	/	800	0.5	UHV
	(6 × 1)	/	910	3.0	UHV
			after (3 × 1) formed		
(001)	(2 × 1)	/	900–950	1.0	UHV
	c(4 × 2)	500 eV, 10 min	1100–1150	0.5–1.0	UHV

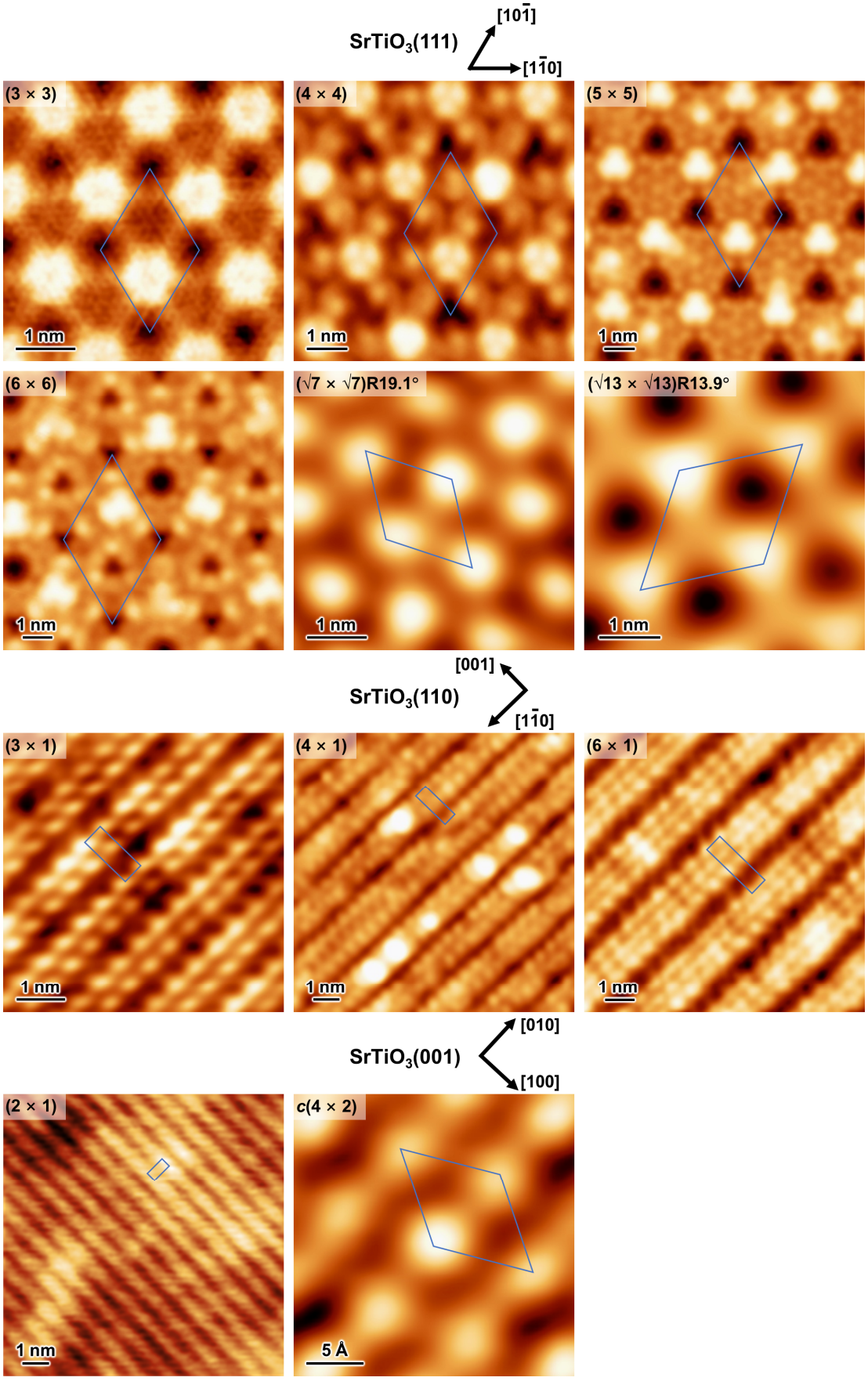

Figure 3.5: STM images of surface reconstructions on $SrTiO_3$(111), (110), and (001), as labelled in their top-left corners. The blue rhombi and rectangles indicate reconstructed surface unit cells (V_s = 0.8–2.5 V, I_t = 0.17–0.38 nA).

Figure 3.5 is a series of small-scale STM images of the reconstructed surfaces of $SrTiO_3$. They are all labelled in their top-left corners, e.g., the first one is the $SrTiO_3$(111)-(3 × 3) surface, prepared using the conditions described in the first row of Table 3.1. In each image, the reconstructed unit cell is drawn in blue. These images are original work and many of these surfaces were used as substrates in the work presented in Chapters 4–7. The substrate names will be frequently referred to later, though their detailed surface morphologies are not directly relevant to my work. Nevertheless, they have been reported in previous studies and are discussed in the Literature Review (section 2.1), including the structural solutions for some of them.[38,43,56,63,65,66,69,85,87,88]

3.3 Crystal and nanostructure growth

3.3.1 MoS_2 crystals

The growth, transfer, and treatments of MoS_2 crystals were carried out by Dr. Wenshuo Xu in the Nanostructured Materials Group in the Department of Materials. They were performed as part of a collaboration that underpins the work in Chapters 4 and 5. Therefore, they are described here for completeness despite not being carried out by the author.

CVD growth of MoS_2

Molybdenum trioxide (MoO_3, powder, ≥ 99.5%, Sigma-Aldrich) and sulphur (S, powder, ≥ 99.5%, Sigma-Aldrich) were used to synthesise MoS_2 monolayers using the atmospheric-pressure CVD method. A schematic diagram of the CVD setup is shown in Figure 3.6. $SrTiO_3$ substrates were placed face-up and downstream with respect to the precursors, which were

20 mg of MoO_3 and 300–450 mg of S, loaded in two tubes with 12 mm and 22 mm diameters, respectively. The system was first flushed with 500 sccm argon to drive off oxygen. Subsequently, sulphur vapour was preintroduced at 180–190 °C for 15 min with a decreased argon flow rate of 150 sccm. This created a sulphur-rich environment, which was maintained by increasing the temperature of sulphur at a rate of 0.7 °C s^{-1} during the synthesis. This environment ensured that the as-grown MoS_2 crystals were triangles with S-edge terminations.[122] The substrates were heated at up to 210 °C at the same time to avoid sulphur condensation. The MoO_3 precursor and $SrTiO_3$ substrates were then heated to 300 °C and 800 °C, respectively. There were three stages in the MoS_2 synthesis, namely, nucleation (20 min with 150 sccm Ar), main growth (25 min with 50 sccm Ar), and atom migration (15 min with 5 sccm Ar), completed by a rapid cooling process.

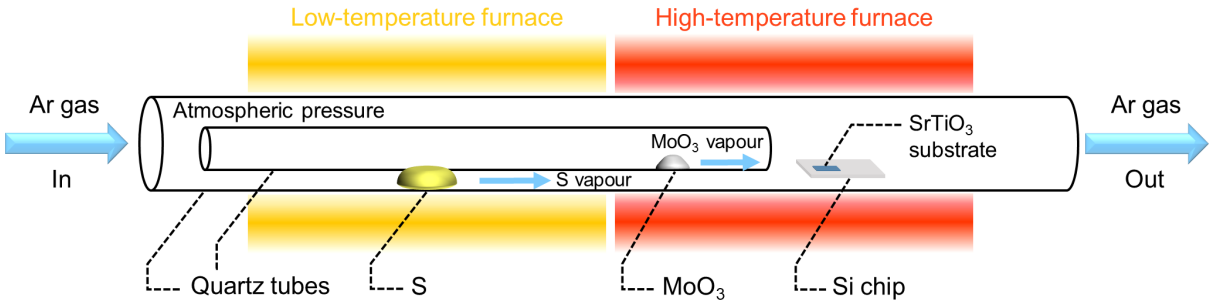

Figure 3.6: Schematic diagram of the CVD setup for the synthesis of MoS_2 crystals. The Si chip serves as a substrate holder. Reprinted from Chen *et al.*, 2019.[115]

Transfer of MoS_2

MoS_2 monolayers grown on a silica (SiO_2)/silicon (Si) substrate were first spin-coated with a thin film of poly(methyl methacrylate) (PMMA, 8 wt % in anisole, 495k molecular weight) at 4500 rpm for 60 s, followed by a 90 s curing process at 180 °C. The SiO_2 layer was etched off by floating the samples on a 1 M potassium hydroxide (KOH, Sigma-Aldrich) aqueous solution at room temperature, so that the planar strain in the MoS_2 monolayers was released. The isolated

film of PMMA/MoS_2 was then rinsed in deionised (DI) water three times for 1 h each time. Following this, a precleaned $SrTiO_3$ substrate was submerged in DI water to support the film. The as-transferred sample was dried overnight in a ventilation environment, after which it was baked at 150 °C for 20 min to enhance the MoS_2−substrate adhesion. The PMMA coating was removed by soaking the sample in a 55 °C acetone bath for 6 h. Finally, to remove the trapped contaminants for a cleaner interface, the sample was annealed at 200 °C for 1 h with 150 sccm argon as the carrier gas.

Sulphur annealing of defective monolayer MoS_2

The defective vacuum-annealed MoS_2 samples and sulphur powder were loaded in two quartz tubes (2 in. diameter) at the centres of two furnaces so that their temperatures could be controlled independently. After the system was flushed with a 500 sccm argon flow for 30 min, MoS_2 and S were heated to 300 and 200 °C, respectively. The sulphur vapour was carried by a 500 sccm argon flow downstream to the MoS_2 sample. The sulphur atmosphere was maintained for 1 h, after which both the MoS_2 samples and S were cooled down.

3.3.2 Gold nanostructures

In the work presented in Chapters 6 and 7, gold was deposited onto $SrTiO_3$ substrates in UHV. This was done using a Createc™ Knudsen cell,[259] or K-cell attached to the STM chamber (Figure 3.1). The setup of such a K-cell is schematically presented in Figure 3.7. Gold was placed in a ceramic crucible with an aperture in its lid, which is oriented towards the sample. The crucible was heated up by the radiation from a filament coil connected to a temperature control unit,[260] which passes a direct current through the coil. The control unit also

simultaneously monitors the temperature via a thermocouple. A water-cooling jacket surrounding the crucible helps to regulate the temperature by preventing excessively fast heating. A shutter above the crucible lid was used to obstruct the sample from any evaporated metal before a stable deposition rate was reached.

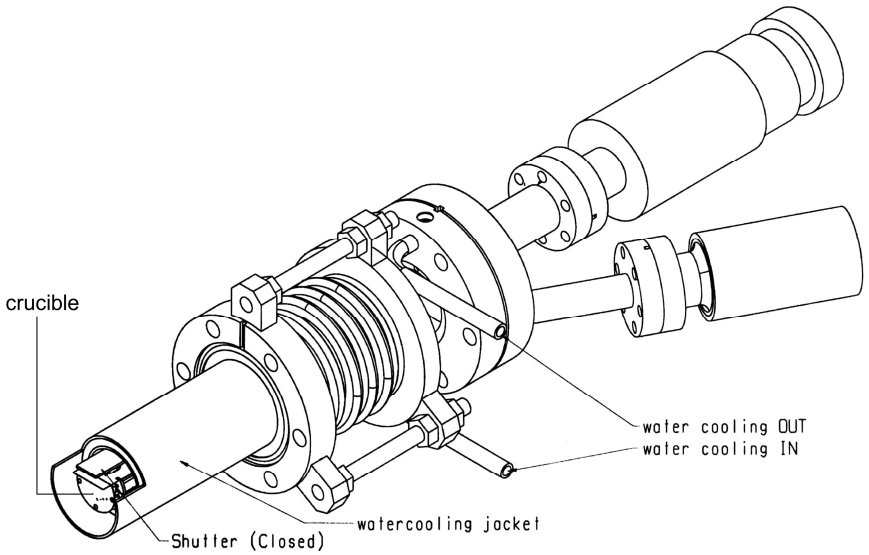

Figure 3.7: Createc™ Knudsen cell. Adapted from Createc Fischer & Co., 2002.[259]

In this thesis, the evaporation of gold took place at a K-cell temperature of 1350 °C. Deposition of gold on $SrTiO_3$ substrates typically occurred at a rate of ~0.025 monolayers min^{-1}.

3.4 Scanning tunnelling microscopy (STM)

STM is a surface sensitive technique and is the main technique used in this thesis. It was developed in the early 1980s, as the first member of the family of scanning probe microscopy (SPM) techniques.[261] It is based upon scanning an extremely sharp tip (3–50 nm radius of curvature) across an object surface (Figure 3.8). The metallic tip and the conducting sample are separated by a narrow vacuum gap (d) of typically between 0.3–1 nm. When a bias voltage (V) is applied between the tip and the sample, a tunnelling current (I_t) results between them, which is a function of a number of factors:[262]

$$I_t \propto V\ \rho_s\ \rho_t\ e^{-kd},$$

where ρ_s is the density of sample states, ρ_t is the density of tip states, k is a constant related to the decay length for the wave functions in a vacuum, and d is the tip–sample separation. Most importantly, the tunnelling current is related to the tip–sample separation by an inverse exponential relationship and is therefore granted an extreme sensitivity to any topographic change of the sample. For the same reason, the overwhelming majority of the tunnelling electrons are between the apex atom of the tip and the topmost atoms of the sample, which determines the surface-sensitive nature of STM. It is noteworthy that the tunnelling current is also proportional to the LDOS of the sample, which means that the tunnelling surface generated by STM is a combination of the surface topography and its LDOS.

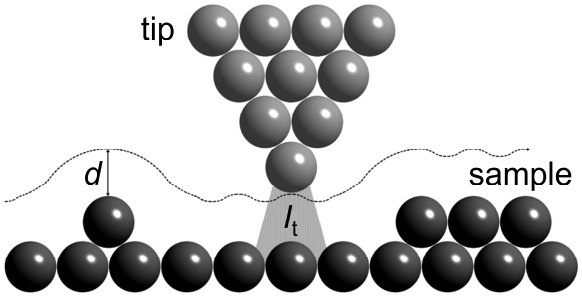

Figure 3.8: Schematic diagram showing the tip–sample interaction in STM. Each sphere represents an atom – the tip is atomically sharp. Reprinted from Castell, 2007.[263]

As the tip scans across the sample surface, it can create the tunnelling map of the sample in two modes (Figure 3.9):

- In the **constant current mode**, the tunnelling current is determined and fixed by the user during the scan. The tip–sample distance is adjusted according to a feedback loop as the tip scans in the *x*-*y* plane, and the *z* movements of the tip are recorded to reconstruct the 3D map of the sample surface. This is the scenario depicted in Figure 3.8.

- In the **constant height mode**, the tip height is fixed during the scan, and the tunnelling current is recorded as a function of *x* and *y*. This mode allows higher scanning speeds but is used less often because the tip is in danger of crashing into any surface protrusions if the sample is not very flat.

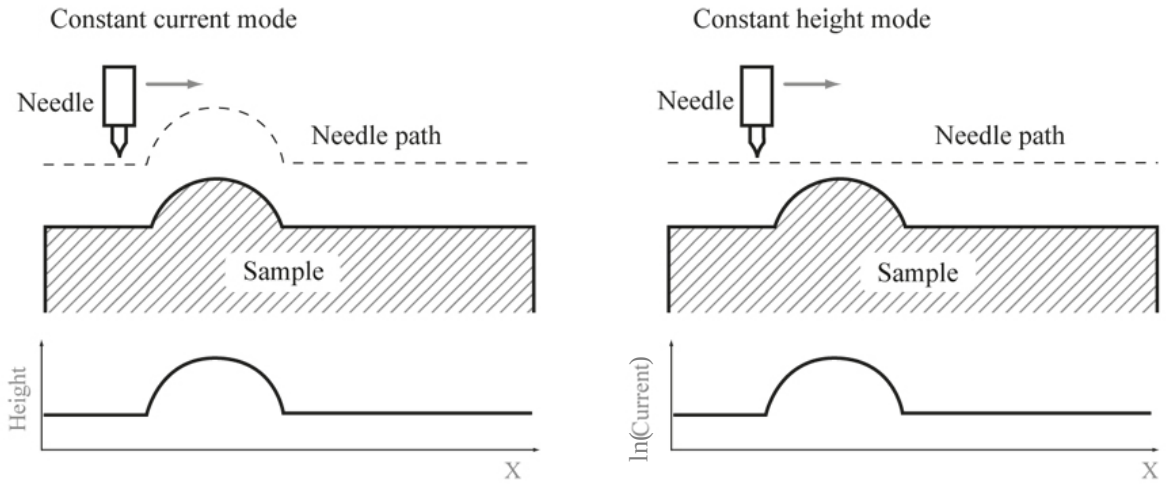

Figure 3.9: Schematic diagrams showing the two operation modes of STM: constant current and constant height. Adapted from Oura *et al.*, 2003.[255]

In this thesis, all STM images were obtained using the constant current mode in the JEOL JSTM 4500s. The bias voltage (V_S) and tunnelling current (I_t) applied to obtain each image are labelled in their figure captions. STM images were processed by *Smart Align*,[264,265] *Gwyddion*, and *WSxM*.[266] *Smart Align* is a newly developed software package by Jones *et al.*[264,265] to correct the scanning distortions and to enhance the signal-to-noise ratio (SNR) in STM images. It works by aligning multiple successive images of the same area and averaging them to calculate a 'reference' image. Raw images are then corrected according to the reference image. The process can be repeated if necessary, using an updated 'reference' image from the previous process. The availability of very high SNR data without the need for smoothing allows quantitative dimensional measurements to be taken with confidence. This was applied to most STM images smaller than 50×50 nm^2 presented in this work.

3.5 X-ray photoelectron spectroscopy (XPS)

XPS was used for compositional analysis of the thermally degraded monolayer MoS_2 (Chapter 5). It measures the surface composition of a solid by directing a monochromatic X-ray beam towards the sample and analysing the energies of the ejected electrons. XPS is based on the photoelectric effect: when the X-ray photons possess a greater amount of energy ($h\upsilon$) than the binding energies of electrons in the material (E_b), the photons will stimulate the emission of core-level electrons from the material, as illustrated in Figure 3.10. The emitted electron is commonly called a photoelectron, and its kinetic energy (E_k) is measured by the spectrometer.

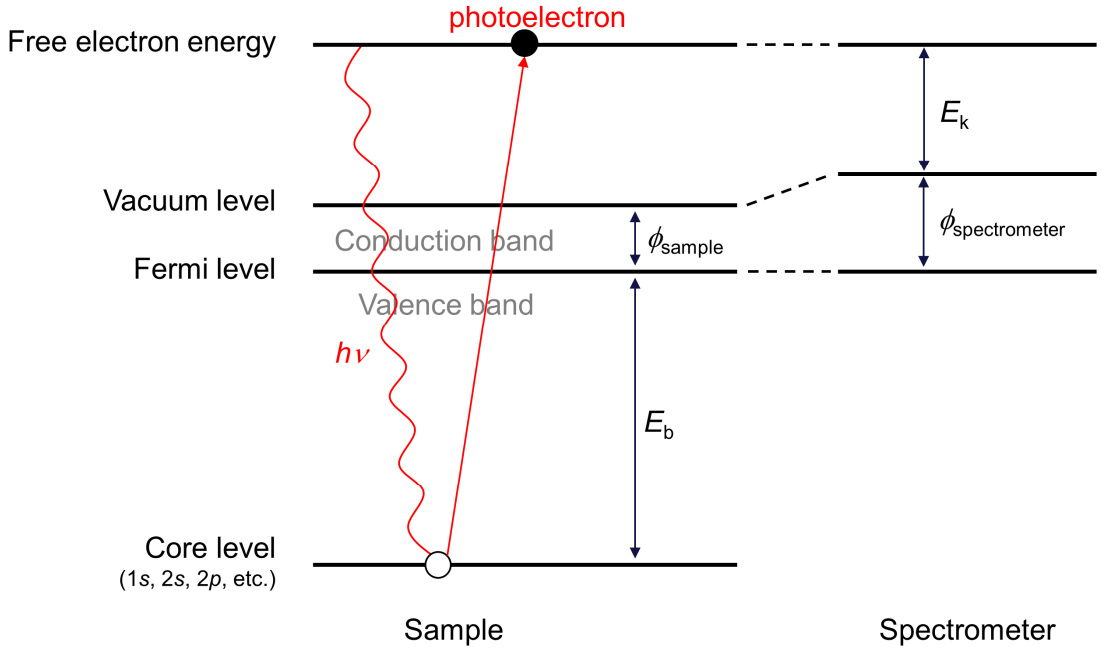

Figure 3.10: Schematic diagram showing the photoemission process of a core electron, where $h\upsilon$ represents the energy of the incident X-ray, E_b is the binding energy of the core electron, ϕ_{sample} is the work function of the sample, $\phi_{spectrometer}$ is the work function of the spectrometer, and E_k is the kinetic energy of the escaped photoelectron.

According to energy conservation based on the work of Ernest Rutherford (1914), the kinetic energy of the photoelectron is given by

$$E_k = h\upsilon - E_b - \phi_{spectrometer},$$

where $h\upsilon$ is the X-ray energy with υ being the frequency of the monoenergetic beam, E_b is the binding energy of the electron in the relevant electronic level, and $\phi_{spectrometer}$ is the work function of the spectrometer. Note that the binding energy (E_b) in the context of electron spectroscopy is scaled to the Fermi level rather than the vacuum level. Also, if the sample is sufficiently conductive and is in ohmic contact with the spectrometer, their Fermi levels will align. Based on the above, the emitted electrons are expected to possess discrete kinetic energies resulting from the set electronic energy levels.

Once the kinetic energy spectrum of the ejected electrons is scanned and recorded by an electron energy analyser, it is turned into a set of XPS peaks at characteristic binding energies, which in turn, provides the elemental information. Because the chemical environment of a particular atom, e.g., its oxidation state, also shifts the binding energies of the photoelectrons, XPS enables the precise determination of the chemical compounds. The XPS peak intensities also reflect the amount of each element present on the surface analysed.[267–269]

The surface sensitivity of XPS makes it suitable for the compositional analysis of monolayer MoS_2 (under 1 nm). Although the penetration depth of X-rays usually exceeds 100 nm,[270] the fact that photoelectrons only emerge from the top few nanometres of the sample is attributed to the inelastic scattering of electrons.[255] Figure 3.11 shows the universal curve of inelastic mean free paths (IMFPs) of electrons at different energies.[271] Soft X-rays used to examine core levels usually have energies in the range 1–3 keV, and at these energies the IMFP is typically shorter than 50 Å (or 5 nm). The escaped electrons are therefore localised to within a few atomic layers, making XPS surface sensitive.

Similar to many other surface sensitive techniques, the effective operation of XPS requires a high vacuum. This is to minimise the electron scattering from residual gas molecules and to maintain an atomically clean sample surface.

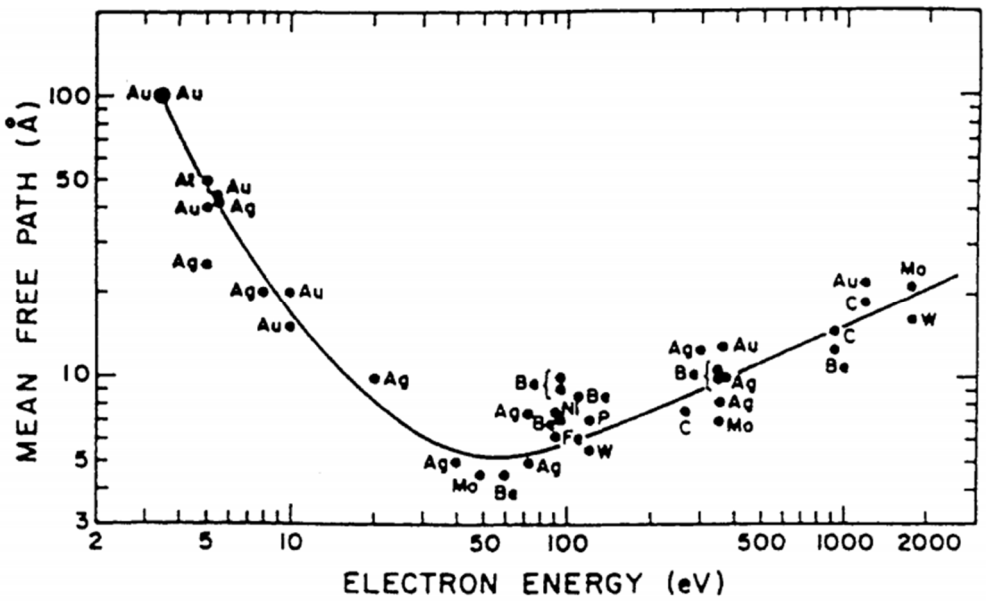

Figure 3.11: Inelastic mean free paths (IMFPs) of electrons in solids as a function of their electron kinetic energy. Reprinted from G. Somarjai, 1981.[271]

In this thesis, XPS experiments were performed by Dr. Philip Holdway (Oxford Materials Characterisation Service) on a Thermo Scientific K-Alpha XPS instrument equipped with a microfocussed monochromated Al X-ray source (1486.6 eV). The source was operated at 12 keV, i.e., an accelerating voltage of 12 kV was applied to the electron beam used to bombard the Al anode to produce X-rays. A 400 μm spot size was used. The analyser was operated at a constant analyser energy (CAE) of 50 eV. Charge neutralisation was applied using a combined low-energy electron/ion flood source. The data acquisition was performed using the *Thermo Scientifics Avantage* software. XPS peaks were fitted using the *CASAXPS* software.

3.6 Scanning electron microscopy (SEM)

In SEM, an electron gun emits a beam of electrons which is accelerated through a voltage (usually 1–50 kV) and focused through a series of lenses. The demagnefied electron beam (spot size 1–10 nm) is scanned across a sample surface, ejecting electrons of a wide range of energies from the surface region.[272] Secondary electrons (SEs), usually with energies of between 2–5 eV,

are used to construct SEM images. The contrast resulting from SE signals is a direct topographical image of the surface because the intensity of emitted SEs are dependent on the local angle of the surface to the primary beam.[273] The attainable resolution of the technique is determined by the minimum spot size of the focused electron beam incident on the surface.

SEM images presented in this thesis were generated by two field emission instruments: a Zeiss Merlin and a Hitachi-4300. The former provides a spatial resolution of 0.8–1.6 nm and the latter of 1.5–5.0 nm. The MoS_2 samples (Chapters 4 and 5) were stuck on pin stubs using carbon sticky pads and the gold samples (Chapter 7) were silver coated. Most images were generated at an accelerating voltage of 3 kV except the tilted images of gold samples (to show the side facets of gold nanocrystals), which were obtained at 2 kV. The SEM images presented in Chapters 4, 5, 7 were taken by Dr. Wenshuo Xu (Nanostructured Materials Group, Oxford), Dr. Krishnan Murugappan (Surface Nanoscience Group, Oxford), and Jiawei Jiang (Professor Todd Group, Oxford). They are included as a critical part of the full understanding of the MoS_2 and gold systems.

3.7 Raman spectroscopy and photoluminescence (PL)

Raman spectroscopy and PL are non-contact and non-destructive spectroscopic techniques which work by illuminating a sample with a laser (i.e., photons). Raman spectroscopy is used to observe the vibrational, rotational, and other low-frequency modes in a material, while PL probes the electronic structure.

In **Raman spectroscopy**, a beam of monochromatic light is impinged upon a sample. During this process, the vast majority of the photons undergo *Rayleigh scattering* (Figure 3.12). In Rayleigh scattering, a photon interacts with the material and raises the electrons to 'virtual'

energy states, which are short-lived (of the order of 10^{-14} seconds) energy levels between quantised electronic states. When the material drops back to its ground state, it releases a photon with the same energy, i.e., the scattered photons have the same wavelength as the incident photons (Figure 3.12). On the other hand, a small proportion of the photons excite the electron cloud to virtual energy states which then relaxes back to vibrational states rather than the ground state. The emitted photon has a lower energy than the incident photon. If the material is initially in an elevated vibrational state before photon excitation and it relaxes into the ground state afterwards, this causes an upshift in the energy of the scattered photon. These are known as *Stokes* and *anti-Stokes Raman scattering*, respectively (Figure 3.12). Bond vibrations and phonon modes lie at unique Raman shifts, determined by the material's crystal structure. Raman spectroscopy therefore provides a structural fingerprint of the material.

PL also results from the absorption of photons, typically in a laser beam. They cause electrons within the sample material to move into permissible excited states. When these electrons return to the ground state (in steps), a combination of radiative and non-radiative processes occur. The excess energies released as radiation can be measured to infer the material compositions,

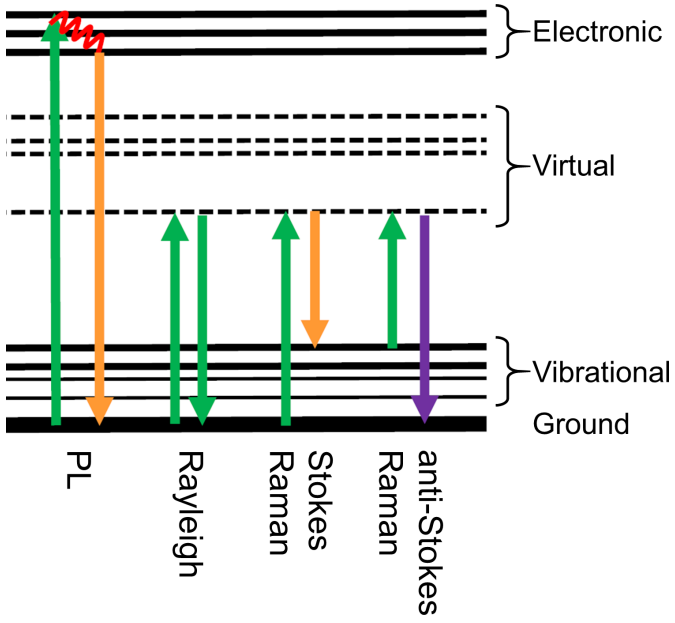

Figure 3.12: Energy diagram of PL emission, Rayleigh scattering, Stokes Raman scattering, and anti-Stokes Raman scattering.

which are directly related to the differences between electronic energy levels of the material. Figure 3.12 is a schematic energy diagram to show the simplified working principles of both Raman spectroscopy and PL.

In this thesis, Raman spectroscopy and PL were conducted on MoS_2 crystals (Chapters 4 and 5) by Dr. Wenshuo Xu (Nanostructured Materials Group, Oxford). They were conducted using a JY Horiba LabRAM ARAMIS imaging confocal Raman microscope with a 532 nm excitation wavelength and 12.5 mW laser power. The laser spot size was ~1 μm, and the acquisition times were 35 s for Raman spectra and 5 s for PL spectra. The Raman and PL results are included in Chapters 4 and 5 because they are critical to developing a full understanding of the MoS_2-on-$SrTiO_3$ system.

3.8 Summary

This chapter introduces the experimental procedures for substrate preparation and the growth of MoS_2 monolayers and gold nanostructures, as well as the techniques used to characterise their morphologies (STM, SEM), compositions (XPS), and optical/structural properties (Raman spectroscopy and PL). Most of these techniques (STM, SEM, and XPS) are surface sensitive. Integrating these characterisation techniques allows us to gain a full picture of the nanostructures and how their properties are manipulated by their substrates.

Chapter 4

Epitaxial Growth of Monolayer MoS_2 on $SrTiO_3$ Single Crystal Substrates

From this chapter onwards, original work is presented, mainly carried out by the author. Where experiments were performed by collaborators this is explicitly stated in the text.

The work in this chapter has been published in Chen *et al. ACS Appl. Nano Mater.* **2018**, *1*, 6976−6988.[136] My contribution to this project includes the following: designing and directing the project, preparing $SrTiO_3$ substrates in UHV, performing STM experiments, all data analysis apart from those of Raman spectroscopy and PL (section 4.2.4), interpretation of all results, and all writing up apart from the initial draft of section 4.2.4.

4.1 Introduction

MoS_2 crystals grown on amorphous substrates such as SiO_2 are randomly oriented.[122] However, when MoS_2 is grown on crystalline substrates, the crystal shapes and orientations are also influenced by their epitaxial interaction with the substrate. Finding suitable substrate materials is an important step towards epitaxy or orientation control in the synthesis of MoS_2 films. The substrates used in my work are electrically conducting Nb-doped (0.5 wt %) $SrTiO_3$ crystals. It was chosen for this study because several surface terminations with different symmetries can be readily prepared.

MoS_2 was grown on the three well-studied $SrTiO_3$ terminations, (111), (110), and (001). The crystallinity of $SrTiO_3$ encourages MoS_2 monolayer crystals to grow epitaxially, and the different symmetries of the three terminations lead to distinct epitaxial behaviour. Overall, the interaction between MoS_2 and $SrTiO_3$ is found to influence the orientations, shapes, and optical properties of MoS_2 monolayers. The ability to regulate these properties of monolayer MoS_2 is important in the synthesis of large-scale layers to create material with minimal grain boundaries and controlled bandgaps. This will improve the potential of monolayer MoS_2 in its nanoelectronic and optoelectronic applications.

4.2 Results

Prior to the presentation of my experimental results, it is helpful to unambiguously define the crystallography of both MoS_2 and $SrTiO_3$ for the purpose of epitaxial analysis. Figure 4.1a.i is the side view of the 3D structure of 2H-MoS_2, the thermodynamically stable polytype of MoS_2.[119] Two other common polytypes are called 1T- and 3R-MoS_2, but they are not discussed here. The 2H-MoS_2 crystal consists of covalently bonded S–Mo–S sandwich layers held

together by vdW forces.[13,14,119] The unit cell is labelled in red, and a single unit cell of the lattice is shown to the right of the red arrow. It is a hexagonal structure with lattice parameters of $a = b = 3.1602$ Å, $c = 12.294$ Å and angles of $\alpha = \beta = 90°$, $\gamma = 120°$; the space group is $P6_3/mmc$ (194).[119] Figure 4.1a.ii is the top view of MoS_2. In common with other hexagonal systems, it is useful to employ a four-index notation to emphasise the equivalence between crystallographically equivalent directions.[274] For example, the a_1, a_2, and a_3 directions in Figure 4.1a.ii are all of the $<2\bar{1}\bar{1}0>$ type,[274,275] which highlights the symmetry of the structure. Many studies term the basal plane of MoS_2 as (0001),[165,276] implying the use of the four-index notation, though the in-plane crystallography tends not to be discussed. Figure 4.1a.iii shows the top view of triangular MoS_2 monolayers, which are 60° (or 180°) rotated with respect to each other. Their S-terminated edges are aligned along the $<2\bar{1}\bar{1}0>$-type directions. It should be noted that the orientations of the two crystals are not equivalent. For example, in the dashed circles the

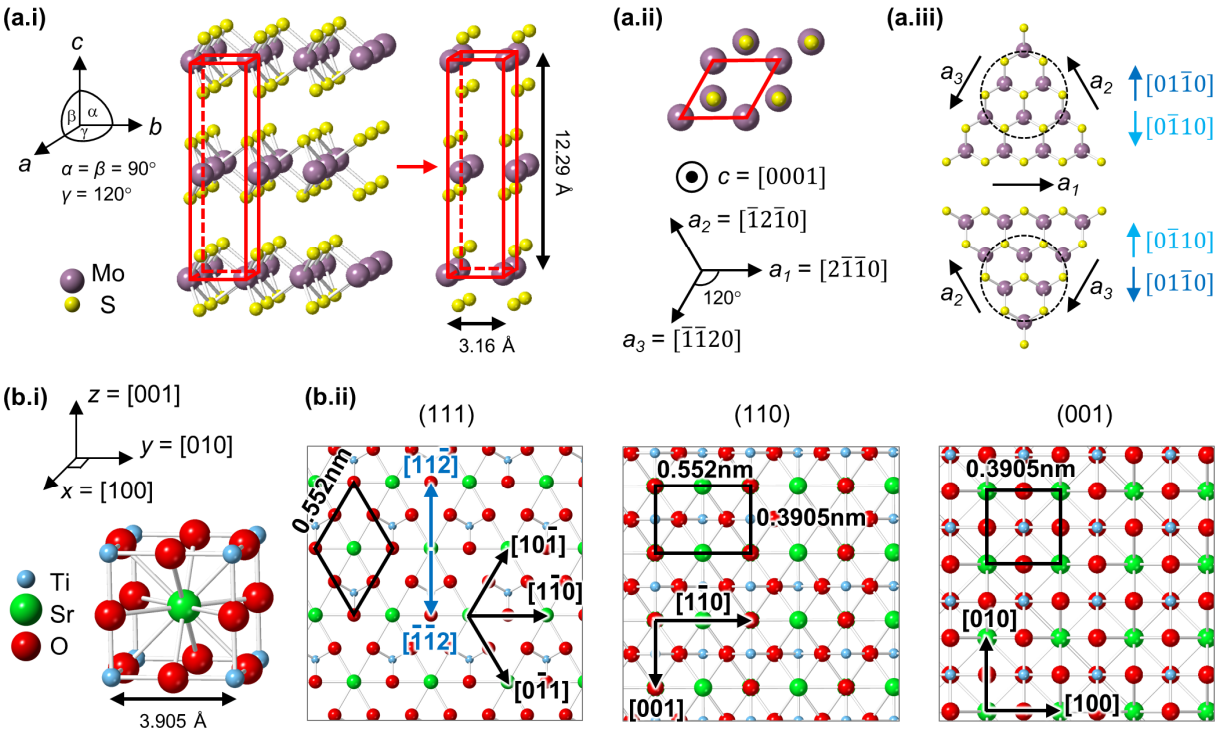

Figure 4.1: Crystal structures of MoS_2 and $SrTiO_3$. (a.i) Bulk MoS_2 with a red rhombic prismatic unit cell. (a.ii) Top view of MoS_2, with the crystallography defined by the four-index notation. (a.iii) Top view of monolayer triangular crystals of MoS_2. (b.i) Unit cell of $SrTiO_3$. (b.ii) Atomic top view of bulk-terminated $SrTiO_3$(111), (110), and (001) planes, with unit cells and lattice directions labelled. In (111), only two layers of atoms are shown for clarity.

two structures have the same skeleton of S atoms, but the Mo atoms are located differently. In other words, if the bottom layer of S atoms choose to orient in a specific way on the substrate, it can result in two different overall configurations due to the Mo atoms. For convenient subsequent analysis, it is useful to define the upwards and downwards crystallographic directions, which are $[01\bar{1}0]$ and $[0\bar{1}10]$, and they are inequivalent. Note that these directions are equivalent in a bulk MoS_2 crystal, which has in-plane hexagonal symmetry, which is reduced to 3-fold symmetry in a monolayer.

The crystal structure of $SrTiO_3$ is described in detail in Chapter 2 (section 2.1) and is summarised here in Figure 4.1b for easy reference. Figure 4.1b.i shows the cubic unit cell of $SrTiO_3$ (a = 3.905 Å)[43] and the three surface terminations of interest in my study are presented in Figure 4.1b.ii. The (111) termination is a 3-fold symmetric surface with a rhombic unit cell drawn in black. Upon close inspection of the unit cell, it can be seen that the upper and lower halves are not equivalent because there is an additional Ti atom in the lower half, one atomic layer down from the topmost Sr and O atoms. The Ti layer reduces the symmetry of the topmost layer from 6-fold to 3-fold. Again, it is helpful to define the upwards and downwards crystallographic directions on $SrTiO_3$(111), $[11\bar{2}]$ and $[\bar{1}\bar{1}2]$, a pair of inequivalent directions. Next, the (110) surface of $SrTiO_3$ has 2-fold symmetry and the unit cell is a rectangle (Figure 4.1b.ii). Finally, $SrTiO_3$(001) has 4-fold symmetry with a square surface unit cell (Figure 4.1b.ii).

As stated in Chapter 3 (section 3.2.1), all my $SrTiO_3$ samples were processed through UHV annealing and/or Ar^+-ion sputtering to remove the polishing damage. The surface reconstructions observed following UHV annealing cannot survive in an ambient environment. Therefore, the interface between the MoS_2 crystals and the $SrTiO_3$ substrates will differ from that of the UHV-prepared samples, but with this procedure, it is ensured that the maximum

degree of substrate crystallinity is created prior to CVD growth.

For the purposes of comparison, I first present data from an amorphous substrate. Figure 4.2 is an SEM image of MoS_2 crystals grown on SiO_2/Si. As one would expect from sulphur-rich growth conditions, the MoS_2 monolayers preferentially adopt triangular geometries.[122] The orientation of any crystal was measured as the angle that it makes with the horizontal line below it, whichever side is smaller (Figure 4.2, top right). Their orientations are randomly distributed, as shown in the histogram in the right-hand panel. The random distribution demonstrates that the vdW interaction between the amorphous substrate and MoS_2 monolayers induces no orientation preferences for the crystal growth.

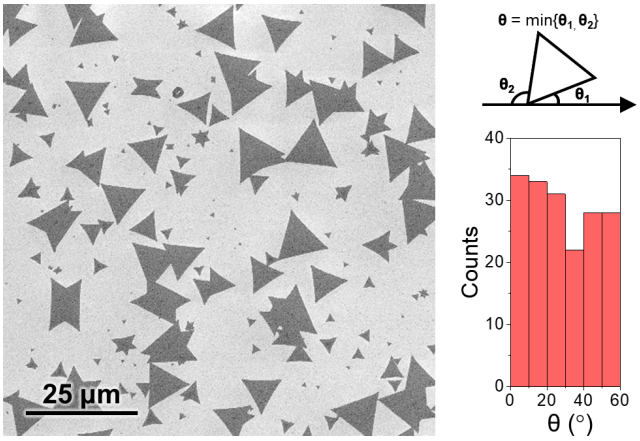

Figure 4.2: SEM image of monolayer MoS_2 crystals on SiO_2/Si and the orientation histogram of the MoS_2 crystals, measured according to the standard in the top-right part of the figure.

4.2.1 MoS_2 on $SrTiO_3$(111)

Figure 4.3a is an STM image of the $SrTiO_3$(111) surface composed of domains of (3 × 3) and (4 × 4) reconstructions,[43,56] with the average terrace step height being measured as 0.23 ± 0.03 nm (d_{111} lattice spacing = 0.225 nm). This surface is generated by Ar^+-ion sputtering at 500 eV for 8 min, and subsequent annealing at 1140 °C for 3 h in 4.5×10^{-4} Pa O_2. Figure 4.3a demonstrates that the outermost surface of my substrate is crystalline. Note that the white dots

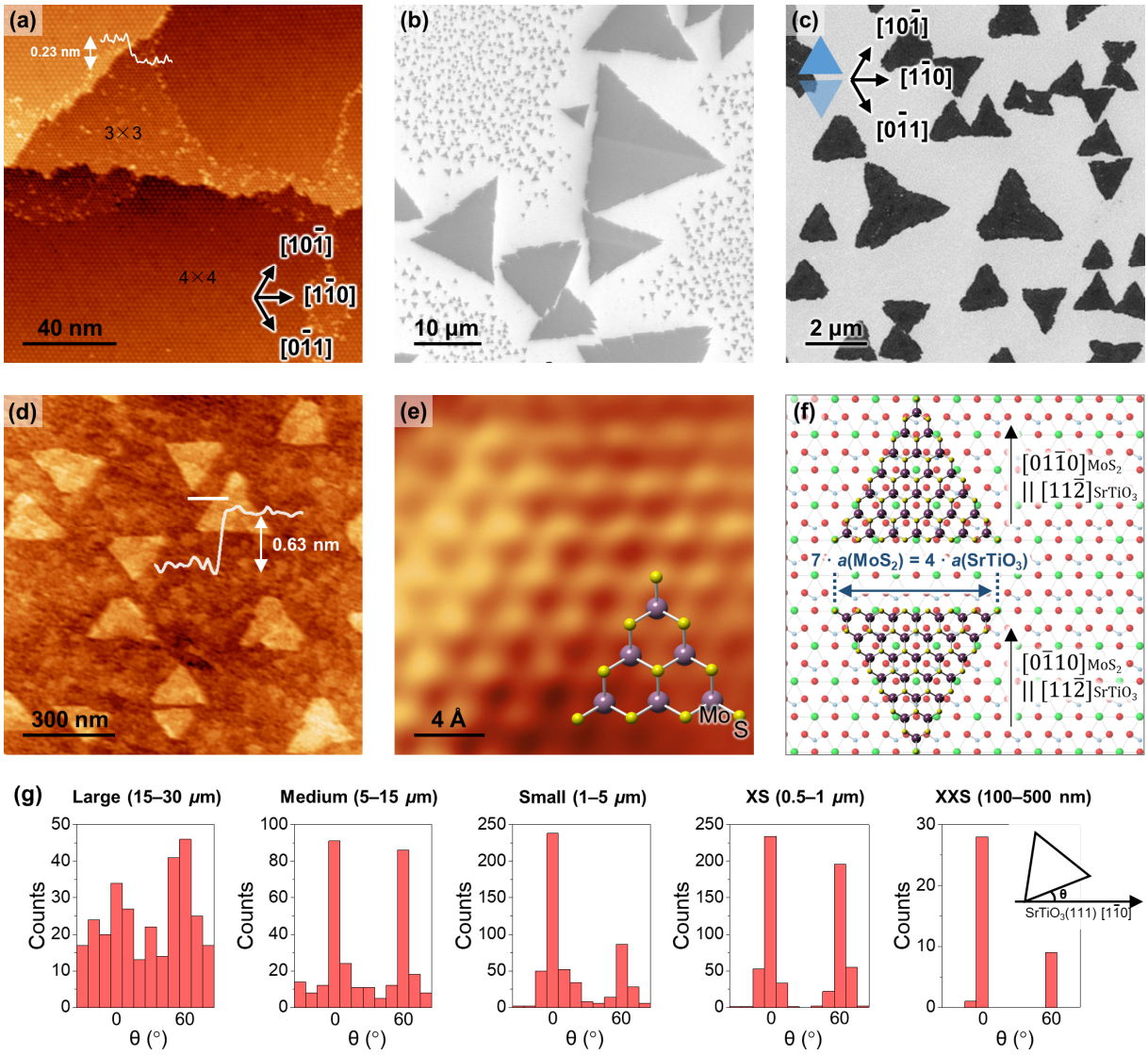

Figure 4.3: Models and images of $SrTiO_3$(111) and MoS_2 on $SrTiO_3$(111). (a) STM image of reconstructed $SrTiO_3$(111), showing terraces with (3 × 3) and (4 × 4) reconstructed domains. Two example domains are labelled. Each step height is 0.23 ± 0.03 nm and corresponds to the d_{111} lattice spacing (V_s = 2.0 V, I_t = 0.38 nA). (b) SEM image showing MoS_2 crystals with a large range of sizes (laterally 0.5–30 μm). (c) SEM image of small crystals (1–3 μm). The preferred crystal orientations are drawn as schematics, where the darker blue triangle is more preferred. (d) STM image showing very small MoS_2 crystals (200–400 nm), with a line profile showing the monolayer thickness (V_s = 1.5 V, I_t = 0.09 nA). (e) Atomically resolved STM image of a MoS_2 monolayer showing a triangular atomic lattice with a periodicity of 3.16 ± 0.09 Å, corresponding to the in-plane S–S distance (V_s = 1.1 V, I_t = 0.14 nA). An atomic model of monolayer MoS_2 is superimposed, assuming that S atoms are imaged by the STM. This image is averaged over 21 frames by *Smart Align*.[264,265] (f) Atomic models showing the two preferred orientations of MoS_2 crystals on $SrTiO_3$(111). The interfacial crystallography is written next to each orientation. Also, seven MoS_2 unit cell lengths (S–S spacings) = four $SrTiO_3$<1$\bar{1}$0> unit lengths (Sr–Sr spacings). The substrate lattice directions in panel (a) also apply to panels (b–f). (g) Orientation histograms of MoS_2 crystals with different sizes, measured according to the standard on the far right.

may be contaminants or regions that are not well reconstructed, which cannot be completely avoided even by careful UHV treatment. They exist in the best STM images of the $SrTiO_3$

surfaces reported.[38,43,63,66–69,76,83,84,86,92,93] In previous epitaxial studies of MoS_2 on crystalline substrates, e.g., *c*-plane sapphire,[114,160] as-received/epi-polished substrates were used. These substrates contain polishing damage and contaminants that are orders of magnitude greater than UHV-treated samples, but epitaxy was still found and studied.

Figure 4.3b shows a typical SEM image of MoS_2 crystals on $SrTiO_3$(111). The larger crystals (those with lateral sizes of over 5 μm) with S-terminated edges[122,277,278] appear to be randomly oriented, but in the close-up image of the smaller crystals (Figure 4.3c), the crystals show more regular alignment. The lattice directions of the $SrTiO_3$(111) substrate are also drawn at the top-left corner for reference: one can see that the small triangles mostly have their three sides parallel to the three <1$\bar{1}$0>-type directions on $SrTiO_3$(111), resulting in two main orientations as represented by the two blue schematic triangles. Another observation is that one of the two preferred orientations is more abundant (the darker blue triangle pointing up). Even smaller crystals were examined by STM, as shown in Figure 4.3d. The STM images show the height of the MoS_2 monolayers to be 0.63 ± 0.06 nm. This agrees with the previously reported value of 0.65 nm.[15,173] An atomically resolved STM image in Figure 4.3e shows a triangular pattern of bright dots with a periodicity of 3.16 ± 0.09 Å, which agrees with the literature value of 3.16 Å.[119] Because monolayer MoS_2 terminates with an outer plane of S atoms, from the topographical point of view, the bright protrusions in STM images are generally thought to be S atoms.[187,279]

The observations regarding epitaxy were statistically visualised by orientation histograms and are shown in Figure 4.3g. Note that in the SEM images (Figure 4.3b,c) some triangles have zigzag or concave edges, which are S-terminated because the MoS_2 crystals were grown in a sulphur-rich environment.[122] When an edge is not completely flat, its direction is measured as that of the straight line connecting its two ends, which is a good estimate of the S-termination

direction.[122] The MoS_2 crystals were grouped into large (15–30 μm), medium (5–15 μm), small (1–5 μm), XS (0.5–1 μm), and XXS (100–500 nm), according to their lateral sizes, i.e., the triangular edge lengths. In all cases, the two highest peaks are at 0° and 60°, indicating the two dominant orientations of MoS_2 crystals: '$(0001)_{MoS_2}\|(111)_{SrTiO_3}$, $[01\bar{1}0]_{MoS_2}\|[11\bar{2}]_{SrTiO_3}$' and '$(0001)_{MoS_2}\|(111)_{SrTiO_3}$, $[0\bar{1}10]_{MoS_2}\|[11\bar{2}]_{SrTiO_3}$'.

In the preferred orientations, MoS_2 and $SrTiO_3$(111) are both symmetry-coincident and lattice-commensurate: the length of seven MoS_2 unit cells (7 × 0.316 nm = 2.212 nm) equals the length of four $SrTiO_3$ unit cells (4 × 0.552 nm = 2.208 nm) with a small difference of < 0.2%, as illustrated in Figure 4.3f. In the histograms in Figure 4.3g, the preferred angular orientations are better defined for smaller crystals, and this can be explained by kinetics. The large crystals undergo a rapid growth process with little time to optimise their orientations relative to the substrate. However, the smaller crystals grow slowly and are able to rotate into orientations that optimise their vdW interaction with the substrate.

Another interesting possibility is that the smaller MoS_2 islands are constrained by the lattice commensuration so that they cannot grow to larger sizes. If so, the crystals would have grown rapidly to a certain size, beyond which it is difficult to expand further due to the lattice constraints. In this case, we should observe a disproportionately large number of crystals at that size. However, such an uneven size distribution is not seen (Figure 4.4). The statistics in Figure 4.3g and Figure 4.4 are based on the analysis of four $SrTiO_3$(111) samples prepared using the same procedure. The data in Figure 4.3g were collected from one random large-scale SEM scan and tens of STM scans of each sample, where each SEM scan contains hundreds of MoS_2 crystals (e.g., Figure 4.3b) while each STM scan contains only a few (e.g., Figure 4.3d being one of the largest-scale STM image obtained). Also, because of the limited scan size of STM (up to 2 × 2 μm^2), STM images selectively reveal XXS crystals only. Hence, the size

distribution data in Figure 4.4 only contain measurements from two random large SEM scans. It can be seen that ~40% of the crystals are smaller than 2 μm and that the distribution possibly follows a Gaussian curve centred at a size of < 2 μm.

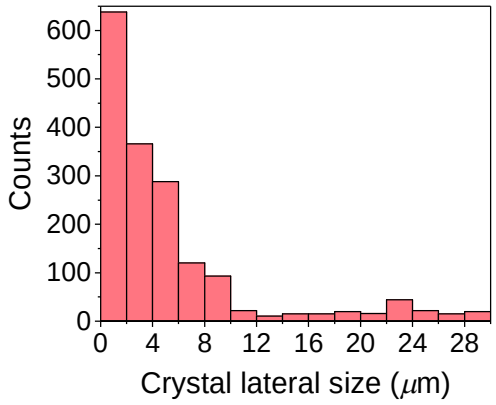

Figure 4.4: Size distribution histogram of MoS_2 crystals on $SrTiO_3$(111).

It is likely that one of the two preferred orientations is thermodynamically more stable. Particularly in the histograms of small and XXS crystals, there is a statistically significant difference between the heights of the two peaks. In Figure 4.3f are the atomic models of the two preferred orientations, in which the MoS_2 crystals sit in the same way as those in Figure 4.1a.iii. It was illustrated in Figure 4.1a.iii and b.ii that on both monolayer MoS_2 and $SrTiO_3$(111), the crystallographic directions pointing up and down are distinct. Hence, the two orientations of MoS_2 crystals on $SrTiO_3$(111) shown in Figure 4.3f are physically distinct, and their respective interfacial crystallography is labelled next to them. It is concluded that one of the two orientations is favoured, but they are not distinguishable from my results.

4.2.2 MoS_2 on $SrTiO_3$(110)

The $SrTiO_3$(110) substrates are treated in UHV to create a well-defined crystalline top surface. An STM image of the terraces is presented in Figure 4.5a, produced by annealing at 890 °C for

2 h, followed by another anneal at 910 °C for 3 h, both in UHV. This surface mainly consists of the (6 × 1) reconstruction.[63,65,66]

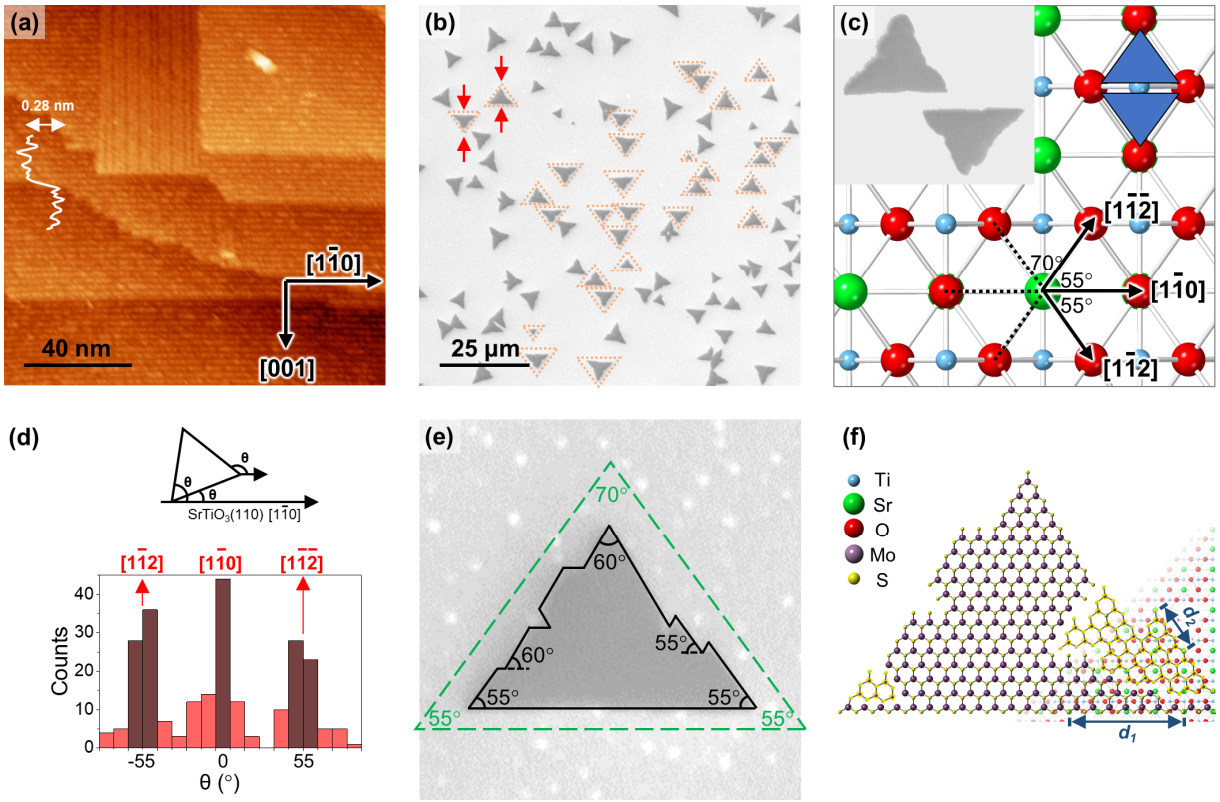

Figure 4.5: Models and images of $SrTiO_3$(110) and MoS_2 on $SrTiO_3$(110). (a) STM image of $SrTiO_3$(110) showing terraces mainly made of the (6 × 1) reconstruction. Each step height is 0.28 ± 0.04 nm, corresponding to the d_{110} lattice spacing (V_s = 1.0 V, I_t = 0.40 nA). (b) SEM image of MoS_2 on $SrTiO_3$(110). Some crystal shapes are 'compressed' along the [001] direction compared to equilateral triangles (outlined by orange dashed lines and red arrows at the top left). (c) Blue schematic triangles on the atomic model of $SrTiO_3$(110) representing the most commonly observed crystal orientations of MoS_2. The inset is an SEM image of MoS_2 crystals with the preferred orientations. (d) Edge orientation histogram of MoS_2 crystals on $SrTiO_3$(110), measured according to the standard above. (e) SEM image of a typically shaped MoS_2 crystal, with its rough edges highlighted in black. (f) Atomic model of a MoS_2 crystal on $SrTiO_3$(110), with the same shape in panel (e). The rotated lattice parts are highlighted in yellow. d_1 = seven MoS_2 unit cell lengths (S–S spacings) = four $SrTiO_3$[1$\bar{1}$0] unit lengths (Sr–Sr spacings). d_2 = three MoS_2 unit cell lengths (S–S spacings) = one $SrTiO_3$[1$\bar{1}\bar{2}$] unit length (Sr–Sr spacing). The substrate lattice directions in panel (a) also apply to panels (b,c,e,f).

Figure 4.5b is a typical SEM image of MoS_2 on $SrTiO_3$(110), from which it is noticeable that some triangles appear to be vertically distorted compared to the shape of equilateral triangles. This is illustrated on two of them by the red arrows at the top left of the image. There are two most commonly observed orientations, which are shown in the SEM image in Figure 4.5c and also drawn as blue schematic triangles on the atomic model of the substrate. Compared with

the substrate lattice, they each have their three sides parallel to $[1\bar{1}0]$, $[1\bar{1}\bar{2}]$, and $[1\bar{1}2]$ of the $SrTiO_3(110)$ substrate. In this case the direction of each crystal edge was measured according to the standard in Figure 4.5d. In the resulting histogram, which is based on measurements from a random large-scale SEM image, the brown peaks correspond to the three directions identified above, as expected. For example, $[1\bar{1}\bar{2}]$ is at 55° anticlockwise relative to $[1\bar{1}0]$, which is also shown in Figure 4.5c. If we refer to Figure 4.5c, we can see that such triangles with their edges parallel to $[1\bar{1}0]$, $[1\bar{1}\bar{2}]$, and $[1\bar{1}2]$ have three internal angles of 70°, 55°, and 55°.

The $[1\bar{1}0]$ direction is favoured because of the 7:4 coincidence epitaxy, similar to the case on $SrTiO_3(111)$. However, on $SrTiO_3(110)$, only one edge of any MoS_2 triangle can align with such a direction. Nevertheless, among those low-index (i.e., relatively close-packed) lattice directions which are at ~60° to $<1\bar{1}0>$, the $<1\bar{1}\bar{2}>$ directions are favoured for two reasons. The first one is again lattice commensuration: the unit length along $<1\bar{1}\bar{2}>$ is 0.9564 nm, which is three times the in-plane S–S distance in MoS_2 (0.316 nm), with a 0.9% difference. Secondly, $[1\bar{1}0]$, $[1\bar{1}\bar{2}]$, and $[1\bar{1}2]$ on $SrTiO_3(110)$ form a set of directions arranged in a nearly regular-hexagonal way (Figure 4.5c), with included angles of 70°, 55°, 55°.

In practice, an equilateral triangle of MoS_2 cannot be distorted to a 70°/55°/55° triangle while maintaining a perfect crystal structure; this would require an unphysical compressive strain of 18%. Figure 4.5e is a close-up SEM image of a crystal with its edges outlined in black, with an overall shape of a 70°/55°/55° triangle. Some internal angles are still 60°, which point to a perfect MoS_2 lattice, while some angles are closer to 55°, meaning the lattice may have been partially rotated and/or distorted to align one edge with $<1\bar{1}\bar{2}>$. Figure 4.5f presents an atomic model of MoS_2 that follows the shape in Figure 4.5e, including the zigzags and the notches along the edges with a sulphur termination. The bottom edge of the crystal is parallel to $[1\bar{1}0]$ on the substrate, along the labelled d_1, which is a distance corresponding to seven unit lengths

in MoS_2 and four unit lengths along $SrTiO_3[1\bar{1}0]$. The MoS_2 crystal also has some parts of its lattice rotated to align one edge with $<1\bar{1}\bar{2}>$ of $SrTiO_3$, highlighted in yellow. d_2 is labelled along the $[1\bar{1}2]$ direction, and its length represents one unit length along $[1\bar{1}2]$ and three unit lengths in MoS_2. The fact that this MoS_2 crystal tries to align with both $<1\bar{1}0>$ and $<1\bar{1}\bar{2}>$ inevitably induces lattice defects (e.g., around the rotated areas) plus a small degree of lattice distortion. The associated strain is confirmed by PL (section 4.2.4). On $SrTiO_3$(110), the interfacial crystallographic relationship is '$(0001)_{MoS_2}\|(110)_{SrTiO_3}$, $[2\bar{1}\bar{1}0]_{MoS_2}\|[1\bar{1}0]_{SrTiO_3}$' and partially '$(0001)_{MoS_2}\|(110)_{SrTiO_3}$, $[2\bar{1}\bar{1}0]_{MoS_2}\|[1\bar{1}\bar{2}]_{SrTiO_3}$'.

4.2.3 MoS_2 on $SrTiO_3$(001)

On the final surface in my study, $SrTiO_3$(001), the $c(4 \times 2)$ reconstruction was generated, as shown in Figure 4.6a.[69,87,88] It was produced by Ar^+-ion sputtering at 500 eV for 10 min, followed by annealing at 1100 °C for 30 min in UHV.

MoS_2 crystals grown on $SrTiO_3$(001) clearly show a distinct morphology compared with that on the other $SrTiO_3$ terminations (Figure 4.6b). The dendritic growth of MoS_2 on $SrTiO_3$(001) has been studied by Zhang *et al.*[280,281] and will not be discussed further here. For comparison, during the same CVD growth on an amorphous silica substrate, placed side by side with the $SrTiO_3$ sample, the MoS_2 crystals are perfectly sharp and triangular (Figure 4.2). Therefore, the dendritic growth can be safely attributed to the substrate effect of $SrTiO_3$(001).

To consistently study the epitaxy of compact crystals, compact triangular crystals were obtained when the precursors were placed closer to the substrate in the CVD furnace.[280] The resulting crystals are shown in Figure 4.6c, which are compact and much larger than the dendrites (note

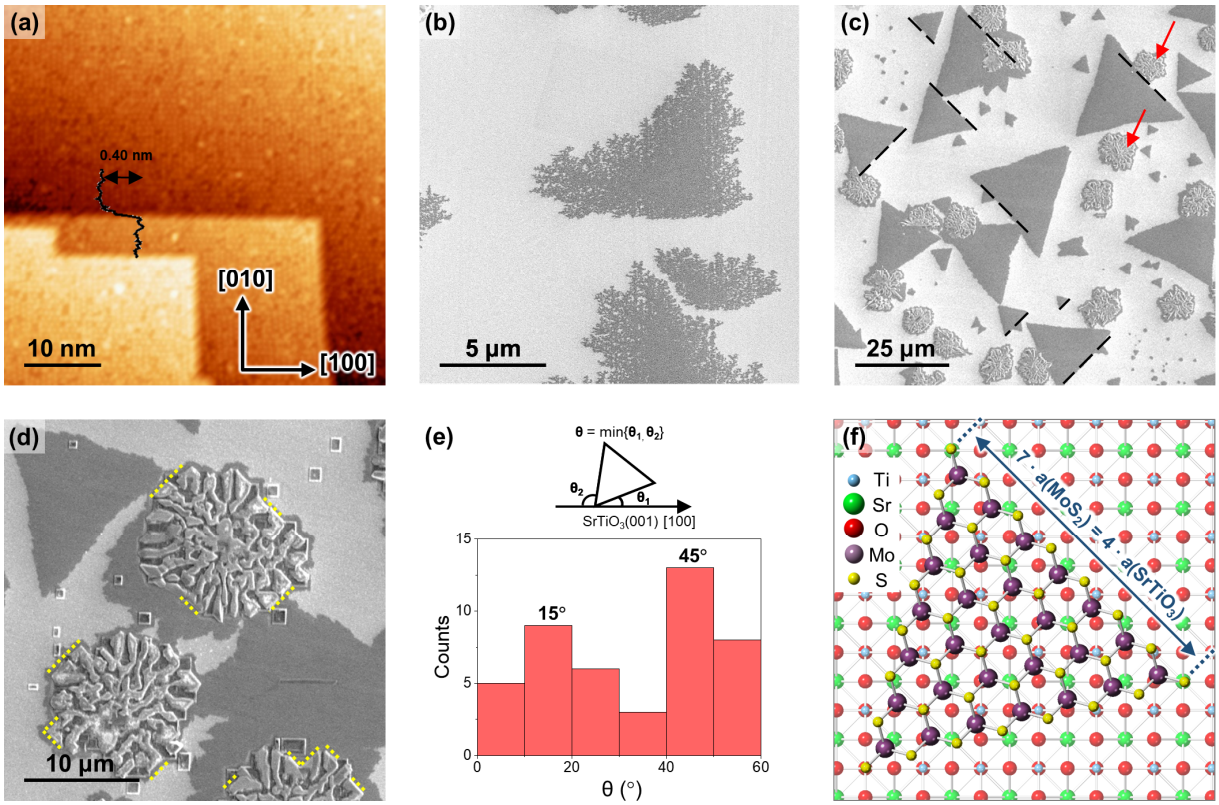

Figure 4.6: Models and images of $SrTiO_3$(001) and MoS_2 on $SrTiO_3$(001). (a) STM image of $SrTiO_3$(001) showing terraces consisting of the $c(4 \times 2)$ reconstruction. The step height is 0.40 ± 0.04 nm, corresponding to the d_{001} lattice spacing (V_s = 2.0 V, I_t = 0.15 nA). (b) SEM image of MoS_2 crystals on $SrTiO_3$(001) with a dendritic morphology. (c) SEM image of MoS_2 crystals on $SrTiO_3$(001) grown with a shorter source–substrate distance in the CVD furnace. The monolayer crystals (dark triangles) are compact and much larger than the dendrites, with few-layer (to bulk) MoS_2 also formed (indicated by red arrows). (d) SEM images of few-layer (to bulk) MoS_2 structures. (e) Orientation histogram of monolayer MoS_2 crystals, measured according to the standard above. (f) Atomic model of MoS_2 on $SrTiO_3$(001). Seven MoS_2 unit cell lengths (S–S spacings) = four $SrTiO_3[1\bar{1}0]$ unit lengths (Sr–Sr spacings). The substrate lattice directions in panel (a) also apply to panels (b,c,d,f).

the very different scale bars in Figure 4.6b and c), and no dendrites are observed. Using these growth conditions, it was difficult to completely avoid building up few-layer (to bulk) MoS_2 structures, as indicated by the red arrows. A close-up SEM image of these structures is shown in Figure 4.6d. The monolayer MoS_2 crystals in Figure 4.6c (dark triangles) are measured in terms of their crystal orientations, and the resulting histogram is shown in Figure 4.6e, which is based on measurements from a random large-scale SEM image. Two peaks are identified at 15° and 45°, relative to the substrate [100] direction. They are two crystallographically equivalent orientations because of the 4-fold symmetry of $SrTiO_3$(001). The interfacial

crystallographic relationship can be described as ' $(0001)_{MoS_2} \parallel (001)_{SrTiO_3}$, $[2\bar{1}\bar{1}0]_{MoS_2} \| [1\bar{1}0]_{SrTiO_3}$'.

Again, in these orientations, one edge of the triangular MoS_2 crystal aligns with the <$1\bar{1}0$> directions on $SrTiO_3$(001) because of the 7:4 coincidence epitaxy. A selection of such edges is highlighted by black dashed lines in Figure 4.6c. It is also interesting to note that even the few-layer (to bulk) MoS_2 structures have many of their edges aligned with the <$1\bar{1}0$> directions on $SrTiO_3$(001), as highlighted in yellow in Figure 4.6d. An atomic model is drawn in Figure 4.6f to show an example monolayer crystal and the lattice commensuration. It should be noted that the histogram peaks at 15° and 45° are not sharp, because the crystals measured are mostly large (15–30 μm), and their growth is more kinetically controlled than for the smaller ones, as discussed in section 4.2.1.

4.2.4 Raman spectroscopy and PL

Raman and PL spectroscopy were performed by my collaborator, Dr. Wenshuo Xu, to investigate some of the structural properties of the CVD-grown MoS_2 on different substrates. The experimental results were also analysed by Dr. Xu, who constructed Figure 4.7 and 4.8. The Raman and PL spectra are known to be influenced by the layer thickness,[133] lattice strain,[137,140–144] doping level,[282,283] and lattice defects[132] of MoS_2. These depend on the substrate surface (Figure 4.7a,b), the MoS_2 crystal morphology (Figure 4.7c,d), and the MoS_2 layer number (Figure 4.7e,f). Detailed information can be extracted through Lorentzian fitting of the PL spectra of monolayer MoS_2 on different substrates (Figure 4.8). In addition to the samples mentioned previously, MoS_2 monolayer crystals transferred onto a $SrTiO_3$ substrate were also studied. This sample serves as a reference for strain calculations as the crystals have released

their strain during the transfer process. Note that the transferred sample is also Nb-doped (0.5 wt %) and was annealed after the transfer to remove the trapped contaminants and to improve the MoS_2−$SrTiO_3$ interfacial adhesion. Therefore, its doping level can be considered nearly the same as that in the MoS_2 directly grown on $SrTiO_3$.

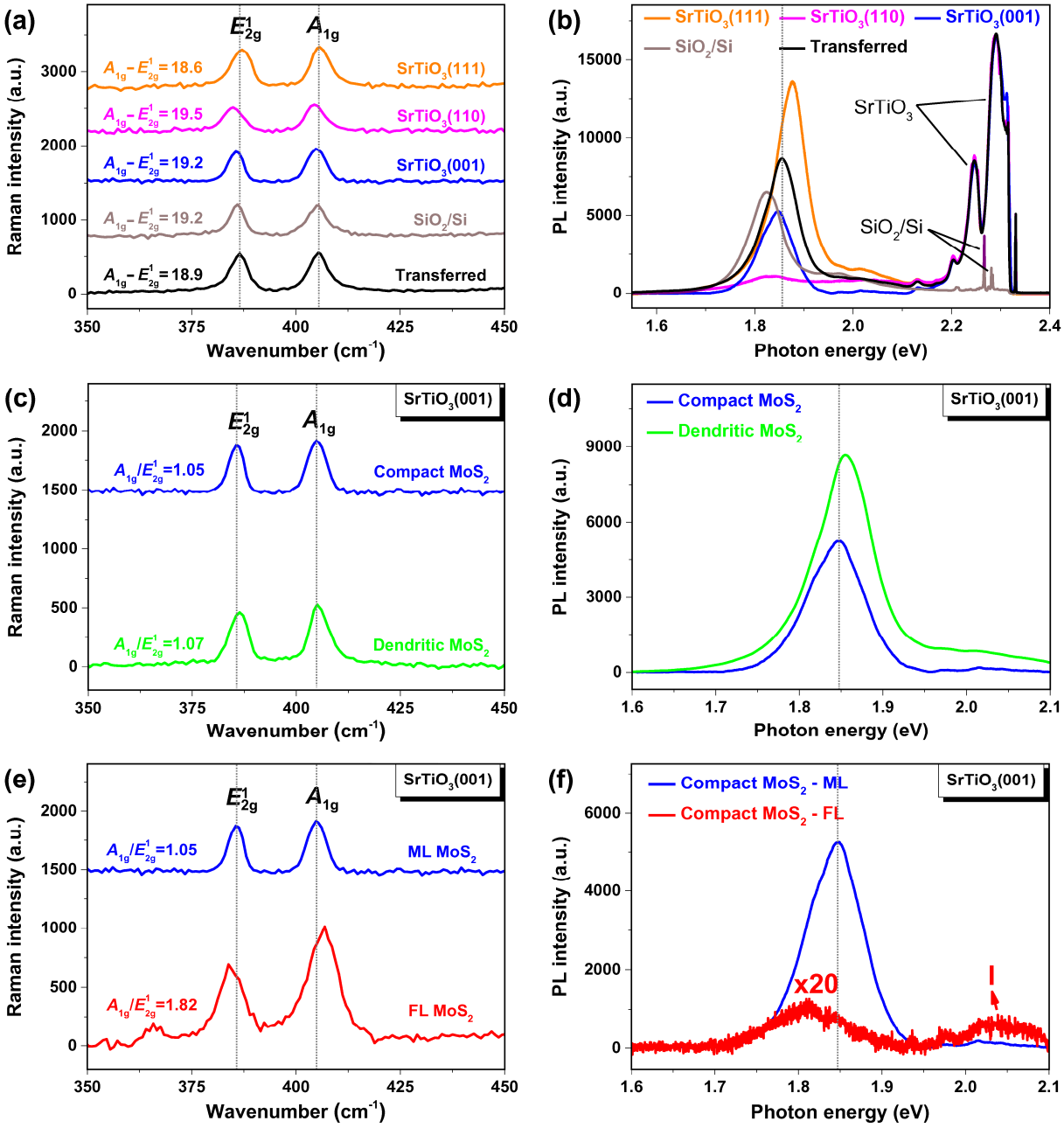

Figure 4.7: Raman and PL measurements. (a,c,e) Raman and (b,d,f) PL spectra of MoS_2 crystals (a,b) on different substrate surfaces, i.e., $SrTiO_3$(111), (110), (001), SiO_2/Si, and MoS_2 transferred onto $SrTiO_3$, (c,d) with different morphologies, i.e., compact and dendritic MoS_2 crystals, and (e,f) with different layer numbers, i.e., monolayer (ML) and few-layer (FL) MoS_2. 'I' indicates the indirect optical transition.

Figure 4.7a,c,e shows the two characteristic Raman modes of MoS_2, E^1_{2g} (382.0−384.3 cm^{-1}) and A_{1g} (403.0−407.5 cm^{-1}).[133] The E^1_{2g} and A_{1g} modes are preferentially excited for terrace and edge terminations, respectively.[157] Therefore, the relative integrated intensities of A_{1g} and E^1_{2g} can provide information on the texture of MoS_2.[127,157,158] Regardless of the substrate, all of the MoS_2 monolayers dominated by terrace sites exhibit similar integrated intensity ratios of A_{1g}/E^1_{2g} ~1.05, whereas the few-layer MoS_2 terminated more by edges shows an increased ratio of A_{1g}/E^1_{2g} ~1.82 (Figure 4.7a,c,e), conforming well to those reported previously.[127,133] Also, the frequency difference between A_{1g} and E^1_{2g} modes can be used to precisely determine the layer number of MoS_2. Our values are ≤ 19.5 cm^{-1} for all the monolayer MoS_2 and ≥ 23.1 cm^{-1} for the few-layer MoS_2 (Figure 4.7a,c,e), in good agreement with the literature.[133] An example of the few-layer structures is shown in Figure 4.6d. Figure 4.7f presents the PL of the monolayer and few-layer MoS_2 on the same substrate termination, $SrTiO_3$(001). In addition to the direct transitions (K→K) involving two split valence bands for the emissions of A and B excitons, few-layer MoS_2 shows an additional peak (I) originating from the indirect transition (Λ→Γ) (see Figure 2.13b in Chapter 2).[13,14,284] Compared to the monolayer MoS_2, the few-layer MoS_2 exhibits much weaker PL with lower emission energies (monolayer – 1.85 eV for A excitons and 2.02 eV for B excitons; few-layer – 1.81 eV for A excitons, 1.98 eV for B excitons, and 2.04 eV for indirect excitons).

The lattice strain in MoS_2 develops via two processes. The first is epitaxial growth associated with the lattice mismatch between MoS_2 and the substrate. The second is the post-CVD fast cooling, during which strain develops due to the different thermal expansion coefficients (TECs) of MoS_2 and the substrate.[135] The TEC of the as-prepared 2H-phase MoS_2 ($\alpha_{MoS_2,a}$ = 1.9 × 10^{-6} K^{-1} and $\alpha_{MoS_2,c}$ = 8.65 × 10^{-6} K^{-1}, 293–1073 K)[285] is approximately an order of magnitude larger than that of SiO_2 (typical value α_{SiO_2} = 5.6 × 10^{-7} K^{-1}),[286] while it is about an order of

magnitude smaller than that of $SrTiO_3$ (α_{SrTiO_3} = 3.23 × 10^{-5} K^{-1}, 300–1800 K).[287] As a result, in the fast-cooling stage following MoS_2 growth, tensile strain develops in the SiO_2-supported MoS_2, whereas compressive strain is introduced in MoS_2 on $SrTiO_3$.[135] The tensile and compressive strains respectively lead to red- and blueshifts of the E^1_{2g} and A_{1g} Raman peaks and the A-exciton PL peak, relative to the transferred sample (Figure 4.7a,b).[137,140–144] However, these three peaks are all red-shifted for the monolayer MoS_2 crystals grown on $SrTiO_3$(110) and (001), which is attributed to epitaxial growth. As manifested in Figure 4.5 and 4.6, the MoS_2 monolayer crystals show a large lattice mismatch with the $SrTiO_3$(110) and (001) terminations, leading to the tensile strain. To estimate the growth-induced tensile strains in the MoS_2 monolayers grown on $SrTiO_3$(110) and (001), we use their peak shifts of the E^1_{2g} Raman mode with respect to that on $SrTiO_3$(111).[145] As stated in section 4.2.1, the small difference of < 0.2% in the lattice parameters between MoS_2 and $SrTiO_3$(111) should give rise to a compressive strain of ~0.18% in the MoS_2 adlayer. Taking this into account, the growth-induced tensile strain is ~0.58% on $SrTiO_3$(110), caused by the attempt of MoS_2 crystal edges to align with both <$1\bar{1}0$> and <$1\bar{1}\bar{2}$> crystallographic directions. It is ~0.34% on $SrTiO_3$(001), ascribed to the lattice mismatch along the two non-epitaxial edges of the monolayer MoS_2 crystal. Finally, the growth-induced strain can be considered negligible in the monolayer MoS_2 grown on SiO_2/Si because of the amorphous substrate surface, which leads to the random orientations of MoS_2 crystals in Figure 4.2.

Figure 4.7b also shows that the tensile strains in the monolayer MoS_2 supported on $SrTiO_3$(110), $SrTiO_3$(001), and SiO_2/Si substrates commonly lead to decreased PL intensities compared to the transferred sample.[137] In particular, significant PL quenching is observed on $SrTiO_3$(110), which stems from the epitaxy-induced lattice defects in the crystals previously shown in Figure 4.5f, which will be discussed later (Figure 4.8). However, on $SrTiO_3$(111), the PL intensity is enhanced by 58% with a slightly narrower peak width (decrease in the full width at half

maximum ΔFWHM = 7.05 meV) compared to the transferred sample because of the compressive strain,[141] which agrees with the Raman results.

Moreover, the crystal morphology also impacts the strain level in MoS_2. As shown in Figure 4.7c,d, the dendritic MoS_2 crystals on $SrTiO_3$(001) display small blueshifts of Raman peaks and the A-exciton PL peak relative to the compact triangular crystals. (Note that the E^1_{2g} Raman mode corresponding to the in-plane Mo−S phonon is more sensitive to strain than the A_{1g} mode corresponding to out-of-plane Mo−S phonon.[137,141–145]) This is because the dendrites could have partially released the growth-induced tensile strain by generating numerous fragmental edges. This suppresses the deterioration of the MoS_2 lattice and its optical properties, which also results in the stronger PL intensity of the dendrites.

The peak positions in Figure 4.7 were simply identified as the maximum-intensity positions. The PL spectra are also fitted with Lorentzian peaks by Dr. Wenshuo Xu (Figure 4.8), and four peaks are fitted in each spectrum: the A and A^- peaks for A-exciton emission, the B peak for B-exciton emission, and localised states (LSs) correlated with the structural disorder of MoS_2.[132] During the peak fitting, the only constraint applied was the spacing between A and A^- peaks (24 meV), which is related to the binding energy of A^- trions.[131] All other parameters were kept free, including the individual peak positions and the areas under the peaks. Background was not subtracted as it is sufficiently weak to be neglected in the range of 1.64–2.10 eV (Figure 4.8). The LS peaks indicate the defect levels in the as-grown MoS_2 crystals: $SrTiO_3$(110) > $SrTiO_3$(001) > $SrTiO_3$(111). This depends on the degree of lattice mismatch between MoS_2 and the $SrTiO_3$ surface termination. In addition to the neutral A exciton, the negatively charged exciton (trion, A^-) in Figure 4.8 suggests *n*-type doping in the monolayer MoS_2 on all substrates. The intensity ratio of trion-to-exciton peaks (A^-/A) can be used to infer the doping level.[129] The larger A^-/A ratio on the SiO_2/Si substrate proves that the charge impurities induce heavier *n*-

doping into the supported MoS_2 than the Nb in $SrTiO_3$ substrates. Nonetheless, the doping level of MoS_2 on all $SrTiO_3$ substrates (all Nb-doped at 0.5 wt %) is the same. Therefore, the growth-induced strains can be safely deduced from the Raman and the A-exciton PL peak positions of MoS_2 on different terminations of $SrTiO_3$.

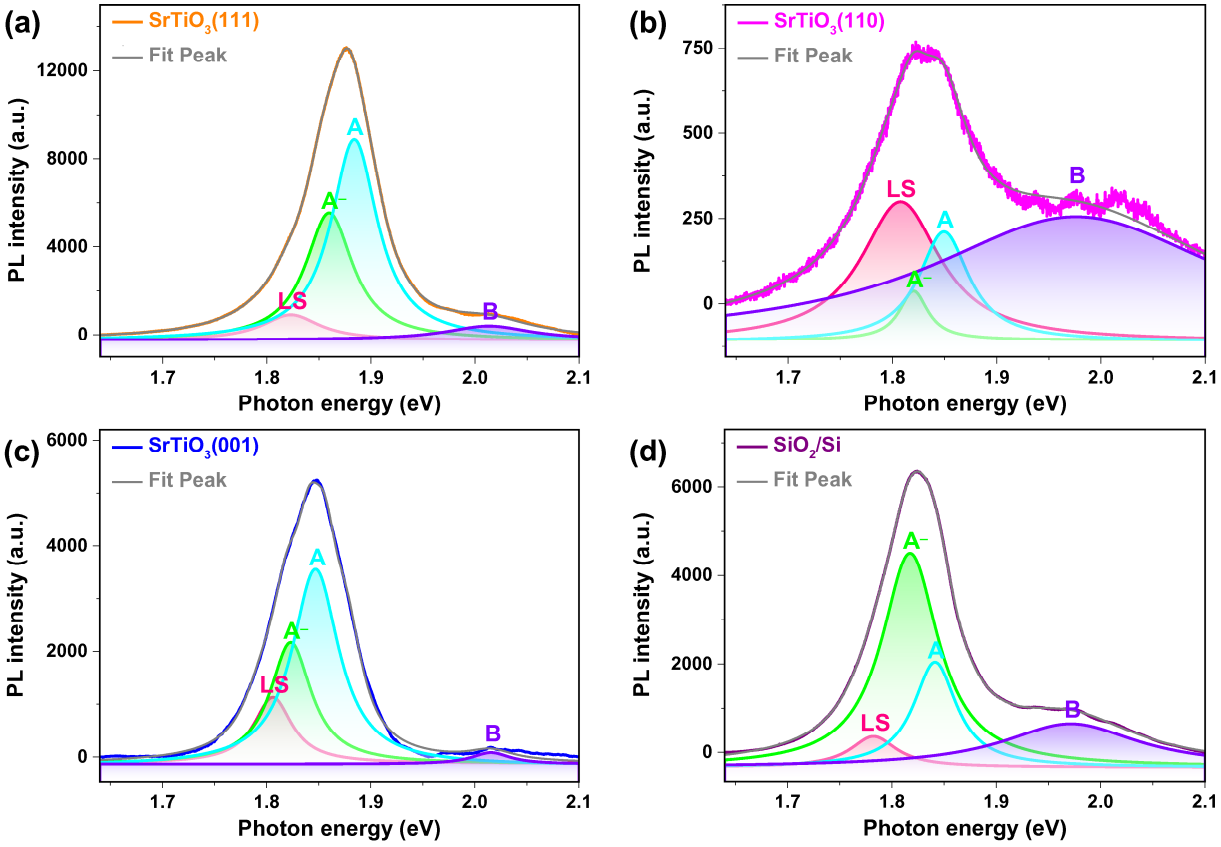

Figure 4.8: Lorentzian-fitted PL spectra of monolayer MoS_2 crystals grown on (a) $SrTiO_3$(111), (b) $SrTiO_3$(110), (c) $SrTiO_3$(001), and (d) SiO_2/Si substrates, revealing the presence of A excitons (A), negatively charged A excitons (trions, A^-), B excitons (B), and localised states (LSs).

4.3 Discussion

It has been shown that on three different crystal terminations of $SrTiO_3$, MoS_2 crystals tend to adopt the orientations that allow their lattice to match that of the substrate via coincidence epitaxy. The equilibrium orientations and crystal shapes maximise the number of directions along which this is achieved. The interfacial vdW bonding is strengthened in the epitaxial

orientations via lattice registry, giving rise to a greater number of bonding sites and closer proximity between the two layers. Therefore, when a MoS_2 nucleus is free to rotate in the initial stage, it gets 'locked' into the lowest-energy orientation,[160] i.e., in the epitaxial configurations we observed. Other bonding types, e.g., electrostatic attraction[114] and chemical bonds,[288] are less likely to exist between MoS_2 and $SrTiO_3$. This is because they are stronger than vdW bonding by orders of magnitude and would lock the MoS_2 monolayers exclusively into certain orientations, e.g., as observed on Au(111).[277] Gold, an electronegative metal, is a very different substrate from $SrTiO_3$, an oxide ceramic, and can interact with MoS_2 via a stronger bonding type. Nb doping (0.5 wt %), which makes $SrTiO_3$ conductive, may also have played a role in its bonding with MoS_2 monolayers, but any effects are expected to be minimal.

On $SrTiO_3$(111), it is advantageous to align the $<2\bar{1}\bar{1}0>$ directions of MoS_2 with $<1\bar{1}0>$ on $SrTiO_3$ with a favourable coincidence lattice registry. In previous studies of MoS_2 grown on ceramic substrates, SiO_2 does not induce epitaxy because it is amorphous;[122] *c*-plane sapphire, another 3-fold-symmetric substrate, reveals similar preferred orientations to those of MoS_2 on $SrTiO_3$(111) (0° and 60°).[114,160] In these orientations, either interfacial electrostatic attraction (as a result of charge transfer)[114] or greatly enhanced vdW bonding[160] was proposed. It was not explicitly mentioned why the interfacial bonding prefers particular orientations, but this is likely to be the good lattice registry between MoS_2 and sapphire. Their in-plane periodicities, 0.316 nm for MoS_2 and 0.476 nm for sapphire, have a 2:3 ratio with a 0.4% difference.[114] Therefore I speculate that both $SrTiO_3$(111) and *c*-plane sapphire show similar low-energy coincidence epitaxial relationships because of lattice commensuration with negligible strain.

Also, one of the two lattice-coincident orientations on $SrTiO_3$(111) is more strongly preferred, and a similar situation is found in the MoS_2-on-Au(111) system. An Au(111) substrate has a face-centred-cubic (fcc) bulk structure, which, along its [111] direction, can terminate either on

an fcc or a hexagonal-close-packed (hcp) site.[289] These two types of domains have identical surface atomic arrangements that are rotated by 180° with respect to each other. Theoretical studies by Bruix *et al.* reveal a very slim energy difference (16 meV per unit cell) between the 'MoS_2-on-hcp' and 'MoS_2-on-fcc' configurations,[169] but the crystals turn out to exclusively orient in only one way.[277] The termination of Au(111) alternates between hcp and fcc across a ridge of the herringbone structure, so that the MoS_2 triangles 'flipping' their directions across each ridge means the same stacking. This exclusivity is also assisted by a much slower growth method adopted than CVD, which results in nanometre-sized crystals (all < 8 nm).[277] On the other hand, $SrTiO_3$(111) shows a uniform termination with surface step heights always equivalent to the d_{111} lattice parameter.[38,43] Hence, the 0° and 60° orientations of MoS_2 are indeed distinct, possibly with a very small but noticeable energy difference like on Au(111).

On $SrTiO_3$(110), the strong tendency to maximise coincidence epitaxial directions (i.e., $<1\bar{1}0>$ and $<1\bar{1}\bar{2}>$) competes with the equilibrium shape of the MoS_2 crystals. To accommodate the shape distortions, there is an increased defect density and an additional element of strain energy. These both increase the lattice energy of MoS_2 but must have been overcome by the reduction in the interfacial energy because of the improved bonding. Even on $SrTiO_3$(001), where it is only possible to satisfy one direction of good coincidence epitaxy along $<1\bar{1}0>$, the MoS_2 crystals still show a preference to orient in such a way.

It is worth noting that, because the substrate surface reconstructions prepared in vacuum do not usually survive in atmosphere down to the atomic level (though atomic terraces still remain), we do not know what the exact interface is at the time of CVD growth of MoS_2. It cannot be the bulk termination of $SrTiO_3$ because the surface bonds tend to rearrange themselves to stabilise surface polarity. However, we do know that there are certain ways in which $SrTiO_3$ reconstructs. For example, $SrTiO_3$(111)-(4 × 4) is one of the lowest-energy reconstruction of

the (111) termination, which forms most easily in partial pressures of oxygen.[43,56] If MoS_2 grows on $SrTiO_3$(111)-(4 × 4), the substrate periodicity (i.e., the unit length along <$1\bar{1}0$>) becomes four times that of the bulk. The coincidence epitaxy then turns into a 7:1 ratio, which is an attractive epitaxial relationship. On $SrTiO_3$(110), (1 × 4), (3 × 4), (4 × 4), and (6 × 4) reconstructions have been reported previously,[63,290] which make the periodicity along <$1\bar{1}0$> four times that in the bulk as well. Similarly on $SrTiO_3$(001), there is a (4 × 4) reconstruction which does the same thing;[82] there is also a *c*(4 × 4) reconstruction, which makes the periodicity along <$1\bar{1}0$> $2\sqrt{2}$ times that of the bulk, and this turns the coincidence epitaxy into a 5:1 ratio with a mismatch of 1.2%.[82,93]

Based on the above, my understanding of what drives the epitaxy is the interfacial lattice commensuration between <$2\bar{1}\bar{1}0$> (i.e., the sulphur edge directions) of MoS_2 and <$1\bar{1}0$> on $SrTiO_3$. The strength of this vdW interaction is stressed, which can powerfully control the growth of MoS_2 crystals. Developing a deeper understanding of MoS_2 epitaxy is an important step towards integrating MoS_2 in future novel electronic devices. This is because when MoS_2 is grown in perfect lattice registry with its crystalline substrate, grain boundaries are eliminated. This allows large-area monolayers of MoS_2 to be grown even when there are multiple nucleation sites.

Finally, it is mentioned that it is very difficult to obtain atomically resolved STM images of MoS_2 on a ceramic substrate, and a high-resolution image like Figure 4.3e is rare. If such images could be obtained on all terminations of $SrTiO_3$ substrates, they would provide useful information on the strain or lattice distortions in monolayer MoS_2. Many good atomic images of MoS_2 monolayers on Au(111) have been reported,[165,169,187,277,278] but it was difficult for the same group of researchers to obtain high resolution images of MoS_2 on TiO_2.[288] It is not yet clear to us why it is a lot harder to image MoS_2 on ceramic substrates than on metal substrates.

Possibly metal substrates have a more uniform charge distribution and also free electrons that they can donate to the MoS_2 layer, which helps STM imaging, a technique based on electron tunnelling. This is no doubt an interesting area for future study.

4.4 Conclusions

In summary, the orientations and shapes of MoS_2 crystals are strongly influenced by substrate interactions with $SrTiO_3$. The equilibrium orientations maximise the interfacial vdW bonding via coincidence epitaxy and hence enhanced bonding, which is assisted by lattice defects and crystal shape distortions when possible. This offers a broader interpretation of epitaxy, which involves minimisation of the total energy of the system in a more complex way. It is the sum of the lattice energy of MoS_2 (to maintain its equilateral triangular shape) and the interfacial energy associated with the MoS_2–substrate interactions. The results also confirm that the vdW interaction is sufficiently strong to regulate epitaxy in a powerful way. The strain levels in MoS_2 are found to be adjusted by the different epitaxial relations with the substrate. This allows us more rigorous control in the synthesis of large-scale uniform MoS_2 layers for optimal electronic properties and enables the manipulation of inbuilt strains to fine-tune the bandgap, which improve the applicability of monolayer MoS_2 in next-generation nanoelectronic devices.

Chapter 5

Thermal Degradation of Monolayer MoS_2 on $SrTiO_3$ Supports

The work in this chapter has been published in Chen *et al. J. Phys. Chem. C* **2019**, *123*, 3876−3885.[115] My contribution to this project includes the following: designing and directing the project, preparing $SrTiO_3$ substrates in UHV, performing STM experiments, all data analysis apart from those of Raman spectroscopy and PL (in sections 5.2.3 and 5.2.5), interpretation of all results, and all writing up apart from the initial draft of section 5.2.3.

5.1 Introduction

Monolayer MoS_2 is a wide-bandgap semiconductor suitable for use in high-temperature electronics.[173,174] It is therefore important to understand its thermal stability. In this chapter, we examine the thermal decomposition in vacuum of monolayer MoS_2 supported on the single crystal substrate $SrTiO_3$. In contrast to most of the studies mentioned in the Literature Review

(section 2.2.5), here monolayer MoS_2 islands are exclusively studied, which are of greater technological interest compared with thicker MoS_2 crystals. In vacuum, we exclude the effects of oxygen in the atmosphere so that all changes upon annealing can be attributed to MoS_2 itself and its oxide substrate. This setup allows us to assess how MoS_2 crystals would behave in devices that require high-temperature processing.

The step-by-step changes in MoS_2 monolayers were tracked from their initial degradation at 700 °C to the complete evaporation of MoO_x (x = 2–3) residues at temperatures above 1000 °C. The changes were monitored by optical microscopy (OM), SEM, STM, XPS, PL, and Raman spectroscopy. Although the optical properties of MoS_2 crystals deteriorated to a large extent after annealing in vacuum, it was found that they can be partially recovered via a follow-up annealing treatment in a sulphur atmosphere. This raises the possibility of healing any non-substantial defects via a sulphur-annealing step during the fabrication of MoS_2-based devices.

5.2 Results

In Chapter 4 and also in our publication,[136] we reported the distinct epitaxial behaviour of MoS_2 crystals on the (111), (110), and (001) substrate terminations of $SrTiO_3$ but here no marked differences were noticed between their thermal stabilities on the different $SrTiO_3$ terminations. The terminations used in each case are specified in the figure captions of the relevant images.

In this chapter, the as-grown MoS_2 samples were introduced into the UHV-STM chamber for annealing using the same method as that of substrate preparation (section 3.2.2). A schematic setup is shown in Figure 5.1. The temperature was ramped up and down at a rate of 2.5−5.5 °C min^{-1}, and each anneal lasted 0.5−5.5 h.

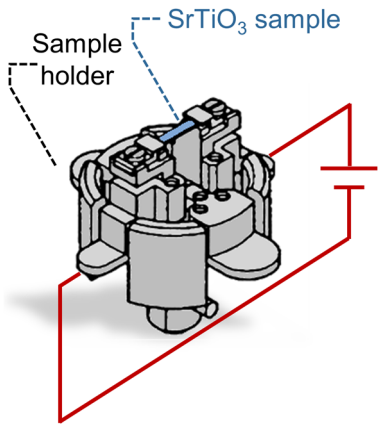

Figure 5.1: UHV sample holder for direct resistive heating for both $SrTiO_3$ substrate preparation and the thermal annealing of MoS_2 crystals on $SrTiO_3$.

5.2.1 SEM and STM experiments

MoS_2 crystals on a $SrTiO_3$(111) substrate were annealed in UHV for 2 h with a temperature gradient across the sample. The temperature was 700 °C at the cooler end, and 800 °C at the hotter end. SEM images were taken after the sample was cooled down (Figure 5.2a.i, ii). The crystals at the cool end (Figure 5.2a.i) are clear and black; they look no different from the as-grown crystals. Towards the hotter end, the crystals appear fainter (Figure 5.2a.ii). Figure 5.2a.ii was acquired soon after Figure 5.2a.i with the same brightness and contrast settings, which means that the contrast between the MoS_2 crystals and the substrate has changed. Although the more detailed internal structure cannot be resolved by SEM, it is expected that the MoS_2 crystals have degraded through desulphurisation. Figure 5.2b.i,b.ii shows another pair of images demonstrating the effect of UHV annealing at 1150 °C for 3 h. This treatment further lowers the visibility of the crystals, where they have clearly decomposed, with some residues remaining in triangular shapes. Similar survivor traces have been observed after a lift-off process of WS_2.[291]

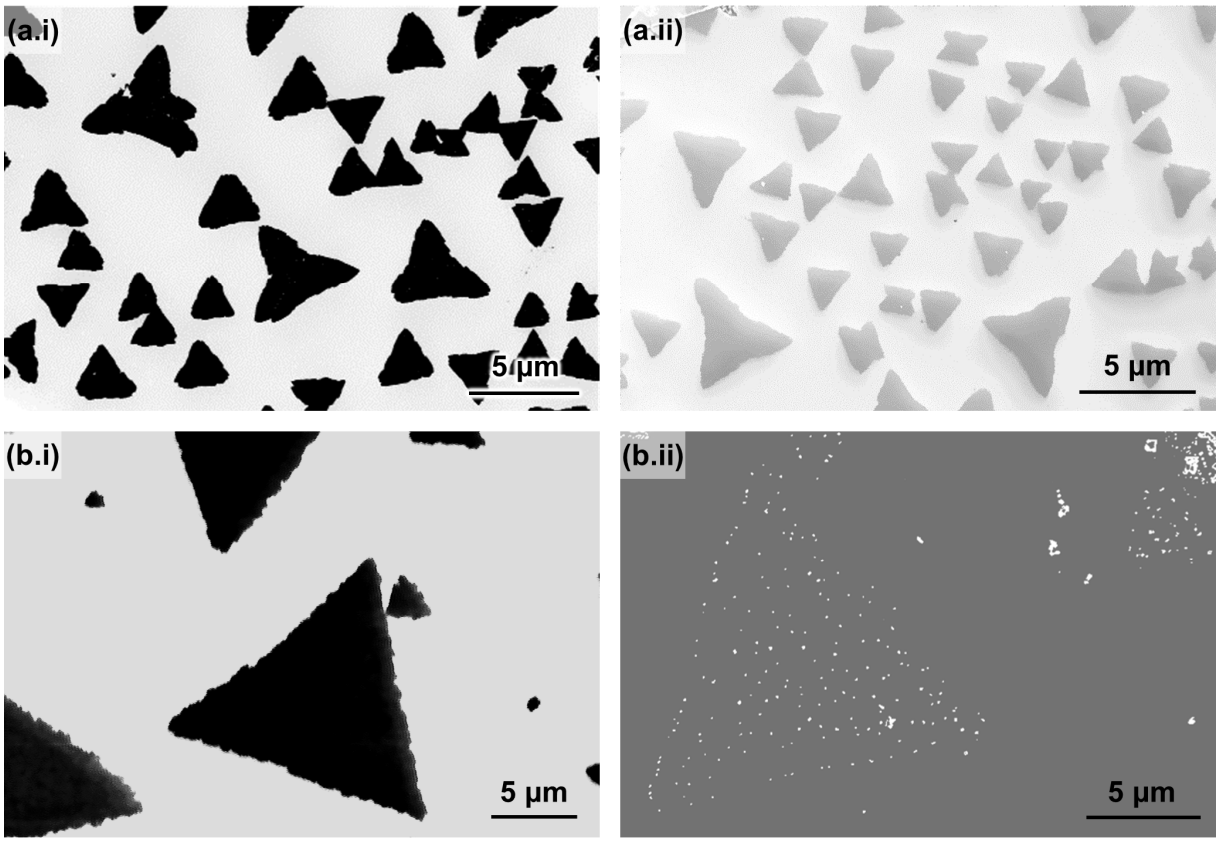

Figure 5.2: SEM images of MoS_2 crystals on $SrTiO_3$ substrates after UHV annealing at (a.i) 700 °C and (a.ii) 800 °C for 2 h on $SrTiO_3$(111) and (b.i) before and (b.ii) after UHV annealing at 1150 °C for 3 h on $SrTiO_3$(001). The contrast in (b.ii) is enhanced to show the residues.

STM studies can elucidate the structural transformations at higher resolution than SEM. Below 700 °C, the samples are only degassed; i.e., adsorbates and contaminants are removed. Not much difference is seen after these gentle UHV anneals in STM. The MoS_2 layer is uniform and conforms well to the substrate terraces with a thickness of 0.63 ± 0.06 nm (Figure 5.3a), which is typical of a monolayer.[15,173] The atomic model of MoS_2 overlaid shows the orientation of the triangular crystal, and it also applies to the other panels in Figure 5.3. The $SrTiO_3$(111) substrate was processed to generate a (4 × 4) reconstruction in UHV before the CVD growth of MoS_2;[43,56] although the reconstruction would not have survived in an ambient environment, the terraces still remain. Figure 5.3a.i,a.ii shows two high-magnification images illustrating the typical morphologies outside of and on top of the MoS_2 monolayer, respectively. There are clusters of small triangles aligned on the substrate with a periodicity of 2.20 ± 0.05 nm (Figure 5.3a.i), and these islands are seen to raise the height of the MoS_2 monolayer (Figure 5.3a.ii).

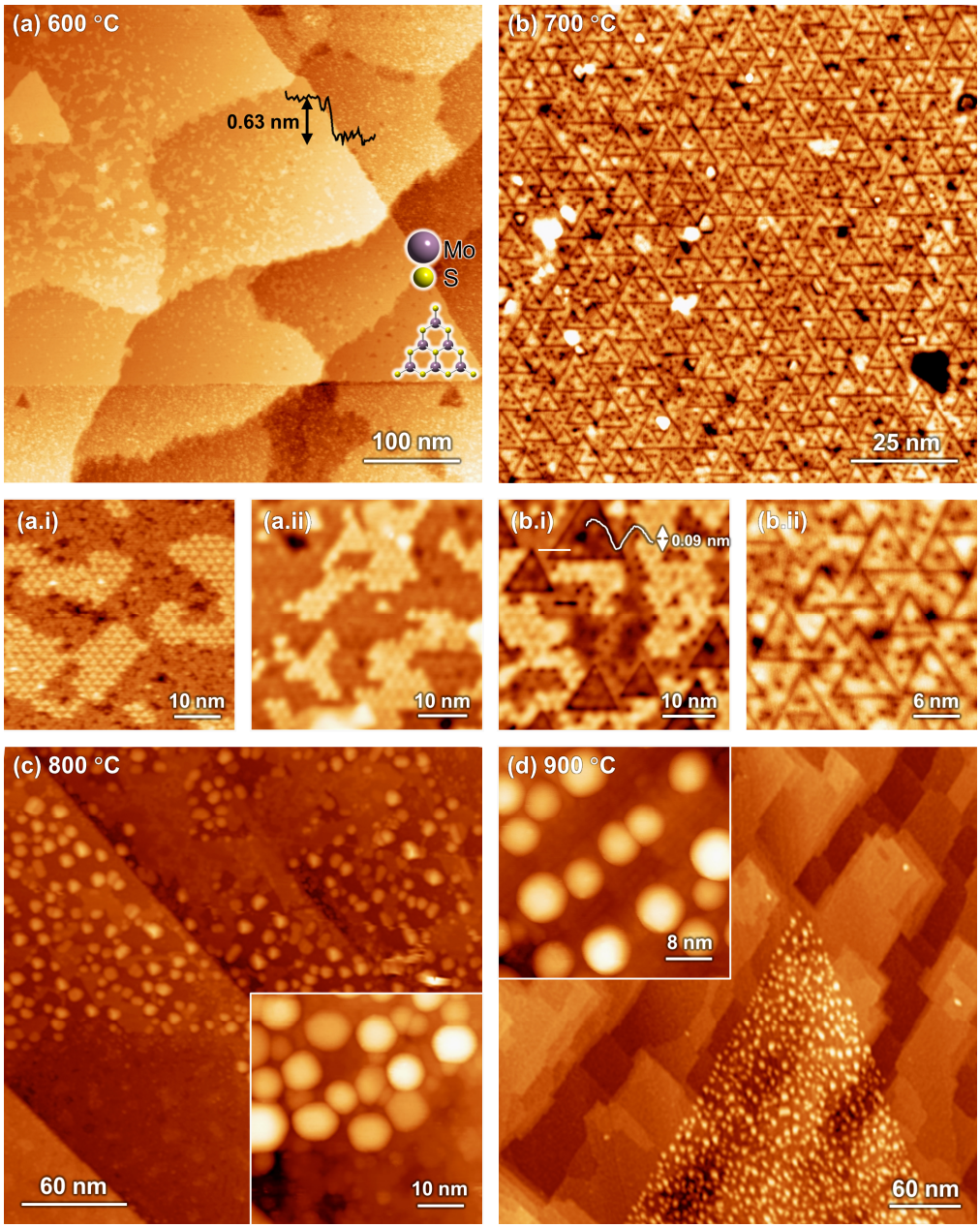

Figure 5.3: STM images of various stages of the thermal degradation of monolayer MoS_2 crystals. (a) MoS_2 monolayer with a smooth surface at up to 600 °C, conforming well to the substrate terraces (V_s = 2.0 V, I_t = 0.05 nA). The monolayer has a typical thickness of 0.63 ± 0.06 nm. The atomic model of MoS_2 overlaid illustrates the lattice orientation, and it also applies to the other panels. (a.i,ii) Zoomed-in images of the morphologies of the $SrTiO_3$(111) substrate and the MoS_2 monolayer, respectively (a.i: V_s = 2.0 V, I_t = 0.10 nA; a.ii: V_s = 2.0 V, I_t = 0.03 nA). (b) Triangular etch trenches on the MoS_2 monolayer on $SrTiO_3$(111) formed during UHV annealing at 700 °C (V_s = 2.0 V, I_t = 0.11 nA). (b.ii) Details of the etch trenches (V_s = 2.0 V, I_t = 0.11 nA). (b.i) An area similar to that in (a.ii), for comparison, except for a higher annealing temperature. A line profile across a trench shows a dip of 0.09 nm (V_s = 2.0 V, I_t = 0.03 nA). (c) Degradation of the MoS_2 monolayer into particles while partially retaining the film upon UHV annealing at 800 °C. The substrate is $SrTiO_3$(001)-*c*(4 × 2) with straight terraces (V_s = 2.0 V, I_t = 0.05 nA). The inset is a high-magnification image (V_s = 2.0 V, I_t = 0.05 nA). (d) Residual particles left at 900 °C, which remain in the original triangular shape of the MoS_2 crystal, on a $SrTiO_3$(110)-(4 × 1) substrate (V_s = 2.0 V, I_t = 0.05 nA). The inset shows the details of the residues (V_s = 1.5 V, I_t = 0.20 nA). All images are single scans except (a.ii) and (b.i), which are averaged over 16 and 22 frames by *Smart Align*,[264,265] respectively.

These clusters are believed to be due to an intermediate step during the high-temperature formation of the $SrTiO_3(111)$-(4 × 4) reconstruction and will not be discussed further.

After being UHV-annealed at 700 °C, the MoS_2 crystals start to degrade and triangular etch trenches appear, as shown in Figure 5.3b. The trenches are typically measured to be less than 0.1 nm deep. The etch lines run in three directions along the $<2\bar{1}\bar{1}0>$-type crystallographic directions of MoS_2, which are the S-terminated edge directions of the triangular MoS_2 crystal (cf. the atomic model of MoS_2 in Figure 5.3a). The high-magnification image in Figure 5.3b.ii shows that there are etch dots as well as etch lines. Figure 5.3b.i shows an area similar to that in Figure 5.3a.ii but annealed at 700 °C. It has a complex morphology in which the clusters protruding from the substrate are still visible and the triangular etch trenches coexist with them. The etch dots and lines are likely to be due to the preferential evaporation of sulphur from the MoS_2 monolayers.

At UHV annealing temperatures above 800 °C, the MoS_2 crystals decompose into particles. Figure 5.3c shows a MoS_2 monolayer (on top of $SrTiO_3(001)$-*c*(4 × 2) substrate terraces) that has partially degraded into particles.[69,87,88] When the annealing temperature exceeds 900 °C, the MoS_2 crystals degrade entirely and only particle residues are observed in place of the original triangular crystals (Figure 5.3d). Below the particles is the reconstructed $SrTiO_3(110)$-(4 × 1) substrate.[63,65,66] The residual particles are typically 2–5 nm high and 5–10 nm in diameter.

5.2.2 XPS analysis

The pristine and thermally decomposed products of MoS_2 crystals were investigated by XPS. Figure 5.4 shows the core-level spectra from the Mo 3*d* and S 2*p* regions of the samples. In

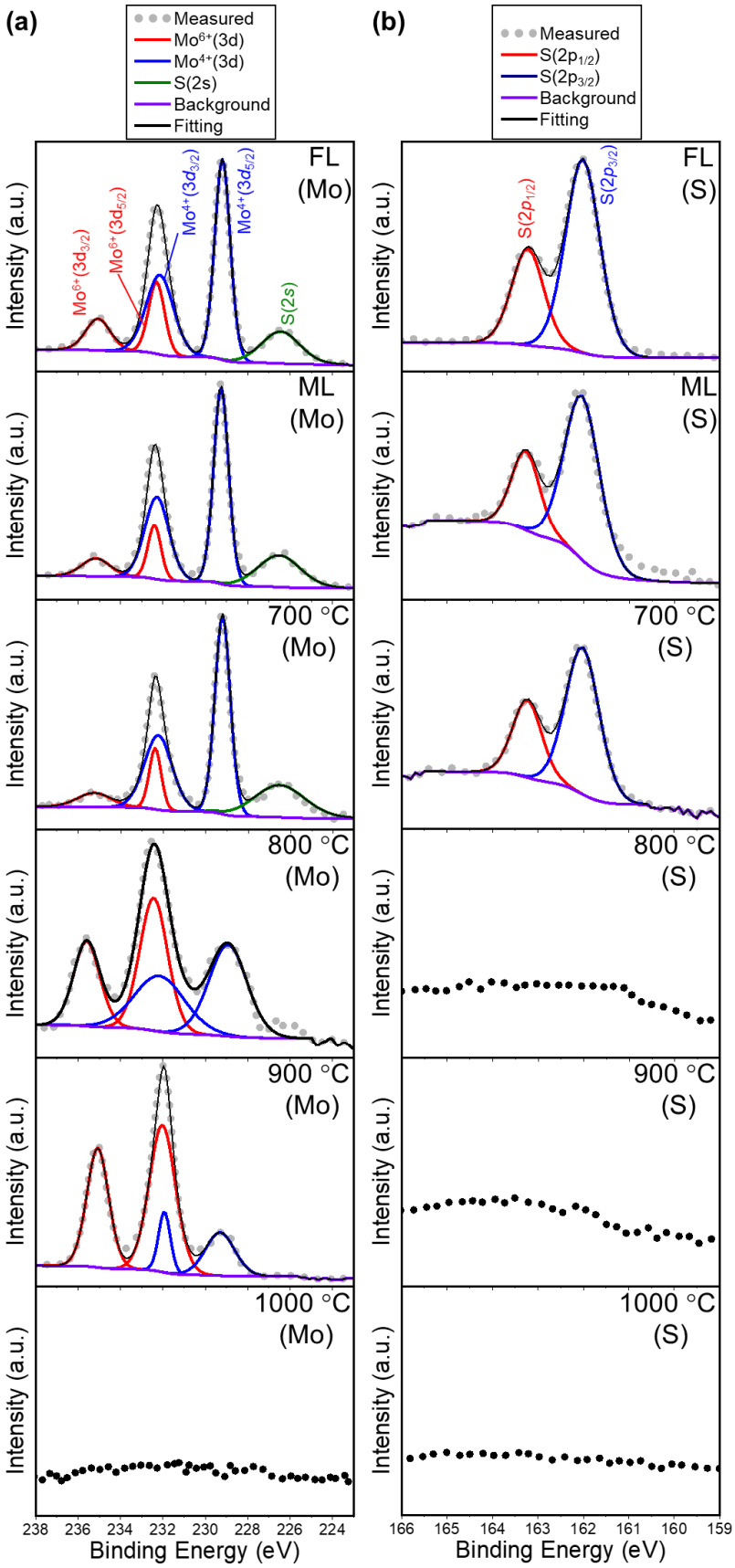

Figure 5.4: XPS spectra of the (a) Mo 3*d* and (b) S 2*p* core-level peaks of the MoS_2 crystals grown on $SrTiO_3$ substrates. From top to bottom: as-grown few-layer (FL) MoS_2 crystals, as-grown monolayer (ML) MoS_2 crystals, and monolayer MoS_2 crystals UHV-annealed at 700 °C, 800 °C, 900 °C, and 1000 °C.

each column, from top to bottom, the spectra compare the compositions of differently treated samples, as labelled in the top-right corner of each figure: as-grown few-layer (FL) MoS_2 crystals, as-grown monolayer (ML) MoS_2 crystals, and monolayer MoS_2 crystals UHV-annealed at 700 °C, 800 °C, 900 °C, and 1000 °C.

In the molybdenum spectra (Figure 5.4a), it can be seen that Mo exists in both the Mo^{6+} and Mo^{4+} ionisation states. Both of these ionisation states have a doublet peak in their 3*d* spectra: 235.2 ± 0.21 eV and 232.3 ± 0.17 eV correspond to Mo^{6+} $3d_{3/2}$ and Mo^{6+} $3d_{5/2}$, respectively, typical of MoO_3,[292] and 232.1 ± 0.14 eV and 229.2 ± 0.14 eV correspond to Mo^{4+} $3d_{3/2}$ and Mo^{4+} $3d_{5/2}$, respectively, typical of MoS_2 and MoO_2.[293–296] It should be noted that the Mo^{6+} $3d_{5/2}$ and Mo^{4+} $3d_{3/2}$ peaks are almost coincident, giving rise to the characteristic three-peak shape of Mo^{6+} and Mo^{4+}.[296] Along with the Mo peaks, another peak observed at 226.3 ± 0.29 eV belongs to S 2*s*.[294] In the sulphur spectra (Figure 5.4b), the S 2*p* peaks are observed at 163.2 ± 0.03 eV and 162.0 ± 0.02 eV, representing S $2p_{1/2}$ and S $2p_{3/2}$ orbital splitting, respectively.[297]

The Gaussian peak fitting was done in *CASAXPS*. The raw spectra of all samples were firstly calibrated by fixing the Sr $3d_{5/2}$ peak of $SrTiO_3$ at 133.1 eV (an averaged value from the literature),[298–300] to correct for the sideways shifts between different samples. This step in XPS analysis is usually done using the C 1*s* peak but this peak in one of my samples appeared at a binding energy that is smaller than usual by a few eV and was also unreasonably broad. Therefore the Sr $3d_{5/2}$ peak was chosen for calibration instead, which is a substrate element whose core electrons should be minimally affected by the MoS_2 overlayers. Before the peak fitting, background was subtracted (purple lines in Figure 5.4). The peak positions and doublet spacings were kept free while the peak area (*A*) ratios were constrained: $A(d_{3/2}):A(d_{5/2}) = 2:3$ and $A(p_{1/2}):A(p_{3/2}) = 1:2$. The peak positions reported in the previous paragraph are averaged values of the different samples with the errors denoting the standard deviations.

Interpreting the XPS observations, we can infer that the as-grown samples (marked as 'FL' and 'ML') are MoS_2 crystals mixed with a small amount of the unreacted MoO_3 precursor and the intermediate product MoO_2.[301] Sulphur completely leaves the structure at a temperature of between 700 °C and 800 °C, after which MoS_2 is fully oxidised. At increasingly higher temperatures, the amount of Mo^{6+} increases because more MoO_3 is formed as MoS_2 is oxidised by the $SrTiO_3$ substrate. Afterwards, all of the molybdenum oxides evaporate at $T > 1000$ °C.

The relative amounts of MoO_3, MoO_2, and MoS_2 in various samples are estimated from the areas under the Gaussian curves of Mo^{6+}, Mo^{4+}, and S^{2-}. Note that both MoO_2 and MoS_2 contribute to the Mo^{4+} peaks at almost identical peak positions,[293–296] so their contributions are not distinguishable solely from the Mo^{4+} peaks. To quantify the stoichiometries, relative sensitivity factors (RSF) of different elements are used to scale the measured peak areas to give meaningful atomic ratios. This is done by dividing $A(Mo^{6+}\ 3d)$ and $A(Mo^{4+}\ 3d)$ by RSF(Mo 3*d*) = 2.75 and dividing A(S 2*p*) by RSF(S 2*p*) = 0.54,[302] giving the 'scaled peak areas' of Mo^{6+}, Mo^{4+}, and S^{2-}. For a given sample, the 'scaled peak areas' are proportional to the amounts of Mo^{6+}, Mo^{4+}, and S^{2-} present, which in turn give the relative amounts of the species MoO_3, MoO_2, and MoS_2.

The results are plotted in Figure 5.5, with errors carried forward from the uncertainties during peak fitting throughout the calculations described in the previous paragraph. The FL, ML, and 700 °C UHV-annealed samples have similar amounts of MoO_3, MoO_2, and MoS_2, where the oxides are the unreacted/incompletely reacted precursor.[301] The FL sample has slightly more MoO_3 than the ML sample because it had a larger amount of precursors deposited. At 700 °C, there is a slightly increased amount of MoO_2 and a virtually unchanged amount of MoO_3 when compared to those of the ML pristine sample. This means that at 700 °C a small but noticeable amount of MoS_2 has been converted into MoO_2 (but not MoO_3 yet). At 800 °C, the % MoS_2 value rapidly decreases to a negligibly small percentage and similar amounts of MoO_2 and

MoO_3 are present. At 900 °C, more than 75% of the residue is MoO_3. Therefore, the compositional change is likely to follow the route $MoS_2 \rightarrow MoO_2 \rightarrow MoO_3$. At $T \geq 1000$ °C, all of the molybdenum compounds have evaporated and to indicate this, their atomic percentages have been set to zero.

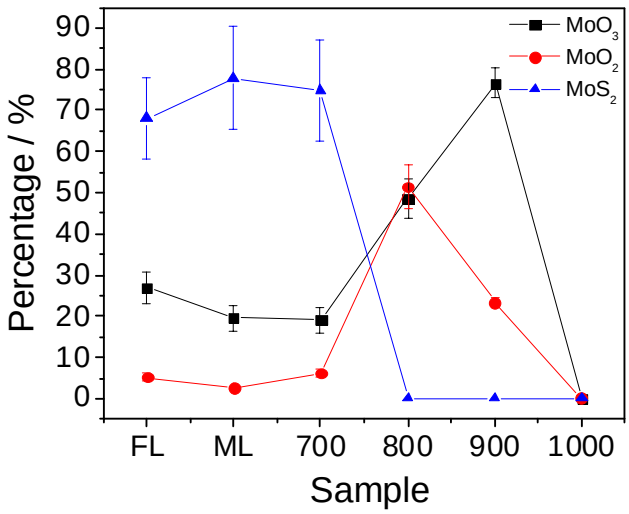

Figure 5.5: Atomic percentages of substances in the as-grown MoS_2 crystals (few-layer and monolayer) and MoS_2 monolayers UHV-annealed at 700 °C, 800 °C, 900 °C, and 1000 °C.

5.2.3 PL and Raman spectroscopy

To gain further insight into the thermal degradation of MoS_2 crystals, PL and Raman spectroscopy were carried out by my collaborator, Dr. Wenshuo Xu, who also analysed the experimental results and constructed Figure 5.6. Upon laser excitation, the as-grown sample exhibits a strong PL peak at the photon energy of 1.88 eV (black curve in Figure 5.6a), characteristic of monolayer MoS_2.[13,14,124–126] In the Raman spectrum (black curve in Figure 5.6b), there are two peaks at 382.2 cm^{-1} and 403.0 cm^{-1}, corresponding to the in-plane E^1_{2g} and out-of-plane A_{1g} vibrational modes of MoS_2, respectively.[133,303] The frequency difference of ~20 cm^{-1} between the peaks is the signature of MoS_2 monolayers, whereas the difference for

thicker and bulk MoS_2 is ~25 cm^{-1}.[118,122,126,133,134,303] UHV annealing at 700 °C results in significantly decreased intensities of the PL and Raman peaks (red curves in Figure 5.6), demonstrating the deteriorated crystallinity of the MoS_2 monolayers. When the UHV annealing temperature reaches 800 °C, no PL or Raman signals can be observed (green curves in Figure 5.6).

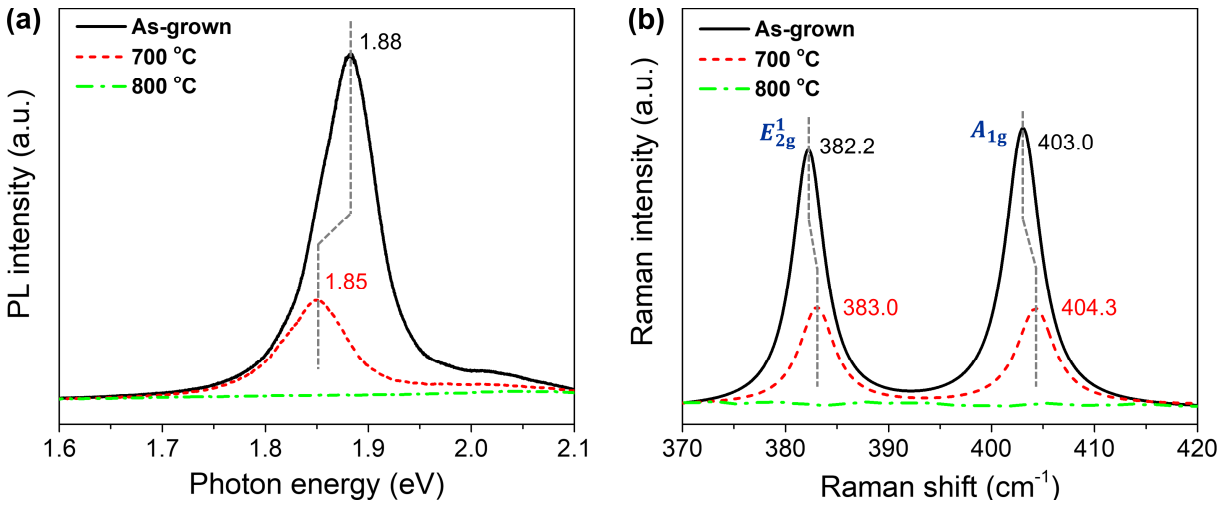

Figure 5.6: (a) PL spectra of monolayer MoS_2 crystals on $SrTiO_3$(111) and (b) Raman spectra of monolayer MoS_2 crystals on $SrTiO_3$(001): as-grown (black), UHV-annealed at 700 °C (red), and UHV-annealed at 800 °C (green).

Both PL and Raman peaks have shifted after the samples were UHV-annealed at 700 °C. Before the peak shifts are discussed, it should be mentioned that strains build up in the MoS_2 crystals during the fast-cooling process in the CVD reactor, as discussed earlier in section 4.2.4. This is due to the different thermal expansion coefficients (TECs) of MoS_2 and the $SrTiO_3$ substrate.[135] The TEC of the as-prepared 2H-phase MoS_2 ($\alpha_{MoS_2,a}$ = 1.9 × 10^{-6} K^{-1} and $\alpha_{MoS_2,c}$ = 8.65 × 10^{-6} K^{-1}, 293–1073 K) is approximately one order of magnitude smaller than that of $SrTiO_3$ (α_{SrTiO_3} = 3.23 × 10^{-5} K^{-1}, 300–1800 K).[285,287] This difference introduces compressive strain in the MoS_2 layers on $SrTiO_3$. In addition, there are strains induced by the epitaxial relationship on different terminations of $SrTiO_3$ substrates, which are compressive on $SrTiO_3$(111) and tensile on $SrTiO_3$(001).[136] Overall, MoS_2 crystals on $SrTiO_3$(111) are in compression and those on $SrTiO_3$(001) are in tension.[136]

The post-annealing PL peak position of MoS_2 on $SrTiO_3$(111) shifts to a lower photon energy (redshift), as shown in Figure 5.6a. This is because the compressive strain in the MoS_2 crystals is partially released: the TEC-induced strain is released by the low heating/cooling rates (2.5–5.5 °C min^{-1}) before and after the 700 °C UHV annealing, and the epitaxy-induced strain is released by the degradation of the MoS_2 crystal structure. The redshift could be additionally attributed to more localised states,[127] which in turn are associated with structural defects.[132]

After being UHV-annealed at 700 °C, the Raman peaks of MoS_2 on $SrTiO_3$(001) are both shifted to higher wavenumbers (stiffening/blue-shifting), accompanied by peak broadening. This is again due to a release of strain, although the strain was initially tensile in the case of a (001)-terminated $SrTiO_3$ substrate.

5.2.4 Optical microscopy (OM)

UHV annealing at up to 1000 °C does not appear to affect the MoS_2 crystal shapes when investigated using OM only. Above 1000 °C, the crystals evaporate and can no longer be seen by OM. Figure 5.7 shows some MoS_2 crystals on $SrTiO_3$(110) imaged by OM (a) before and (b) after UHV annealing at 1000 °C for 5.5 h. As previously shown, substantial changes occur in the internal structure: the triangles in Figure 5.7a are pristine MoS_2 crystals, whereas those in Figure 5.7b are residual MoO_3 nanoparticles retaining the original triangular footprint. However, OM does not show any apparent differences and care should therefore be taken when using OM on its own to describe the quality of MoS_2 crystals.

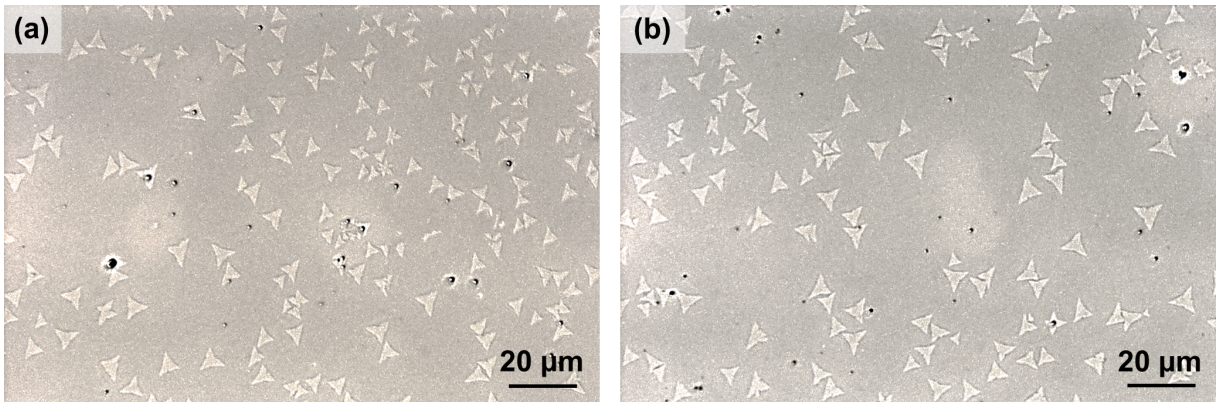

Figure 5.7: Optical microscope images of MoS_2 crystals on $SrTiO_3$(110) (a) before and (b) after UHV annealing at 1000 °C for 5.5 h.

5.2.5 Sulphur annealing

To study whether we could heal the defects formed in the MoS_2 monolayers, we created a sulphur atmosphere in the CVD reactor at an elevated temperature and transported the sulphur vapour to the MoS_2 surface by an argon flow. The sulphur annealing and the subsequent Raman and PL analysis were performed by my collaborator, Dr. Wenshuo Xu. The sulphur annealing was carried out using the CVD setup (Figure 3.6 in Chapter 3) without MoO_3 in the inner quartz tube. As indicated by SEM, the 700 °C UHV-annealed MoS_2 crystals look similar before (Figure 5.2a.i) and after (Figure 5.8a) sulphur annealing. On the other hand, the 800 °C UHV-annealed crystals (Figure 5.8b) become clear and black, with enhanced contrast when compared with the faint triangles in Figure 5.2a.ii. This indicates partial recovery of the structural degradation. The crystals look similar to the as-grown crystals, although a few more holes are observed in the larger crystals (indicated by red arrows).

The optical properties of the sulphur-annealed samples also partially recover: Figure 5.9a shows that the PL intensity of the 700 °C UHV-annealed MoS_2 crystal is enhanced and the peak position is blue-shifted back to a higher photon energy, close to that of the newly grown MoS_2

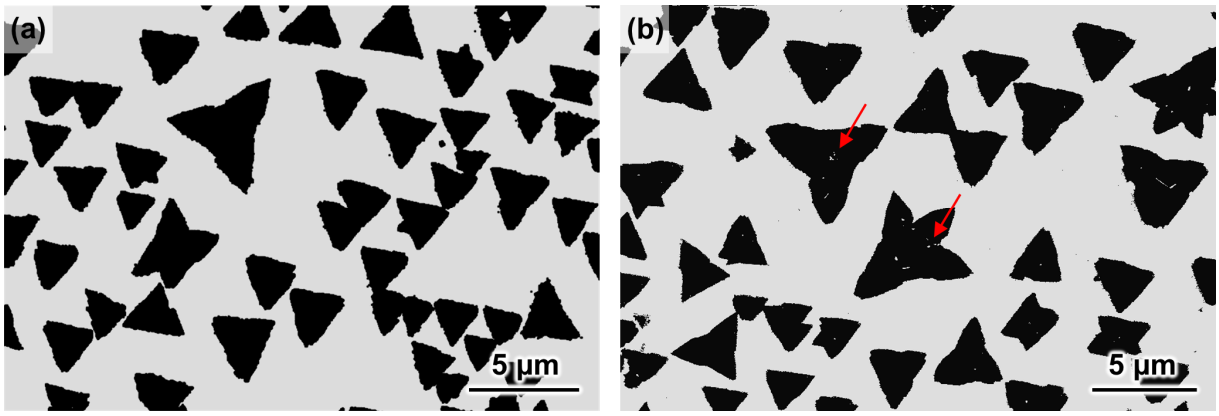

Figure 5.8: SEM images of (a) 700 °C and (b) 800 °C UHV-annealed MoS_2 crystals on $SrTiO_3$(111) substrates after sulphur annealing.

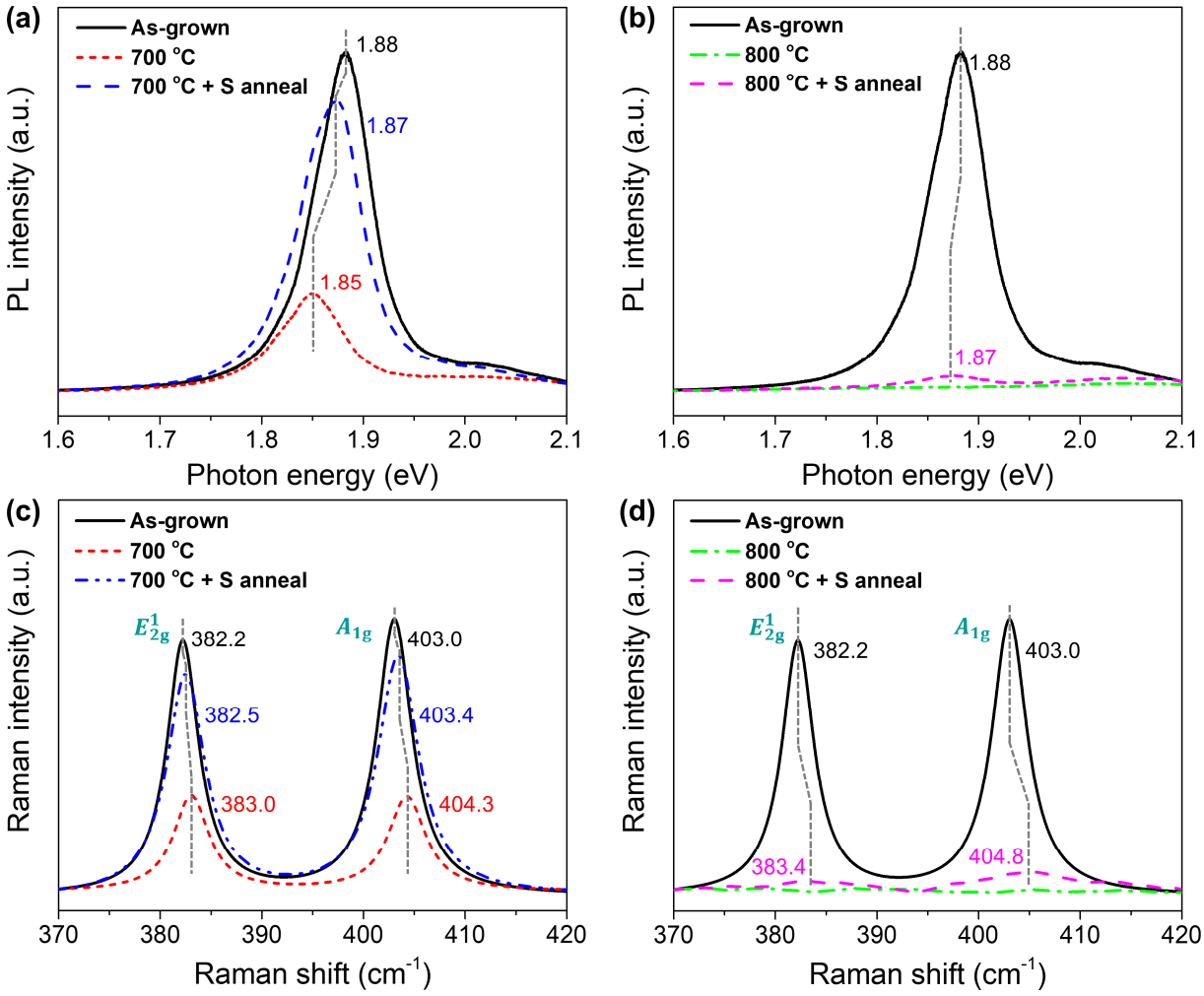

Figure 5.9: (a,b) PL and (c,d) Raman spectra of the sulphur-annealed MoS_2 crystals compared with those before (i.e., as-grown) and after the UHV annealing at (a,c) 700 °C and (b,d) 800 °C. (a,b) PL spectra are measured on MoS_2 crystals supported on $SrTiO_3$(111). (c,d) Raman spectra are measured on MoS_2 crystals supported on $SrTiO_3$(001).

crystals. The Raman signals are also largely restored in terms of the peak intensities and positions (Figure 5.9c). The peak position restoration is due to the epitaxy-induced strains being reintroduced as the MoS_2 crystallinity improves. The strains are compressive on $SrTiO_3$(111) and tensile on $SrTiO_3$(001),[136] leading to the blueshift of the PL peak in Figure 5.9a and the redshifts of the Raman peaks in Figure 5.9c.

On the other hand, after sulphur treatment of the 800 °C UHV-annealed MoS_2 crystals, the recovery of the PL and Raman signals is weak (Figure 5.9b,d). Also, the frequency difference of 21.4 cm^{-1} between them indicates that the healed MoS_2 is a mixture of ML and FL crystals.[133] Note that the presence of FL MoS_2 crystals is not obvious from the PL peak position at 1.87 eV (Figure 5.9b), which corresponds to direct excitonic transitions from ML MoS_2 only.[14] This is because the PL signal strength of FL MoS_2 is negligible compared to that of ML MoS_2.[13]

5.3 Discussion

We now have a deeper understanding of the UHV degradation and healing mechanisms of $SrTiO_3$-supported monolayer MoS_2 crystals, as summarised in Table 5.1. The structural changes start at 700 °C, which is reflected by the compositional change of the sample at 700 °C compared to that of the pristine ML sample in XPS, where slightly less MoS_2 is present (Figure 5.5). The desulphurisation is not visible in SEM (Figure 5.2a.i), but the sulphur vacancies appear as etch dots and lines in STM images (Figure 5.3b). The structural defects are also observed in the decreased PL and Raman intensities (Figure 5.6). For comparison, previous studies show that when MoS_2 is etched in air at lower temperatures of 300–340 °C,[184,185] triangular surface pits rather than etch lines are the first sign of degradation, suggesting the oxidation of Mo into MoO_3 and the removal of sulphur in a volatile state.[183,186]

After the 800 °C UHV annealing, XPS results (Figure 5.4 and 5.5) demonstrate that no sulphur remains and MoO_2 and MoO_3 are formed as the oxidation products of the remaining Mo. The structural change is visualised via the deteriorated contrast in the SEM image (Figure 5.2a.ii). No PL or Raman signals of MoS_2 are observed any more (Figure 5.6). The particles in the STM images (Figure 5.3c) are therefore MoO_x (x = 2–3) particles. At 900 °C, further oxidation occurs and a larger proportion of MoO_3 (> 75%) is detected by XPS (Figure 5.5).

Table 5.1. UHV thermal degradation and sulphur annealing results of MoS_2 crystals on $SrTiO_3$ substrates.

Sample	UHV annealing time (h)	Morphology	Substances (excluding unreacted MoO_3/MoO_2)	Recovery of optical properties upon sulphur annealing
FL	-	Smooth crystal	MoS_2	-
ML	-	Smooth crystal	MoS_2	-
700 °C	0.5–2.0	Crystal + etch trenches	MoS_2 (mainly) + MoO_2	Near full recovery
800 °C	0.5–2.0	Crystal + particles	MoO_2 + MoO_3 (similar amounts)	Weak recovery
900 °C	0.5–1.0	Particles	MoO_2 + MoO_3 (mainly)	No recovery
1000 °C	2.0–5.5	Particles/evaporated	-	No recovery

In the thermally assisted oxidation of monolayer MoS_2 crystals in air, it has been previously reported that sulphur escapes as SO_2,[183,186] leaving oxidised Mo on the surface.[181–186] The thermal degradation of MoS_2 in UHV is likely to follow a different route from that in an O_2-rich environment. I postulate that at 700 °C, the thermal energy breaks the Mo–S covalent bonds and releases the S atoms into the vacuum. This bond-breaking process requires a higher activation temperature compared to that of the oxidation of sulphur in an ambient environment.[181–186] Upon higher-temperature UHV annealing (> 800 °C), the $SrTiO_3$ substrate can supply increasing amounts of oxygen, which oxidises the remaining Mo, converting it into MoO_2 and then into MoO_3.

The high temperature applied to MoS_2 breaks the Mo–S covalent bonds, which are stronger

than the vdW interaction between the MoS_2 sheet and the substrate by orders of magnitude. This explains the observation that the thermal degradation behaviour of MoS_2 on different terminations of $SrTiO_3$ substrates is similar, as only their interfacial vdW interaction with the substrate differs.

Finally, the sulphur annealing process partially heals the MoS_2 crystals, as confirmed by SEM observations (Figure 5.8) and PL and Raman spectroscopy (Figure 5.9). This recovery is due to the sulphur vacancies in the MoS_2 crystals being restored in the hot sulphur atmosphere.[127] However, the recovery is not full for the 700 °C/800 °C treated samples, and the crystals that were UHV annealed at 900 °C or above could not be healed by sulphur annealing at all. This is because once any Mo has been oxidised, it can no longer be sulphurised under the sulphur annealing conditions, or specifically, at a substrate temperature of 300 °C. The reason for this is that the conversion of MoO_3/MoO_2 into MoS_2 requires a higher reaction temperature of 650–800 °C, as in the CVD growth of MoS_2.[127,301] Also, MoO_3/MoO_2 has to be in the gaseous phase for the sulphurisation reaction to occur.[127,301] Although there may be a low vapour pressure of MoO_3/MoO_2 at 300 °C, the high argon flow rate of 500 sccm would quickly remove any vaporised Mo oxides downstream in the furnace. Therefore, no sulphurisation of the Mo oxides occurred during the sulphur annealing and any recovered MoS_2 is due to the filling of sulphur vacancies only. For this process to be possible, the Mo atoms need to have largely remained in their original lattice positions of MoS_2 so that the sulphur can easily fill the vacancies. This is true for the crystals that were UHV annealed at 700 °C and 800 °C: the former only lost a small amount of sulphur (Figure 5.4 and 5.5) and remained as a film with some etch trenches (Figure 5.3b); the latter lost all sulphur (Figure 5.4 and 5.5) but survived partly as film (Figure 5.3c). The more film-structure that survived, the stronger the recovery of the optical properties (Figure 5.9). Also, after the 800 °C UHV annealing, because the film has partially turned into granules, the recovered MoS_2 has some FL crystals mixed with it, as mentioned at the end of section 5.2.5.

The partial recovery of the 700 °C/800 °C UHV-annealed samples also tells us that in these samples there is a certain amount of MoS_2 that has lost sulphur but has not been oxidised after UHV annealing. However, in the XPS calculations that produced Figure 5.5, any Mo^{4+} without sulphur was attributed to MoO_2. The calculations are hence not perfect but remain a good estimate of the relative amounts of MoO_3, MoO_2, and MoS_2 given the XPS data available. A further issue is that a proportion of Mo that may be present in the metallic state in UHV will become oxidised during the ambient transfer to the XPS chamber.

5.4 Conclusions

This study uncovers the thermal degradation behaviour of monolayer MoS_2 in UHV because of sulphur loss, which begins at 700 °C. The sulphur vacancies can be filled by annealing the crystals in a hot sulphur atmosphere, and the optical properties of monolayer MoS_2 can nearly be fully recovered. At higher UHV annealing temperatures, the remaining Mo is oxidised by the $SrTiO_3$ substrates into MoO_2 and MoO_3. The sulphur annealing no longer takes effect when all the Mo has been oxidised, which happens at a temperature of between 800 °C and 900 °C in UHV. The MoS_2 crystal shapes are stable upon annealing until the residual MoO_3 particles evaporate at above 1000 °C. This infers that any triangular crystals that look intact under low-magnification OM and SEM may not mean pristine MoS_2 and OM should be used with care. It is concluded that for retaining the properties of MoS_2 it is important to avoid desulphurisation and its exposure to oxygen, including the use of oxide substrates. The sulphur vacancies can be restored in a vaporous sulphur environment, whereas the oxidation cannot be reversed. This study provides helpful insight for expanding the high-temperature applications of monolayer MoS_2 crystals in electronics and sensors.

Chapter 6

Gold Particle Nucleation Behaviour on $SrTiO_3$ Substrates

6.1 Introduction

For catalysis-related applications, metal clusters are usually supported on oxide substrates. Oxide supports have been shown to manipulate the activity of the gold catalyst.[304–308] The properties of 2D gold structures are influenced by their substrates to a greater extent than 3D particles.[233] Most importantly, the formation of the 2D islands is a direct consequence of their interaction with the oxide substrates. For example, in some studies oxide substrates have been shown to mediate charge transfer to the supported gold clusters, enhancing their desirable properties by stabilising them in the 2D form.[232,233,238–241,250–253]

The three substrates used in my work are $SrTiO_3$ single crystals epi-polished on the (001) and (111) surfaces: $SrTiO_3$(001)-(2 × 1),[69,89] $SrTiO_3$(001)-*c*(4 × 2),[69,85,88] and $SrTiO_3$(111)-(4 × 4)+(6 × 6).[43,56] $SrTiO_3$(001)-(2 × 1) is the only surface of $SrTiO_3$ capable of stabilising gold

monolayers (MLs), which are the nucleation shape of gold islands on this substrate. On the other two, gold forms multiply twinned particles (MTPs) at small sizes. On all three substrates, when gold islands grow larger, they convert into single crystals (SCs) with a truncated octahedral shape. This chapter focuses on gold MLs, in which their shapes, structures, and dewetting behaviour are presented. The possible origin of ML formation is also explored and their dewetting phenomenon is discussed in terms of energetics. These results will help us improve the potential of gold MLs in future catalytic applications.

6.2 Results

6.2.1 Single crystals, monolayers, and multiply twinned particles

Figure 6.1 shows STM images of gold islands on the three different $SrTiO_3$ substrates: (a,b) $SrTiO_3$(001)-(2 × 1), (c,f) $SrTiO_3$(001)-*c*(4 × 2), and (d,e) $SrTiO_3$(111)-(4 × 4)+(6 × 6). Figure 6.1a.i and a.ii are the 2D and 3D versions of the same image, respectively, and similarly for Figure 6.1b,c,d. On all three substrates, the gold SCs have a (111) base and a (111) top facet of the truncated triangular shape.

On $SrTiO_3$(001)-(2 × 1), the crystal heights are labelled below each crystal (Figure 6.1a.ii,b.ii), where it can be seen that in addition to the gold SCs, a few irregularly shaped, flat gold islands are also present. A few examples are indicated by grey arrows. These islands are gold MLs, which have previously been reported on $SrTiO_3$(001)-(2 × 1).[212] I confirm that they are not seen on any other surface of $SrTiO_3$. Based on the first histogram in Figure 6.2a showing the island volumes of MLs and SCs, I speculate that the gold islands nucleate as MLs on $SrTiO_3$(001)-(2 × 1), which are the energetically favourable form in the small-size regime as opposed to the

SCs. However, they may retain their nucleation shapes when they grow beyond the critical size at which they should convert into SCs.

In previous studies, gold MLs have been observed on various oxide substrates including FeO,[232,233] MgO,[233–239] CaO,[239–241], CeO_2,[242] TiO_2,[243,244] and $SrTiO_3$.[212] They were only found

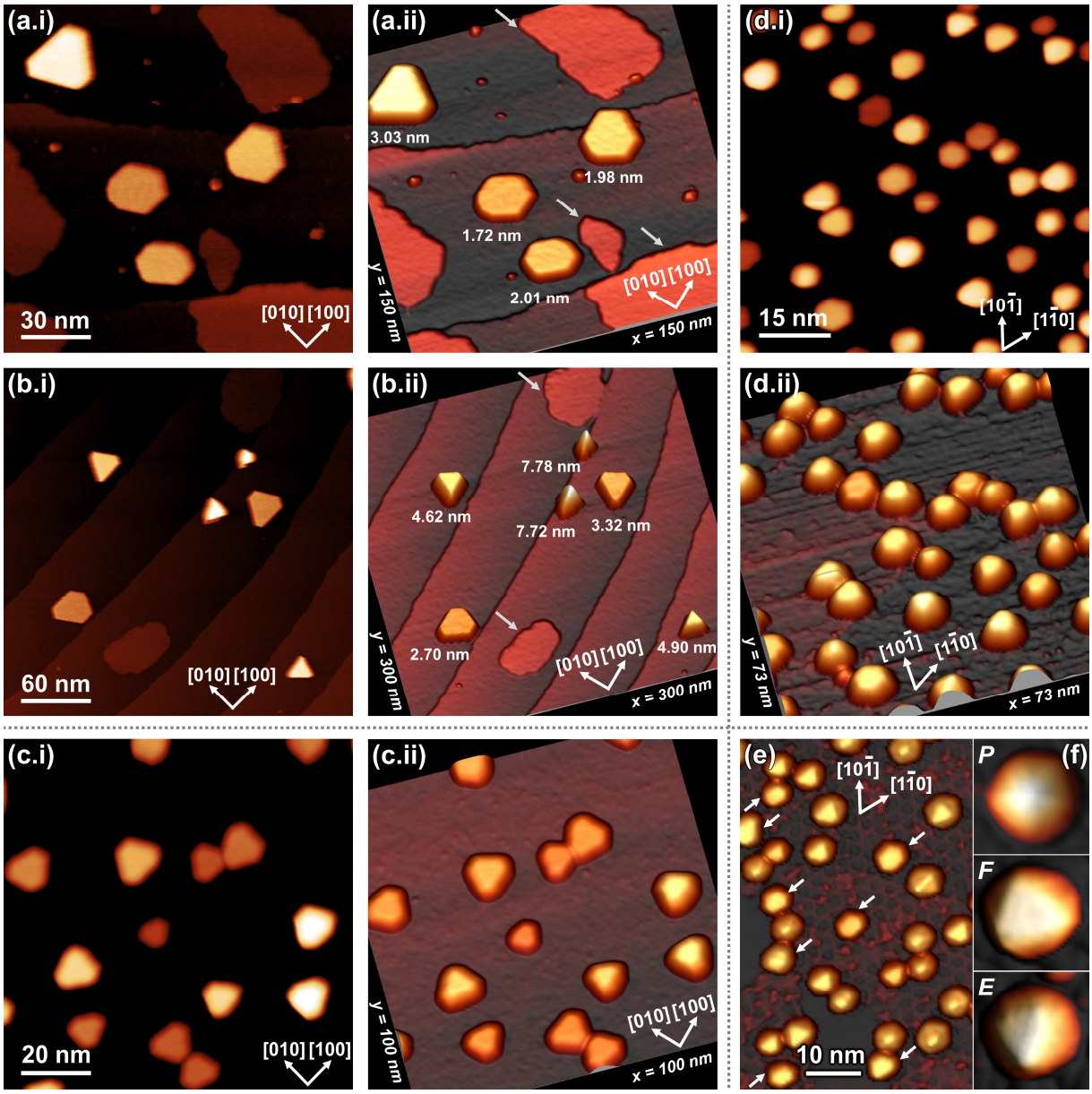

Figure 6.1: STM images of gold islands on (a,b) $SrTiO_3$(001)-(2 × 1) (a: V_s = 1.0 V, I_t = 0.05 nA; b: V_s = 1.5 V, I_t = 0.10 nA), (c,f) $SrTiO_3$(001)-*c*(4 × 2) (both V_s = 4.0 V, I_t = 0.05 nA), and (d,e) $SrTiO_3$(111)-(4 × 4)+(6 × 6) (d: V_s = 3.8 V, I_t = 0.03 nA; e: V_s = 4.0 V, I_t = 0.10 nA). Panels (a.i) and (a.ii) are the 2D and 3D versions of the same image, respectively, and similarly for panels (b,c,d). In (a,b), gold monolayers are indicated by grey arrows and the crystal heights are labelled below each crystal. In (e), gold MTPs coexist with SCs. All SCs are indicated by white arrows. Three close-up images of MTPs are shown in (f), with point (P), face (F), and edge (E) orientations.

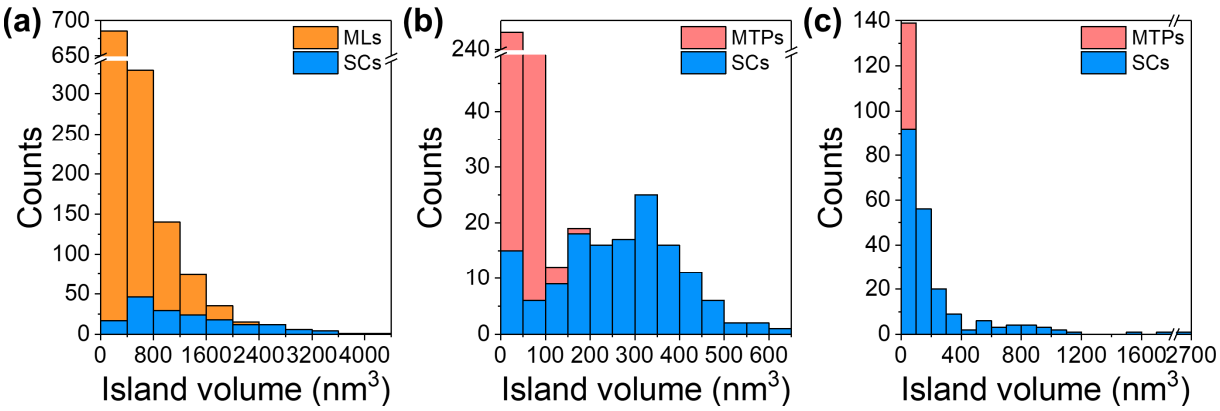

Figure 6.2: Gold island volume histograms of MLs, MTPs, and SCs on (a) $SrTiO_3$(001)-(2 × 1), (b) $SrTiO_3$(001)-*c*(4 × 2), and (c) $SrTiO_3$(111)-(4 × 4)+(6 × 6).

at low coverages of gold and under kinetically-limited conditions,[212,232,233,235,243,244] as expected for a nucleation state. Previously reported MLs contain up to 500 atoms on CaO and MgO films[237,241] and are up to ~200 nm^3 in volume on $SrTiO_3$(001)-(2 × 1).[212] Comparatively, the MLs observed in my study are larger, and the largest ML island seen is 2320 ± 35 nm^3 in volume. The volume of a ML is calculated by multiplying its area by the ML thickness, the latter of which is assumed to be d_{111} of gold = 0.235 nm. A ML area is averaged over a few measurements from the STM image, with random errors resulting from the blurred ML edges. The error of ± 35 nm^3 in the crystal volume denotes the standard deviation.

On $SrTiO_3$(001)-*c*(4 × 2) and $SrTiO_3$(111)-(4 × 4)+(6 × 6), MTPs are observed in addition to SCs, the coexistence of which is shown in Figure 6.1e, where all SCs are indicated by white arrows. The MTPs are supported icosahedra, which are polyhedra with 20 faces in their free-standing form. The MTPs in Figure 6.1e adopt various orientations of icosahedra, and the three main ones are shown in the close-up images in Figure 6.1f, termed as point (P), face (F), and edge (E) orientations in previous reports.[212,226] These MTPs only have {111} facets, the lowest-energy termination. Therefore they are a particle form with a reduced surface energy at the cost of strain and twinning energies,[196,216,217] usually observed at smaller sizes than their single-crystal counterparts.[220,223–225] Again, this is evidenced by the histograms in Figure 6.2b,c,

illustrating that MTPs are the nucleation shape of gold islands on substrate surfaces other than $SrTiO_3$(001)-(2 × 1), where the substrate does not satisfy the condition to stabilise MLs.

6.2.2 Monolayer structure

More details of the gold MLs on $SrTiO_3$(001)-(2 × 1) are shown in Figure 6.3. The MLs and SCs coexist when the substrate is kept at 200 °C or above during deposition. Below 200 °C, MLs are exclusively formed. In general, a larger proportion of SCs are formed when (1) the substrate temperature during deposition is higher; (2) the gold islands are post-annealed at > 350 °C; (3) a higher coverage of gold is deposited. These observations are consistent with my model that the ML–SC transition is a size effect, because the MLs only form under diffusion-limited conditions. The gold MLs in Figure 6.3 were deposited with the same coverage (0.25 ML) but at different substrate temperatures: (a) 100°C, (b–d) 230 °C, (e) 300 °C, and (f) 350 °C. Gold SCs are not included in Figure 6.3 in order to show the MLs more clearly, but Figure 6.1a,b illustrates their coexistence, achieved at substrate temperatures of 300 °C and 400 °C, respectively.

The MLs formed at 100 °C (Figure 6.3a) are relatively small and irregular. They show a square pattern of spots, which is clearer in Figure 6.3b, in which the larger ML island was grown at a substrate temperature of 230°C. The square pattern has a periodicity of 1.54 ± 0.06 nm. A similar pattern was observed on gold MLs on $SrTiO_3$(001)-(2 × 1) by Silly and Castell,[212] though the periodicity was less clear. The pattern was thought to result from the frustrated commensurate epitaxy between gold and the substrate.[212] However, the low-energy electron diffraction (LEED) pattern of the sample appears to contain only signals from the (2 × 1)-reconstructed $SrTiO_3$(001) substrate. In other words, no additional LEED spots appeared after

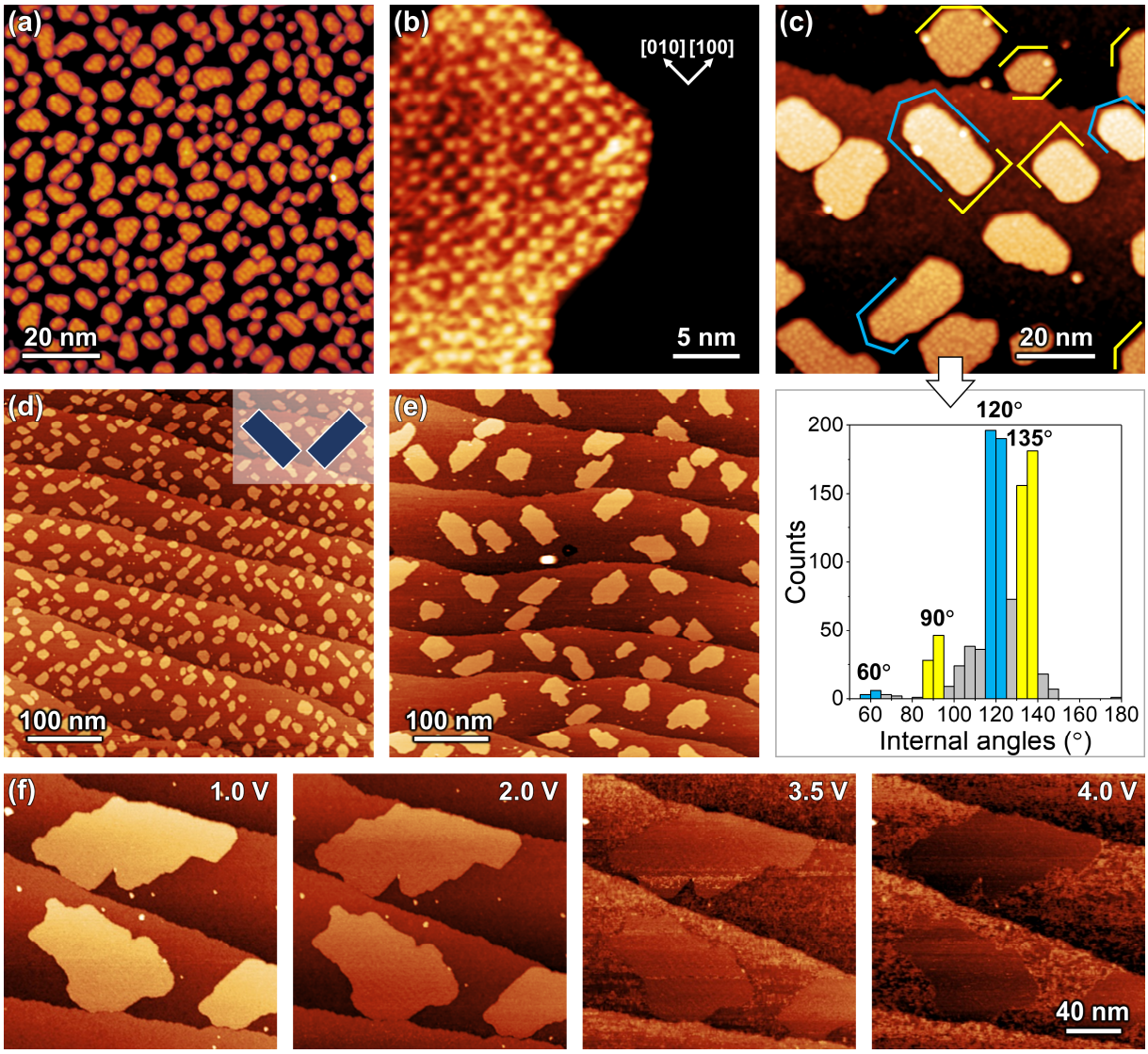

Figure 6.3: STM images of gold MLs on $SrTiO_3$(001)-(2 × 1), deposited at substrate temperatures of (a) 100°C, (b–d) 230 °C, (e) 300 °C, and (f) 350 °C, with increasing island sizes. (a,b) Square pattern on gold MLs with a periodicity of 1.54 ± 0.06 nm (a: V_s = 1.0 V, I_t = 0.15 nA; b: V_s = 0.3 V, I_t = 0.15 nA). The substrate lattice directions in panel (b) apply to all panels. (c) Gold MLs with internal angles of 60°/120° (labelled in blue) and 90°/135° (labelled in yellow) (V_s = 0.6 V, I_t = 0.15 nA). They have similar populations, as shown in the histogram below the image. (d,e) Quasi-rectangular shapes of (d) small and (e) medium-sized ML islands, which tend to orient their longer sides with <100> directions on the substrate, as shown in the schematic drawings in the inset of (d) (d: V_s = 1.0 V, I_t = 0.08 nA; e: V_s = 1.0 V, I_t = 0.10 nA). (f) Irregular large ML islands, whose shapes are constrained by the substrate terrace sizes. The four images are of the same area obtained with different imaging biases, as labelled in their top-right corners (I_t = 0.10 nA). Images (a–c) are averaged over 30, 56, and 16 frames by *Smart Align*,[264,265] respectively. Images (d–f) are single scans.

the gold MLs were grown. This absence possibly indicates a completely disordered structure of the MLs. Alternatively, the LEED spots of MLs may overlap with those of the substrate. The latter is possible because the MLs show some structural features: in Figure 6.3c, when the MLs

have some straight edges, they usually have internal angles of 60°/120° (labelled in blue) and 90°/135° (labelled in yellow). The blue angles indicate hexagonal packing of gold atoms (i.e., an fcc (111)-type structure) and the yellow angles point to square packing (i.e., an fcc (001)-type structure). Also, the blue and yellow angles are similar in population, as shown in the histogram below Figure 6.3c. Both of these structures try to align as many of their island edges as possible with the <100>-type directions on the substrate, cf. the substrate lattice directions labelled in Figure 6.3b, which apply to all panels. For the square-packed gold structure, its lowest-energy termination would be along $SrTiO_3$<100>, in which case its edges would orient at 90° to each other. However, 135° angles are more frequently observed, which suggests that some island edges are aligned with $SrTiO_3$<110>. This may be a higher-energy epitaxial alignment, but it reduces the total perimeter of the island. Here, this apparently mixed (111)/(001) structure of gold MLs is different from the pure (111) structure reported previously.[232,239] On MgO(001) and FeO(111) thin-film substrates, the atomic structure of gold MLs was resolved by STM to be a hexagonal Au(111) structure with a periodicity of 2.89 Å, as in bulk gold.[232,239]

The large-scale STM image in Figure 6.3d shows that the MLs are quasi-rectangles, with their longer sides aligned with the <100> directions on the substrate. The rectangular shapes may result from the mixture of (111)-type, (001)-type, and disordered structures of gold MLs, but they always have two longer sides parallel to $SrTiO_3$<100>. The rectangular shapes are also evident when the MLs further increase in size, as shown in Figure 6.3e, in which the MLs were grown at a higher substrate temperature (300 °C) than those in Figure 6.3d (230 °C). Figure 6.3f shows some of the largest MLs observed, which are irregular in shape because their growth is constrained by the terrace widths of the substrate. The four images in Figure 6.3f were taken over the same area with different imaging biases, and the gold MLs exhibit decreasing apparent heights with increasing imaging bias. The 2D islands appear as protrusions at 1.0 V and 2.0 V,

the same elevation as the substrate at 3.5 V, and faint depressions at 4.0 V. Similar effects have been reported in previous studies.[212,234,239,241] The reason is that the apparent height of gold in STM depends on the relative surface local density of states (LDOS) of the gold and the substrate, and different parts of their LDOS energy spectra are accessed at different imaging biases.[212,239,241]

6.2.3 Dewetting of monolayers

Figure 6.4a shows two *in situ* STM images of the same area of gold islands on $SrTiO_3$(001)-(2 × 1), which have been annealed at 420 °C for (i) 16 min and (ii) 51 min. During the annealing, many ML islands disappeared, possibly because they dissociated and joined larger islands (Ostwald ripening). Alternatively, they might have simply wetted the STM tip during scanning. The gold MLs were seen to transform into SCs by dewetting the vicinal gold atoms, e.g., the island indicated by the arrows. The volume of the ML island in Figure 6.4a.i is measured to be 86 ± 1.3 nm^3 and the corresponding SC island in Figure 6.4a.ii has a volume of 160 ± 11 nm^3. The increase in volume could be due to Ostwald ripening or the gold (wetted on the STM tip) redepositing onto this island as the tip scanned across it. The crystal in Figure 6.4a.ii is 2.37 ± 0.09 nm in height, corresponding to 10 atomic layers of gold. Figure 6.4b is another *in situ* STM image of gold islands held at 350 °C. A noticeable proportion of the ML islands have a hexagonal shape (indicated by the arrows), and many of them are close to regular hexagons. They are no longer quasi-rectangles as in Figure 6.3d,e because the gold atoms may become close-packed as a hexagonal ML (with an fcc (111)-type structure), where its six sides are crystallographically equivalent, because the edges have not yet differentiated themselves into {111} and {001} side facets. During the dewetting, three alternating sides of the hexagon develop into {111} side facets and the other three into {001}.

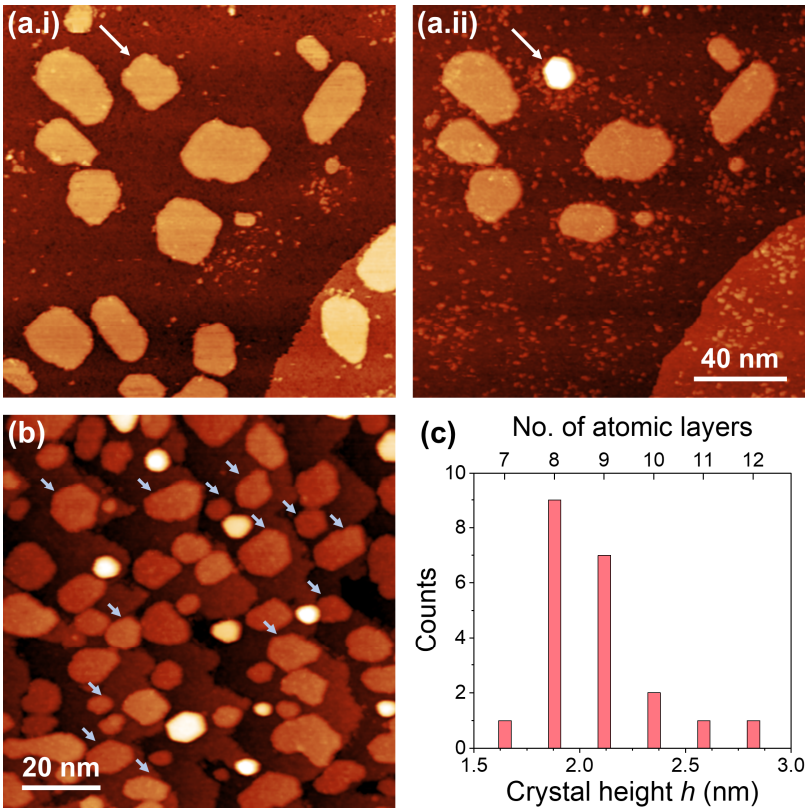

Figure 6.4: Transition of gold MLs into SCs and a crystal height histogram. (a) *In situ* STM images of the same area showing gold islands on $SrTiO_3$(001)-(2 × 1) held at 420 °C for (i) 16 min and (ii) 51 min. The ML island indicated by the arrow converts into a SC from (a.i) to (a.ii) (both V_s = 1.2 V, I_t = 0.10 nA). (b) *In situ* STM image of gold MLs and SCs on $SrTiO_3$(001)-(2 × 1) held at 350 °C. Some hexagonal MLs are indicated by arrows (V_s = 1.2 V, I_t = 0.10 nA). (c) Histogram showing the quantisation of gold crystal heights.

Figure 6.4c shows that the gold crystal heights are quantised into steps of 0.235 nm, which corresponds to the gold (111) interplanar spacing. Also, although the apparent ML heights are bias-dependent (Figure 6.3f), the measured crystal heights are minimally influenced by the imaging bias. This is confirmed by the same crystal imaged at biases of 1.0–4.0 V (the range of biases used to image gold crystals in this thesis), and the crystal shows the same height. With the confidence in accurate height measurements, I point out an interesting observation: the flattest crystals observed on $SrTiO_3$(001)-(2 × 1) consist of a minimum of five atomic layers, whereas on $SrTiO_3$(001)-*c*(4 × 2) and $SrTiO_3$(111)-(4 × 4)+(6 × 6), 2–4-layer crystals have been found. This is because MLs are the nucleation shape of small gold islands on $SrTiO_3$(001)-(2 × 1), which represent a local minimum in energy. Under diffusion-limited conditions, there is a

growth barrier to 3D crystals. This activation barrier appears to require the assembly of five atomic layers at a minimum.

6.3 Discussion

It is believed that the gold MLs are stabilised by the $SrTiO_3(001)$-(2×1) substrate. $SrTiO_3(001)$-(2×1) is special amongst all $SrTiO_3$ surfaces because (i) it is the only known hydroxylated surface and (ii) it has a significantly higher surface energy than other reconstructions,[89] e.g., higher than the $SrTiO_3(001)$-$c(4 \times 2)$ surface by 0.4–0.6 J m^{-2}.[90,91] The high substrate surface energy (γ_s) encourages gold to wet. If we define γ_m as the surface energy of a gold ML per unit area and γ_{im} as the gold ML–substrate interfacial energy, the condition for wetting is $\gamma_{m} + \gamma_{im} - \gamma_s < 0$ (if we neglect the edge energy of MLs for now).[212] This condition is satisfied only on $SrTiO_3(001)$-(2×1) because of its high value of γ_s. The ML formation may also be assisted by the ML–substrate interfacial energy (γ_{im}) being lower than the crystal–substrate interfacial energy (γ_{ic}).[212] A SC has a (111) base but a ML adopts a different structure as it has no rigid crystal structure imposed on it. When the gold atoms form a ML, they would naturally close-pack themselves in a hexagonal way, i.e., in an fcc (111)-type structure, for the highest packing efficiency. However, as the ML sits on a substrate with square symmetry, it would try to develop an epitaxial relationship with the substrate whilst remaining close packed. Therefore the relaxed ML structure is neither purely (111) nor (001).

The relaxation can be easily accommodated by the high elasticity of gold: among all the noble metals (which do not naturally form oxides), gold is the most elastic with a Young's modulus E(Au) = 79 GPa, compared with others like E(Pt) = 168 GPa and E(W) = 411 GPa.[309] Also, $E_{<100>}(SrTiO_3)$ = 225–265 GPa,[310,311] which means that any interfacial misfit strain would be

most likely incorporated in gold rather than in $SrTiO_3$. Such a low value of E(Au) is possibly one of the reasons for gold being the only noble metal that has been observed to wet oxide substrates, since a low stiffness is a necessary condition for ML structure relaxation and hence a stronger interfacial bond.

In previous reports, the wetting of gold on oxide supports has been explained by two mechanisms: a low-energy interface with the substrate[212] and charge transfer from the substrate.[239–241] The model that I propose above is largely based on the first mechanism, while the second one (charge transfer) may be an auxiliary factor. Since the relaxed gold ML structure has an enhanced bonding with the substrate, this can facilitate a greater amount of charge transfer from the substrate to the electronegative gold.[233] In effect, this further reduces the ML–substrate interfacial energy γ_{im}. It is noted in the literature that charge transfer is possible with gold because of its high electronegativity, and other metals with lower electron affinities such as Pd do not exhibit any charge transfer.[233] Electron transfer from the oxide substrate into the gold islands induces a polarisation effect and improves the electrostatic attraction between them. This stabilises the planar arrangement of gold islands because the enhanced metal–oxide adhesion encourages gold islands to maximise their contact area with the oxide support.[239–241] In past studies in which charge transfer was identified as the reason for ML formation, the charge transfer was achieved via either electron tunnelling through an ultrathin oxide film supported on an underlying metal substrate,[232,233,238,239,241,250–253] or charge donation from dopants in the oxide matrix.[236,239,240] The latter is also a possibility in my system, as the $SrTiO_3$ substrates are *n*-doped by Nb at 0.5 wt %.

The gold–substrate bonds possibly involve the –OH groups on $SrTiO_3$(001)-(2 × 1), as illustrated by the schematic drawings in Figure 6.5. Figure 6.5a shows that the substrate is terminated with –OH groups. When a gold ML forms on top, the gold may directly bond with hydrogen, which donates electrons to gold (Figure 6.5b). The charge transfer from the substrate

to the gold ML would result in a strong dipole moment, indicated by the green arrow. Alternatively, the hydrogen could bind to the top of the ML (Figure 6.5c). In this case the gold ML would attract electrons from both the substrate and the hydrogen on top. The resulting dipoles would neutralise each other, making this setup more energetically favourable than that in Figure 6.5b.

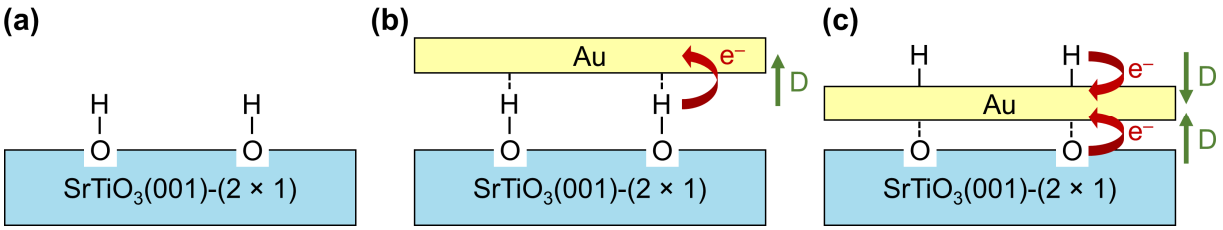

Figure 6.5: Schematic drawings of (a) the $SrTiO_3$(001)-(2 × 1) substrate, showing the surface –OH groups and (b,c) two possible scenarios of bonding between a gold ML and the substrate. The red arrows show the electron transfer and the green arrows represent the dipole moments.

Since the MLs are the nucleation shape, and the flattest crystals observed on $SrTiO_3$(001)-(2 × 1) have five layers, the plot in Figure 6.6 is proposed as a qualitative representation of the relative energies of equilibrium SCs, MLs, and few-layer SCs. Position A in the plot is the critical volume beyond which MLs transform into SCs. In my experiments, the smallest SC has a volume of 44 ± 8.6 nm^3, so I expect A to be a volume of this order of magnitude. Nevertheless, as mentioned previously, the MLs may retain their nucleation shapes beyond the critical volume. For the few-layer SCs, the energies of the bilayer, trilayer, and quadralayer crystals are always higher than that of the ML. Higher crystals (from pentalayer onwards) are energetically more favourable than MLs beyond a certain volume, as indicated by position B. As a rough estimate of B, the smallest pentalayer crystal observed in my experiments is measured to be 190 ± 12 nm^3 in volume.

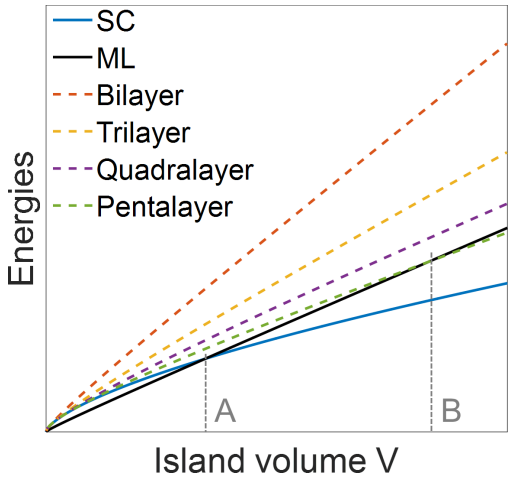

Figure 6.6: Energies of equilibrium SC, ML, and bi-/tri-/quadra-/pentalayer crystals plotted against island volume. A = the critical volume for ML → SC transition and B = the volume beyond which a pentalayer crystal has a lower energy than a ML.

The plots are based on these energy expressions:

$$E_{\mathrm{c}} = \alpha_{\mathrm{crystal}} V^{\frac{2}{3}}, \tag{6.1}$$

$$E_{\mathrm{m}} = (\gamma_{\mathrm{m}} + \gamma^{*}) \cdot \frac{V}{d_{111}} + \gamma_{\mathrm{e}} \cdot A_{\mathrm{e}}, \tag{6.2}$$

$$E_{\mathrm{fixed}\,h} = \frac{\begin{array}{l} V\left(64\gamma_{111}^{5} - 128\gamma_{001}^{2}\gamma_{111}^{3} - 128\gamma_{001}^{2}\gamma_{111}^{2}\gamma^{*} + 16\gamma_{001}^{4}\gamma_{111} + 16\gamma_{001}^{4}\gamma^{*} + 64\gamma_{111}^{4}\gamma^{*}\right) + \\ h^{3}\left(22\sqrt{3}\gamma_{111}^{5} + 18\gamma_{001}\gamma_{111}^{4} - 29\sqrt{3}\gamma_{001}^{2}\gamma_{111}^{3} + 4\sqrt{3}\gamma_{001}^{4}\gamma_{111} + 4\sqrt{3}\gamma_{001}^{4}\gamma^{*} + \right. \\ 22\sqrt{3}\gamma_{111}^{4}\gamma^{*} + 18\gamma_{001}\gamma_{111}^{3}\gamma^{*} - 29\sqrt{3}\gamma_{001}^{2}\gamma_{111}^{2}\gamma^{*}\left.\right) + h^{2}\left(4\sqrt{3}\gamma_{001}^{5} - 6\gamma_{001}^{2}\gamma_{111}^{3} + \right. \\ \left. 14\sqrt{3}\gamma_{001}\gamma_{111}^{4} - 33\sqrt{3}\gamma_{001}^{3}\gamma_{111}^{2} - 6\gamma_{001}^{2}\gamma_{111}^{2}\gamma^{*} - 2\sqrt{3}\gamma_{001}\gamma_{111}^{3}\gamma^{*} - \sqrt{3}\gamma_{001}^{3}\gamma_{111}\gamma^{*}\right)\left[12h^{2} - \right. \\ \left. 32\sqrt{3}\frac{V}{h} - 24\sqrt{3}\frac{\gamma_{111}}{\gamma_{001}}h^{2} + 192\frac{\gamma_{111}}{\gamma_{001}}\frac{V}{h} + 33\left(\frac{\gamma_{111}}{\gamma_{001}}\right)^{2}h^{2} + 64\sqrt{3}\left(\frac{\gamma_{111}}{\gamma_{001}}\right)^{2}\frac{V}{h}\right]^{\frac{1}{2}} \end{array}}{16h(\gamma_{001}^{4} - 8\gamma_{001}^{2}\gamma_{111}^{2} + 4\gamma_{111}^{4})}, \tag{6.3}$$

where E_{c} = equilibrium crystal energy, E_{m} = ML energy, $E_{\mathrm{fixed}\,h}$ = energy of few-layer crystals. The height $h = 2d_{111}$ for bilayers, $h = 3d_{111}$ for trilayers, etc., where d_{111} = interplanar distance between adjacent Au(111) planes = 0.235 nm. V stands for island volume. The energy $\gamma^{*} = \gamma_{\mathrm{i}} - \gamma_{\mathrm{s}}$ is lower for MLs than for SCs, because $\gamma_{\mathrm{im}} < \gamma_{\mathrm{ic}}$. γ_{m} is ML energy per unit area, which would equal γ_{111}, say, if the ML adopts a pure (111) structure. γ_{e} is edge energy per unit area of a ML and A_{e} is its edge area. Finally, $\alpha_{\mathrm{crystal}}$ is a function of γ_{111}, γ_{001}, and γ^{*} depending on the crystal

geometry, which, together with the form of equation (6.1), is to be elaborated on further in Chapter 7. Equations (6.2) and (6.3) are derived in sections B.1 and B.2.4 in Appendix B, respectively.

The plots are not quantitatively meaningful because (1) the atomic structure of MLs is still unknown; (2) the shapes of the gold SCs in my experiments do not reflect the true values of γ_{111}, γ_{001}, and γ^*; (3) the SCs do not follow the Wulff shape. The second and third points are the key points of study in Chapter 7.

6.4 Conclusions and future work

When gold islands are small in size, they form MLs on $SrTiO_3$(001)-(2 × 1) and MTPs on $SrTiO_3$(001)-*c*(4 × 2) and $SrTiO_3$(111)-(4 × 4)+(6 × 6). At larger sizes, their equilibrium morphology is SCs with truncated triangular top facets on all three substrates. In my study the largest ML stabilised by $SrTiO_3$(001)-(2 × 1) is 2320 ± 35 nm^3 in volume, much larger than in previous reports. In STM, the MLs show a square pattern of spots with a periodicity of 1.54 ± 0.06 nm. They usually adopt quasi-rectangular shapes, with their longer sides parallel to $SrTiO_3$<100>. When the MLs have straight edges, they usually have internal angles of 60°/120° and 90°/135°, indicating mixed hexagonal and square packing of gold atoms. When they convert into SCs, they do so by dewetting the vicinal gold atoms. The flattest crystals observed on $SrTiO_3$(001)-(2 × 1) consist of a minimum of five atomic layers. This can be explained by the fact that the MLs, as the nucleation shape of gold islands, represent a local minimum in energy and it is not energetically favourable to convert into SCs flatter than five layers. Finally, it is proposed that the MLs are stabilised by the high surface energy of the $SrTiO_3$(001)-(2 × 1) substrate and the low-energy interface between them. The latter is allowed by the flexible ML

structure that possibly relaxes to better bond with the substrate. This chapter demonstrates the power of the oxide substrate in stabilising the 2D islands of gold and in manipulating their shapes and structure. For gold MLs, a catalytically interesting material, further research would be critical to realising its full potential.

6.4.1 Atomic structure: STM and/or DFT

To develop a full understanding of the gold MLs, it is critical to experimentally verify their atomic structure. Although a square pattern with a periodicity of 1.54 ± 0.06 nm has been observed in STM (Figure 6.3a,b), it was difficult to resolve their structure at the atomic level. So far, two auxiliary methods have been attempted. In the first method, the gold MLs were imaged *in situ* when held at the liquid nitrogen temperature (77 K) to minimise any atomic vibrations. In the second method, the MLs were annealed at 320 °C for 24 h and cooled down to room temperature for STM imaging. This was done in the hope that the MLs could improve their interfacial contact with the substrate without turning into nanocrystals, which might reveal a more regular moiré pattern or even the atoms themselves. However, both methods were unsuccessful. Yet, STM remains a possible way of disclosing the ML atomic arrangements if better quality samples can be prepared.

Another way to explore the atomic structure is DFT modelling, if the square pattern in Figure 6.3a,b is a moiré superstructure. The periodicity of 1.54 nm may correspond to four times the lattice units of $SrTiO_3$(001): 4 × 0.3905 nm = 1.56 nm. Still, decoding a superstructure of this size may be challenging without higher resolution STM data to provide more clues.

6.4.2 Electronic structure: ARPES or XPS

The exceptional chemical activity of nanosized gold is often attributed to charge transfer from the oxide substrate to the gold nanoparticles, but the majority of studies on their detailed electronic structure rely on modelling.[191] It is possible to map the band structure of ML gold on $SrTiO_3$(001)-(2 × 1) substrates by angle-resolved photoemission spectroscopy (ARPES), e.g., using the high resolution (HR)-ARPES tool on the I05 beamline at Diamond Light Source.

The Au-on-$SrTiO_3$ material system is unique in being able to stabilise large areas of epitaxial gold MLs that are up to 100 nm in diameter. When a sub-monolayer of gold is being evaporated onto the $SrTiO_3$(001)-(2 × 1) substrate, the optimal substrate temperature is approximately 350 °C for the growth of MLs of decent sizes (> 70 nm in diameter). A lower substrate temperature would limit the diffusivity and result in MLs that are too small. A higher temperature would cause too many nanocrystals to grow. If large enough MLs are grown, their band structure may be mapped using ARPES.

Increasing the annealing temperature to > 500 °C will lead to total dewetting, which results in a population of epitaxial gold nanocrystals. This allows us to compare the band structures of gold in its ML, nanocrystal, and bulk crystal forms to ascertain the electronic origin of the catalytic activity of the ML state. Clearly, another set of ARPES data on the bare $SrTiO_3$(001)-(2 × 1) substrate is needed to isolate the band structures of the supported gold MLs and nanocrystals. ARPES studies have been carried out on $SrTiO_3$(001),[312,313] but to the best of my knowledge there have been no reports of ARPES of gold on $SrTiO_3$(001), or indeed of ARPES of any ML-gold-on-oxide system. Since the substrate is not fully covered by ML gold, I expect to see small changes in the electronic band structure of $SrTiO_3$(001)-(2 × 1). The shifts of the $SrTiO_3$ bands will suggest how they are altered by their interaction with the highly

electronegative gold. This in turn provides information on the charge transfer from $SrTiO_3$ to gold and how this influences the catalytic properties of nanogold.

A remaining issue is that although the ML islands exhibit some structural features, e.g., their semi-regular shapes and epitaxy with the substrate (Figure 6.3), they lack a LEED pattern. This suggests that their atomic structure is not homogeneous, but a LEED pattern is an essential way to verify the structural quality of gold MLs when the ARPES facility does not have an STM attached. Also, if the MLs are not fully crystalline, the 'angular resolution' feature of ARPES is not meaningful.

Another possible way to check the formation of gold MLs *in situ* would be XPS. When gold MLs convert into nanocrystals upon an anneal, XPS peaks of the sample will shift, and this helps us to distinguish the formation of MLs and nanocrystals. The relative peak intensities of gold and $SrTiO_3$ will tell us the right coverage of gold to deposit, which forms MLs. In fact, the XPS data on their own would be useful as they provide information on the electronic states of gold MLs. Similar to ARPES, XPS should show that the core levels of gold shift significantly upon the transition from MLs to nanocrystals, though only ARPES would be able to show their Fermi levels and surface states.

Chapter 7

Shapes of Epitaxial Gold Nanocrystals on $SrTiO_3$ Substrates

7.1 Introduction

Morphological control of gold nanoclusters is important as their catalytic and optical properties are highly shape dependent. Gold nanoparticles used in catalysis are usually prepared on oxide substrates, which can serve as a template for nanocrystal epitaxy.[236] More importantly, the atomic structure, chemistry, and surface energy of the substrate surface are all determining factors of the nanocrystal morphology.[29,90,203,208,307,314,315]

The same substrates as in Chapter 6 are used: $SrTiO_3$(001)-(2 × 1),[69,89] $SrTiO_3$(001)-*c*(4 × 2),[69,85,88] and $SrTiO_3$(111)-(4 × 4)+(6 × 6).[43,56] These surfaces are found to modify the gold crystal shapes through interfacial strain, by promoting the growth of {111} and {001} crystal facets differently, and by encouraging reentrant facets to grow out. These findings are a key step towards the controlled synthesis of nanocrystal shapes, which is important for optimising

their properties for the development of catalytic materials, biological sensors, and photonic devices.[316]

7.2 Results and discussion

7.2.1 Crystal epitaxy

For the purpose of epitaxy and strain analysis, it is helpful to clarify the crystallography of gold on $SrTiO_3$. Figure 7.1a shows a cubic unit cell of gold with an fcc structure, with a lattice constant of 4.078 Å. The closest Au–Au periodicity is therefore $4.078/\sqrt{2} = 2.884$ Å. The STM images of gold crystals on $SrTiO_3$ are shown in Figure 6.1 in Chapter 6. Their truncated triangular top facets indicate that gold forms the crystal shape modelled in Figure 7.1b,c, which has (111) top and base facets and {111} and {001} side facets. It can be seen from Figure 7.1c that the six edges of the crystal all align with the $<1\bar{1}0>$-type directions of gold. A single Au(111) layer is 6-fold symmetric, while a 3D fcc packed structure reduces it to 3-fold. Therefore, the three longer and the three shorter crystal edges in Figure 7.1c are not equivalent to one another.

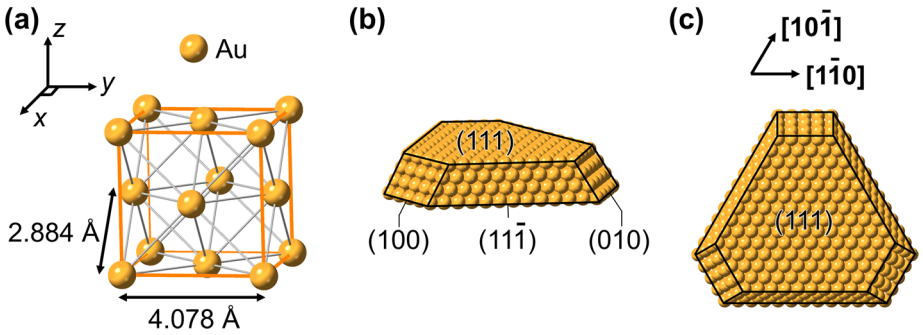

Figure 7.1: Crystal structure of gold. (a) Fcc unit cell of gold outlined in orange, with a lattice constant of 4.078 Å. The Au–Au bonds are in grey with a bond length of 2.884 Å. (b,c) Space-filling atomic models of a gold crystal with a (111) top facet (tilted and top views). In the top view, the six crystal edges align with the $<1\bar{1}0>$-type directions of gold.

From STM images like Figure 6.1a–c, the gold crystal orientations on $SrTiO_3(001)$ are measured according to the diagram at the top of Figure 7.2a. The following histograms present the results on $SrTiO_3(001)$-(2 × 1) (upper) and -*c*(4 × 2) (lower). In both, two peaks are identified at 0° and 30°, relative to the substrate [100] direction. They are two crystallographically equivalent orientations because of the 4-fold symmetry of $SrTiO_3(001)$. Therefore, the preferred epitaxial orientation of gold crystals on $SrTiO_3(001)$ is such that their three longer $<1\bar{1}0>$ edges align with the <100> directions on $SrTiO_3(001)$. This results in four epitaxially equivalent footprints of gold crystals on $SrTiO_3(001)$ shown in Figure 7.2b, two of which correspond to the 0° peak and the other to the 30° peak. The interfacial crystallographic relationship can be described as $(111)_{Au}\|(001)_{SrTiO_3}$, $[1\bar{1}0]_{Au}\|[100]_{SrTiO_3}$. A distance *d* is labelled by blue arrows in Figure 7.2b, which describes the coincidence epitaxy: four unit cells (bond lengths) of gold match three unit cells along $SrTiO_3[100]$: $d = 4 \times 2.884$ Å = 11.536 Å ≈ 3×3.905 Å = 11.715 Å, with a 1.5% tensile misfit strain in gold.

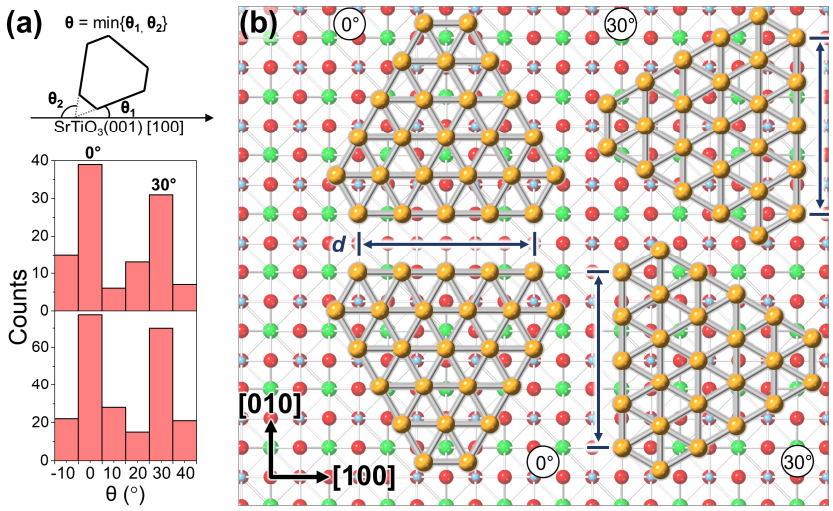

Figure 7.2: Gold crystals on $SrTiO_3(001)$. (a) Orientation histograms of gold crystals on $SrTiO_3(001)$-(2 × 1) (upper) and -*c*(4 × 2) (lower), measured according to the diagram above. (b) Four preferred orientations of gold crystals on $SrTiO_3(001)$. *d* = four Au unit lengths (bond lengths) = three $SrTiO_3[100]$ unit lengths. The substrate lattice directions are labelled. For clarity, only one layer of gold atoms is shown.

On $SrTiO_3(111)$-(4 × 4)+(6 × 6), the gold crystals tend to align their longer $<1\bar{1}0>$ edges with the three-fold symmetric $<1\bar{1}0>$ directions on $SrTiO_3$ (Figure 6.1d,e). This is statistically

illustrated by the histogram in Figure 7.3a. The two peaks at 0° and 60° correspond to the two crystal orientations drawn in Figure 7.3b. The coincidence epitaxy results from the similar lattice constants of gold and $SrTiO_3$: 4.078 Å ≈ 3.905 Å, with a 4.4% compressive misfit strain in gold. In addition to the lattice commensuration, Au(111) and $SrTiO_3$(111) are also symmetry coincident. This means that the epitaxial match between them is more powerful (two-dimensional) because there is epitaxy in both the $[10\bar{1}]$ and the $[1\bar{1}0]$ directions on $SrTiO_3$(111). Conversely, the match between Au(111) and $SrTiO_3$(001) is one-dimensional because there is only epitaxy along one of the <100> directions on $SrTiO_3$(001). The stronger epitaxial match can be visually seen from the better atomic overlap in Figure 7.3b than in Figure 7.2b.

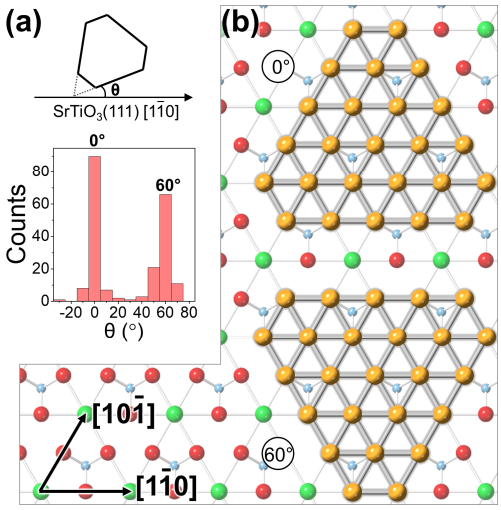

Figure 7.3: Gold crystals on $SrTiO_3$(111). (a) Orientation histogram of gold crystals on $SrTiO_3$(111)-(4 × 4)+(6 × 6), measured according to the diagram above. (b) Two preferred orientations of gold crystals on $SrTiO_3$(111). The substrate lattice directions are labelled. For clarity, only one layer of gold atoms and two layers of atoms in $SrTiO_3$(111) are shown.

The epitaxial relationship on $SrTiO_3$(111) can be described as $(111)_{Au} \parallel (111)_{SrTiO_3}$, $[1\bar{1}0]_{Au} \parallel [1\bar{1}0]_{SrTiO_3}$. Note that in Figure 7.3b, although only one layer of gold atoms is included for clarity, multilayer gold crystals are 3-fold symmetric as explained earlier. Since the $SrTiO_3$(111) substrate is 3-fold symmetric as well, the orientations of the two gold crystals in Figure 7.3b, differing by 60°, are not equivalent. Their inequivalence can also be seen from

an SEM image of gold crystals on $SrTiO_3$(111)-(4 × 4)+(6 × 6) (later in Figure 7.6f), in which the crystals have only one exclusive orientation. The large crystals were post-annealed at 600 °C for 5 h, and they are more likely to have reached a thermodynamically optimised state than the smaller crystals observed in STM without post-deposition thermal treatments.

When the gold crystals are high enough, their Wulff shape suggests that they should form reentrant facets (Figure 7.4a). However, in my study these reentrant facets grow out and the {001} facets extend all the way down to the substrate, as shown in Figure 7.4b. The reason for the formation of this 'growth shape' will be explained later (section 7.2.4). Prior to presenting my experimental results, it is useful to define three dimensions that characterise the crystal growth shape (Figure 7.4b): *l* is the width across the top (111) facet measured from the middle of one {001} side facet to the middle of the opposite {111} side facet; *s* is the width of a {001} facet; *h* is the crystal height. From the STM images in Figure 6.1, it can be seen that the gold crystals on various substrates differ slightly in their shapes, e.g., some are more pointed (smaller *s*) and some are closer to hexagons (larger *s*).

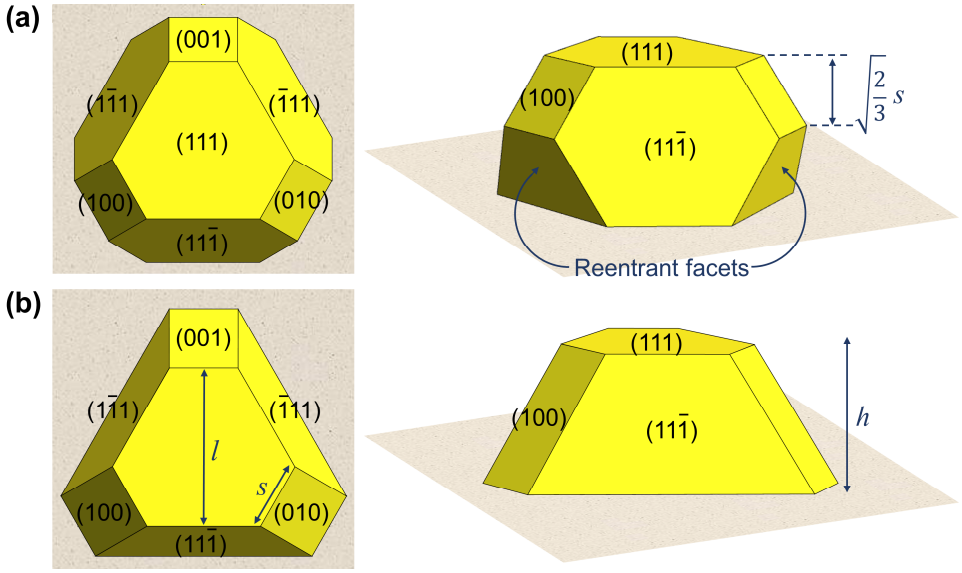

Figure 7.4: (a) Wulff and (b) growth shapes of gold crystals on a substrate: top view (left) and tilted view (right). The three important crystal dimensions, *l*, *s*, and *h* are labelled in (b). In (a), once the crystal height exceeds $\sqrt{2/3}\,s$, the Wulff shape has reentrant facets.

7.2.2 Height-to-width ratio (*h*/*l*)

For a crystal supported on a lattice-mismatched substrate, its total energy has three contributions: the formation energy (negative), the surface/interface energies (positive), and the strain energy due to the lattice mismatch (positive).[317–319] In the absence of any interfacial misfit strain, e.g., on a lattice-matched or amorphous substrate, the thermodynamically optimised shape of a gold crystal is predicted by minimising its surface/interface energies. This is described by the Winterbottom construction, in which a free crystal with the Wulff shape is truncated by the substrate.[206,207] The height-to-width ratio (*h*/*l*) should then be a constant on a given substrate.

The *h*/*l* ratio of gold crystals on the three $SrTiO_3$ substrates is calculated from measurements and plotted against the crystal height *h* (Figure 7.5a). The gold crystals chosen to be measured were all grown on a substrate held at 300 °C or above to best ensure that the crystals were kinetically capable of reaching their equilibrium shapes. Nevertheless, the data in Figure 7.5a represent crystals that are both growing and shrinking due to the Oswald ripening phenomenon. I find that on all three substrates there is a positive relationship between *h*/*l* and *h* and a red

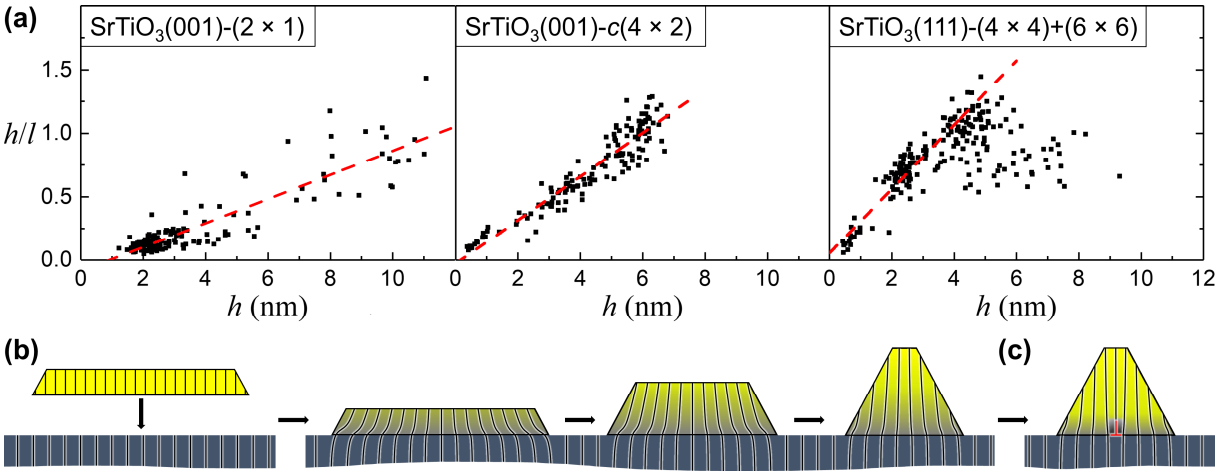

Figure 7.5: Height-to-width (*h*/*l*) ratio of gold crystals and schematic sketches. (a) *h*/*l* plotted against crystal height on $SrTiO_3$(001)-(2 × 1), $SrTiO_3$(001)-*c*(4 × 2), and $SrTiO_3$(111)-(4 × 4)+(6 × 6). A linear regression line (red) is fitted to each dataset. (b,c) Schematic drawings of gold crystals (yellow) and the substrate (dark blue). The vertical black lines represent lattice planes. (b) Heightening of the gold crystal, which helps to relieve the strain resulting from the interfacial lattice misfit. The strain field strength is indicated by the shade of grey. (c) A strained crystal reducing its strain by losing full coherency and forming a misfit dislocation (red) at the interface.

linear regression line is fitted in each case to guide the eye. On $SrTiO_3$(111)-(4 × 4)+(6 × 6), when h > 4 nm the h/l ratio starts to level out and these data points were left out when the linear trendline was fitted. The fact that a higher crystal has a higher h/l ratio cannot be explained by kinetic arguments, because kinetics would favour the opposite: the higher a crystal, the more difficult for additional atoms to climb up the side facets, which in turn means a lower h/l ratio.

The non-constant h/l ratio is explained by the lattice misfit at the Au–$SrTiO_3$ interface, which is 1.5% tensile in gold on $SrTiO_3$(001) and 4.4% compressive in gold on $SrTiO_3$(111). Since my gold crystals were grown at substrate temperatures of 300–400 °C (and occasionally post-annealed at 500–600 °C – see Figure 7.6b–f), an additional interfacial strain develops due to the different thermal expansion coefficients of gold (1.42×10^{-5} K^{-1})[320] and $SrTiO_3$ (3.23×10^{-5} K^{-1}).[287] However, given my treatment temperatures, the magnitude of this thermally induced strain is up to ~1% only. Misfit strains of such magnitude (a few percent in total) have been observed to be accommodated with full coherency between Au and TiO_2,[314] and this is also likely to be the case in my Au-on-$SrTiO_3$ system, certainly for small crystals.

The h/l ratio of gold crystals increases with the crystal height (Figure 7.5a) because crystal heightening can help to release the interfacial strain,[318,319,321,322] as shown by the schematic drawings in Figure 7.5b. The gold crystals (yellow) are strained by the lattice-mismatched substrate (dark blue), where the interfacial atoms are displaced from their ideal lattice positions. The strain field (grey) decays as it moves away from the interface. The black lines represent the lattice planes, which become vertical if the epitaxial strain is fully relieved. The average strain field within the gold crystal is reduced by crystal heightening, e.g., the top facet of the highest crystal in Figure 7.5b is close to being strain-free.

The gradients of the fitted trendlines in Figure 7.5a indicate the rates at which the h/l ratios increase with h. This rate is the smallest on $SrTiO_3$(001)-(2 × 1) (0.095 ± 0.003), followed by

$SrTiO_3$(001)-*c*(4 × 2) (0.172 ± 0.005), and the greatest on $SrTiO_3$(111)-(4 × 4)+(6 × 6) (0.253 ± 0.011). There is a correlation between these rates and four factors: (1) the Au–$SrTiO_3$ interfacial energy, (2) the degree of epitaxial lattice mismatch, (3) whether the epitaxial match is along only one or both crystal directions on the substrate surface, and (4) the relative stiffness of the substrate compared to that of the crystal.[321,322] The fourth factor can be assumed to very similar for all three substrates as the bulk material is the same.

The $SrTiO_3$(111)-(4 × 4)+(6 × 6) substrate displays the highest gradient of *h*/*l* for two reasons. Firstly, it has a higher misfit strain with gold (4.4%) than the other two substrates (1.5%). Secondly, the epitaxial match on $SrTiO_3$(111) is more powerful (2D) than that on $SrTiO_3$(001) (1D) (Figure 7.2b versus Figure 7.3b). The gradients on $SrTiO_3$(001)-(2 × 1) and -*c*(4 × 2) also differ because the surface energy (γ_s) of (2 × 1) is higher than that of *c*(4 × 2) by 0.4–0.6 J m^{-2}.[90,91] The higher γ_s encourages a higher degree of wetting, i.e., a lower value of *h*/*l* at a given height *h*, and hence a lower gradient of *h*/*l*.

In Figure 7.5a, the 'anomalous' points when *h* > 4 nm on $SrTiO_3$(111)-(4 × 4)+(6 × 6) can be explained by interfacial dislocations: at a critical thickness of ~4 nm, the accumulated strain energy eventually induces plastic relaxation at the Au–$SrTiO_3$ interface.[318,321,322] This is illustrated by the sketch in Figure 7.5c, in which the coherent (dislocation-free) island partially relieves the misfit strain by introducing a misfit dislocation at the interface, drawn in red. The dislocation is introduced at the cost of additional strain energy around the dislocation core, which is shown schematically by the darker area around the dislocation in Figure 7.5c. On $SrTiO_3$(001)-(2 × 1) and -*c*(4 × 2), the linear trend of *h*/*l* remains up to the highest gold crystals I observed, suggesting that the critical thickness for dislocation introduction has not been reached on $SrTiO_3$(001) at up to *h* = 12 nm. The earlier introduction of dislocations on the $SrTiO_3$(111)-(4 × 4)+(6 × 6) substrate is due to two factors mentioned earlier: (i) the greater misfit strain (4.4% versus 1.5%) and (ii) the stronger epitaxy (2D versus 1D).

For comparison, in a previous study by Silly and Castell,[212] the *h*/*l* ratio of gold crystals on $SrTiO_3$(001)-(2 × 1) was reported to be a constant with crystal volume: 0.42 ± 0.05. Measurements were made of 22 crystals in total and the largest one was just over 1000 nm^3 in volume. Here, in Figure 7.5a I present 154 data points on $SrTiO_3$(001)-(2 × 1) and the crystals span a greater size range: about half of them are over 1000 nm^3 in volume and the largest one is 4030 ± 94 nm^3. The gold crystals measured in the previous paper correspond to a smaller range of data (*h* ~1.7–3.4 nm) with *h*/*l* = 0.42 ± 0.05,[212] and the constant *h*/*l* ratio reported may simply be due to the limited range. Nevertheless, within the same height range (1.7–3.4 nm), my average value of *h*/*l* is 0.14 ± 0.08, which is noticeably smaller than 0.42. This difference can be attributed to my different growth parameters: in the previous paper, 0.8 ML of gold was deposited onto the substrate heated to 400 °C;[212] in my study, 0.25–0.50 ML of gold (66% at 0.25 ML) was deposited onto the substrate kept at 300–400 °C. The main difference is the larger deposition amount of gold in the previous study, which resulted in a visibly higher density of the gold crystals.[212] A higher density of crystals means that a greater proportion of the evaporated gold lands directly on the top facets of the growing crystals, hence resulting in a greater *h*/*l* ratio. The difference in the *h*/*l* ratios of the two datasets serves to illustrate how sensitive this ratio is to the parameters under which the experiments are performed. This point is discussed in detail in the review by Marks and Peng,[316] who point out that each nanocrystal in a distribution is either growing or shrinking, and may even be changing form, e.g., from an fcc crystal to a multiply twinned particle (MTP). This is a result of Ostwald ripening, during which larger particles grow at the expense of smaller ones. This phenomenon occurs continuously, though only at a noticeable rate at elevated temperatures. Therefore, the gold crystals observed and measured only represent a snapshot of their evolution towards absolute thermodynamic equilibrium. This means that thermodynamic models are only ever an approximation to experimentally derived data.

Accordingly, the gold crystals should ideally be treated at high temperatures (e.g., close to their melting point) to promote the mobility of gold atoms, to allow the gold crystals to evolve towards their thermodynamically equilibrium shape as much as possible. This is the reason why I held the substrates at above 300 °C during gold crystal growth. However, the substrate temperature was usually kept below 400 °C because higher growth temperatures resulted in crystals that were too high to be scanned by the STM tip, e.g., when h > ~10 nm. Nevertheless, I annealed a few samples at 500–600 °C for SEM studies (see Figure 7.6b–f), which indeed enhanced the kinetics towards equilibrium. For example, as mentioned in section 7.2.1, the gold crystals on $SrTiO_3$(111)-(4 × 4)+(6 × 6) grown at 300–400 °C mainly adopt two orientations (Figure 6.1d and Figure 7.3), which are known to be inequivalent because of the 3-fold symmetry of both gold and $SrTiO_3$(111). After the gold crystals were post-annealed at 600 °C, only one exclusive orientation was observed (Figure 7.6f), which must be the thermodynamically favoured epitaxial orientation.

It is widely reported in the literature that for a crystal grown on a lattice-mismatched substrate, the interfacial strain opposes wetting and leads to a higher h/l ratio, though most of the past studies are computational.[318,319,321,322] Therefore, when we minimise the total energy of a gold crystal to thermodynamically optimise its shape, we need to include its strain energy in addition to its surface/interface energies. The strain energy is a complex function of the crystal and substrate stiffness, the lattice misfit between them, the crystal volume, and the crystal shape.[318,322] A few reports also mention that the h/l ratio increases with increasing lattice misfit, increasing strain-free h/l ratio, and increasing substrate/crystal stiffness ratio.[321,322] These are consistent with my observations for the three h/l ratio gradients on the three $SrTiO_3$ substrates.

Additionally, the strain should propagate from the interface into both the crystal and the underlying substrate,[318,321,322] but for simplicity Figure 7.5b,c only shows the strain field (grey) in the gold crystals. As mentioned in section 6.3, gold has a relatively low Young's modulus of

E(Au) = 79 GPa,[309] compared with $E_{<100>}(SrTiO_3)$ = 225–265 GPa.[310,311] Hence it is expected that the interfacial misfit strain would be largely taken up in the gold crystals. This is also due to the small size of gold crystals that allows them to relax more easily parallel to the substrate surface plane.

It has also been reported that as the interfacial strain energy accumulates in an epitaxially substrate-supported crystal, interfacial dislocations will be introduced at a critical thickness.[318,321,322] In my Au-on-$SrTiO_3$ system, dislocations are more likely to be generated in gold than in $SrTiO_3$ (as drawn in Figure 7.5c). This is because the dislocation energy per unit length is $\propto Gb^2$, where G is the shear modulus and $\boldsymbol{b}$ is the Burgers vector. These values are both smaller in gold: G(Au) = 27 GPa,[309] $G_{<100>}(SrTiO_3)$ = 121 GPa,[311] b(Au) = 2.884 Å, and $b(SrTiO_3)$ = 3.905 Å.

When a dislocation is introduced, it partially releases the interfacial strain and abruptly modifies the equilibrium shape, resulting in a reduced h/l ratio. Thermodynamically the growing crystal will have an oscillating or sawtooth h/l ratio as successive dislocations are introduced.[321–323] This behaviour has been calculated for the Ge-on-Si(001) system.[323] In my Au-on-$SrTiO_3$(111) system, the period of oscillation in the gold crystal basal plane width is calculated to be 5.49 nm (= the strain-free dislocation separation), which corresponds to an oscillation period in the crystal height of 5.18 nm. In Figure 7.5a, on $SrTiO_3$(111)-(4 × 4)+(6 × 6) the nucleation of the first dislocations occurs at $h \approx 4$ nm, upon which the h/l ratio drops. Thereafter, the h/l ratio should rise until $h \approx 4 + 5.18 \approx 9$ nm, when it should suddenly drop again. My data are not of a sufficient quality to clearly show this oscillation. However, there are three misfit dislocations introduced per 5.18 nm period, along the three $<1\bar{1}0>$ directions in the gold (111) plane. Unless they are all introduced at the same time, the dramatic drop in the h/l ratio will not be easily observed. On the $SrTiO_3$(001) substrates, the oscillation period in the crystal base width is

calculated to be 18.74 nm, corresponding to a period of 17.67 nm in the crystal height. These values fall outside my data range in Figure 7.5a.

Finally, I comment that although the *h*/*l* ratio is not a constant due to the interfacial strain, in some studies, e.g., of Pt and Pd nanocrystals,[324,325] the 'interfacial energy' was still calculated from the nanocrystal geometry based on the Winterbottom construction. As the crystal aspect ratio was also observed to heighten, the 'interfacial energy' appears to increase with increasing crystal height, which was explained by the interfacial strain and strain relief by dislocations.[324] However, I do not think that in my case this is a helpful analysis method because the interfacial energy is an area-dependent term that increases in magnitude as misfit dislocations are introduced, whereas the strain is a volume-dependent term that decreases when strain-relieving misfit dislocations are introduced.

7.2.3 A_{111}/A_{001} or *s*/*l* ratio

In addition to the *h*/*l* ratio, the other geometric ratio that together defines the gold crystal shape is the ratio between *s* and *l* (Figure 7.4b). The *s*/*l* ratio is a direct measure of the ratio between the {111} and {001} surface areas (A_{111}/A_{001}). This depends on the surface energies of gold, γ_{111} and γ_{001},[214] as well as the growth velocities along <111> and <001> directions of the crystal.[222] Thermodynamically the *s*/*l* ratio is a constant irrespective of the supporting substrate, and it is related to the surface energies via $\frac{\gamma_{111}}{\gamma_{001}} = \frac{1}{\sqrt{3}} + \frac{s}{2l}$. However, the growth velocities of the crystallographic facets are differently influenced by the local environment, which, when outside UHV, can involve hydrocarbons in air, CO gas, and other adsorbates.[215]

In Figure 7.6a, the *s*/*l* ratio on the three $SrTiO_3$ substrates is plotted against crystal height *h*. Again, only those crystals grown at > 300 °C were measured, which are reasonably close to

their equilibrium shapes. Apart from the flat crystals on $SrTiO_3$(001)-(2 × 1) for which $h < 4$ nm, the *s*/*l* ratio is a constant, with values of 0.15 ± 0.07 on $SrTiO_3$(001)-(2 × 1), 0.28 ± 0.06 on $SrTiO_3$(001)-*c*(4 × 2), and 0.46 ± 0.09 on $SrTiO_3$(111)-(4 × 4)+(6 × 6). Since the gold crystals were grown and characterised in UHV, their different *s*/*l* ratios on different substrates are unexpected.

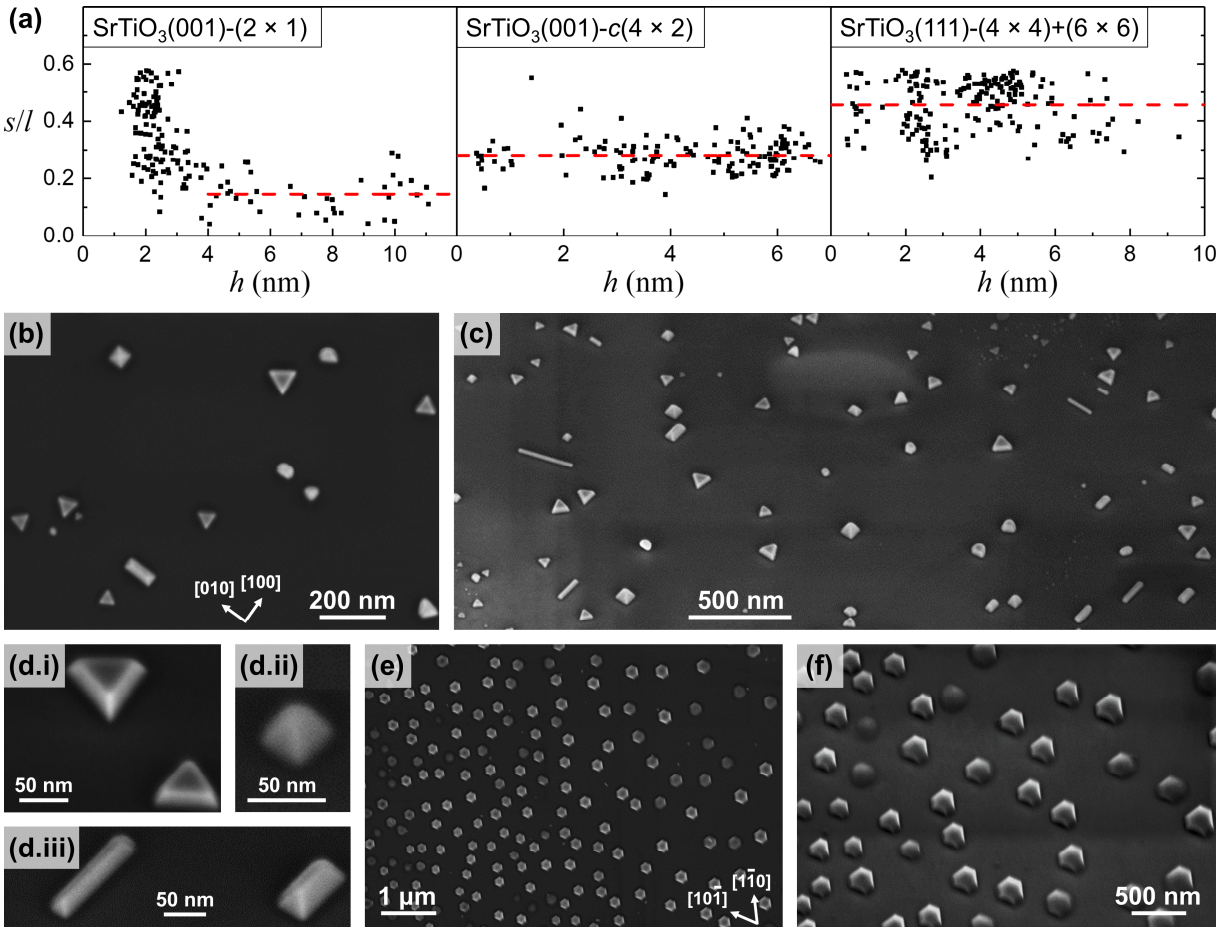

Figure 7.6: *s*/*l* ratio of gold crystals and SEM images. (a) *s*/*l* ratio measured from STM images plotted against crystal height on $SrTiO_3$(001)-(2 × 1), $SrTiO_3$(001)-*c*(4 × 2), and $SrTiO_3$(111)-(4 × 4)+(6 × 6). (b–d) SEM images of gold crystals on $SrTiO_3$(001)-(2 × 1): (b) top view, (c) tilted view (40°), and (d) high-magnification images of the three typical crystal shapes: (d.i) triangles, (d.ii) pyramids, and (d.iii) huts. (e) Top view and (f) tilted view (40°) of gold crystals on $SrTiO_3$(111)-(4 × 4)+(6 × 6).

Among all three substrates, $SrTiO_3$(111)-(4 × 4)+(6 × 6) gives rise to the largest *s*/*l* ratio. In the STM images in Figure 6.1d, the gold crystal top facets are close to regular hexagons. Consistently, Figure 7.6e,f shows two SEM images (top and tilted views) of gold crystals on $SrTiO_3$(111)-(4 × 4)+(6 × 6), in which the large crystals were obtained following a post anneal

at 600 °C for 5 h. Their *s*/*l* ratio is measured to be 0.55 ± 0.02, within the range of values obtained from STM images, 0.46 ± 0.09.

On the other hand, the relatively high gold crystals (h > 4 nm) on $SrTiO_3$(001)-(2 × 1) have very small {001} facets that are barely visible. The crystal top facets look like triangles without truncation, e.g., the highest (brightest) four crystals in Figure 6.1b. This is also confirmed by the triangular crystals in Figure 7.6b–d, which are SEM images of some large crystals on $SrTiO_3$(001)-(2 × 1) prepared by a post anneal at 500 °C for 1 h. On $SrTiO_3$(001)-(2 × 1), three crystal shapes are observed: 'triangles', 'pyramids', and 'huts', as shown in the three high-magnification images in Figure 7.6d.i–iii, in this order. They are all produced by different orientations of the Wulff shape of gold, and their crystallographic interfaces with the substrates are (111), (001), and (110), respectively.[90] In Figure 7.6b–d, the triangles and pyramids do not show any visible {001} facets and the huts are trying to grow infinitely long to minimise the proportion of {001} facets. These are in good agreement with the *s*/*l* plot for $SrTiO_3$(001)-(2 × 1) (Figure 7.6a), in which the equilibrium *s*/*l* ratio = 0.15 ± 0.07 at large crystal heights.

As an aside, thermodynamically the three crystal shapes (triangles, pyramids, and huts) are not expected to coexist on the same substrate. Silly and Castell explained that the lowest energy morphology depends on $\gamma^* = \gamma_{interface} - \gamma_{substrate}$ (or $\gamma_i - \gamma_s$).[90] For example, the stable structure of fcc Pd crystals was reported to be the hut shape on $SrTiO_3$(001)-(2 × 1) and the pyramid shape on $SrTiO_3$(001)-*c*(4 × 2).[90] In my system, the truncated triangular crystals are identified as the thermodynamically favoured shape on all three substrates. It is the only shape observed for small crystals under STM (Figure 6.1) and the most frequently observed shape for large crystals under SEM (Figure 7.6b–f). The pyramids and huts may nucleate randomly and become stuck in these metastable orientations due to kinetics.[316]

Interestingly, the flat crystals (h < 4 nm) on $SrTiO_3$(001)-(2 × 1) have a decreasing s/l ratio with increasing crystal height, from $\frac{1}{\sqrt{3}}$ (≈ 0.58) to the equilibrium value of 0.15 (Figure 7.6a). s/l equals $\frac{1}{\sqrt{3}}$ when the crystal top facet is a regular hexagon. In section 6.2.3 it is shown that while being annealed at 350 °C, the gold MLs on $SrTiO_3$(001)-(2 × 1) tend to develop into regular hexagons, possibly in preparation for their conversion into crystals (Figure 6.4b). In Figure 6.1a.ii,b.ii, the crystal heights are labelled below each crystal and we can see that the higher a crystal is, the more 'pointed' its top facet is, i.e., smaller {001} side facets. Hence, the varying s/l ratio of the flat crystals can be attributed to their transition from or the dewetting phenomenon of MLs. In Figure 6.1a the flattest crystal (h = 1.72 nm) even has a curved edge, which may be a residual feature from an irregularly shaped ML. In section 6.2.3 it is also mentioned that the flattest crystals observed on $SrTiO_3$(001)-(2 × 1) consist of a minimum of five atomic layers due to the presence of MLs as the nucleation shape. Accordingly, the data points for $SrTiO_3$(001)-(2 × 1) in Figure 7.5a and Figure 7.6a only start from h ~1.2 nm.

Now I explain the possible origin of the different s/l ratios of gold crystals on the three $SrTiO_3$ substrates. In my study, the gold crystals were prepared in a UHV environment nearly free of gaseous adsorbates, so their different s/l ratios have to be attributed to their interaction with the substrates. Previously, when gold crystals were studied in UHV, e.g., on CeO_2(001) and $SrTiO_3$(001)-(2 × 1) substrates,[208,212] they grew into the truncated triangular shape as well. However, in these studies the s/l ratio of the crystals was not specifically analysed. I have not reached a firm conclusion of the mechanism by which the substrates influence the s/l ratio, but a few possibilities are discussed below.

Firstly, the three $SrTiO_3$ substrates certainly interact with the gold crystals differently at the interface. For example, the interfacial strain is calculated to be 1.5% on $SrTiO_3$(001) and 4.4% on $SrTiO_3$(111). However, I propose that the interfacial interaction itself is not the direct cause

of the different *s*/*l* ratios. Taking the $SrTiO_3$(001)-(2 × 1) substrate as an example: any interfacial effect may possibly cause the {001} side facets of a truncated triangular gold crystal to shrink, but the interface should not affect the (001) top facet of a pyramidal crystal. However, the latter is also seen to be minimised (Figure 7.6b–d).

The second possibility is the encapsulation of gold crystals by an oxide layer from the substrate, known as the strong metal-support interaction (SMSI).[326–328] Encapsulation by an oxide layer is driven by the reduction in the metal facet energies. One would expect the {111} and {001} gold facets to undergo different degrees of energy reduction. Hence, this would influence the *s*/*l* ratio. However, metal particles encapsulated by TiO_x layers usually exhibit superstructures or moiré patterns under STM observation,[326,328,329] which are not seen on my gold crystals. For example, when fcc Pd crystals with a (111) base are grown on nanostructured $SrTiO_3$(001), they exhibit two clear moiré patterns: the 'wagon wheel' and the 'hexagonal superstructure'.[326] When (111)-based Pd crystals are supported on TiO_2(110) substrates, two superstructures named 'pinwheels' and 'zigzags' are observed.[328,329] I have not found publications on TiO_x-encapsulated gold crystals, but superstructures formed by TiO_x ultrathin films on an Au(111) surface have been reported: 'honeycomb', 'pinwheel', and triangular islands.[330] In my system, the absence of any overlayer structures on the gold crystal top facets means that there is no evidence for TiO_x encapsulation.

A third possibility is the presence of surfactants originating from the $SrTiO_3$ substrates. The $SrTiO_3$(001)-(2 × 1) surface is hydroxylated, i.e., it is terminated with –OH groups.[89] The oxygen is part of TiO_5 or TiO_6 groups, but the hydrogen can desorb from the substrate so that the gold crystals grown on this surface may become hydrogen-terminated. The hydrogen may preferentially bind to the {111} facets compared with the {001} facets, inhibiting the growth along <111> directions. Another way to depict this scenario is that the hydrogen surfactant reduces the facet energy of {111} to a greater extent than that of {001}, promoting the growth

of {111} facets. Nevertheless, it is not obvious to us what surfactants might arise from the other two substrates, $SrTiO_3$(001)-*c*(4 × 2) and $SrTiO_3$(111)-(4 × 4)+(6 × 6). According to previous studies, these two surfaces are both based on Ti-centred polyhedral building blocks (TiO_4, TiO_5, and TiO_6) in the top few layers and are not terminated with any easily dissociable species.[56,88]

Previous reports on gold crystal shapes are mostly from crystals grown in solution, e.g., using the polyol synthetic method.[21,195–198] During solvent-based growth, the ratio between the {111} and {001} surface areas (A_{111}/A_{001}) is heavily influenced by the selective adsorption of surfactants on certain crystallographic planes.[195–199,231] This gives rise to crystal shapes that range from octahedra (purely {111}-terminated) to cubes (purely {001}-terminated).[195–198,205] For example, it was discovered that higher concentrations of poly(vinyl pyrrolidone) (PVP) and poly(diallyldimethylammonium) chloride (PDDA) encourage the formation of a higher proportion of {111} facets.[195–197] On the other hand, {001} facets of gold crystals were reported to be stabilised by silver ions and cetyltrimethylammonium bromide (CTAB).[195,198,199,231]

7.2.4 Wulff and growth shapes

The SEM images of gold crystals in Figure 7.6c,d,f were taken with the samples tilted at 40° and there is no evidence of any reentrant facets. According to the geometry of the Wulff crystal (Figure 7.4a), reentrant facets should appear if the crystal height is greater than $\sqrt{\frac{2}{3}}l$. I know from STM images that 75% of my crystals grown at > 300 °C satisfy the condition that $h > \sqrt{\frac{2}{3}}l$; 85% of my crystals grown at > 350 °C satisfy this condition. Provided that the gold crystals in Figure 7.6b–f were treated at 500 °C and above, most of the hexagonal or triangular crystals would show reentrant facets if they followed the Wulff shape. However, when kinetics

play a key part, an enhancement factor is added to the growth velocity of the reentrant facets.[222] An analogy is that in heterogeneous nucleation, the nucleation energy is lower on a notched surface than on a smooth surface. The bottom of a reentrant facet acts as such a notch and the atoms attaching to such a site form additional bonds with the substrate. Therefore, for an equilibrium crystal with the shape in Figure 7.4a, the attachment energy of additional gold atoms to the reentrant {111} facets would be lower than that to the top (111) facet. Moreover, most gold atoms arrive at a crystal sideways from the substrate surface due to Ostwald ripening rather than from the top during the gold evaporation. Hence reentrant facets typically grow out.

Now I discuss the geometries and energies of the Wulff and growth shapes. When $\frac{\gamma_{001}}{\gamma_{111}} \geq \sqrt{3}$, the Wulff shape of a gold crystal does not have {001} facets and is an octahedron (Figure 7.7a). The first row of drawings in Figure 7.7a shows how the Wulff shape (yellow) can be cut to produce the three substrate-supported crystal shapes: 'triangle', 'pyramid', and 'hut' (orange). The triangular and pyramidal crystals both have reentrant facets. When these reentrant facets grow out, their corresponding growth shapes result, as illustrated in the second row in Figure 7.7a. Note that the hut shape has four {111} end facets, two on each end, and they are perpendicular to the substrate. Therefore, the hut does not have reentrant facets (with a contact angle of > 90° with the substrate), and hence its growth shape is the same as its Wulff shape. When $1 < \frac{\gamma_{001}}{\gamma_{111}} < \sqrt{3}$, {001} and {111} facets of the gold crystals coexist and the Wulff shape is a truncated octahedron (Figure 7.7b). Figure 7.7b shows a similar table of sketches to Figure 7.7a. When {001} facets are present, the 'triangular' crystal has a truncated triangular top facet, and is therefore called a 'hexagon' for simplicity.

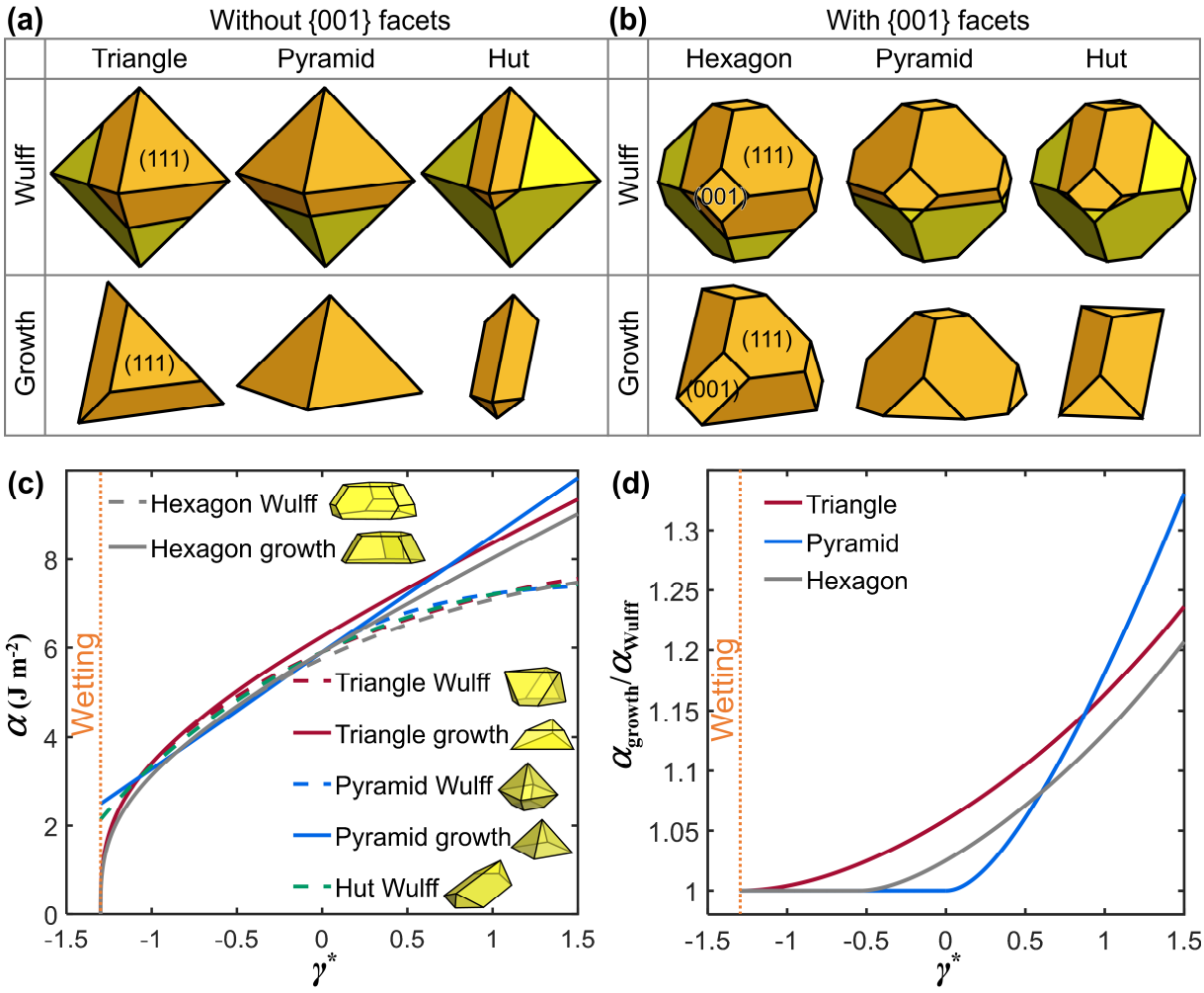

Figure 7.7: Geometries and energies of the Wulff and growth shapes of gold crystals. (a) Geometries of {111}-terminated gold crystals. The first row shows the Wulff shapes (yellow) being cut to produce triangular, pyramidal, and hut crystals (orange). Their corresponding growth shapes are drawn below them in the second row. (b) Wulff and growth shapes of gold crystals with both {111} and {001} facets. With {001} facets present, the triangular crystal has a truncated triangular top facet and is called a 'hexagon' for simplicity. (c) Plots of α versus γ^* for the Wulff and growth shapes of the triangle, pyramid, hut, and hexagon. (d) Plots of growth-to-Wulff α ratios for the triangle, pyramid, and hexagon. In (c,d), facet energies of γ_{111} = 1.3 J m^{-2} and γ_{001} = 1.6 J m^{-2} are used for gold;[331] gold wets the substrate when $\gamma^* < -\gamma_{111} = -1.3$ J m^{-2}.

As mentioned in section 7.2.2, the total energy of a substrate-supported crystal consists of the formation energy, the surface/interface energies, and the strain energy.[317–319] For a crystal with a given volume, its Wulff and growth shapes have the same formation energy. Their surface/interface energies and strain energies will differ, though I do not have sufficient information to accurately calculate their strain energies. However, I can estimate the surface/interface energies of the three crystal shapes: the Wulff and growth shapes of triangles/hexagons, the Wulff and growth shapes of pyramids, and the Wulff shape of huts. The

total surface/interface energy of a nanocrystal can be parameterised as $E = \alpha_{\text{shape}} V^{\frac{2}{3}}$,[90,317] where V is the crystal volume and α_{shape} is discussed below for the two cases where there either are, or are not {001} facets present.

Without the {001} facets, i.e., when $\frac{\gamma_{001}}{\gamma_{111}} \geq \sqrt{3}$, the following relationships can be derived:

$$\alpha_{\text{triangle Wulff}} = 3^{\frac{7}{6}} \cdot 2^{-\frac{2}{3}} (8\gamma_{111}^3 + 9\gamma_{111}^2 \gamma^* - \gamma^{*3})^{\frac{1}{3}}, \tag{7.1}$$

$$\alpha_{\text{triangle growth}} = \frac{3}{2} \left[\sqrt{3}(19\gamma_{111}^3 + 27\gamma_{111}^2 \gamma^* + 9\gamma_{111}\gamma^{*2} + \gamma^{*3})\right]^{\frac{1}{3}}, \tag{7.2}$$

$$\alpha_{\text{pyramid Wulff}} = 3^{\frac{2}{3}} \left(6\sqrt{3}\gamma_{111}^3 + 18\gamma_{111}^2 \gamma^* - 6\sqrt{3}\gamma_{111}\gamma^{*2} + 2\gamma^{*3}\right)^{\frac{1}{3}}, \tag{7.3}$$

$$\alpha_{\text{pyramid growth}} = 18^{\frac{1}{3}} \left(\sqrt{3}\gamma_{111} + \gamma^*\right), \tag{7.4}$$

$$\alpha_{\text{hut Wulff}} = 3^{\frac{2}{3}} \cdot 2^{-\frac{1}{6}} \left(\sqrt{6}\gamma_{111} - \gamma^*\right)^{\frac{1}{3}} \left(\sqrt{6}\gamma_{111} + 2\gamma^*\right)^{\frac{2}{3}}. \tag{7.5}$$

The α_{shape} formulae can also be derived for crystals when {001} facets are present, i.e., when $1 < \frac{\gamma_{001}}{\gamma_{111}} < \sqrt{3}$. We only focus on the (111)-based crystals, which are the experimentally observed equilibrium shape, and they are called 'hexagons' with {001} facets present. Now,

$$\alpha_{\text{hexagon Wulff}} = 3 \cdot 2^{-\frac{2}{3}} \left(8\gamma_{001}^3 - 24\sqrt{3}\gamma_{001}^2 \gamma_{111} + 72\gamma_{001}\gamma_{111}^2 - 16\sqrt{3}\gamma_{111}^3 + 9\sqrt{3}\gamma_{111}^2 \gamma^* - \sqrt{3}\gamma^{*3}\right)^{\frac{1}{3}}, \tag{7.6}$$

$$\alpha_{\text{hexagon growth}} = \frac{3}{2} \left\{(\gamma_{111} + \gamma^*)\left[72\gamma_{001}\gamma_{111} - 12\sqrt{3}\gamma_{001}^2 + \sqrt{3}(\gamma^{*2} + 8\gamma_{111}\gamma^* - 17\gamma_{111}^2)\right]\right\}^{\frac{1}{3}}. \tag{7.7}$$

Equations (7.1)–(7.7) are derived in Appendix B (section B.2). α_{shape} is plotted as a function of γ^* in Figure 7.7c using the theoretical values of γ_{111} = 1.3 J m^{-2} and γ_{001} = 1.6 J m^{-2}.[331] The corresponding shapes are sketched in the legend. For the triangular, pyramidal, and hexagonal crystals, their Wulff shape is always lower in energy than their growth shape. The growth/Wulff

energy discrepancy increases with increasing γ^*, as shown in the plot of their α ratios in Figure 7.7d. At a practical value of γ^* such as –0.5 J m^{-2}, there is a reasonably small discrepancy between the surface/interface energies of the Wulff and growth shape (< 3%). This is a condition that helps the growth shapes to survive.

For the pyramid, its Wulff shape is the same as the growth shape when the Wulff point of the crystal (or the midpoint of the Wulff octahedron) is below the substrate surface. Therefore their α plots in Figure 7.7c (two blue lines) only start to diverge when $\gamma^* > 0$. For the hexagon, the energies of its Wulff and growth shapes only start to diverge at $\gamma^* = –0.5$ J m^{-2} (two grey lines in Figure 7.7c), because for any lower value of γ^* the Wulff crystal does not yet have reentrant facets using values of $\gamma_{111} = 1.3$ J m^{-2} and $\gamma_{001} = 1.6$ J m^{-2}. Mathematically, the value $\gamma^* = –0.5$ J m^{-2} is obtained from the three simultaneous equations (B.4), (B.5), and (B.13) in Appendix B (section B.2).

It is noteworthy that the condition for wetting is $\gamma_{m} + \gamma_{im} - \gamma_s < 0$ (if the edge energy of MLs is ignored), where γ_m is the surface energy of a gold ML per unit area and γ_{im} is the ML–substrate interfacial energy. Since $\gamma^* = \gamma_{im} - \gamma_s$, the equation above can be rearranged as $\gamma^* < -\gamma_m$. The value of γ_m is unknown but in a ML, the closest packing possible of the gold atoms corresponds to an Au(111) structure, with a surface energy of $\gamma_{111} = 1.3$ J m^{-2}. Therefore in Figure 7.7c,d, when $\gamma^* < –1.3$ J m^{-2} gold wets the substrate and the α plots of the crystals are only physically meaningful outside this regime.

The energy calculations presented in Figure 7.7c,d are only a qualitative comparison between the Wulff and growth shapes, because they do not take into account the effects of the crystal–substrate interfacial strain (section 7.2.2) and the chemical environments (section 7.2.3). Because of the latter, the A_{111}/A_{001} ratio of experimentally observed gold crystals is affected by surfactant adsorption on their {111} and {001} facets. It is therefore not a true reflection of the

pristine gold facet energies (γ_{111} and γ_{001}). Hence, my use of γ_{111} = 1.3 J m^{-2} and γ_{001} = 1.6 J m^{-2} is only an estimate.

Additionally, I would like to comment that the growth shape of the triangular crystal in Figure 7.7a has a truncated tetrahedral shape and is terminated with {111} planes only. If such a crystal grew into a full tetrahedron, geometrically it would be the constituent part of MTPs, e.g., decahedra and icosahedra (though these structures are not 'built up' by the tetrahedra, but rather form by twinning). Gold crystals with the truncated tetrahedral shape have been previously observed as free-standing crystals prepared in solution,[195,196] but the authors did not relate them to the Wulff shape. Here, we understand that this shape is a deviation from the {111}-terminated Wulff shape, i.e., an octahedron cut by the substrate, upon which the reentrant facets grow out. It is difficult to explain why in previous studies the free-standing gold crystals also ended up with this growth shape,[195,196] as there were no substrates to encourage the growing out of reentrant facets. It is possibly attributable to their very rapid growth and the small energy difference between the Wulff and growth shapes. Alternatively, some of the crystals might have attached to the test tube walls during growth.

Finally, on some substrate-supported gold nanocrystals, reentrant facets have been observed previously, e.g., on CeO_2 and TiO_2 substrates.[208,308,314,332–334] These gold crystals adopt the same equilibrium shape as that in my work, with an Au(111) interface with the substrate. They were characterised by STEM and typically have a lateral size of ~5 nm, cf. my gold crystals in the SEM images (Figure 7.6b–f), which are 50–300 nm laterally. In some of the previous studies, a deposition–precipitation method was used to prepare the gold crystals.[208,308,332] A few grams of the oxide particles (CeO_2 and TiO_2) were dispersed into an aqueous solution of $HAuCl_4$. Following centrifugation, washing, and drying, the samples were calcinated at 300–400 °C in air, which led to the decomposition of the Au(III) complexes into gold metal particles. This is

in essence a solvent-based growth method, and the presence of gold reentrant facets is not surprising.[222]

However, in some other studies gold was deposited onto TiO_2 substrates using an electron-beam evaporator at a rate of 0.33 Å min^{-1} in vacuum.[314,333,334] The sample was then annealed at 400–700 °C to promote the formation of equilibrium crystal shapes. This protocol is similar to mine, where I deposited gold at an even lower rate (~0.06 Å min^{-1}) and annealed the crystals at similar temperatures (500–600 °C) before taking the SEM images (Figure 7.6b–f). I believe that the presence of reentrant facets on their gold crystals is due to their smaller crystal sizes. When the diameter of a gold particle is smaller than ~20 nm, their melting point drops below that of bulk gold (1064 °C), and it is calculated to be ~700 °C for a 5 nm-diameter particle.[335,336] Therefore, in Ref.[314,333,334] the gold crystals were post-annealed at temperatures close to their melting point. They may have become molten hemispheres during the thermal treatment, which, when cooled down, are expected to reach the thermodynamically optimised shapes, i.e., the Wulff shapes with reentrant facets present.

7.3 Conclusions

In conclusion, the gold crystal shapes are strongly influenced by their interaction with the $SrTiO_3$ substrates: $SrTiO_3$(001)-(2 × 1), $SrTiO_3$(001)-*c*(4 × 2), and $SrTiO_3$(111)-(4 × 4)+(6 × 6). The crystal shape is not self-similar between different crystal sizes. The *h*/*l* ratio increases with the crystal height *h* on all three substrates, because crystal heightening partially releases the interfacial strain caused by the lattice mismatch. The *s*/*l* ratio, which is a direct measure of A_{111}/A_{001}, is found to differ on the three substrates. This may be due to the selective adsorption of surfactants on the {111} and {001} gold facets. One possible surfactant is chemisorbed

hydrogen on the hydroxylated $SrTiO_3$(001)-(2 × 1) surface. The flat crystals on $SrTiO_3$(001)-(2 × 1) (h < 4 nm) are an exception, where their s/l ratio decays from $\frac{1}{\sqrt{3}}$ towards the equilibrium value of 0.15 with increasing h. This is likely to relate to the dewetting process from MLs. Also, the crystal reentrant facets are not observed because these concave facets typically grow out due to kinetics. These growth shapes are slightly higher in energy than their thermodynamic Wulff shape, and the energy discrepancy is greater at larger values of γ^*. This study demonstrates the influence of the detailed nature of oxide substrate surfaces on the shape of epitaxial gold nanocrystals, which is a phenomenon critical to the rational tuning of their catalytic and optical properties. Further research in this area would be important with respect to realising their full potential in catalysis, biological sensing, and photonics.

Chapter 8

Conclusions

8.1 Overview

This thesis reports the synthesis and characterisation of two materials supported on single crystal $SrTiO_3$ substrates: monolayer MoS_2 crystals and gold nanostructures. These studies establish the influence of the substrate material on the epitaxial and thermal behaviour of MoS_2 monolayers, as well as on the shapes of gold nanostructures. Chapters 4 and 5 present the results from CVD-grown MoS_2 monolayers on three different terminations of $SrTiO_3$ substrates. The MoS_2 crystals were structurally characterised by SEM and STM, optically characterised by Raman spectroscopy and PL, and electronically characterised by XPS. In Chapters 6 and 7, the gold monolayers and nanocrystals were studied by STM and SEM. The energies of the monolayers and of the Wulff and growth shapes of nanocrystals were calculated to explain their formation. Conclusions have already been drawn at the end of each chapter, but some summarising remarks are collated below to present a clearer picture of the work presented in this thesis.

8.2 Monolayer MoS_2 crystals on $SrTiO_3$

Finding suitable substrate materials is an important step towards epitaxy or orientation control in the synthesis of MoS_2 films. In Chapter 4, when MoS_2 monolayers are grown on three different terminations of $SrTiO_3$ substrates, their crystal shapes and orientations are influenced by their epitaxial interaction with the substrate. On $SrTiO_3$(111), the monolayer MoS_2 crystals form equilateral triangles with two main orientations, in which they align their $<2\bar{1}\bar{1}0>$-type directions (i.e., the sulphur-terminated edge directions) with the $<1\bar{1}0>$-type directions on $SrTiO_3$. This arrangement allows near-perfect coincidence epitaxy between seven MoS_2 unit cells and four $SrTiO_3$ unit cells. On $SrTiO_3$(110), the MoS_2 crystals tend to align their edges with both the $<1\bar{1}0>$ and $<1\bar{1}\bar{2}>$ directions on $SrTiO_3$ as these both provide favourable coincidence lattice registry. This distorts the crystal shapes and introduces an additional strain detectable by photoluminescence. When triangular MoS_2 crystals are grown on $SrTiO_3$(001), they again show a preference to align their edges with the $<1\bar{1}0>$ directions on $SrTiO_3$. These observations can be explained if the interfacial vdW bonding between MoS_2 monolayers and $SrTiO_3$ is greatest when maximum commensuration between the lattices is achieved. Therefore, a key finding of the work in Chapter 4 is that the vdW interaction between MoS_2 and $SrTiO_3$ substrates determines the supported crystal shapes and orientations by epitaxial relations. Controlled crystal orientations make the growth of large sheets of MoS_2 possible when there are multiple nucleation sites. This minimises the number of grain boundaries and optimises the electronic properties of the material, e.g., charge mobility, which is crucial for the application of monolayer MoS_2 in next-generation nanoelectronic devices.

Chapter 5 reports the results of a study on thermal degradation of MoS_2 monolayers supported on $SrTiO_3$ substrates in UHV. This study was conducted to further our understanding of the thermal stability of monolayer MoS_2, a wide-bandgap semiconductor suitable for use in high-

temperature electronics. The study was carried out on the (111), (110), and (001) terminations of $SrTiO_3$ substrates, but MoS_2 was found to degrade on all these surfaces in a similar way. By STM, MoS_2 monolayer crystals were shown to maintain their structure at up to 700 °C in UHV, at which point triangular etch trenches appear along the <$2\bar{1}\bar{1}0$> lattice directions (i.e., sulphur-terminated edge directions) of the MoS_2 crystals. The trenches are due to the preferential loss of sulphur, allowing molybdenum to be oxidised by oxygen originating from the $SrTiO_3$ substrate. The intensities of the A-exciton PL peak and the E^1_{2g} and A_{1g} Raman signals are reduced significantly following treatment at this temperature. The crystals continue to degrade at higher annealing temperatures in UHV until they transform into MoO_x (x = 2–3) particles at 800–900 °C, and the optical properties characteristic of MoS_2 are lost entirely in PL and Raman spectra. The initial sulphur loss and the formation of MoO_x are confirmed by XPS. The macroscopic triangular shapes of the MoS_2 crystals are retained until the residual particles evaporate at above 1000 °C. The optical properties of the 700 °C and 800 °C UHV-annealed samples can be partially recovered upon sulphur annealing. This work establishes a pathway of the thermal degradation of $SrTiO_3$-supported monolayer MoS_2 in vacuum from smooth MoS_2 crystals to crystals with sulphur vacancies (etch trenches), followed by MoO_2 and finally MoO_3 particles. It was also demonstrated that sulphur annealing can be used to heal the defects before oxidation occurs. This study contributes to our understanding of the thermal stability of monolayer MoS_2 and paves the way for its future application in high-temperature electronics and sensors.

8.3 Gold monolayers and nanocrystals on $SrTiO_3$

Chapters 6 and 7 report the morphology of gold islands grown on three $SrTiO_3$ single crystal substrates. Gold nucleates as monolayers on $SrTiO_3$(001)-(2 × 1) and as multiply twinned

particles on $SrTiO_3$(001)-*c*(4 × 2) and $SrTiO_3$(111)-(4 × 4)+(6 × 6). These are the stable morphologies in the small-size regime as opposed to their single-crystal counterparts. Chapter 6 is focused on STM work of gold monolayers stabilised by the $SrTiO_3$(001)-(2 × 1) substrate, among which the largest monolayer observed is 2320 ± 35 nm^3 in volume. These monolayers are usually quasi-rectangles in shape, which align their two longer sides with the <100> directions on the substrate. In STM, they also exhibit a square pattern of spots with a periodicity of 1.54 ± 0.06 nm. The monolayers are thought to adopt mixed hexagonal and square packing of atoms because of their frequently observed internal angles of 60°/120° and 90°/135°. This nucleation shape needs to overcome an energy barrier when they convert into nanocrystals, which is likely the reason why the flattest crystals observed on $SrTiO_3$(001)-(2 × 1) consist of a minimum of five atomic layers. It is also speculated that the monolayers are stabilised by the high surface energy of the $SrTiO_3$(001)-(2 × 1) substrate and the low-energy interface between them. The atomic structure of gold monolayers and their interaction with the substrate would be an interesting topic for future study, since the oxide substrate has demonstrated its power in generating gold monolayers, a catalytically interesting material.

At larger sizes, the equilibrium morphology of gold islands is single crystals with a truncated octahedral shape with {111} and {001} facets. Chapter 7 reports the shapes of gold nanocrystals which deviate from the equilibrium Wulff shape due to the influence of the $SrTiO_3$ single crystal substrates. The gold crystals are characterised by STM and SEM. On all three substrate surfaces, i.e., $SrTiO_3$(001)-(2 × 1), $SrTiO_3$(001)-*c*(4 × 2), and $SrTiO_3$(111)-(4 × 4)+(6 × 6), the height-to-width ratio of the gold crystals is not a constant as would be expected for equilibrium crystals, but instead it increases with crystal height. I propose that as the crystals increase in size, their aspect ratio heightens to relax the interfacial strain. The ratio between the {111} and {001} surface areas of the gold crystals is found to differ on the three substrates, which is speculated to be due to the selective adsorption of surfactants on the {111} and {001} gold facets resulting

from the different substrate surfaces. Reentrant facets of gold crystals that should be present according to their Wulff shape are not observed because these concave sites typically grow out due to kinetic considerations. This study demonstrates the significant effect of the crystal facet termination and surface reconstruction of an oxide substrate on the shape of supported gold nanocrystals.

8.4 Future work

In Chapter 4, the shapes and orientations of monolayer MoS_2 crystals are influenced by their vdW interaction with the $SrTiO_3$ substrates. Because it was difficult to atomically resolve the MoS_2 crystals in STM (explained in section 4.3), this study will benefit from theoretical calculations, which would allow us to verify a number of things. These include the vdW interfacial bonding, the 7:4 coincidence epitaxy between the $<2\bar{1}\bar{1}0>$-type directions of MoS_2 and the $<1\bar{1}0>$-type directions of $SrTiO_3$, the distorted lattice structure of MoS_2 crystals, and the precise strains in them.

To build on Chapters 4 and 5, I could apply the epitaxial and thermal studies to other 2D TMDCs such as tungsten disulphide (WS_2). They have different bandgap energies but all hold much promise for applications in nanoelectronics and optoelectronics.[15,97] The same studies could be repeated, i.e., characterising the crystal structures, shapes, and optical properties of the TMDCs grown on $SrTiO_3$ single crystals by CVD. Their epitaxial and thermal behaviour will enhance our control over their functional properties and consequently broaden their applications.

It is uncommon to observe metal wetting layers on oxide substrates, so the gold monolayers described in Chapter 6 are an interesting system to investigate in more detail. To explore them at a fundamental level, I have to understand their atomic and electronic structures. Their atomic

arrangement may be probed by STM and further studied by DFT. Their electronic states can be explored by XPS and ARPES. Compared to XPS, ARPES would provide additional interesting data on the Fermi level and surface states of gold monolayers. The details of these potential studies are described in section 6.4.

The work in Chapter 6 and 7 could be extended by testing the catalytic and optical properties of the gold nanostructures, since their functional properties are heavily shape dependent. The testing can be conducted on the differently shaped nanocrystals as well as the gold monolayers, whose shapes are regulated by the $SrTiO_3$ substrates. A classic example of nanogold catalysation would be that of the CO oxidation reaction. This can be carried out by exposing the gold nanostructures to a gaseous mixture of CO, O_2, and N_2 in a fixed-bed flow reactor.[337] This is possible with gold nanocrystals because they can survive outside UHV, e.g., the SEM images in Figure 7.6b–f were obtained after the gold crystal samples were transferred in air to the SEM chamber. On the other hand, gold monolayers do not survive an ambient environment. However, small amounts of CO and O_2 can be dosed in UHV onto the samples. These fundamental studies can be used to identify the adsorption sites of CO and O_2, e.g., the corners, the edges, and terraces sites including {111} and {001}. Being able to quantify the site-specific catalytic activity of nanogold is a vital step towards its application as a real catalyst. Optical characterisation can be done by dark field scattering using unpolarised white light to obtain localised surface plasmon resonance (LSPR) spectra of single gold nanoclusters.[21] If a quantitative relationship could be established between their functional properties and their shapes, we would be able to fine tune these properties by manipulating their substrates.

Exploring the possibilities above would advance our understanding of the substrate effects of $SrTiO_3$ on the supported 2D and nanomaterials. This will ultimately improve our capability to tailor such nanomaterials for electronic and catalytic applications.

Appendix A: Reported surface reconstructions of $SrTiO_3$ (Chapter 2)

Table A.1: Summary of reported reconstructions on $SrTiO_3$(111).

Year ref.	Reconstruction	Ar^+-ion sputtering	Annealing temp. (°C)	Annealing time	Environment	
1998 47	(4 × 4)	no	1200	5 min	UHV	
2005 54	(9/5 × 9/5) + (3 × 3)	sputtered (conditions not specified)	1050	10 h	pO_2 = 1.0 atm	
			1050	5 h	pO_2 = 0.2/0.4 atm	
			950/1125	5 h	pO_2 = 0.2 atm	
	(9/5 × 9/5) + (3 × 3) + (6 × 6)		1150	5 h	pO_2 = 1.0 atm	
			1050	5 h	pO_2 = 0.6 atm	
			950	5 h	pO_2 = 0.2 atm	
	(6 × 6)		1110	5 h	pO_2 = 1.0 atm	
			1050	5 h	pO_2 = 0.8/1.0 atm	
			1050	0.5 h	pO_2 = 0.0 atm	
			1000	5 h	pO_2 = 0.5 atm	
			850	5 h	pO_2 = 0.2 atm	
	(4 × 4) + (6 × 6)		900	5 h	pO_2 = 0.2 atm	
	(4 × 4)		1050	5 h	not specified	
2007 38	(√7 × √7)R19.1° + (√13 × √13)R13.9°	no	850	30 min	UHV	
2008 43	(4 × 4) + (6 × 6)	500 eV, 10 min	950	30 min	UHV	
	(5 × 5)	500 eV, 20 min	1000	30 min	UHV	
	(3 × 3)	500 eV, 10 min	1000	5 h	4.5×10^{-4} Pa O_2	
	(9/5 × 9/5)	500 eV, 10 min	1000	10 h	1 atm pure air	
	TiO(111)-(2 × 2)	sputtered (conditions not specified)	1400	not specified	UHV	
2008 45	(9/5 × 9/5) + (3 × 3) + (6 × 6)	sputtered (conditions not specified)	850–1100	0.5–10 h	O_2 + N_2/Ar	
2013 57	(4 × 4) with SrO_3 termination	1 keV/8 μA, 10 min	~900	1 h	5.5×10^{-6} Pa O_2 + Sr and Ti deposition	
	(6 × 6) with Ti termination					
	(5 × 5) with Ti termination					
2014 55	(5 × 5)	500 eV, 20 min	1050	30 min	UHV	
	(5 × 5) + (6 × 6)		1120	30 min	UHV	*
	(6 × 6)		1150	1 h	UHV	**
	(4 × 4) + (6 × 6) (larger) + disordered	500 eV, 6 min	950	30 min	UHV	
	(4 × 4) (larger) + (6 × 6)		1000–1050	1 h	UHV	*
	(4 × 4) + (6 × 6) (mainly)		1100	1 h	UHV	*

	(4 × 4) + (6 × 6)	500 eV, 6 min	950	2 h	4.5×10^{-4} Pa O_2	
	(4 × 4)		1050	not specified	4.5×10^{-4} Pa O_2	*
	(3 × 3) + (4 × 4)		1100	2 h	4.5×10^{-4} Pa O_2	*
	(3 × 3) (mainly) + (4 × 4)		1150	3 h	4.5×10^{-4} Pa O_2	*
	(2 × 2) + (3 × 3) (mainly)		1200	5 h	6.0×10^{-4} Pa O_2	*
	(2 × 2) (mainly) + (3 × 3)		1280	5 h	6.0×10^{-4} Pa O_2	*
2015 56	(4 × 4)	500 eV, 6 min	1000	1 h	UHV	
	(3 × 3)		1150	5 h	4.5×10^{-4} Pa O_2	*
	(2 × 2)		1280	5 h	6×10^{-4} Pa O_2	*
** when the treatment is in addition to the line above (i.e., NOT from a fresh sample)*						
*** when the treatment is in addition to two lines above*						

Table A.2: Summary of reported reconstructions on $SrTiO_3$(110).

Year ref.	Reconstruction	Ar^+-ion sputtering	Annealing temp. (°C)	Annealing time	Environment	
1994 80	(4 × 4)	no	780	1 h	UHV	
	(4 × 2) + (? × 3)		1000	15 h	O_2 flowing	
	(4 × 2) + (? × 4) or (4 × 4)		1100	15 h	O_2 flowing	
1995 338	~(5 × 2)	no	800	3 h	UHV	
	~(5 × 2) + ~(4 × 2)		1200	2–5 min	UHV	
	c(2 × 6)		1200	2–5 min, repeated	UHV	
1997 290	(2 × 5)	no	960	2 h	UHV	
	(3 × 4)		900	4 h	UHV	
			910	2 h	UHV	
	(4 × 7)		1120	10 min	UHV	*
	(4 × 4)		960	20 h	UHV	
	(6 × 4)	960 °C, 30 min	960	1 h	UHV	*
	(6 × 4)	900 °C, 1 h	900	30 min	UHV	**
2003 339	(1 × 1) + (1 × 2)	no	900	1 h	Air	
2004 340	(1 × 1) + (1 × 2)		1000	1 h	UHV	
2008 63	(3 × 1) + (1 × 4)	no	875	2 h	UHV	
	(4 × 1) + (3 × 1)		1100	2 h	UHV	
	(6 × 1) + (1 × 2)		1275	2 h	UHV	
** when the treatment is in addition to the line above (i.e., NOT from a fresh sample)*						
*** when the treatment is in addition to two lines above*						

Table A.3: Summary of reported reconstructions on $SrTiO_3$(001).

Year ref.	Reconstruction	Etch-ing	Ar^+-ion sputtering	Annealing temp. (°C)	Annealing time	Environ-ment	

Appendix A: Reported surface reconstructions of $SrTiO_3$ (Chapter 2)

1990 [71]	(1 × 1)	BHF, 30–60 s	no	600	1 h	5×10^{-4} Pa O_2	
1990 [72]	(1 × 1) + (2 × 2)	no	no	700	1 h	UHV	
	(2 × 2)			890	30 min	Air	
1993 [73]	(1 × 1)	no	no	800	2 min	UHV	
1993 [73] **1994** [341,342]	(√5 × √5)R26.6°	no	no	1200	2 min	UHV	
1994 [80]	(2 × 1)	no	no	750–800	1 h	HV	
	(√13 × √13)R33.7° + *c*(6 × 2)			800–1100	15 h	O_2 flowing	
1995 [74]	(1 × 1)	no	no	600	10–120 min	UHV	
	(2 × 1)			800	20–120 min	UHV	
	(2 × 1)			850–900	2 h	HV	
	(1 × 1) + (2 × 1)			850–900	10 min	HV	
	(1 × 1)			750–780	30 min	15 Pa O_2	
	(2 × 1) + (2 × 2)			900–950	30–120 min	HV	
	(2 × 2)			1000–1200	2–20 min	UHV	
1996 [343]	*c*(6 × 2)	no	no	950–1000	4–5 h	Pure O_2	
				950	2 h	UHV	
1999 [75]	(1 × 1)	BHF, 30–60 s	no	600–750	1 h	5×10^{-4} Pa O_2	
	(2 × 2)			650–730	1 h	UHV	
1999 [81]	(2 × 2)	no	no	< 700	a few h	10^{-5} Pa O_2	
1999 [76]	(2 × 1)	no	no	950	2 h	UHV	
	c(4 × 2)			950	2 h	10^{-5}–10^{-3} Pa H_2	
	(1 × 1)			750	not specified	UHV	
	(2 × 1)			950	2 h	5×10^{-5} Pa H_2	*
	c(6 × 2)			1000	3 h	O_2 flowing	
				950	2 h	5×10^{-5} Pa H_2	
	c(6 × 2)			1000	3 h	O_2 flowing	
				950	2 h	UHV	
2000 [77]	(1 × 1)	no	sputtered (conditions not specified)	630	not specified	1×10^{-4} Pa O_2	
2001 [78]	(1 × 1)	BHF, 10 min	no	800	2 min	UHV	
	(√5 × √5)R26.6°			1200	2 min	UHV	
2002 [69]	(1 × 1)	BHF, 10 min	no	600	30 min	UHV	
	(1 × 2) + (2 × 1)			600–900	30 min	UHV	
	c(4 × 4) + (2 × 1)			900–1400	≥ 30 min	UHV	*
	c(4 × 2)	BHF, 10 min	500 eV, 10 min	900–1400	15 min	UHV	
2002 [85]	*c*(4 × 2)	BHF, 10 min	500 eV, 10 min	750	15 min	UHV	
				860	5 min	UHV	*

	(6 × 2) (nanolines) + *c*(4 × 2)			870–970	10–30 min	UHV	*
	(6 × 2) (nanolines) + nanodots			890–1000	10–33 min	UHV	*
	c(4 × 2)			1235	3 min	UHV	*
2002 344	(2 × 1)	no	4.8 kV ion milled	950–1000	not specified	O_2 flowing	
2003 87	*c*(4 × 2)	no	4.8 kV ion milled	850–930	not specified	O_2 flowing	
2003 82	*c*(4 × 4) + (2 × 2)	BHF, 10 min	no	1000	20 min	UHV	
	(4 × 4)			1150	several s	UHV	*
	(4 × 4) + (√5 × √5)R26.6°			1180	several s	UHV	*
	(√5 × √5)R26.6°			1200	several s	UHV	*
	(√13 × √13)R33.7°			1250	several s	UHV	*
2004 92	(6 × 2) + (9 × 2) (nanolines)	no	3 keV	875	20 h	UHV	
	TiO_2(001) (anatase)-(1 × 4) + (1 × 5)			1200	1 h	UHV	*
2006 84	(2 × 1)	no	0.5–3.0 keV, 7–15 min	800	30 min	UHV	
	(6 × 2) (dilines)			850	30 min	UHV	*
	(6 × 2) (meta-dilines)			1000	30 min	UHV	*
	(9 × 2) (trilines)		0.5–3.0 keV, 7–15 min	950	30 min	UHV	
	(12 × 2) (tetralines)			1000	> 1 h	UHV	
	(6 × 8)			950	30 min, repeatedly	UHV	*
	(7 × 4) (crossdots, or nanodots)		0.5–3.0 keV, 7–15 min	930–970	30 min, repeatedly	UHV	
2006 83	(2 × 2)	BHF	no	950	2 h	UHV	
	(2 × 2) with dotted row structures			1030	1 h	UHV	*
	c(4 × 4)			1030	1 h	UHV	*
2006 86	*c*(4 × 2) + (6 × 2) (dilines)	no	500 eV, 10 min	800	> 6 h	UHV	
	(6 × 2) (dilines)			825	24 h	UHV	
	(9 × 2) (trilines)			> 825	> 2 days	UHV	
	(6 × 8)			> 825	> 4 days	UHV	
2007 93	*c*(4 × 4)	no	no	1000	1 h	UHV	
	(√5 × √5)R26.6°			1350	> 80 min	UHV	*
	(√5 × √5)R26.6° (highly ordered)			1400–1500	5–15 min	UHV	*
2007 345	*c*(4 × 2)	no	no	925–1115	1 h	1.5×10^{-6} Pa H_2	
	(4√2 × √2)R45° (mainly) + (2 × 2) overlayer	no	no	700	10 h	O_2 flowing	
	(4√2 × √2)R45° + (2 × 2) overlayer + *c*(6 × 2)	no	no	900	10 h	O_2 flowing	
	c(6 × 2) + (4 × 4)			1100	10 h	O_2 flowing	
	c(4√2 × 2√2)R45°			1000	1 h	UHV	*
	c(4 × 4)			1200	1 h	UHV	*
	(4√2 × √2)R45°			1000	10 h	Artificial air (N_2 + O_2)	
	c(4 × 4)			1200	1 h	UHV	*
** when the treatment is in addition to the line above (i.e., NOT from a fresh sample)*							

Appendix B: Derivations of equations in Chapters 6 and 7

The equations in Chapters 6 and 7 are concerned with the geometries and surface/interface energies of gold monolayers and nanocrystals.

B.1 Gold monolayers

For a monolayer, its total energy E_{m} is the sum of its terrace energy, interfacial energy, and edge energy, i.e.,

$$\boldsymbol{E_{\mathbf{m}}} = \gamma_{\mathrm{m}} \cdot A_{\mathrm{m}} + \gamma^{*} \cdot A_{\mathrm{m}} + \gamma_{\mathrm{e}} \cdot A_{\mathrm{e}}$$

$$= (\gamma_{\mathrm{m}} + \gamma^{*}) \cdot A_{\mathrm{m}} + \gamma_{\mathrm{e}} \cdot A_{\mathrm{e}}$$

$$= (\boldsymbol{\gamma_{\mathbf{m}}} + \boldsymbol{\gamma^{*}}) \cdot \frac{\boldsymbol{V}}{\boldsymbol{d_{111}}} + \boldsymbol{\gamma_{\mathbf{e}}} \cdot \boldsymbol{A_{\mathbf{e}}}. \qquad \textbf{(6.2)}$$

The last step makes use of $A_{\mathrm{m}} = \frac{V}{d_{111}}$, i.e., it is assumed that the monolayer thickness is d_{111} = the interplanar distance between adjacent Au(111) planes = 0.235 nm. All terms in equation (6.2) are defined section 6.3.

Other equations in Chapters 6 and 7 are all related to the Wulff and growth shapes of gold crystals, which will be derived below. To present a clear and systematic picture of the crystal geometries, the equations will be derived in a different order from their appearance in the main text, but they will all be clearly numbered and written in bold font.

B.2 (111)-based gold crystals

B.2.1 Wulff construction

It is helpful to start with the Wulff construction of a free-standing gold crystal (Figure B.1) and define the angles α and β: α is the acute angle between a {111} and a {001} plane and β is the angle between two {111} planes. It follows that $\cos\alpha = \frac{1}{\sqrt{3}}$, $\sin\alpha = \sqrt{\frac{2}{3}}$, $\cos\beta = \frac{1}{3}$, and $\sin\beta = \frac{2\sqrt{2}}{3}$, which will be used a few times later. The distance l is the width across the top (111) facet measured from the middle of one {001} side facet to the middle of the opposite {111} side facet. The distance s is the width of a {001} facet, as defined earlier in Figure 7.4.

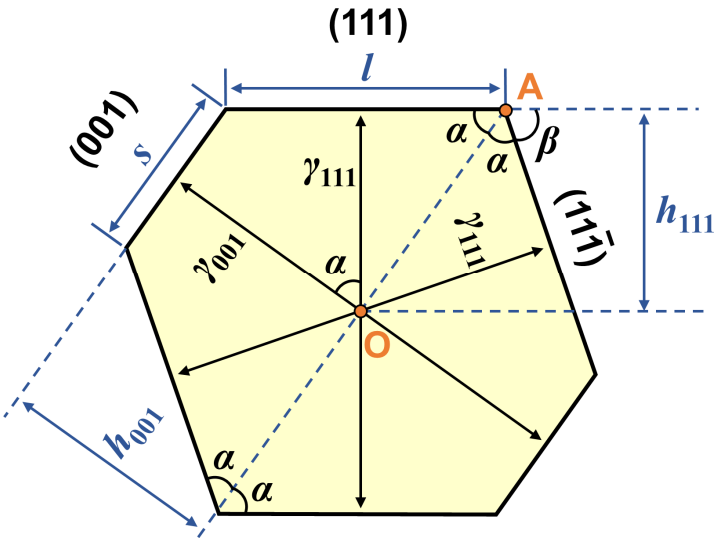

Figure B.1: Wulff construction of a free-standing fcc gold crystal, where O = Wulff point.

As mentioned in Chapter 2 (section 2.3.2), in a Wulff crystal, the perpendicular distance of a crystal surface from the Wulff point (h_{hkl}) is proportional to the surface energy per unit area of that surface (γ_{hkl}).[202] For the Wulff crystal in Figure B.1,

$$\frac{\gamma_{111}}{\gamma_{001}} = \frac{h_{111}}{h_{001}}, \tag{B.1}$$

where

$$h_{111} = \mathrm{OA} \cdot \sin\alpha = \left(l \cdot \cos\alpha + \frac{s}{2}\right) \cdot \sin\alpha = \frac{\sqrt{2}}{3} l + \frac{s}{\sqrt{6}}, \tag{B.2}$$

$$h_{001} = l \cdot \sin\alpha = \sqrt{\frac{2}{3}} l. \tag{B.3}$$

Substituting equations (B.2) and (B.3) into equation (B.1) gives

$$\frac{\gamma_{111}}{\gamma_{001}} = \frac{1}{\sqrt{3}} + \frac{s}{2l}. \tag{B.4}$$

B.2.2 Hexagon Wulff

A substrate-supported gold crystal adopts a 'hexagonal' shape when it has (111) top and base facets and {111} and {001} side facets. A cross section of a hexagonal crystal is illustrated in Figure B.2a in orange, with a crystal height of h. For {111} and {001} facets to be exposed in addition to {111}, i.e., $s > 0$, it has to be satisfied that $1 < \frac{\gamma_{001}}{\gamma_{111}} < \sqrt{3}$, as can be deduced from equation (B.4). Most of the crystals observed in my experiments have a height of between h_1 and h_2, as labelled in Figure B.2.

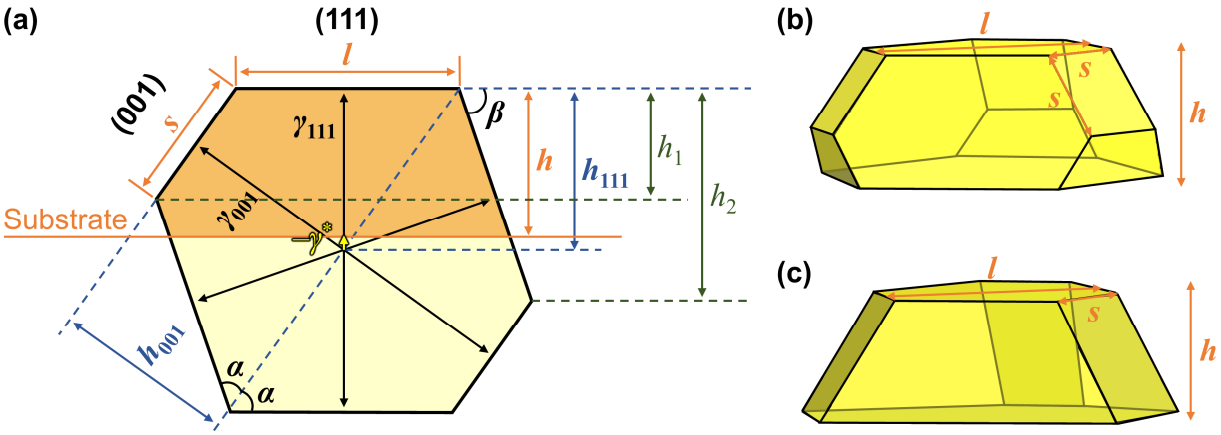

Figure B.2: Supported hexagonal gold crystal. (a) The Winterbottom construction of the supported crystal (in orange) and the 3D (b) Wulff and (c) growth shapes of the crystal.

From geometry,

$$h_1 = s \cdot \sin\alpha = \sqrt{\frac{2}{3}}s, \tag{B.5}$$

$$h_2 = l \cdot \sin\beta = \frac{2\sqrt{2}}{3}l. \tag{B.6}$$

Surface areas and volume

Figure B.2b shows a 3D sketch of the Wulff shape of a hexagonal crystal. Before its surface/interface energies are analysed, it is useful to write out the expressions for its surface areas (*A*) and volume (*V*). Its area terms include A_{001} = the total area of its {001} facets (three square side facets), A_{111} = the total area of its {111} facets (a truncated triangular top facet and six side facets), and A_i = its interfacial area with the substrate (a truncated triangle).

From geometry, its areas and volume can be written out as functions of the dimensions *l*, *s*, and *h*. Next, the variable *s* can be eliminated by expressing *s* as a function of *l* according to equation (B.4). The variable *h* can also be eliminated by introducing a useful ratio $k = \frac{h}{l}$, so that *h* is replaced by *kl*. Following these steps, we obtain

$$A_{001} = 12l^2\left(\frac{\gamma_{111}}{\gamma_{001}} - \frac{1}{\sqrt{3}}\right)^2, \tag{B.7}$$

$$A_{111} = l^2\left[24\frac{\gamma_{111}}{\gamma_{001}} - 4\sqrt{3} - 11\sqrt{3}\left(\frac{\gamma_{111}}{\gamma_{001}}\right)^2 + \frac{9}{\sqrt{2}}\frac{\gamma_{111}}{\gamma_{001}}k\right], \tag{B.8}$$

$$A_i = l^2\left[\sqrt{3}\left(\frac{\gamma_{111}}{\gamma_{001}}\right)^2 - \frac{3\sqrt{3}}{4}k^2 + \frac{3}{\sqrt{2}}\frac{\gamma_{111}}{\gamma_{001}}k\right], \tag{B.9}$$

$$V = l^3\left[\frac{4}{3}\sqrt{\frac{2}{3}} - 4\sqrt{2}\frac{\gamma_{111}}{\gamma_{001}} + 4\sqrt{6}\left(\frac{\gamma_{111}}{\gamma_{001}}\right)^2 - 4\sqrt{2}\left(\frac{\gamma_{111}}{\gamma_{001}}\right)^3 + \sqrt{3}\left(\frac{\gamma_{111}}{\gamma_{001}}\right)^2 k + \frac{3}{2\sqrt{2}}\frac{\gamma_{111}}{\gamma_{001}}k^2 - \frac{\sqrt{3}}{4}k^3\right]. \tag{B.10}$$

Finding the equilibrium ratio *k*

In Figure B.2a, according to the Winterbottom construction,[206]

$$\frac{-\gamma^*}{\gamma_{111}} = \frac{h_{111} - h}{h_{111}}. \tag{B.11}$$

Rearranging equation (B.11) to make γ^* the subject and combing the result with equations (B.1) and (B.3) will give

$$\gamma^* = \sqrt{\frac{3}{2}}\frac{h}{l}\gamma_{001} - \gamma_{111}, \tag{B.12}$$

where $\frac{h}{l} = k$. Therefore, equation (B.12) can be rearranged to give

$$k = \sqrt{\frac{2}{3}}\frac{\gamma^* + \gamma_{111}}{\gamma_{001}}. \tag{B.13}$$

Equation (B.13) can also be worked out by noting that for a crystal with a given volume, its total surface/interface energy (E_c) is minimised. E_c of the hexagon in Figure B.2b is given by

$$E_c = \gamma_{001}A_{001} + \gamma_{111}A_{111} + \gamma^* A_i. \tag{B.14}$$

Differentiating E_c with respect to k gives

$$\frac{dE_c}{dk} = \gamma_{001}\frac{dA_{001}}{dk} + \gamma_{111}\frac{dA_{111}}{dk} + \gamma^*\frac{dA_i}{dk}. \tag{B.15}$$

Since A_{001}, A_{111}, and A_{i} are functions of the variables l and k, as shown earlier in equations (B.7)–(B.9), it follows that the terms $\frac{\mathrm{d}A_{001}}{\mathrm{d}k}$, $\frac{\mathrm{d}A_{111}}{\mathrm{d}k}$, and $\frac{\mathrm{d}A_{\mathrm{i}}}{\mathrm{d}k}$ are functions of l, k, and $\frac{\mathrm{d}l}{\mathrm{d}k}$. The variable $\frac{\mathrm{d}l}{\mathrm{d}k}$ can be eliminated by the following steps: (i) differentiating the crystal volume, i.e., equation (B.10) with respect to k, which gives an expression for $\frac{\mathrm{d}V}{\mathrm{d}k}$ as a function of l, k, and $\frac{\mathrm{d}l}{\mathrm{d}k}$, i.e., $\frac{\mathrm{d}V}{\mathrm{d}k} = f(l, k, \frac{\mathrm{d}l}{\mathrm{d}k})$; (ii) equating $f(l, k, \frac{\mathrm{d}l}{\mathrm{d}k})$ to zero because for a crystal with a given volume, $\frac{\mathrm{d}V}{\mathrm{d}k}$ = 0; (iii) rearranging the result to make $\frac{\mathrm{d}l}{\mathrm{d}k}$ the subject, which gives us $\frac{\mathrm{d}l}{\mathrm{d}k} = f(l, k)$; (iv) substituting $\frac{\mathrm{d}l}{\mathrm{d}k} = f(l, k)$ into equation (B.15), to obtain $\frac{\mathrm{d}E_{\mathrm{c}}}{\mathrm{d}k} = f(l, k)$. Finally, equating $\frac{\mathrm{d}E_{\mathrm{c}}}{\mathrm{d}k} = f(l, k)$ to zero and rearranging the result to make k the subject will lead to equation (B.13).

Expressing $E_{\text{hexagon Wulff}}$ as $\alpha_{\text{hexagon Wulff}}V^{\frac{2}{3}}$

Substituting equations (B.7)–(B.9) into equation (B.14) gives us an expression for E_{c} in terms of l and k below, in which E_{c} is also replaced by $E_{\text{hexgon Wulff}}$ to be specific:

$$E_{\text{hexgon Wulff}} = \gamma_{001} \cdot 12l^2 \left(\frac{\gamma_{111}}{\gamma_{001}} - \frac{1}{\sqrt{3}}\right)^2 + \gamma_{111} \cdot l^2 \left[24\frac{\gamma_{111}}{\gamma_{001}} - 4\sqrt{3} - 11\sqrt{3}\left(\frac{\gamma_{111}}{\gamma_{001}}\right)^2 + \frac{9}{\sqrt{2}}\frac{\gamma_{111}}{\gamma_{001}}k\right]$$
$$+ \gamma^* \cdot l^2 \left[\sqrt{3}\left(\frac{\gamma_{111}}{\gamma_{001}}\right)^2 - \frac{3\sqrt{3}}{4}k^2 + \frac{3}{\sqrt{2}}\frac{\gamma_{111}}{\gamma_{001}}k\right]. \quad \text{(B.16)}$$

The variable l can be eliminated by rearranging equation (B.10) to make l^2 the subject and substituting $l^2 = f(V, k)$ into equation (B.16). The variable k can then be eliminated by substituting equation (B.13) into equation (B.16). These steps result in an expression for $E_{\text{hexgon Wulff}}$ in terms of the variable V only – other remaining symbols are all constants: γ_{111}, γ_{001}, and γ^*: $E_{\text{hexgon Wulff}} = \alpha_{\text{hexagon Wulff}}V^{\frac{2}{3}}$. The expression for $\alpha_{\text{hexagon Wulff}}$ is equation (7.6) in Chapter 7:

$$\alpha_{\text{hexagon Wulff}} = 3\cdot 2^{-\frac{2}{3}}\left(8\gamma_{001}^3 - 24\sqrt{3}\gamma_{001}^2\gamma_{111} + 72\gamma_{001}\gamma_{111}^2 - 16\sqrt{3}\gamma_{111}^3 + 9\sqrt{3}\gamma_{111}^2\gamma^* - \sqrt{3}\gamma^{*3}\right)^{\frac{1}{3}}. \quad \textbf{(7.6)}$$

B.2.3 Hexagon growth

Surface areas and volume

The growth shape of a hexagonal crystal is sketched in Figure B.2c. Its area terms include A_{001} = the total area of its {001} facets (three rectangular side facets), A_{111} = the total area of its {111} facets (a truncated triangular top facet and three trapezium side facets), and A_i = its interfacial area with the substrate (a truncated triangle). From geometry and the mathematical steps described in section B.2.2, its areas (A) and volume (V) are given by

$$A_{001} = 3\sqrt{6}kl^2\left(\frac{\gamma_{111}}{\gamma_{001}} - \frac{1}{\sqrt{3}}\right), \quad \text{(B.17)}$$

$$A_{111} = l^2\left[\frac{9\sqrt{3}}{8}k^2 + 3\sqrt{6}k - \frac{9}{\sqrt{2}}\frac{\gamma_{111}}{\gamma_{001}}k + 6\frac{\gamma_{111}}{\gamma_{001}} - 2\sqrt{3}\left(\frac{\gamma_{111}}{\gamma_{001}}\right)^2 - \sqrt{3}\right], \quad \text{(B.18)}$$

$$A_i = l^2\left[\frac{3\sqrt{3}}{8}k^2 + \frac{3}{\sqrt{2}}\frac{\gamma_{111}}{\gamma_{001}}k + 6\frac{\gamma_{111}}{\gamma_{001}} - 2\sqrt{3}\left(\frac{\gamma_{111}}{\gamma_{001}}\right)^2 - \sqrt{3}\right], \quad \text{(B.19)}$$

$$V = kl^3\left[-2\sqrt{3}\left(\frac{\gamma_{111}}{\gamma_{001}}\right)^2 + \frac{\sqrt{3}}{8}k^2 + \frac{3}{2\sqrt{2}}\frac{\gamma_{111}}{\gamma_{001}}k + 6\frac{\gamma_{111}}{\gamma_{001}} - \sqrt{3}\right]. \quad \text{(B.20)}$$

Finding the equilibrium ratio *k*

The Winterbottom construction does not apply to the growth shape of a hexagonal crystal, but the equilibrium value of $k = \frac{h}{l}$ can still be found by minimising E_c. It is the same procedure as that described in section B.2.2, starting with equations (B.14) and (B.15), noting that the

expressions for A_{001}, A_{111}, and A_i in this case are described by equations (B.17)–(B.19) above. The final expression for k is the same as that for the Wulff shape, i.e., equation (B.13).

Expressing $E_{\text{hexagon growth}}$ as $\alpha_{\text{hexagon growth}}V^{\frac{2}{3}}$

Substituting equations (B.17)–(B.19) into equation (B.14) gives an expression for E_c or $E_{\text{hexagon growth}}$ in terms of l and k:

$$E_{\text{hexagon growth}} = \gamma_{001} \cdot 3\sqrt{6}kl^2\left(\frac{\gamma_{111}}{\gamma_{001}} - \frac{1}{\sqrt{3}}\right) + \gamma_{111} \cdot l^2\left[\frac{9\sqrt{3}}{8}k^2 + 3\sqrt{6}k - \frac{9}{\sqrt{2}}\frac{\gamma_{111}}{\gamma_{001}}k + 6\frac{\gamma_{111}}{\gamma_{001}} - 2\sqrt{3}\left(\frac{\gamma_{111}}{\gamma_{001}}\right)^2 - \sqrt{3}\right] + \gamma^* \cdot l^2\left[\frac{3\sqrt{3}}{8}k^2 + \frac{3}{\sqrt{2}}\frac{\gamma_{111}}{\gamma_{001}}k + 6\frac{\gamma_{111}}{\gamma_{001}} - 2\sqrt{3}\left(\frac{\gamma_{111}}{\gamma_{001}}\right)^2 - \sqrt{3}\right]. \quad \text{(B.21)}$$

The variable l can be eliminated by rearranging equation (B.20) to make l^2 the subject and substituting $l^2 = f(V,k)$ into equation (B.21). The variable k can then be eliminated by substituting equation (B.13) into equation (B.21). These steps result in an expression of the form $E_{\text{hexgon Wulff}} = \alpha_{\text{hexagon Wulff}}V^{\frac{2}{3}}$, where $\alpha_{\text{hexagon Wulff}}$ is given by

$$\boldsymbol{\alpha_{\text{hexagon growth}} = \frac{3}{2}\left\{(\gamma_{111} + \gamma^*)\left[72\gamma_{001}\gamma_{111} - 12\sqrt{3}\gamma_{001}^2 + \sqrt{3}(\gamma^{*2} + 8\gamma_{111}\gamma^* - 17\gamma_{111}^2)\right]\right\}^{\frac{1}{3}}}. \quad \textbf{(7.7)}$$

B.2.4 Fixed-*h* hexagon

Hexagonal crystals need to be assumed to adopt fixed heights rather than their equilibrium aspect ratio when the energies of few-layer gold crystals (bilayer, trilayer, etc.) are studied in

Chapter 6 (section 6.3). For these flat crystals, it is likely that $h \leq \sqrt{\frac{2}{3}}s$, i.e., they are not sufficiently high to have any reentrant facets. Even if $h > \sqrt{\frac{2}{3}}s$, which, in theory, is possible for trilayer and higher crystals, the crystals are likely to adopt the growth shape, as discussed in section 7.2.4. Therefore $h \leq \sqrt{\frac{2}{3}}s$ is assumed in the subsequent analysis in this section.

Volume

The volume expression for a fixed-height hexagonal crystal is a modified version of equation (B.20), without the term $k = \frac{h}{l}$ being introduced since h is a constant. The volume is

$$V = h\left[-2\sqrt{3}\left(\frac{\gamma_{111}}{\gamma_{001}}\right)^2 l^2 + \frac{\sqrt{3}}{8}h^2 + \frac{3}{2\sqrt{2}}\frac{\gamma_{111}}{\gamma_{001}}hl + 6\frac{\gamma_{111}}{\gamma_{001}}l^2 - \sqrt{3}l^2\right]. \qquad \text{(B.22)}$$

Finding $E_{\text{fixed } h}$

Similarly, the energy expression for a fixed-height hexagonal crystal is a modified version of equation (B.21) without the k term being introduced:

$$\begin{aligned} E_{\text{fixed } h} = {} & \gamma_{001} \cdot 3\sqrt{6}\left(\frac{\gamma_{111}}{\gamma_{001}} - \frac{1}{\sqrt{3}}\right)hl \\ & + \gamma_{111}\left[\frac{9\sqrt{3}}{8}h^2 + 3\sqrt{6}hl - \frac{9}{\sqrt{2}}\frac{\gamma_{111}}{\gamma_{001}}hl + 6\frac{\gamma_{111}}{\gamma_{001}}l^2 - 2\sqrt{3}\left(\frac{\gamma_{111}}{\gamma_{001}}\right)^2 l^2 - \sqrt{3}l^2\right] \\ & + \gamma^*\left[\frac{3\sqrt{3}}{8}h^2 + \frac{3}{\sqrt{2}}\frac{\gamma_{111}}{\gamma_{001}}hl + 6\frac{\gamma_{111}}{\gamma_{001}}l^2 - 2\sqrt{3}\left(\frac{\gamma_{111}}{\gamma_{001}}\right)^2 l^2 - \sqrt{3}l^2\right]. \end{aligned} \qquad \text{(B.23)}$$

To eliminate the variable l in equation (B.23), we can rearrange equation (B.22) to give a quadratic equation of l:

$$\left[-2\sqrt{3}\left(\frac{\gamma_{111}}{\gamma_{001}}\right)^2+6\frac{\gamma_{111}}{\gamma_{001}}-\sqrt{3}\right]l^2+\left(\frac{3}{2\sqrt{2}}\frac{\gamma_{111}}{\gamma_{001}}h\right)l+\left(\frac{\sqrt{3}}{8}h^2-\frac{V}{h}\right)=0. \tag{B.24}$$

Solving equation (B.24) for l and selecting the possible root will give

$$l=\frac{3\frac{\gamma_{111}}{\gamma_{001}}h-\left[33\left(\frac{\gamma_{111}}{\gamma_{001}}\right)^2h^2-64\sqrt{3}\left(\frac{\gamma_{111}}{\gamma_{001}}\right)^2\frac{V}{h}-24\sqrt{3}\frac{\gamma_{111}}{\gamma_{001}}h^2+192\frac{\gamma_{111}}{\gamma_{001}}\frac{V}{h}+12h^2-32\sqrt{3}\frac{V}{h}\right]^{\frac{1}{2}}}{4\sqrt{2}\left[2\sqrt{3}\left(\frac{\gamma_{111}}{\gamma_{001}}\right)^2-6\frac{\gamma_{111}}{\gamma_{001}}+\sqrt{3}\right]}. \tag{B.25}$$

Note that to tell the signs of the two roots, the values γ_{111} = 1.3 J m^{-2} and γ_{001} = 1.6 J m^{-2} are assumed.[331] Substituting equation (B.25) into (B.23) and simplifying it give us equation (6.3) in Chapter 6:

$$\boldsymbol{E_{\text{fixed }h}=\frac{\begin{array}{l}V\left(64\gamma_{111}^5-128\gamma_{001}^2\gamma_{111}^3-128\gamma_{001}^2\gamma_{111}^2\gamma^*+16\gamma_{001}^4\gamma_{111}+16\gamma_{001}^4\gamma^*+\right.\\ \left.64\gamma_{111}^4\gamma^*\right)+h^3\left(22\sqrt{3}\gamma_{111}^5+18\gamma_{001}\gamma_{111}^4-29\sqrt{3}\gamma_{001}^2\gamma_{111}^3+4\sqrt{3}\gamma_{001}^4\gamma_{111}+\right.\\ 4\sqrt{3}\gamma_{001}^4\gamma^*+22\sqrt{3}\gamma_{111}^4\gamma^*+18\gamma_{001}\gamma_{111}^3\gamma^*-29\sqrt{3}\gamma_{001}^2\gamma_{111}^2\gamma^*\left.\right)+h^2\left(4\sqrt{3}\gamma_{001}^5-\right.\\ 6\gamma_{001}^2\gamma_{111}^3+14\sqrt{3}\gamma_{001}\gamma_{111}^4-33\sqrt{3}\gamma_{001}^3\gamma_{111}^2-6\gamma_{001}^2\gamma_{111}^2\gamma^*-2\sqrt{3}\gamma_{001}\gamma_{111}^3\gamma^*-\\ \left.\sqrt{3}\gamma_{001}^3\gamma_{111}\gamma^*\right)\left[12h^2-32\sqrt{3}\frac{V}{h}-24\sqrt{3}\frac{\gamma_{111}}{\gamma_{001}}h^2+192\frac{\gamma_{111}}{\gamma_{001}}\frac{V}{h}+33\left(\frac{\gamma_{111}}{\gamma_{001}}\right)^2h^2+\right.\\ \left.64\sqrt{3}\left(\frac{\gamma_{111}}{\gamma_{001}}\right)^2\frac{V}{h}\right]^{\frac{1}{2}}\end{array}}{16h(\gamma_{001}^4-8\gamma_{001}^2\gamma_{111}^2+4\gamma_{111}^4)}}. \tag{6.3}$$

B.2.5 Triangle Wulff

For a 'hexagonal' crystal, its top facet becomes 'triangular' if no {001} facets are exposed. This is possible when $\frac{\gamma_{001}}{\gamma_{111}}\geq\sqrt{3}$ – substituting $\gamma_{001}=\sqrt{3}\gamma_{111}$ into equation (B.4) returns s = 0. A cross section of a triangular crystal is illustrated in Figure B.3a in orange, with a crystal height of h.

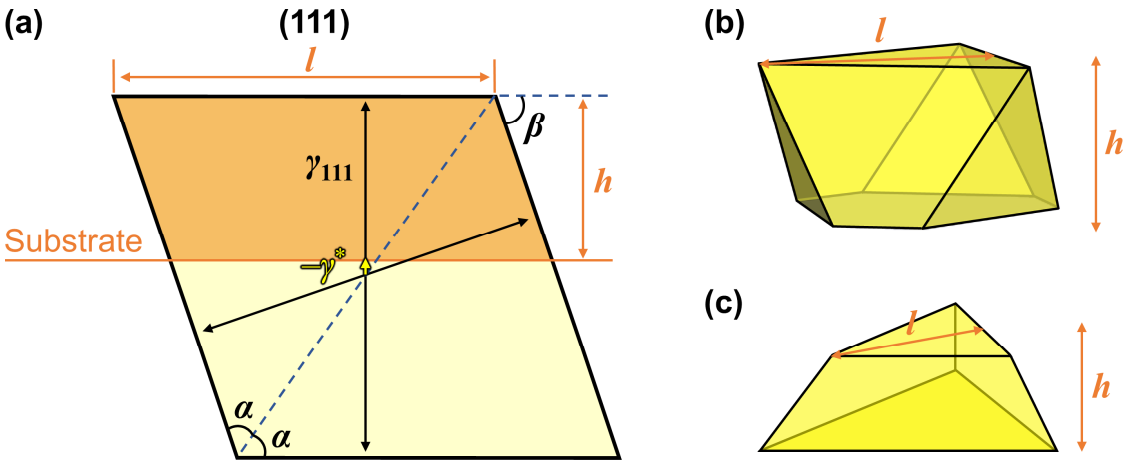

Figure B.3: Supported triangular gold crystal. (a) The Winterbottom construction of the supported crystal (in orange) and the 3D (b) Wulff and (c) growth shapes of the crystal.

Surface areas and volume

The Wulff shape of a triangular crystal is sketched in Figure B.3b. Its total {111} area A_{111} covers an equilateral-triangular top facet and six side facets. Its interfacial area A_i with the substrate has a truncated triangular shape. From geometry, its surface areas (A) and volume (V) are given by functions of l and k, where $k = \frac{h}{l}$:

$$A_{111} = l^2\left(\frac{1}{\sqrt{3}} + 3\sqrt{\frac{3}{2}}k\right), \tag{B.26}$$

$$A_i = l^2\left(\frac{1}{\sqrt{3}} + \sqrt{\frac{3}{2}}k - \frac{3\sqrt{3}}{4}k^2\right), \tag{B.27}$$

$$V = kl^3\left(\frac{1}{\sqrt{3}} + \frac{1}{2}\sqrt{\frac{3}{2}}k - \frac{\sqrt{3}}{4}k^2\right). \tag{B.28}$$

Equations (B.26)–(B.28) can also be obtained by substituting $\gamma_{001} = \sqrt{3}\gamma_{111}$ into equations (B.8)–(B.10). Also, substituting $\gamma_{001} = \sqrt{3}\gamma_{111}$ into equation (B.7) gives $A_{001} = 0$, as expected.

Finding the equilibrium ratio *k*

The derivation of k for a hexagonal crystal (section B.2.2) also applies to a triangular crystal, i.e., it can be done either from the Winterbottom construction (Figure B.3a) or by minimising E_c. For a triangular crystal,

$$k = \frac{\sqrt{2}}{3}\frac{\gamma^* + \gamma_{111}}{\gamma_{111}}, \tag{B.29}$$

which is the same as equation (B.13), noting that $\gamma_{001} = \sqrt{3}\gamma_{111}$.

Expressing $E_{\text{triangle Wulff}}$ as $\alpha_{\text{triangle Wulff}}V^{\frac{2}{3}}$

Substituting $A_{001} = 0$ and equations (B.26), (B.27) into equation (B.14) gives an expression for E_c or $E_{\text{triangle Wulff}}$ in terms of l and k:

$$E_{\text{triangle Wulff}} = \gamma_{111} \cdot l^2\left(\frac{1}{\sqrt{3}} + 3\sqrt{\frac{3}{2}}k\right) + \gamma^* \cdot l^2\left(\frac{1}{\sqrt{3}} + \sqrt{\frac{3}{2}}k - \frac{3\sqrt{3}}{4}k^2\right). \tag{B.30}$$

The variable l can be eliminated by rearranging equation (B.28) to make l^2 the subject and substituting $l^2 = f(V,k)$ into equation (B.30). The variable k can then be eliminated by substituting equation (B.29) into equation (B.30). These steps result in an expression of the form $E_{\text{triangle Wulff}} = \alpha_{\text{triangle Wulff}}V^{\frac{2}{3}}$, where $\alpha_{\text{triangle Wulff}}$ is given by

$$\boldsymbol{\alpha_{\text{triangle Wulff}} = 3^{\frac{7}{6}}\cdot 2^{-\frac{2}{3}}\left(8\gamma_{111}^3 + 9\gamma_{111}^2\gamma^* - \gamma^{*3}\right)^{\frac{1}{3}}.} \tag{7.1}$$

Equation (7.1) can also be obtained by substituting $\gamma_{001} = \sqrt{3}\gamma_{111}$ into equation (7.6).

B.2.6 Triangle growth

Surface areas and volume

The growth shape of a triangular crystal is sketched in Figure B.3c. For such a crystal (a truncated tetrahedron), A_{111} = the total area of its {111} facets (an equilateral-triangular top facet and three trapezium side facets) and A_{i} = its interfacial area with the substrate (an equilateral triangle). From geometry,

$$A_{111} = l^2\left(\frac{1}{\sqrt{3}} + 3\sqrt{\frac{3}{2}}k + \frac{9\sqrt{3}}{8}k^2\right), \tag{B.31}$$

$$A_{\mathrm{i}} = l^2\left(\frac{1}{\sqrt{3}} + \sqrt{\frac{3}{2}}k + \frac{3\sqrt{3}}{8}k^2\right), \tag{B.32}$$

$$V = kl^3\left(\frac{1}{\sqrt{3}} + \frac{1}{2}\sqrt{\frac{3}{2}}k + \frac{\sqrt{3}}{8}k^2\right). \tag{B.33}$$

Equations (B.31)–(B.33) can also be obtained by substituting $\gamma_{001} = \sqrt{3}\gamma_{111}$ into equations (B.18)–(B.20). Also, substituting $\gamma_{001} = \sqrt{3}\gamma_{111}$ into equation (B.17) gives $A_{001} = 0$, as expected.

Finding the equilibrium ratio *k*

The growth shape of a triangular crystal is the no-{001} version of the growth shape of a hexagonal crystal. Therefore, the equilibrium ratio k is obtained by substituting $\gamma_{001} = \sqrt{3}\gamma_{111}$ into equation (B.13). The result is the same as equation (B.29).

Expressing $E_{\text{triangle growth}}$ as $\alpha_{\text{triangle growth}}V^{\frac{2}{3}}$

Substituting $A_{001} = 0$ and equations (B.31), (B.32) into equation (B.14) gives an expression for E_c or $E_{\text{triangle growth}}$ in terms of l and k:

$$E_{\text{triangle growth}} = \gamma_{111} \cdot l^2 \left(\frac{1}{\sqrt{3}} + 3\sqrt{\frac{3}{2}}k + \frac{9\sqrt{3}}{8}k^2 \right) + \gamma^* \cdot l^2 \left(\frac{1}{\sqrt{3}} + \sqrt{\frac{3}{2}}k + \frac{3\sqrt{3}}{8}k^2 \right). \quad \text{(B.34)}$$

The variable l can be eliminated by rearranging equation (B.33) to make l^2 the subject and substituting $l^2 = f(V, k)$ into equation (B.34). The variable k can then be eliminated by substituting equation (B.29) into equation (B.34). These steps result in an expression of the form $E_{\text{triangle growth}} = \alpha_{\text{triangle growth}} V^{\frac{2}{3}}$, where $\alpha_{\text{triangle growth}}$ is given by

$$\boldsymbol{\alpha_{\text{triangle growth}} = \frac{3}{2}\left[\sqrt{3}\left(19\gamma_{111}^3 + 27\gamma_{111}^2\gamma^* + 9\gamma_{111}\gamma^{*2} + \gamma^{*3}\right)\right]^{\frac{1}{3}}.} \quad \textbf{(7.2)}$$

Equation (7.2) can also be obtained by substituting $\gamma_{001} = \sqrt{3}\gamma_{111}$ into equation (7.7).

B.3 (001)-based gold crystals

B.3.1 Pyramid Wulff

A substrate-supported gold crystal adopts a pyramidal shape when it has a (001) base. A cross section of a pyramidal crystal is illustrated in Figure B.4a in orange, with a crystal height of h. Its crystal length l is defined as the length of the basal square. Here it is assumed that $\frac{\gamma_{001}}{\gamma_{111}} \geq \sqrt{3}$ and no {001} facets are exposed.

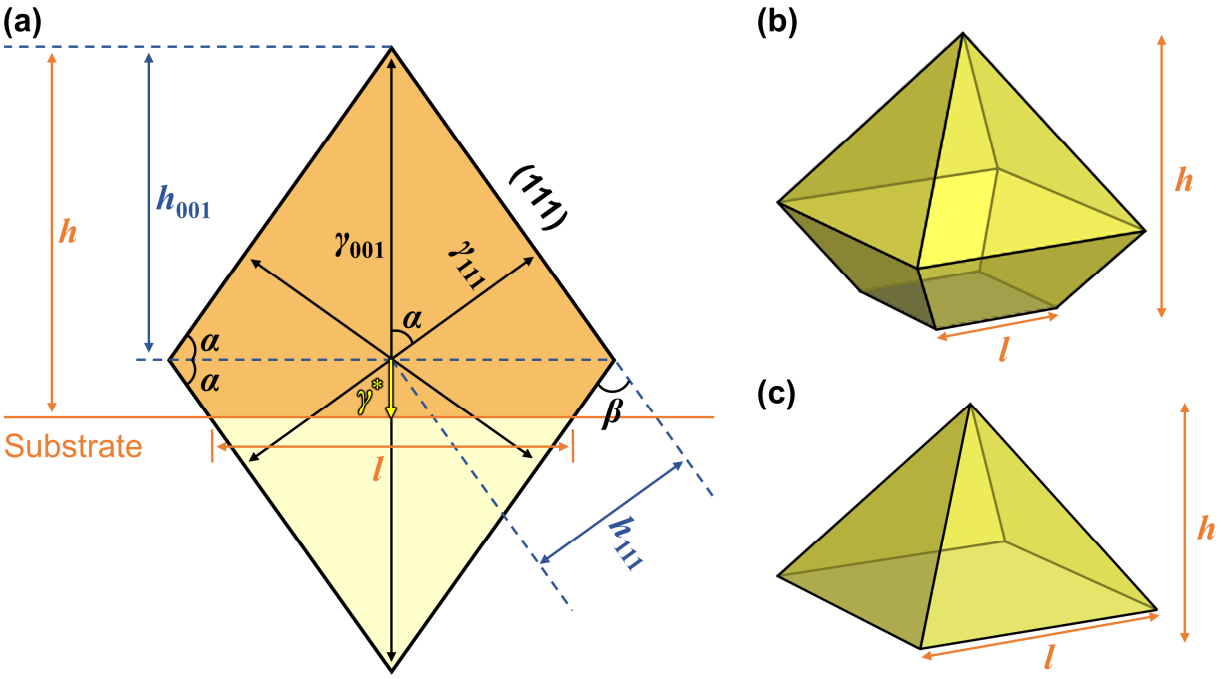

Figure B.4: Supported pyramidal gold crystal. (a) The Winterbottom construction of the supported crystal (in orange) and the 3D (b) Wulff and (c) growth shapes of the crystal.

Surface areas and volume

The Wulff shape of a pyramidal crystal is sketched in Figure B.4b. It has eight {111} side facets and a square (001) interface with the substrate. To write out its surface areas (A) and its volume (V), in this case it is convenient to introduce another ratio $k' = \frac{l}{h}$, which is the reciprocal of k. It follows that its areas and volume can be expressed as functions of h and k':

$$A_{111} = h^2\left(-\frac{\sqrt{3}}{2}k'^2 + \sqrt{6}k' + \sqrt{3}\right), \tag{B.35}$$

$$A_{\mathrm{i}} = k'^2 h^2, \tag{B.36}$$

$$V = h^3\left(-\frac{k'^3}{4\sqrt{2}} + \frac{k'^2}{4} + \frac{k'}{2\sqrt{2}} + \frac{1}{6}\right). \tag{B.37}$$

Finding the equilibrium ratio *k'*

In Figure B.4a, according to the Winterbottom construction,[206]

$$\frac{\gamma^*}{\gamma_{001}} = \frac{h - h_{001}}{h_{001}}. \tag{B.38}$$

Working with the geometry in Figure B.4a, we can relate h_{001} to l and h:

$$h_{001} = \frac{1}{2}\left(\frac{l}{\sqrt{2}} + h\right). \tag{B.39}$$

Substituting equation (B.39) and $\gamma_{001} = \sqrt{3}\gamma_{111}$ into equation (B.38), we obtain

$$\frac{\gamma^*}{\sqrt{3}\gamma_{111}} = \frac{\sqrt{2} - \frac{l}{h}}{\sqrt{2} + \frac{l}{h}}, \tag{B.40}$$

where $\frac{l}{h} = k'$. Therefore, equation (B.40) can be rearranged to give

$$k' = \frac{\sqrt{6}\gamma_{111} - \sqrt{2}\gamma^*}{\sqrt{3}\gamma_{111} + \gamma^*}. \tag{B.41}$$

Equation (B.41) can also be worked out by noting that for a crystal with a given volume, its total surface/interface energy (E_c) is minimised. E_c of the pyramid in Figure B.4b is given by

$$E_c = \gamma_{111}A_{111} + \gamma^* A_i. \tag{B.42}$$

Differentiating E_c with respect to k' gives

$$\frac{dE_c}{dk'} = \gamma_{111}\frac{dA_{111}}{dk'} + \gamma^*\frac{dA_i}{dk'}. \tag{B.43}$$

Since A_{111} and A_i are functions of the variables h and k', as shown earlier in equations (B.35) and (B.36), it follows that the terms $\frac{dA_{111}}{dk'}$, and $\frac{dA_i}{dk'}$ are functions of h, k', and $\frac{dh}{dk'}$. The variable

$\frac{\mathrm{d}h}{\mathrm{d}k'}$ can be eliminated by the following steps: (i) differentiating the crystal volume, i.e., equation (B.37) with respect to *k*', which gives an expression for $\frac{\mathrm{d}V}{\mathrm{d}k'}$ as a function of *h*, *k*, and $\frac{\mathrm{d}h}{\mathrm{d}k'}$, i.e., $\frac{\mathrm{d}V}{\mathrm{d}k'} = f(h, k', \frac{\mathrm{d}h}{\mathrm{d}k'})$; (ii) equating $f(h, k', \frac{\mathrm{d}h}{\mathrm{d}k'})$ to zero because for a crystal with a given volume, $\frac{\mathrm{d}V}{\mathrm{d}k'}$ = 0; (iii) rearranging the result to make $\frac{\mathrm{d}h}{\mathrm{d}k'}$ the subject, which gives us $\frac{\mathrm{d}h}{\mathrm{d}k'} = f(h, k')$; (iv) substituting $\frac{\mathrm{d}h}{\mathrm{d}k'} = f(h, k')$ into equation (B.43), to obtain $\frac{\mathrm{d}E_\mathrm{c}}{\mathrm{d}k'} = f(h, k')$. Finally, equating $\frac{\mathrm{d}E_\mathrm{c}}{\mathrm{d}k'} = f(h, k')$ to zero and rearranging the result to make *k*' the subject will lead to equation (B.41).

Expressing $E_{\text{pyramid Wulff}}$ as $\alpha_{\text{pyramid Wulff}} V^{\frac{2}{3}}$

Substituting equations (B.35) and (B.36) into equation (B.42) gives an expression for E_c or $E_{\text{pyramid Wulff}}$ in terms of *h* and *k*':

$$E_{\text{pyramid Wulff}} = \gamma_{111} \cdot h^2 \left(-\frac{\sqrt{3}}{2} k'^2 + \sqrt{6} k' + \sqrt{3} \right) + \gamma^* \cdot k'^2 h^2. \qquad \text{(B.44)}$$

The variable *h* can be eliminated by rearranging equation (B.37) to make h^2 the subject and substituting $h^2 = f(V, k')$ into equation (B.44). The variable *k*' can then be eliminated by substituting equation (B.41) into equation (B.44). These steps result in an expression of the form $E_{\text{pyramid Wulff}} = \alpha_{\text{pyramid Wulff}} V^{\frac{2}{3}}$, where $\alpha_{\text{pyramid Wulff}}$ is given by

$$\boldsymbol{\alpha_{\text{pyramid Wulff}} = 3^{\frac{2}{3}} \left(6\sqrt{3}\gamma_{111}^3 + 18\gamma_{111}^2 \gamma^* - 6\sqrt{3}\gamma_{111}\gamma^{*2} + 2\gamma^{*3} \right)^{\frac{1}{3}}.} \qquad \textbf{(7.3)}$$

B.3.2 Pyramid growth

Surface areas and volume

The growth shape of a pyramidal crystal is sketched in Figure B.4c. For such a crystal, A_{111} = the total area of its {111} facets (four side facets of the equilateral triangular shape) and A_i = its interfacial area with the substrate (a square). From geometry,

$$A_{111} = 2\sqrt{3}h^2, \tag{B.45}$$

$$A_i = 2h^2, \tag{B.46}$$

$$V = \frac{2}{3}h^3. \tag{B.47}$$

Fixed ratio *k'*

For the growth shape of a pyramid, its aspect ratio is fixed because the crystal shape is defined by four {111} side facets and a square (001) base (Figure B.4c). Therefore, $k' = \frac{l}{h}$ is a constant which, according to geometry, is equal to $\sqrt{2}$.

Expressing $E_{\text{pyramid growth}}$ as $\alpha_{\text{pyramid growth}} V^{\frac{2}{3}}$

Substituting equations (B.45) and (B.46) into equation (B.42) gives an expression for E_c or $E_{\text{pyramid growth}}$ in terms of h and k':

$$E_{\text{pyramid growth}} = \gamma_{111} \cdot 2\sqrt{3}h^2 + \gamma^* \cdot 2h^2. \tag{B.48}$$

The variable h can be eliminated by rearranging equation (B.47) to obtain $h^2 = \left(\frac{3}{2}V\right)^{\frac{2}{3}}$, which is then substituted into equation (B.48). This gives an expression of the form $E_{\text{pyramid growth}} = \alpha_{\text{pyramid growth}} V^{\frac{2}{3}}$, where $\alpha_{\text{pyramid growth}}$ is given by

$$\boldsymbol{\alpha_{\text{pyramid growth}} = 18^{\frac{1}{3}}\left(\sqrt{3}\gamma_{111} + \gamma^*\right).} \qquad \textbf{(7.4)}$$

B.4 (110)-based gold crystals (hut Wulff)

A substrate-supported gold crystal adopts a hut shape when it has a (110) base facet. A cross section of a hut crystal is illustrated in Figure B.5a in orange, with a crystal height of h. Its crystal length l is defined as the length of top ridge, which is equal to the base length (Figure B.5b). Here it is assumed that $\frac{\gamma_{001}}{\gamma_{111}} \geq \sqrt{3}$ and no {001} facets are exposed.

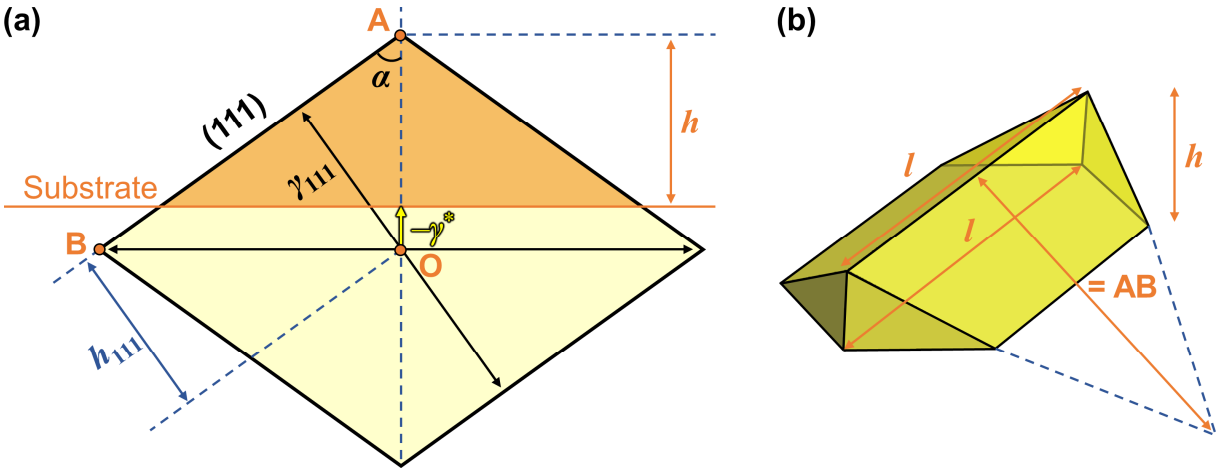

Figure B.5: Supported hut gold crystal. (a) The Winterbottom construction of the supported crystal (in orange) and (b) the 3D Wulff shape of the crystal.

Surface areas and volume

The Wulff shape of a hut crystal is sketched in Figure B.5b. It has six {111} side facets and a (110) interface with the substrate. Again, if we define $k' = \frac{l}{h}$, its surface areas (*A*) and volume (*V*) are given by

$$A_{111} = 2\sqrt{3}k'h^2, \tag{B.49}$$

$$A_{\mathrm{i}} = 2\sqrt{2}(k' - 1)h^2, \tag{B.50}$$

$$V = \sqrt{2}\left(k' - \frac{2}{3}\right)h^3. \tag{B.51}$$

Finding the equilibrium ratio *k'*

In Figure B.5a, according to the Winterbottom construction,[206]

$$\frac{-\gamma^*}{\gamma_{111}} = \frac{\mathrm{OA} - h}{h_{111}}. \tag{B.52}$$

The length AB in Figure B.5a is also labelled in Figure B.5b. In Figure B.5b, one of the crystal side facets, when extended by the blue dashed lines, is an equilateral triangle. This is one of the {111} faces of the free-standing octahedral Wulff shape. In this triangle, it can be seen that

$$\mathrm{AB} = \frac{\sqrt{3}}{2}l. \tag{B.53}$$

Considering the triangle OAB in Figure B.5a,

$$\mathrm{OA} = \mathrm{AB} \cdot \cos\alpha = \frac{\sqrt{3}}{2}l \cdot \frac{1}{\sqrt{3}} = \frac{l}{2}, \tag{B.54}$$

$$h_{111} = \mathrm{OA} \cdot \sin\alpha = \frac{l}{2} \cdot \sqrt{\frac{2}{3}} = \frac{l}{\sqrt{6}}. \tag{B.55}$$

Substituting equation (B.55) into equation (B.52) and rearranging it to make *k*' the subject,

$$k' = \frac{2\sqrt{6}\gamma_{111}}{2\gamma^* + \sqrt{6}\gamma_{111}}. \tag{B.56}$$

Equation (B.56) can also be worked out by minimising E_c using the method described in section B.3.1, starting with equations (B.42) and (B.43), noting that the expressions for A_{111} and A_i in this case are described by equations (B.49) and (B.50) above.

Expressing $E_{\text{hut Wulff}}$ as $\alpha_{\text{hut Wulff}} V^{\frac{2}{3}}$

Substituting equations (B.49) and (B.50) into equation (B.42) gives an expression for E_c or $E_{\text{hut Wulff}}$ in terms of *h* and *k*':

$$E_{\text{hut Wulff}} = \gamma_{111} \cdot 2\sqrt{3}k'h^2 + \gamma^* \cdot 2\sqrt{2}(k'-1)h^2. \tag{B.57}$$

The variable *h* can be eliminated by rearranging equation (B.51) to obtain $h^2 = \left[\frac{V}{\sqrt{2}\left(k'-\frac{2}{3}\right)}\right]^{\frac{2}{3}}$, which is substituted into equation (B.57). The variable *k*' can then be eliminated by substituting equation (B.56) into equation (B.57). These steps give an expression of the form $E_{\text{hut Wulff}} = \alpha_{\text{hut Wulff}} V^{\frac{2}{3}}$, where $\alpha_{\text{hut Wulff}}$ is given by

$$\boldsymbol{\alpha_{\text{hut Wulff}} = 3^{\frac{2}{3}} \cdot 2^{-\frac{1}{6}} \left(\sqrt{6}\gamma_{111} - \gamma^*\right)^{\frac{1}{3}} \left(\sqrt{6}\gamma_{111} + 2\gamma^*\right)^{\frac{2}{3}}}. \tag{7.5}$$

References

(1) Gulde, M. *Development of an Ultrafast Low-Energy Electron Diffraction Setup*; Springer, 2015.

(2) Somorjai, G. A.; Li, Y. *Introduction to Surface Chemistry and Catalysis*, 2nd ed.; Wiley-Blackwell: New York, 2010.

(3) Kucuk, A.; Clare, A. G.; Jones, L. E. Differences Between Surface and Bulk Properties of Glass Melts. *J. Non. Cryst. Solids* **2000**, *261*, 28–38.

(4) Mahboubeh, H. Theory of Adsorption, Diffusion and Spinpolarization of Mn on Si(001) and Si(111) Substrates (Ph.D. Thesis), Free University of Berlin, 2006.

(5) Schlier, R. E.; Farnsworth, H. E. Structure and Adsorption Characteristics of Clean Surfaces of Germanium and Silicon. *J. Chem. Phys.* **1959**, *30*, 917–926.

(6) Takayanagi, K.; Tanishiro, Y.; Takahashi, S.; Takahashi, M. Structure Analysis of Si(111)-7 × 7 Reconstructed Surface by Transmission Electron Diffraction. *Surf. Sci.* **1985**, *164*, 367–392.

(7) Lüth, H. *Solid Surfaces, Interfaces and Thin Films*, 4th ed.; Springer: New York, 2001.

(8) Markovic, N. M.; Schmidt, T. J. Oxygen Reduction Reaction on Pt and Pt Bimetallic Surfaces: A Selective Review. *Fuel Cells* **2001**, *1*, 105–116.

(9) Zhuiykov, S. *Nanostructured Semiconductor Oxides for the Next Generation of Electronics and Functional Devices*; Woodhead Publishing: Cambridge, 2014.

(10) Mourik, V.; Zuo, K.; Frolov, S. M.; Plissard, S. R.; Bakkers, E. P. A. M.; Kouwenhoven, L. P. Signatures of Majorana Fermions in Hybrid Superconductor-Semiconductor Nanowire Devices. *Science* **2012**, *336*, 1003–1007.

(11) Li, Y.; Qi, Z.; Liu, M.; Wang, Y.; Cheng, X.; Zhang, G.; Sheng, L. Photoluminescence of Monolayer MoS_2 on $LaAlO_3$ and $SrTiO_3$ Substrates. *Nanoscale* **2014**, *6*, 15248–15254.

(12) Habermeier, H. U. Substrate Surface Engineering for Tailoring Properties of Functional Ceramic Thin Films. *Phys. Status Solidi* **2004**, *1*, 1614–1619.

(13) Mak, K. F.; Lee, C.; Hone, J.; Shan, J.; Heinz, T. F. Atomically Thin MoS_2: A New Direct-Gap Semiconductor. *Phys. Rev. Lett.* **2010**, *105*, 136805.

(14) Splendiani, A.; Sun, L.; Zhang, Y.; Li, T.; Kim, J.; Chim, C.-Y.; Galli, G.; Wang, F. Emerging Photoluminescence in Monolayer MoS_2. *Nano Lett.* **2010**, *10*, 1271–1275.

(15) Radisavljevic, B.; Radenovic, A.; Brivio, J.; Giacometti, V.; Kis, A. Single-Layer MoS_2 Transistors. *Nat. Nanotechnol.* **2011**, *6*, 147–150.

(16) Li, H.; Wu, J.; Yin, Z.; Zhang, H. Preparation and Applications of Mechanically Exfoliated Single-Layer and Multilayer MoS_2 and WSe_2 Nanosheets. *Acc. Chem. Res.* **2014**, *47*, 1067–1075.

(17) Haruta, M.; Kobayashi, T.; Sano, H.; Yamada, N. Novel Gold Catalysts for the Oxidation

of Carbon Monoxide at a Temperature for Below 0 °C. *Chem. Lett.* **1987**, 405–408.

(18) Lee, K. S.; El-Sayed, M. A. Gold and Silver Nanoparticles in Sensing and Imaging: Sensitivity of Plasmon Response to Size, Shape, and Metal Composition. *J. Phys. Chem. B* **2006**, *110*, 19220–19225.

(19) Anker, J. N.; Hall, W. P.; Lyanders, O.; Shah, N. C.; Zhao, J.; Van Duyne, R. P. Biosensing with Plasmonic Nanosensers. *Nat. Mater.* **2008**, *6*, 442–453.

(20) Mayer, K. M.; Hafner, J. H. Localized Surface Plasmon Resonance Biosensors. *Chem. Rev.* **2011**, *111*, 3828–3857.

(21) Ringe, E.; Langille, M. R.; Sohn, K.; Zhang, J.; Huang, J.; Mirkin, C. A.; Van Duyne, R. P.; Marks, L. D. Plasmon Length: A Universal Parameter to Describe Size Effects in Gold Nanoparticles. *J. Phys. Chem. Lett.* **2012**, *3*, 1479−1483.

(22) Wolfram, T.; Morin, F. J. A Conceptual Model for Surface States and Catalysis on *d*-Band Perovskites. *Appl. Phys.* **1975**, *8*, 125–141.

(23) Powell, R. A.; Spicer, W. E. Photoemission Investigation of Surface States on Strontium Titanate. *Phys. Rev. B* **1976**, *13*, 2601–2604.

(24) Henrich, V. E.; Dresselhaus, G.; Zeiger, H. J. Surface Defects and the Electronic Structure of $SrTiO_3$ Surfaces. *Phys. Rev. B* **1978**, *17*, 4908–4921.

(25) Wrighton, M. S.; Wolczanski, P. T.; Ellis, A. B. Photoelectrolysis of Water by Irradiation of Platinized *n*-Type Semiconducting Metal Oxides. *J. Solid State Chem.* **1977**, *22*, 17–29.

(26) Mavroides, J. G.; Kafalas, J. A.; Kolesar, D. F. Photoelectrolysis of Water in Cells with $SrTiO_3$ Anodes. *Appl. Phys. Lett.* **1976**, *28*, 241–243.

(27) Menesklou, W.; Schreiner, H.-J.; Härdtl, K. H.; Ivers-Tiffée, E. High Temperature Oxygen Sensors Based on Doped $SrTiO_3$. *Sensors Actuators B Chem.* **1999**, *59*, 184–189.

(28) Agrawal, V. Nucleation and Growth of $DyBa_2Cu_3O_{7-x}$ Thin Films on $SrTiO_3$ Substrates Studied by Transmission Electron Microscopy and Atomic Force Microscopy. *J. Vac. Sci. Technol. A* **1992**, *10*, 1531–1536.

(29) Enterkin, J. A.; Poeppelmeier, K. R.; Marks, L. D. Oriented Catalytic Platinum Nanoparticles on High Surface Area Strontium Titanate Nanocuboids. *Nano Lett.* **2011**, *11*, 993–997.

(30) Enterkin, J. A.; Setthapun, W.; Elam, J. W.; Christensen, S. T.; Rabuffetti, F. A.; Marks, L. D.; Stair, P. C.; Poeppelmeier, K. R.; Marshall, C. L. Propane Oxidation Over $Pt/SrTiO_3$ Nanocuboids. *ACS Catal.* **2011**, *1*, 629–635.

(31) Ohtomo, A.; Muller, D. A.; Grazul, J. L.; Hwang, H. Y. Artificial Charge-Modulation in Atomic-Scale Perovskite Titanate Superlattices. *Nature* **2002**, *419*, 378–380.

(32) Ohtomo, A.; Hwang, H. Y. A High-Mobility Electron Gas at the $LaAlO_3/SrTiO_3$ Heterointerface. *Nature* **2004**, *427*, 423–426.

(33) Noland, J. A. Optical Absorption of Single-Crystal Strontium Titanate. *Phys. Rev.* **1954**, *94*, 724.

(34) Li, N.; Yao, K. L. The Electronic and Optical Properties of Carbon-Doped $SrTiO_3$: Density Functional Characterization. *AIP Adv.* **2012**, *2*, 032135.

(35) Lo, W. J.; Somorjai, G. A. Temperature-Dependent Surface Structure, Composition, and Electronic Properties of the Clean $SrTiO_3$(111) Crystal Face: Low-Energy-Electron Diffraction, Auger-Electron Spectroscopy, Electron Energy Loss, and Ultraviolet-Photoelectron Spectroscopy Studies. *Phys. Rev. B* **1978**, *17*, 4942–4950.

(36) Schooley, J. F.; Hosler, W. R.; Cohen, M. L. Superconductivity in Semiconducting $SrTiO_3$. *Phys. Rev. Lett.* **1964**, *12*, 474–475.

(37) Schooley, J. F.; Hosler, W. R.; Ambler, E.; Becker, J. H.; Cohen, M. L.; Koonce, C. S. Dependence of the Superconducting Transition Temperature on Carrier Concentration in Semiconducting $SrTiO_3$. *Phys. Rev. Lett.* **1965**, *14*, 305–307.

(38) Russell, B. C.; Castell, M. R. ($\sqrt{13} \times \sqrt{13}$)R13.9° and ($\sqrt{7} \times \sqrt{7}$)R19.1° Reconstructions of the Polar $SrTiO_3$(111) Surface. *Phys. Rev. B* **2007**, *75*, 155433.

(39) Marshall, M. S. J.; Castell, M. R. Shape Transitions of Epitaxial Islands During Strained Layer Growth: Anatase TiO_2(001) on $SrTiO_3$(001). *Phys. Rev. Lett.* **2009**, *102*, 146102.

(40) Dai, S.; Lu, H.; Chen, F.; Chen, Z.; Ren, Z. Y.; Ng, D. H. L. In-Doped $SrTiO_3$ Ceramic Thin Films. *Appl. Phys. Lett.* **2002**, *80*, 3545.

(41) Wenk, H.-R.; Bulakh, A. *Minerals: Their Constitution and Origin*; Cambridge University Press: New York, 2004.

(42) Furuhata, Y.; Nakamura, E.; Sawaguchi, E. *Landolt-Börnstein, Group III*; 1969; Vol. 16.

(43) Russell, B. C.; Castell, M. R. Surface of Sputtered and Annealed Polar $SrTiO_3$(111): TiO_x-Rich ($n \times n$) Reconstructions. *J. Phys. Chem. C* **2008**, *112*, 6538–6545.

(44) Pojani, A.; Finocchi, F.; Noguera, C. Polarity on the $SrTiO_3$(111) and (110) Surfaces. *Surf. Sci.* **1999**, *442*, 179–198.

(45) Chiaramonti, A. N.; Lanier, C. H.; Marks, L. D.; Stair, P. C. Time, Temperature, and Oxygen Partial Pressure-Dependent Surface Reconstructions on $SrTiO_3$(111): A Systematic Study of Oxygen-Rich Conditions. *Surf. Sci.* **2008**, *602*, 3018–3025.

(46) Tasker, P. W. The Stability of Ionic Crystal Surfaces. *J. Phys. C Solid State Phys.* **1979**, *12*, 4977–4984.

(47) Haruyama, Y.; Aiura, Y.; Bando, H.; Nishihara, Y.; Kato, H. Annealing Temperature Dependence on the Electronic Structure of the Reduced $SrTiO_3$(111) Surface. *J. Electron Spectros. Relat. Phenomena* **1998**, *88–91*, 695–699.

(48) Sekiguchi, S.; Fujimoto, M.; Kang, M.-G.; Koizumi, S.; Cho, S.-B.; Tanaka, J. Structure Analysis of $SrTiO_3$(111) Polar Surfaces. *Jpn. J. Appl. Phys.* **1998**, *37*, 4140–4143.

(49) Sekiguchi, S. Atomic Force Microscopic Observation of $SrTiO_3$ Polar Surface. *Solid State Ionics* **1998**, *108*, 73–79.

(50) Ferrer, S.; Somorjai, G. A. UPS and XPS Studies of the Chemisorption of O_2, H_2 and H_2O on Reduced and Stoichiometric $SrTiO_3$(111) Surfaces; the Effects of Illumination. *Surf. Sci.* **1980**, *94*, 41–56.

(51) Tanaka, H.; Kawai, T. Surface Structure of Reduced SrTiO3(111) Observed by Scanning Tunneling Microscopy. *Surf. Sci.* **1996**, *365*, 437–442.

(52) Sigmund, W. M. M.; Rotov, M.; Aldinger, F.; Jiang, Q. D.; Brunen, J.; Zegenhagen, J. A Titanium-Rich (111) Surface of $SrTiO_3$ Single Crystals by Thermal Annealing. *Appl. Phys. A* **1997**, *64*, 219–220.

(53) Pojani, A.; Finocchi, F.; Noguera, C. A Theoretical Study of the Unreconstructed Polar (111) Face of $SrTiO_3$. *Appl. Surf. Sci.* **1999**, *142*, 177–181.

(54) Chiaramonti, A. N. Structure and Thermodynamics of Model Catalytic Oxide Surfaces (Ph.D. Thesis), Northwestern University, 2005.

(55) ur Rahman, S. Probing the Effect of Oxygen Vacancies in Strontium Titanate Single Crystals (Ph.D. Thesis), University of Oxford, 2014.

(56) Marks, L. D.; Chiaramonti, A. N.; ur Rahman, S.; Castell, M. R. Transition from Order to Configurational Disorder for Surface Reconstructions on $SrTiO_3$(111). *Phys. Rev. Lett.* **2015**, *114*, 226101.

(57) Feng, J.; Zhu, X.; Guo, J. Reconstructions on $SrTiO_3$(111) Surface Tuned by Ti/Sr Deposition. *Surf. Sci.* **2013**, *614*, 38–45.

(58) Adachi, Y.; Kohiki, S.; Wagatsuma, K.; Oku, M. Changes in the Chemical State of Monocrystalline $SrTiO_3$ Surface by Argon Ion Bombardment. *Appl. Surf. Sci.* **1999**, *143*, 272–276.

(59) Kan, D.; Terashima, T.; Kanda, R.; Masuno, A.; Tanaka, K.; Chu, S.; Kan, H.; Ishizumi, A.; Kanemitsu, Y.; Shimakawa, Y.; et al. Blue-Light Emission at Room Temperature from Ar^+-Irradiated $SrTiO_3$. *Nat. Mater.* **2005**, *4*, 816–819.

(60) Sung, K. D.; Kumar, R.; Pratap Singh, A.; Kim, C. S.; Yee, K. J.; Jung, J. H. Photoluminescence of High Energy Ar^+-Irradiated $SrTiO_3$ Single Crystal. *Phys. B* **2010**, *405*, 2581–2584.

(61) Andersen, T. K.; Wang, S.; Castell, M. R.; Fong, D. D.; Marks, L. D. Single-Layer TiO_x Reconstructions on $SrTiO_3$(111): ($\sqrt{7} \times \sqrt{7}$)R19.1° ($\sqrt{13} \times \sqrt{13}$)R13.9°, and Related Structures. *Surf. Sci.* **2018**, *675*, 36–41.

(62) Heifets, E.; Goddard, W. A.; Kotomin, E. A.; Eglitis, R. I.; Borstel, G. *Ab Initio* Calculations of the $SrTiO_3$ (110) Polar Surface. *Phys. Rev. B* **2004**, *69*, 035408.

(63) Russell, B. C.; Castell, M. R. Reconstructions on the Polar $SrTiO_3$(110) Surface: Analysis Using STM, LEED, and AES. *Phys. Rev. B* **2008**, *77*, 245414.

(64) Akoh, H.; Camerlingo, C.; Takada, S. Anisotropic Josephson Junctions of Y-Ba-Cu-O/Au/Nb Film Sandwiches. *Appl. Phys. Lett.* **1990**, *56*, 1487–1489.

(65) Enterkin, J. A.; Subramanian, A. K.; Russell, B. C.; Castell, M. R.; Poeppelmeier, K. R.; Marks, L. D. A Homologous Series of Structures on the Surface of $SrTiO_3$(110). *Nat. Mater.* **2010**, *9*, 245–248.

(66) Wang, Z.; Loon, A.; Subramanian, A.; Gerhold, S.; McDermott, E.; Enterkin, J. A.; Hieckel, M.; Russell, B. C.; Green, R. J.; Moewes, A.; et al. Transition from Reconstruction toward Thin Film on the (110) Surface of Strontium Titanate. *Nano Lett.*

2016, *16*, 2407–2412.

(67) Wang, Z.; Feng, J.; Yang, Y.; Yao, Y.; Gu, L.; Yang, F.; Guo, Q.; Guo, J. Cation Stoichiometry Optimization of $SrTiO_3$ (110) Thin Films with Atomic Precision in Homogeneous Molecular Beam Epitaxy. *Appl. Phys. Lett.* **2012**, *100*, 051602.

(68) Yang, F.; Liang, Y.; Liu, L.-X.; Zhu, Q.; Wang, W.-H.; Zhu, X.-T.; Guo, J.-D. Controlled Growth of Complex Polar Oxide Films with Atomically Precise Molecular Beam Epitaxy. *Front. Phys.* **2018**, *13*, 136802.

(69) Castell, M. R. Scanning Tunneling Microscopy of Reconstructions on the $SrTiO_3$(001) Surface. *Surf. Sci.* **2002**, *505*, 1–13.

(70) Lippmaa, M.; Kawasaki, M.; Ohtomo, A.; Sato, T.; Iwatsuki, M.; Koinuma, H. Observation of $SrTiO_3$ Step Edge Dynamics by Real-Time High-Temperature STM. *Appl. Surf. Sci.* **1998**, *130–132*, 582–586.

(71) Ikeda, A.; Nishimura, T.; Morishita, T.; Kido, Y. Surface Relaxation and Rumpling of TiO_2-Terminated $SrTiO_3$(001) Determined by Medium Energy Ion Scattering. *Surf. Sci.* **1999**, *435*, 520–524.

(72) Andersen, J. E. T.; Møller, P. J. Impurity-Induced 900 °C (2×2) Surface Reconstruction of $SrTiO_3$(100). *Appl. Phys. Lett.* **1990**, *56*, 1847–1849.

(73) Tanaka, H.; Matsumoto, T.; Kawai, T.; Kawai, S. Surface Structure and Electronic Property of Reduced $SrTiO_3$(100) Surface Observed by Scanning Tunneling Microscopy/Spectroscopy. *Jpn. J. Appl. Phys.* **1993**, *32*, 1405–1409.

(74) Jiang, Q. D.; Zegenhagen, J. $SrTiO_3$(001) Surfaces and Growth of Ultra-Thin $GdBa_2Cu_3O_{7-x}$ Films Studied by LEED/AES and UHV-STM. *Surf. Sci.* **1995**, *338*, L882–L888.

(75) Nishimura, T.; Ikeda, A.; Namba, H.; Morishita, T.; Kido, Y. Structure Change of TiO_2-Terminated $SrTiO_3$(001) Surfaces by Annealing in O_2 Atmosphere and Ultrahigh Vacuum. *Surf. Sci.* **1999**, *421*, 273–278.

(76) Jiang, D.; Zegenhagen, J. *c*(6 × 2) and *c*(4 × 2) Reconstruction of $SrTiO_3$(001). *Surf. Sci.* **1999**, *425*, 343–354.

(77) Charlton, G.; Brennan, S.; Muryn, C. A.; McGrath, R.; Norman, D.; Turner, T. S.; Thornton, G. Surface Relaxation of $SrTiO_3$(001). *Surf. Sci.* **2000**, *457*, L376–L380.

(78) Kubo, T.; Nozoye, H. Surface Structure of $SrTiO_3$(110)-($\sqrt{5} \times \sqrt{5}$)-R26.6°. *Phys. Rev. Lett.* **2001**, *86*, 1801–1804.

(79) Kawasaki, M.; Yamamoto, K.; Maeda, T.; Tsuchiya, R.; Shinohara, M.; Ishiyama, O.; Yonezawa, T.; Yoshimoto, M.; Koinuma, H.; Takahashi, K.; et al. Atomic Control of the $SrTiO_3$ Crystal Surface. *Science* **1994**, *266*, 1540–1542.

(80) Naito, M.; Sato, H. Reflection High-Energy Electron Diffraction Study on the $SrTiO_3$ Surface Structure. *Phys. C* **1994**, *229*, 1–11.

(81) Moller, P. J.; Komolov, S. A.; Lazneva, E. F. Selective Growth of a MgO(100)-*c*(2 × 2) Superstructure on a $SrTiO_3$(100)-(2 × 2) Substrate. *Surf. Sci.* **1999**, *425*, 15–21.

(82) Kubo, T.; Nozoye, H. Surface Structure of $SrTiO_3$(100). *Surf. Sci.* **2003**, *542*, 177–191.

(83) Silly, F.; Newell, D. T.; Castell, M. R. $SrTiO_3$(001) Reconstructions: The (2 × 2) to *c*(4 × 4) Transition. *Surf. Sci.* **2006**, *600*, L219–L223.

(84) Deak, D. S.; Silly, F.; Newell, D. T.; Castell, M. R. Ordering of TiO_2-Based Nanostructures on $SrTiO_3$(001) Surfaces. *J. Phys. Chem. B* **2006**, *110*, 9246–9251.

(85) Castell, M. R. Nanostructures on the $SrTiO_3$(001) Surface Studied by STM. *Surf. Sci.* **2002**, *516*, 33–42.

(86) Marsh, H. L.; Deak, D. S.; Silly, F.; Kirkland, A. I.; Castell, M. R. Hot STM of Nanostructure Dynamics on $SrTiO_3$(001). *Nanotechnology* **2006**, *17*, 3543–3548.

(87) Erdman, N.; Warschkow, O.; Asta, M.; Poeppelmeier, K. R.; Ellis, D. E.; Marks, L. D. Surface Structures of $SrTiO_3$ (001): A TiO_2-Rich Reconstruction with a *c*(4 × 2) Unit Cell. *J. Am. Chem. Soc.* **2003**, *125*, 10050–10056.

(88) Becerra-Toledo, A. E.; Marshall, M. S. J.; Castell, M. R.; Marks, L. D. *c*(4 × 2) and Related Structural Units on the $SrTiO_3$(001) Surface: Scanning Tunneling Microscopy, Density Functional Theory, and Atomic Structure. *J. Chem. Phys.* **2012**, *136*, 214701.

(89) Becerra-Toledo, A. E.; Castell, M. R.; Marks, L. D. Water Adsorption on $SrTiO_3$(001): I. Experimental and Simulated STM. *Surf. Sci.* **2012**, *606*, 762–765.

(90) Silly, F.; Castell, M. R. Selecting the Shape of Supported Metal Nanocrystals: Pd Huts, Hexagons, or Pyramids on $SrTiO_3$(001). *Phys. Rev. Lett.* **2005**, *94*, 046103.

(91) Warschkow, O.; Asta, M.; Erdman, N.; Poeppelmeier, K. R.; Ellis, D. E.; Marks, L. D. TiO_2-Rich Reconstructions of $SrTiO_3$(001): A Theoretical Study of Structural Patterns. *Surf. Sci.* **2004**, *573*, 446–456.

(92) Silly, F.; Castell, M. R. Formation of Single-Domain Anatase TiO_2(001)-(1×4) Islands on $SrTiO_3$(001) after Thermal Annealing. *Appl. Phys. Lett.* **2004**, *85*, 3223–3225.

(93) Newell, D. T.; Harrison, A.; Silly, F.; Castell, M. R. $SrTiO_3$(001)-($\sqrt{5}$ × $\sqrt{5}$)-R26.6° Reconstruction: A Surface Resulting from Phase Separation in a Reducing Environment. *Phys. Rev. B* **2007**, *75*, 205429.

(94) Novoselov, K. S.; Jiang, D.; Schedin, F.; Booth, T. J.; Khotkevich, V. V; Morozov, S. V; Geim, A. K. Two-Dimensional Atomic Crystals. *Proc. Natl. Acad. Sci.* **2005**, *102*, 10451–10453.

(95) Miró, P.; Audiffred, M.; Heine, T. An Atlas of Two-Dimensional Materials. *Chem. Soc. Rev.* **2014**, *43*, 6537–6554.

(96) Butler, S. Z.; Hollen, S. M.; Cao, L.; Cui, Y.; Gupta, J. A.; Gutiérrez, H. R.; Heinz, T. F.; Hong, S. S.; Huang, J.; Ismach, A. F.; et al. Progress, Challenges, and Opportunities in Two-Dimensional Materials Beyond Graphene. *ACS Nano* **2013**, *7*, 2898–2926.

(97) Wang, Q. H.; Kalantar-Zadeh, K.; Kis, A.; Coleman, J. N.; Strano, M. S. Electronics and Optoelectronics of Two-Dimensional Transition Metal Dichalcogenides. *Nat. Nanotechnol.* **2012**, *7*, 699–712.

(98) Mak, K. F.; He, K.; Shan, J.; Heinz, T. F. Control of Valley Polarization in Monolayer MoS_2 by Optical Helicity. *Nat. Nanotechnol.* **2012**, *7*, 494–498.

(99) Zeng, H.; Dai, J.; Yao, W.; Xiao, D.; Cui, X. Valley Polarization in MoS_2 Monolayers

by Optical Pumping. *Nat. Nanotechnol.* **2012**, *7*, 490–493.

(100) Davelou, D.; Kopidakis, G.; Kioseoglou, G.; Remediakis, I. N. MoS_2 Nanostructures: Semiconductors with Metallic Edges. *Solid State Commun.* **2014**, *192*, 42–46.

(101) Bollinger, M. V.; Lauritsen, J. V.; Jacobsen, K. W.; Nørskov, J. K.; Helveg, S.; Besenbacher, F. One-Dimensional Metallic Edge States in MoS_2. *Phys. Rev. Lett.* **2001**, *87*, 196803.

(102) Pavlovic, S.; Peeters, F. M. Electronic Properties of Triangular and Hexagonal MoS_2 Quantum Dots. *Phys. Rev. B* **2015**, *91*, 155410.

(103) Segarra, C.; Planelles, J.; Ulloa, S. E. Edge States in Dichalcogenide Nanoribbons and Triangular Quantum Dots. *Phys. Rev. B* **2016**, *93*, 085312.

(104) Ryder, C. R.; Wood, J. D.; Wells, S. A.; Hersam, M. C. Chemically Tailoring Semiconducting Two-Dimensional Transition Metal Dichalcogenides and Black Phosphorus. *ACS Nano* **2016**, *10*, 3900–3917.

(105) Jariwala, D.; Sangwan, V. K.; Lauhon, L. J.; Marks, T. J.; Hersam, M. C. Emerging Device Applications for Semiconducting Two-Dimensional Transition Metal Dichalcogenides. *ACS Nano* **2014**, *8*, 1102–1120.

(106) Kioseoglou, G.; Hanbicki, A. T.; Currie, M.; Friedman, A. L.; Jonker, B. T. Optical Polarization and Intervalley Scattering in Single Layers of MoS_2 and $MoSe_2$. *Sci. Rep.* **2016**, *6*, 25041.

(107) Fivaz, R.; Mooser, E. Mobility of Charge Carriers in Semiconducting Layer Structures. *Phys. Rev.* **1967**, *163*, 743–755.

(108) Lee, G.-H.; Yu, Y.-J.; Cui, X.; Petrone, N.; Lee, C.-H.; Choi, M. S.; Lee, D.-Y.; Lee, C.; Yoo, W. J.; Watanabe, K.; et al. Flexible and Transparent MoS_2 Field-Effect Transistors on Hexagonal Boron Nitride-Graphene Heterostructures. *ACS Nano* **2013**, *7*, 7931–7936.

(109) Schwierz, F. Graphene Transistorsle. *Nat. Nanotechnol.* **2010**, *5*, 487–496.

(110) Avouris, P.; Chen, Z.; Perebeinos, V. Carbon-Based Electronics. *Nat. Nanotechnol.* **2007**, *2*, 605–615.

(111) Chang, H.-Y.; Yang, S.; Lee, J.; Tao, L.; Hwang, W.-S.; Jena, D.; Lu, N.; Akinwande, D. High-Performance, Highly Bendable MoS_2 Transistors with High-K Dielectrics for Flexible Low-Power Systems. *ACS Nano* **2013**, *7*, 5446–5452.

(112) Pu, J.; Yomogida, Y.; Liu, K.-K.; Li, L.-J.; Iwasa, Y.; Takenobu, T. Highly Flexible MoS_2 Thin-Film Transistors with Ion Gel Dielectrics. *Nano Lett.* **2012**, *12*, 4013–4017.

(113) Lee, Y. H.; Zhang, X. Q.; Zhang, W.; Chang, M. T.; Lin, C. Te; Chang, K. Di; Yu, Y. C.; Wang, J. T. W.; Chang, C. S.; Li, L. J.; et al. Synthesis of Large-Area MoS_2 Atomic Layers with Chemical Vapor Deposition. *Adv. Mater.* **2012**, *24*, 2320–2325.

(114) Ji, Q.; Kan, M.; Zhang, Y.; Guo, Y.; Ma, D.; Shi, J.; Sun, Q.; Chen, Q.; Zhang, Y.; Liu, Z. Unravelling Orientation Distribution and Merging Behavior of Monolayer MoS_2 Domains on Sapphire. *Nano Lett.* **2015**, *15*, 198–205.

(115) Chen, P.; Xu, W.; Gao, Y.; Holdway, P.; Warner, J. H.; Castell, M. R. Thermal Degradation of Monolayer MoS_2 on $SrTiO_3$ Supports. *J. Phys. Chem. C* **2019**, *123*,

3876−3885.

(116) Kappera, R.; Voiry, D.; Yalcin, S. E.; Branch, B.; Gupta, G.; Mohite, A. D.; Chhowalla, M. Phase-Engineered Low-Resistance Contacts for Ultrathin MoS_2 Transistors. *Nat. Mater.* **2014**, *13*, 1128–1134.

(117) Ye, M.; Winslow, D.; Zhang, D.; Pandey, R.; Yap, Y. Recent Advancement on the Optical Properties of Two-Dimensional Molybdenum Disulfide (MoS_2) Thin Films. *Photonics* **2015**, *2*, 288–307.

(118) Eda, G.; Yamaguchi, H.; Voiry, D.; Fujita, T.; Chen, M.; Chhowalla, M. Photoluminescence from Chemically Exfoliated MoS_2. *Nano Lett.* **2011**, *11*, 5111–5116.

(119) Fu, Y.; Feng, X.; Yan, M.-F.; Wang, K.; Wang, S. First Principle Study on Electronic Structure and Optical Phonon Properties of 2H-MoS_2. *Phys. B* **2013**, *426*, 103–107.

(120) van der Zande, A. M.; Huang, P. Y.; Chenet, D. A.; Berkelbach, T. C.; You, Y.; Lee, G.-H.; Heinz, T. F.; Reichman, D. R.; Muller, D. A.; Hone, J. C. Grains and Grain Boundaries in Highly Crystalline Monolayer Molybdenum Disulphide. *Nat. Mater.* **2013**, *12*, 554–561.

(121) Najmaei, S.; Liu, Z.; Zhou, W.; Zou, X.; Shi, G.; Lei, S.; Yakobson, B. I.; Idrobo, J.-C.; Ajayan, P. M.; Lou, J. Vapour Phase Growth and Grain Boundary Structure of Molybdenum Disulphide Atomic Layers. *Nat. Mater.* **2013**, *12*, 754–759.

(122) Wang, S.; Rong, Y.; Fan, Y.; Pacios, M.; Bhaskaran, H.; He, K.; Warner, J. H. Shape Evolution of Monolayer MoS_2 Crystals Grown by Chemical Vapor Deposition. *Chem. Mater.* **2014**, *26*, 6371–6379.

(123) Lee, Y.; Yu, L.; Wang, H.; Shi, Y.; Huang, J.; Chang, T.; Chang, C.; Dresselhaus, M. S.; Palacios, T.; Li, L.; et al. Synthesis and Transfer of Single-Layer Transition Metal Disulfides on Diverse Surfaces. *Nano Lett.* **2013**, *13*, 1852–1857.

(124) Dhakal, K. P.; Duong, D. L.; Lee, J.; Nam, H.; Kim, M.; Kan, M.; Lee, Y. H.; Kim, J. Confocal Absorption Spectral Imaging of MoS_2: Optical Transitions Depending on the Atomic Thickness of Intrinsic and Chemically Doped MoS_2. *Nanoscale* **2014**, *6*, 13028–13035.

(125) Zhou, X.; Kang, K.; Xie, S.; Dadgar, A.; Monahan, N. R.; Zhu, X.-Y.; Park, J.; Pasupathy, A. N. Atomic-Scale Spectroscopy of Gated Monolayer MoS_2. *Nano Lett.* **2016**, *16*, 3148–3154.

(126) Ling, X.; Lee, Y.-H.; Lin, Y.; Fang, W.; Yu, L.; Dresselhaus, M. S.; Kong, J. Role of the Seeding Promoter in MoS_2 Growth by Chemical Vapor Deposition. *Nano Lett.* **2014**, *14*, 464–472.

(127) Xu, W.; Li, S.; Zhou, S.; Lee, J. K.; Wang, S.; Sarwat, S. G.; Wang, X.; Bhaskaran, H.; Pasta, M.; Warner, J. H. Large Dendritic Monolayer MoS_2 Grown by Atmospheric Pressure Chemical Vapor Deposition for Electrocatalysis. *ACS Appl. Mater. Interfaces* **2018**, *10*, 4630–4639.

(128) Kim, J. G.; Yun, W. S.; Jo, S.; Lee, J.; Cho, C.-H. Effect of Interlayer Interactions on Exciton Luminescence in Atomic-Layered MoS_2 Crystals. *Sci. Rep.* **2016**, *6*, 29813.

(129) Wang, S.; Wang, X.; Warner, J. H. All Chemical Vapor Deposition Growth of MoS_2: *h*-

BN Vertical van der Waals Heterostructures. *ACS Nano* **2015**, *9*, 5246–5254.

(130) Mak, K. F.; He, K.; Lee, C.; Lee, G. H.; Hone, J.; Heinz, T. F.; Shan, J. Tightly Bound Trions in Monolayer MoS_2. *Nat. Mater.* **2013**, *12*, 207–211.

(131) Sun, L.; Zhang, X.; Liu, F.; Shen, Y.; Fan, X.; Zheng, S.; Thong, J. T. L.; Liu, Z.; Yang, S. A.; Yang, H. Y. Vacuum Level Dependent Photoluminescence in Chemical Vapor Deposition-Grown Monolayer MoS_2. *Sci. Rep.* **2017**, *7*, 16714.

(132) Qiu, H.; Xu, T.; Wang, Z.; Ren, W.; Nan, H.; Ni, Z.; Chen, Q.; Yuan, S.; Miao, F.; Song, F.; et al. Hopping Transport Through Defect-Induced Localized States in Molybdenum Disulphide. *Nat. Commun.* **2013**, *4*, 2642.

(133) Lee, C.; Yan, H.; Brus, L. E.; Heinz, T. F.; Hone, J.; Ryu, S. Anomalous Lattice Vibrations of Single- and Few-Layer MoS_2. *ACS Nano* **2010**, *4*, 2695–2700.

(134) Yu, Y.; Li, C.; Liu, Y.; Su, L.; Zhang, Y.; Cao, L. Controlled Scalable Synthesis of Uniform, High-Quality Monolayer and Few-Layer MoS_2 Films. *Sci. Rep.* **2013**, *3*, 1866.

(135) Liu, Z.; Amani, M.; Najmaei, S.; Xu, Q.; Zou, X.; Zhou, W.; Yu, T.; Qiu, C.; Birdwell, A. G.; Crowne, F. J.; et al. Strain and Structure Heterogeneity in MoS_2 Atomic Layers Grown by Chemical Vapour Deposition. *Nat. Commun.* **2014**, *5*, 5246.

(136) Chen, P.; Xu, W.; Gao, Y.; Warner, J. H.; Castell, M. R. Epitaxial Growth of Monolayer MoS_2 on $SrTiO_3$ Single Crystal Substrates for Applications in Nanoelectronics. *ACS Appl. Nano Mater.* **2018**, *1*, 6976−6988.

(137) Conley, H. J.; Wang, B.; Ziegler, J. I.; Haglund, R. F.; Pantelides, S. T.; Bolotin, K. I. Bandgap Engineering of Strained Monolayer and Bilayer MoS_2. *Nano Lett.* **2013**, *13*, 3626–3630.

(138) Shen, T.; Penumatcha, A. V.; Appenzeller, J. Strain Engineering for Transition Metal Dichalcogenides Based Field Effect Transistors. *ACS Nano* **2016**, *10*, 4712−4718.

(139) Johari, P.; Shenoy, V. B. Tuning the Electronic Properties of Semiconducting Transition Metal Dichalcogenides by Applying Mechanical Strains. *ACS Nano* **2012**, *6*, 5449–5456.

(140) He, K.; Poole, C.; Mak, K. F.; Shan, J. Experimental Demonstration of Continuous Electronic Structure Tuning via Strain in Atomically Thin MoS_2. *Nano Lett.* **2013**, *13*, 2931–2936.

(141) Hui, Y. Y.; Liu, X.; Jie, W.; Chan, N. Y.; Hao, J.; Hsu, Y.-T.; Li, L.-J.; Guo, W.; Lau, S. P. Exceptional Tunability of Band Energy in a Compressively Strained Trilayer MoS_2 Sheet. *ACS Nano* **2013**, *7*, 7126–7131.

(142) Rice, C.; Young, R. J.; Zan, R.; Bangert, U.; Wolverson, D.; Georgiou, T.; Jalil, R.; Novoselov, K. S. Raman-Scattering Measurements and First-Principles Calculations of Strain-Induced Phonon Shifts in Monolayer MoS_2. *Phys. Rev. B* **2013**, *87*, 081307.

(143) Wang, Y.; Cong, C.; Qiu, C.; Yu, T. Raman Spectroscopy Study of Lattice Vibration and Crystallographic Orientation of Monolayer MoS_2 Under Uniaxial Strain. *Small* **2013**, *9*, 2857–2861.

(144) Scalise, E.; Houssa, M.; Pourtois, G.; Afanas'ev, V. V.; Stesmans, A. First-Principles Study of Strained 2D MoS_2. *Phys. E* **2014**, *56*, 416–421.

(145) Castellanos-Gomez, A.; Roldán, R.; Cappelluti, E.; Buscema, M.; Guinea, F.; van der Zant, H. S. J.; Steele, G. A. Local Strain Engineering in Atomically Thin MoS_2. *Nano Lett.* **2013**, *13*, 5361–5366.

(146) Buscema, M.; Steele, G. A.; van der Zant, H. S. J.; Castellanos-Gomez, A. The Effect of the Substrate on the Raman and Photoluminescence Emission of Single-Layer MoS_2. *Nano Res.* **2014**, *7*, 561–571.

(147) Ghatak, S.; Pal, A. N.; Ghosh, A. Nature of Electronic States in Atomically Thin MoS_2 Field-Effect Transistors. *ACS Nano* **2011**, *5*, 7707–7712.

(148) Pierucci, D.; Henck, H.; Naylor, C. H.; Sediri, H.; Lhuillier, E.; Balan, A.; Rault, J. E.; Dappe, Y. J.; Bertran, F.; Le Févre, P.; et al. Large Area Molybdenum Disulphide-Epitaxial Graphene Vertical van der Waals Heterostructures. *Sci. Rep.* **2016**, *6*, 26656.

(149) Bhanu, U.; Islam, M. R.; Tetard, L.; Khondaker, S. I. Photoluminescence Quenching in Gold-MoS_2 Hybrid Nanoflakes. *Sci. Rep.* **2014**, *4*, 201–204.

(150) Shim, G. W.; Yoo, K.; Seo, S.-B.; Shin, J.; Jung, D. Y.; Kang, I.-S.; Ahn, C. W.; Cho, B. J.; Choi, S.-Y. Large-Area Single-Layer $MoSe_2$ and Its van der Waals Heterostructures. *ACS Nano* **2014**, *8*, 6655–6662.

(151) Mao, N.; Chen, Y.; Liu, D.; Zhang, J.; Xie, L. Solvatochromic Effect on the Photoluminescence of MoS_2 Monolayers. *Small* **2013**, *9*, 1312–1315.

(152) Chakraborty, B.; Bera, A.; Muthu, D. V. S.; Bhowmick, S.; Waghmare, U. V.; Sood, A. K. Symmetry-Dependent Phonon Renormalization in Monolayer MoS_2 Transistor. *Phys. Rev. B* **2012**, *85*, 161403.

(153) Tarasov, A.; Zhang, S.; Tsai, M.-Y.; Campbell, P. M.; Graham, S.; Barlow, S.; Marder, S. R.; Vogel, E. M. Controlled Doping of Large-Area Trilayer MoS_2 with Molecular Reductants and Oxidants. *Adv. Mater.* **2015**, *27*, 1175–1181.

(154) Park, H.-Y.; Dugasani, S. R.; Kang, D.-H.; Jeon, J.; Jang, S. K.; Lee, S.; Roh, Y.; Park, S. H.; Park, J.-H. *n*- and *p*-Type Doping Phenomenon by Artificial DNA and M-DNA on Two-Dimensional Transition Metal Dichalcogenides. *ACS Nano* **2014**, *8*, 11603–11613.

(155) Wei, X.; Yu, Z.; Hu, F.; Cheng, Y.; Yu, L.; Wang, X.; Xiao, M.; Wang, J.; Wang, X.; Shi, Y. Mo−O Bond Doping and Related-Defect Assisted Enhancement of Photoluminescence in Monolayer MoS_2. *AIP Adv.* **2014**, *4*, 123004.

(156) Li, L.; Lee, I.; Lim, D.; Kang, M.; Kim, G.-H.; Aoki, N.; Ochiai, Y.; Watanabe, K.; Taniguchi, T. Raman Shift and Electrical Properties of MoS_2 Bilayer on Boron Nitride Substrate. *Nanotechnology* **2015**, *26*, 295702.

(157) Kong, D.; Wang, H.; Cha, J. J.; Pasta, M.; Koski, K. J.; Yao, J.; Cui, Y. Synthesis of MoS_2 and $MoSe_2$ Films with Vertically Aligned Layers. *Nano Lett.* **2013**, *13*, 1341–1347.

(158) Li, S.; Wang, S.; Salamone, M. M.; Robertson, A. W.; Nayak, S.; Kim, H.; Tsang, S. C. E.; Pasta, M.; Warner, J. H. Edge-Enriched 2D MoS_2 Thin Films Grown by Chemical Vapor Deposition for Enhanced Catalytic Performance. *ACS Catal.* **2017**, *7*, 877–886.

(159) Verble, J. L.; Wieting, T. J. Lattice Mode Degeneracy in MoS_2 and Other Layer Compounds. *Phys. Rev. Lett.* **1970**, *25*, 362–365.

(160) Dumcenco, D.; Ovchinnikov, D.; Marinov, K.; Lazić, P.; Gibertini, M.; Marzari, N.; Sanchez, O. L.; Kung, Y.-C.; Krasnozhon, D.; Chen, M.-W.; et al. Large-Area Epitaxial Monolayer MoS_2. *ACS Nano* **2015**, *9*, 4611–4620.

(161) Najmaei, S.; Amani, M.; Chin, M. L.; Liu, Z.; Birdwell, A. G.; O'Regan, T. P.; Ajayan, P. M.; Dubey, M.; Lou, J. Electrical Transport Properties of Polycrystalline Monolayer Molybdenum Disulfide. *ACS Nano* **2014**, *8*, 7930–7937.

(162) Zhang, J.; Yu, H.; Chen, W.; Tian, X.; Liu, D.; Cheng, M.; Xie, G.; Yang, W.; Yang, R.; Bai, X.; et al. Scalable Growth of High-Quality Polycrystalline MoS_2 Monolayers on SiO_2 with Tunable Grain Sizes. *ACS Nano* **2014**, *8*, 6024–6030.

(163) Ago, H.; Endo, H.; Solís-Fernández, P.; Takizawa, R.; Ohta, Y.; Fujita, Y.; Yamamoto, K.; Tsuji, M. Controlled van der Waals Epitaxy of Monolayer MoS_2 Triangular Domains on Graphene. *ACS Appl. Mater. Interfaces* **2015**, *7*, 5265–5273.

(164) Liu, T.; Temprano, I.; King, D. A.; Driver, S. M.; Jenkins, S. J. Epitaxial Growth of Few-Layer MoS_2(0001) on FeS_2{100}. *Chem. Commun.* **2015**, *51*, 537–540.

(165) Sørensen, S. G.; Füchtbauer, H. G.; Tuxen, A. K.; Walton, A. S.; Lauritsen, J. V. Structure and Electronic Properties of *In Situ* Synthesized Single-Layer MoS_2 on a Gold Surface. *ACS Nano* **2014**, *8*, 6788–6796.

(166) Walton, A. S.; Lauritsen, J. V.; Topsøe, H.; Besenbacher, F. MoS_2 Nanoparticle Morphologies in Hydrodesulfurization Catalysis Studied by Scanning Tunneling Microscopy. *J. Catal.* **2013**, *308*, 306–318.

(167) Reinert, F.; Nicolay, G. Influence of the Herringbone Reconstruction on the Surface Electronic Structure of Au(111). *Appl. Phys. A* **2004**, *78*, 817–821.

(168) Liu, K.; Zhang, L.; Cao, T.; Jin, C.; Qiu, D.; Zhou, Q.; Zettl, A.; Yang, P.; Louie, S. G.; Wang, F. Evolution of Interlayer Coupling in Twisted Molybdenum Disulfide Bilayers. *Nat. Commun.* **2014**, *5*, 4966.

(169) Bruix, A.; Miwa, J. A.; Hauptmann, N.; Wegner, D.; Ulstrup, S.; Grønborg, S. S.; Sanders, C. E.; Dendzik, M.; Grubišić Čabo, A.; Bianchi, M.; et al. Single-Layer MoS_2 on Au(111): Band Gap Renormalization and Substrate Interaction. *Phys. Rev. B* **2016**, *93*, 165422.

(170) Farmanbar, M.; Brocks, G. First-Principles Study of van der Waals Interactions and Lattice Mismatch at MoS_2/Metal Interfaces. *Phys. Rev. B* **2016**, *93*, 085304.

(171) Chen, W.; Santos, E. J. G.; Zhu, W.; Kaxiras, E.; Zhang, Z. Tuning the Electronic and Chemical Properties of Monolayer MoS_2 Adsorbed on Transition Metal Substrates. *Nano Lett.* **2013**, *13*, 509–514.

(172) Yun, W. S.; Lee, J. D. Schottky Barrier Tuning of the Single-Layer MoS_2 on Magnetic Metal Substrates Through Vacancy Defects and Hydrogenation. *Phys. Chem. Chem. Phys.* **2016**, *18*, 31027–31032.

(173) Jiang, C.; Rumyantsev, S. L.; Samnakay, R.; Shur, M. S.; Balandin, A. A. High-Temperature Performance of MoS_2 Thin-Film Transistors: Direct Current and Pulse Current-Voltage Characteristics. *J. Appl. Phys.* **2015**, *117*, 064301.

(174) Neudeck, P. G.; Okojie, R. S.; Chen, L.-Y. High-Temperature Electronics—A Role for

Wide Bandgap Semiconductors? *Proc. IEEE* **2002**, *90*, 1065–1076.

(175) Marx, M.; Nordmann, S.; Knoch, J.; Franzen, C.; Stampfer, C.; Andrzejewski, D.; Kümmell, T.; Bacher, G.; Heuken, M.; Kalisch, H.; et al. Large-Area MoS_2 Deposition via MOVPE. *J. Cryst. Growth* **2017**, *464*, 100–104.

(176) Lamouchi, A.; Assaker, I. B.; Chtourou, R. Effect of Annealing Temperature on the Structural, Optical, and Electrical Properties of MoS_2 Electrodeposited onto Stainless Steel Mesh. *J. Mater. Sci.* **2017**, *52*, 4635–4646.

(177) Barvat, A.; Prakash, N.; Satpati, B.; Singha, S. S.; Kumar, G.; Singh, D. K.; Dogra, A.; Khanna, S. P.; Singha, A.; Pal, P. Emerging Photoluminescence from Bilayer Large-Area 2D MoS_2 Films Grown by Pulsed Laser Deposition on Different Substrates. *J. Appl. Phys.* **2017**, *122*, 015304.

(178) Kaindl, R.; Bayer, B. C.; Resel, R.; Müller, T.; Skakalova, V.; Habler, G.; Abart, R.; Cherevan, A. S.; Eder, D.; Blatter, M.; et al. Growth, Structure and Stability of Sputter-Deposited MoS_2 Thin Films. *Beilstein J. Nanotechnol.* **2017**, *8*, 1115–1126.

(179) Heo, S.; Hayakawa, R.; Wakayama, Y. Carrier Transport Properties of MoS_2 Field-Effect Transistors Produced by Multi-Step Chemical Vapor Deposition Method. *J. Appl. Phys.* **2017**, *121*, 024301.

(180) Ahn, J.-H.; Parkin, W. M.; Naylor, C. H.; Johnson, A. T. C.; Drndić, M. Ambient Effects on Electrical Characteristics of CVD-Grown Monolayer MoS_2 Field-Effect Transistors. *Sci. Rep.* **2017**, *7*, 4075.

(181) Budania, P.; Baine, P. T.; Montgomery, J. H.; McNeill, D. W.; Mitchell, S. J. N.; Modreanu, M.; Hurley, P. K. Effect of Post-Exfoliation Treatments on Mechanically Exfoliated MoS_2. *Mater. Res. Express* **2017**, *4*, 025022.

(182) Ponomarev, E. A.; Neumann-Spallart, M.; Hodes, G.; Lévy-Clément, C. Electrochemical Deposition of MoS_2 Thin Films by Reduction of Tetrathiomolybdate. *Thin Solid Films* **1996**, *280*, 86–89.

(183) Windom, B. C.; Sawyer, W. G.; Hahn, D. W. A Raman Spectroscopic Study of MoS_2 and MoO_3: Applications to Tribological Systems. *Tribol. Lett.* **2011**, *42*, 301–310.

(184) Wu, J.; Li, H.; Yin, Z.; Li, H.; Liu, J.; Cao, X.; Zhang, Q.; Zhang, H. Layer Thinning and Etching of Mechanically Exfoliated MoS_2 Nanosheets by Thermal Annealing in Air. *Small* **2013**, *9*, 3314–3319.

(185) Yamamoto, M.; Einstein, T. L.; Fuhrer, M. S.; Cullen, W. G. Anisotropic Etching of Atomically Thin MoS_2. *J. Phys. Chem. C* **2013**, *117*, 25643–25649.

(186) Bandaru, N.; Kumar, R. S.; Sneed, D.; Tschauner, O.; Baker, J.; Antonio, D.; Luo, S.-N.; Hartmann, T.; Zhao, Y.; Venkat, R. Effect of Pressure and Temperature on Structural Stability of MoS_2. *J. Phys. Chem. C* **2014**, *118*, 3230–3235.

(187) Grønborg, S. S.; Ulstrup, S.; Bianchi, M.; Dendzik, M.; Sanders, C. E.; Lauritsen, J. V.; Hofmann, P.; Miwa, J. A. Synthesis of Epitaxial Single-Layer MoS_2 on Au(111). *Langmuir* **2015**, *31*, 9700–9706.

(188) Liu, D.; Chen, X.; Li, D.; Wang, F.; Luo, X.; Yang, B. Simulation of MoS_2 Crystal Structure and the Experimental Study of Thermal Decomposition. *J. Mol. Struct.* **2010**,

980, 66–71.

(189) Chen, M. S.; Goodman, D. W. Structure-Activity Relationships in Supported Au Catalysts. *Catal. Today* **2006**, *111*, 22–33.

(190) Hvolbæk, B.; Janssens, T. V. W.; Clausen, B. S.; Falsig, H.; Christensen, C. H.; Nørskov, J. K. Catalytic Activity of Au Nanoparticles. *Nano Today* **2007**, *2*, 14–18.

(191) Wang, Y. G.; Mei, D.; Glezakou, V. A.; Li, J.; Rousseau, R. Dynamic Formation of Single-Atom Catalytic Active Sites on Ceria-Supported Gold Nanoparticles. *Nat. Commun.* **2015**, *6*, 6511.

(192) Andoy, N. M.; Zhou, X.; Choudhary, E.; Shen, H.; Liu, G.; Chen, P. Single-Molecule Catalysis Mapping Quantifies Site-Specific Activity and Uncovers Radial Activity Gradient on Single 2D Nanocrystals. *J. Am. Chem. Soc.* **2013**, *135*, 1845–1852.

(193) Tian, N.; Zhou, Z.; Sun, S.; Ding, Y.; Wang, Z. L. Synthesis of Tetrahexahedral Platinum Nanocrystals with High-Index Facets and High Electro-Oxidation Activity. *Science* **2007**, *316*, 732–735.

(194) Boronat, M.; Corma, A. Oxygen Activation on Gold Nanoparticles: Separating the Influence of Particle Size, Particle Shape and Support Interaction. *Dalt. Trans.* **2010**, *39*, 8538–8546.

(195) Kim, F.; Connor, S.; Song, H.; Kuykendall, T.; Yang, P. Platonic Gold Nanocrystals. *Angew. Chemie Int. Ed.* **2004**, *43*, 3673–3677.

(196) Seo, D.; Yoo, C. I.; Chung, I. S.; Park, S. M.; Ryu, S.; Song, H. Shape Adjustment Between Multiply Twinned and Single-Crystalline Polyhedral Gold Nanocrystals: Decahedra, Icosahedra, and Truncated Tetrahedra. *J. Phys. Chem. C* **2008**, *112*, 2469–2475.

(197) Li, C.; Shuford, K. L.; Chen, M.; Lee, E. J.; Cho, S. O. A Facile Polyol Route to Uniform Gold Octahedra with Tailorable Size and Their Optical Properties. *ACS Nano* **2008**, *2*, 1760–1769.

(198) Seo, D.; Ji, C. P.; Song, H. Polyhedral Gold Nanocrystals with O_h Symmetry: From Octahedra to Cubes. *J. Am. Chem. Soc.* **2006**, *128*, 14863–14870.

(199) Sohn, K.; Kim, F.; Pradel, K. C.; Wu, J.; Peng, Y.; Zhou, F.; Huang, J. Construction of Evolutionary Tree for Morphological Engineering of Nanoparticles. *ACS Nano* **2009**, *3*, 2191–2198.

(200) Mulvihill, M.; Tao, A.; Benjauthrit, K.; Arnold, J.; Yang, P. Surface-Enhanced Raman Spectroscopy for Trace Arsenic Detection in Contaminated Water. *Angew. Chemie Int. Ed.* **2008**, *47*, 6456–6460.

(201) Barnard, A. S.; Young, N. P.; Kirkland, A. I.; van Huis, M. A.; Xu, H. Nanogold: A Quantitative Phase Map. *ACS Nano* **2009**, *3*, 1431–1436.

(202) Wulff, G. Z. *Kryst. Miner.* **1901**, *34*, 449–530.

(203) Hansen, K. H.; Worren, T.; Stempel, S.; Lægsgaard, E.; Bäumer, M.; Freund, H.-J.; Besenbacher, F.; Stensgaard, I. Palladium Nanocrystals on Al_2O_3: Structure and Adhesion Energy. *Phys. Rev. Lett.* **2002**, *83*, 4120–4123.

(204) Zucker, R. V.; Chatain, D.; Dahmen, U.; Hagege, S.; Carter, W. C. New Software Tools for the Calculation and Display of Isolated and Attached Interfacial-Energy Minimizing Particle Shapes. *J. Mater. Sci.* **2012**, *47*, 8290–8302.

(205) Wang, Z. L. Transmission Electron Microscopy of Shape-Controlled Nanocrystals and Their Assemblies. *J. Phys. Chem. B* **2000**, *104*, 1153–1175.

(206) Winterbottom, W. L. Equilibrium Shape of a Small Particle in Contact with a Foreign Substrate. *Acta Metall.* **1967**, *15*, 303–310.

(207) Kaishew, R. *Arbeitstagung Festkörper Physik*; Dresden, 1952.

(208) Lin, Y.; Wu, Z.; Wen, J.; Ding, K.; Yang, X.; Poeppelmeier, K. R.; Marks, L. D. Adhesion and Atomic Structures of Gold on Ceria Nanostructures: The Role of Surface Structure and Oxidation State of Ceria Supports. *Nano Lett.* **2015**, *15*, 5375−5381.

(209) Silly, F.; Castell, M. R. Fe Nanocrystal Growth on $SrTiO_3$(001). *Appl. Phys. Lett.* **2005**, *87*, 063106.

(210) Sun, J.; Wu, C.; Silly, F.; Koo, A. A. K.; Dillon, F.; Grobert, N.; Castell, M. R. Controlled Growth of Ni Nanocrystals on $SrTiO_3$ and Their Application in the Catalytic Synthesis of Carbon Nanotubes. *Chem. Commun.* **2013**, *49*, 3748–3750.

(211) Silly, F.; Castell, M. R. Self-Assembled Supported Co Nanocrystals : The Adhesion Energy of Face-Centered-Cubic Co on $SrTiO_3$(001)-(2 × 2). *Appl. Phys. Lett.* **2005**, *87*, 053106.

(212) Silly, F.; Castell, M. R. Bimodal Growth of Au on $SrTiO_3$(001). *Phys. Rev. Lett.* **2006**, *96*, 086104.

(213) Silly, F.; Powell, A. C.; Martin, M. G.; Castell, M. R. Growth Shapes of Supported Pd Nanocrystals on $SrTiO_3$(001). *Phys. Rev. B* **2005**, *72*, 165403.

(214) Castell, M. R. Wulff Shape of Microscopic Voids in UO_2 Crystals. *Phys. Rev. B* **2003**, *68*, 235411.

(215) Barmparis, G. D.; Lodziana, Z.; Lopez, N.; Remediakis, I. N. Nanoparticle Shapes by Using Wulff Constructions and First-Principles Calculations. *Beilstein J. Nanotechnol.* **2015**, *6*, 361–368.

(216) Lofton, C.; Sigmund, W. Mechanisms Controlling Crystal Habits of Gold and Silver Colloids. *Adv. Funct. Mater.* **2005**, *15*, 1197–1208.

(217) Elechiguerra, J. L.; Reyes-Gasga, J.; Yacaman, M. J. The Role of Twinning in Shape Evolution of Anisotropic Noble Metal Nanostructures. *J. Mater. Chem.* **2006**, *16*, 3906–3919.

(218) Ino, S.; Ogawa, S. Multiply Twinned Particles at Earlier Stages of Gold Film Formation on Alkalihalide Crystals. *J. Phys. Soc.* **1967**, *22*, 1365–1374.

(219) Marks, L. D. Modified Wulff Constructions for Twinned Particles. *J. Cryst. Growth* **1983**, *61*, 556—566.

(220) Marks, L. D. Surface Structure and Energetics of Multiply Twinned Particles. *Philos. Mag. A* **1984**, *49*, 81–93.

(221) Hofmeister, H. Shape Variations and Anisotropic Growth of Multiply Twinned Nanoparticles. *Zeitschrift fur Krist.* **2009**, *224*, 528–538.

(222) Ringe, E.; Van Duyne, R. P.; Marks, L. D. Kinetic and Thermodynamic Modified Wulff Constructions for Twinned Nanoparticles. *J. Phys. Chem. C* **2013**, *117*, 15859−15870.

(223) Cleveland, C. L.; Landman, U. The Energetics and Structure of Nickel Clusters: Size Dependence. *J. Chem. Phys.* **1991**, *94*, 7376–7396.

(224) Yacamán, M. J.; Ascencio, J. A.; Liu, H. B.; Gardea-Torresdey, J. Structure Shape and Stability of Nanometric Sized Particles. *J. Vac. Sci. Technol. B* **2001**, *19*, 1091–1103.

(225) Mottet, C.; Goniakowski, J.; Baletto, F.; Ferrando, R.; Treglia, G. Modeling Free and Supported Metallic Nanoclusters: Structure and Dynamics. *Phase Transitions* **2004**, *77*, 101–113.

(226) Silly, F.; Castell, M. R. Growth of Ag Icosahedral Nanocrystals on a $SrTiO_3$(001) Support. *Appl. Phys. Lett.* **2005**, *87*, 213107.

(227) Petroski, J. M.; Wang, Z. L.; Green, T. C.; El-Sayed, M. A. Kinetically Controlled Growth and Shape Formation Mechanism of Platinum Nanoparticles. *J. Phys. Chem. B* **1998**, *102*, 3316–3320.

(228) Yin, Y.; Erdonmez, C.; Aloni, S.; Alivisatos, A. P. Faceting of Nanocrystals During Chemical Transformation: From Solid Silver Spheres to Hollow Gold Octahedra. *J. Am. Chem. Soc.* **2006**, *128*, 12671–12673.

(229) Wiley, B. J.; Xiong, Y.; Li, Z.-Y.; Yin, Y.; Xia, Y. Right Bipyramids of Silver: A New Shape Derived from Single Twinned Seeds. *Nano Lett.* **2006**, *6*, 765–768.

(230) Tao, A.; Sinsermsuksakul, P.; Yang, P. Polyhedral Silver Nanocrystals with Distinct Scattering Signatures. *Angew. Chemie Int. Ed.* **2006**, *45*, 4597–4601.

(231) Johnson, C. J.; Dujardin, E.; Davis, S. A.; Murphy, C. J.; Mann, S. Growth and Form of Gold Nanorods Prepared by Seed-Mediated, Surfactant-Directed Synthesis. *J. Mater. Chem.* **2002**, *12*, 1765–1770.

(232) Lemire, C.; Meyer, R.; Shaikhutdinov, S. K.; Freund, H. J. CO Adsorption on Oxide Supported Gold: From Small Clusters to Monolayer Islands and Three-Dimensional Nanoparticles. *Surf. Sci.* **2004**, *552*, 27–34.

(233) Risse, T.; Shaikhutdinov, S.; Nilius, N.; Sterrer, M.; Freund, H. J. Gold Supported on Thin Oxide Films: From Single Atoms to Nanoparticles. *Acc. Chem. Res.* **2008**, *41*, 949–956.

(234) Lin, X.; Nilius, N.; Freund, H. J.; Walter, M.; Frondelius, P.; Honkala, K.; Häkkinen, H. Quantum Well States in Two-Dimensional Gold Clusters on MgO Thin Films. *Phys. Rev. Lett.* **2009**, *102*, 206801.

(235) Brown, M. A.; Ringleb, F.; Fujimori, Y.; Sterrer, M.; Freund, H. J.; Preda, G.; Pacchioni, G. Initial Formation of Positively Charged Gold on MgO(001) Thin Films: Identification by Experiment and Structural Assignment by Theory. *J. Phys. Chem. C* **2011**, *115*, 10114–10124.

(236) Mammen, N.; Narasimhan, S.; de Gironcoli, S. Tuning the Morphology of Gold Clusters

by Substrate Doping. *J. Am. Chem. Soc.* **2011**, *133*, 2801–2803.

(237) Stiehler, C.; Pan, Y.; Schneider, W. D.; Koskinen, P.; Häkkinen, H.; Nilius, N.; Freund, H. J. Electron Quantization in Arbitrarily Shaped Gold Islands on MgO Thin Films. *Phys. Rev. B* **2013**, *88*, 115415.

(238) Stiehler, C.; Calaza, F.; Schneider, W. D.; Nilius, N.; Freund, H. J. Molecular Adsorption Changes the Quantum Structure of Oxide-Supported Gold Nanoparticles: Chemisorption versus Physisorption. *Phys. Rev. Lett.* **2015**, *115*, 036804.

(239) Cui, Y.; Stiehler, C.; Nilius, N.; Freund, H. J. Probing the Electronic Properties and Charge State of Gold Nanoparticles on Ultrathin MgO versus Thick Doped CaO Films. *Phys. Rev. B* **2015**, *92*, 075444.

(240) Shao, X.; Prada, S.; Giordano, L.; Pacchioni, G.; Nilius, N.; Freund, H. J. Tailoring the Shape of Metal Ad-Particles by Doping the Oxide Support. *Angew. Chemie Int. Ed.* **2011**, *50*, 11525–11527.

(241) Shao, X.; Nilius, N.; Freund, H. J. Crossover from Two- to Three-Dimensional Gold Particle Shapes on CaO Films of Different Thickness. *Phys. Rev. B* **2012**, *85*, 115444.

(242) Pan, Y.; Cui, Y.; Stiehler, C.; Nilius, N.; Freund, H.-J. Gold Adsorption on CeO_2 Thin Films Grown on Ru(0001). *J. Phys. Chem. C* **2013**, *117*, 21879–21885.

(243) Zhang, L.; Persaud, R.; Madey, T. E. Ultrathin Metal Films on a Metal Oxide Surface: Growth of Au on TiO_2 (110). *Phys. Rev. B* **1997**, *56*, 10549–10557.

(244) Parker, S. C.; Grant, A. W.; Bondzie, V. A.; Campbell, C. T. Island Growth Kinetics During Vapor Deposition of Gold onto TiO_2(110). *Surf. Sci.* **1999**, *441*, 10–20.

(245) Chen, M. S.; Goodman, D. W. The Structure of Catalytically Active Gold on Titania. *Science* **2004**, *306*, 252–255.

(246) Herzing, A. A.; Kiely, C. J.; Carley, A. F.; Landon, P.; Hutchings, G. J. Identification of Active Gold Nanoclusters on Iron Oxide Supports for CO Oxidation. *Science* **2008**, *321*, 1331–1336.

(247) Calaza, F.; Stiehler, C.; Fujimori, Y.; Sterrer, M.; Beeg, S.; Ruiz-Oses, M.; Nilius, N.; Heyde, M.; Parviainen, T.; Honkala, K.; et al. Carbon Dioxide Activation and Reaction Induced by Electron Transfer at an Oxide−Metal Interface. *Angew. Chemie Int. Ed.* **2015**, *54*, 12484–12487.

(248) Lai, X.; St. Clair, T. P.; Valden, M.; Goodman, D. W. Scanning Tunneling Microscopy Studies of Metal Clusters Supported on TiO_2 (110): Morphology and Electronic Structure. *Prog. Surf. Sci.* **1998**, *59*, 25–52.

(249) Bäumer, M.; Freund, H.-J. Metal Deposits on Well-Ordered Oxide Films. *Prog. Surf. Sci.* **1999**, *61*, 127–198.

(250) Ricci, D.; Bongiorno, A.; Pacchioni, G.; Landman, U. Bonding Trends and Dimensionality Crossover of Gold Nanoclusters on Metal-Supported MgO Thin Films. *Phys. Rev. Lett.* **2006**, *97*, 036106.

(251) Zhang, C.; Yoon, B.; Landman, U. Predicted Oxidation of CO Catalyzed by Au Nanoclusters on a Thin Defect-Free MgO Film Supported on a Mo(100) Surface. *J. Am.*

Chem. Soc. **2007**, *129*, 2228–2229.

(252) Harding, C.; Habibpour, V.; Kunz, S.; Farnbacher, A. N. S.; Heiz, U.; Yoon, B.; Landman, U. Control and Manipulation of Gold Nanocatalysis: Effects of Metal Oxide Support Thickness and Composition. *J. Am. Chem. Soc.* **2009**, *131*, 538–548.

(253) Sterrer, M.; Risse, T.; Heyde, M.; Rust, H. P.; Freund, H. J. Crossover from Three-Dimensional to Two-Dimensional Geometries of Au Nanostructures on Thin MgO(001) Films: A Confirmation of Theoretical Predictions. *Phys. Rev. Lett.* **2007**, *98*, 206103.

(254) Yoon, B.; Landman, U. Electric Field Control of Structure, Dimensionality, and Reactivity of Gold Nanoclusters on Metal-Supported MgO Films. *Phys. Rev. Lett.* **2008**, *100*, 056102.

(255) Oura, K.; Lifshits, V. G.; Saranin, A.; Zotov, A. V.; Katayama, M. *Surface Science: An Introduction*, 1st ed.; Springer: Berlin, 2003.

(256) Marshall, M. Nanostructured Strontium Titanate Surfaces, University of Oxford, 2009.

(257) JEOL Ltd. *JEOL Instruction Manual: JSPM-4500S/TM-51021 Ultrahigh Vacuum Scanning Tunneling Microscope*; 2000.

(258) VG Microtech. *EX03 Ion Gun System: Operating Manual*; 2000.

(259) Createc Fischer & Co. *Single Filament Effusion Cell SFC-H-5-SH: Instruction Manual*; 2002.

(260) Createc Fischer & Co. *Control Unit CU-2404-700-DC: Instruction Manual*; 2002.

(261) Chattopadhyay, K. K.; Banerjee, A. N. *Introduction to Nanoscience and Nanotechnology*; PHI Learning, 2009.

(262) Castell, M. R. Scanning Tunneling Microscopy of Surfaces and Nanostructures. In *Nanocharacterisation*; Kirkland, A. I., Haigh, S. J., Eds.; The Royal Society of Chemistry, 2015; pp 66–93.

(263) Castell, M. R. Scanning Tunnelling Microscopy of Surfaces and Nanostructures. In *Nanocharacterisation*; Hutchison, J., Kirkland, A., Eds.; RSC Publishing, 2007; pp 66–93.

(264) Jones, L.; Wang, S.; Hu, X.; ur Rahman, S.; Castell, M. R. Maximising the Resolving Power of the Scanning Tunneling Microscope. *Adv. Struct. Chem. Imaging* **2018**, *4*, 7.

(265) Jones, L.; Yang, H.; Pennycook, T. J.; Marshall, M. S. J.; Van Aert, S.; Browning, N. D.; Castell, M. R.; Nellist, P. D. Smart Align—A New Tool for Robust Non-Rigid Registration of Scanning Microscope Data. *Adv. Struct. Chem. Imaging* **2015**, *1*, 8.

(266) Horcas, I.; Fernández, R.; Gómez-Rodríguez, J. M.; Colchero, J.; Gómez-Herrero, J.; Baro, A. M. WSXM: A Software for Scanning Probe Microscopy and a Tool for Nanotechnology. *Rev. Sci. Instrum.* **2007**, *78*, 013705.

(267) Ratner, B. D.; Castner, D. G. *Surface Analysis: The Principal Techniques*, 2nd ed.; Vickerman, J. C., Gilmore, I. S., Eds.; John Wiley & Sons, 2009.

(268) van der Heide, P. *X-Ray Photoelectron Spectroscopy: An Introduction to Principles and Practices*; John Wiley & Sons, 2012.

(269) Nefedov, V. I. *X-Ray Photoelectron Spectroscopy of Solid Surfaces*; CRC Press, 1988.

(270) Kawa, J.; Adachi, H.; Kitajima, Y.; Maeda, K.; Hayakawa, S.; Gohshi, Y. Inelastic Mean Free Path of Photoelectrons Photoelectron in Ag Determined by Total Reflection X-Ray Photoelectron Spectroscopy. *Anal. Sci.* **1997**, *13*, 797–801.

(271) Somarjai, G. *Chemistry in Two Dimensions: Surfaces*; Cornell University Press: Ithaca, 1981.

(272) Thornton, P. R. *Scanning Electron Microscopy: Applications to Materials and Device Science*, 1st ed.; Springer US, 1968.

(273) Castle, J. E.; Zhdan, P. A. Characterization of Surface Topography by SEM and SFM: Problems and Solutions. *J. Phys. D. Appl. Phys.* **1997**, *30*, 722.

(274) Moffatt, W. G.; Pearsall, G. W.; Wulff, J. *Structure and Properties of Materials (Volume 1: Structure)*; John Wiley & Sons Inc., 1964.

(275) Niewczas, M. Lattice Correspondence During Twinning in Hexagonal Close-Packed Crystals. *Acta Mater.* **2010**, *58*, 5848–5857.

(276) Dai, Z.; Jin, W.; Grady, M.; Sadowski, J. T.; Dadap, J. I.; Osgood, R. M.; Pohl, K. Surface Structure of Bulk 2H-MoS_2(0001) and Exfoliated Suspended Monolayer MoS_2: A Selected Area Low Energy Electron Diffraction Study. *Surf. Sci.* **2017**, *660*, 16–21.

(277) Helveg, S.; Lauritsen, J. V.; Lægsgaard, E.; Stensgaard, I.; Nørskov, J. K.; Clausen, B. S.; Topsøe, H.; Besenbacher, F. Atomic-Scale Structure of Single-Layer MoS_2 Nanoclusters. *Phys. Rev. Lett.* **2000**, *84*, 951–954.

(278) Lauritsen, J. V.; Kibsgaard, J.; Topsøe, H.; Helveg, S.; Clausen, B. S.; Lægsgaard, E.; Besenbacher, F. Size-Dependent Structure of MoS_2 Nanocrystals. *Nat. Nanotechnol.* **2007**, *2*, 53–58.

(279) Magonov, S. N.; Whangbo, M.-H. Interpreting STM and AFM Images. *Adv. Mater.* **1994**, *6*, 355–371.

(280) Zhang, Y.; Ji, Q.; Han, G.-F.; Ju, J.; Shi, J.; Ma, D.; Sun, J.; Zhang, Y.; Li, M.; Lang, X. Y.; et al. Dendritic, Transferable, Strictly Monolayer MoS_2 Flakes Synthesized on $SrTiO_3$ Single Crystals for Efficient Electrocatalytic Applications. *ACS Nano* **2014**, *8*, 8617–8624.

(281) Zhang, Y.; Ji, Q.; Wen, J.; Li, J.; Li, C.; Shi, J.; Zhou, X.; Shi, K.; Chen, H.; Li, Y.; et al. Monolayer MoS_2 Dendrites on a Symmetry-Disparate $SrTiO_3$ (001) Substrate: Formation Mechanism and Interface Interaction. *Adv. Funct. Mater.* **2016**, *26*, 3299–3305.

(282) Azcatl, A.; Qin, X.; Prakash, A.; Zhang, C.; Cheng, L.; Wang, Q.; Lu, N.; Kim, M. J.; Kim, J.; Cho, K.; et al. Covalent Nitrogen Doping and Compressive Strain in MoS_2 by Remote N_2 Plasma Exposure. *Nano Lett.* **2016**, *16*, 5437–5443.

(283) Nipane, A.; Karmakar, D.; Kaushik, N.; Karande, S.; Lodha, S. Few-Layer MoS_2 *p*-Type Devices Enabled by Selective Doping Using Low Energy Phosphorus Implantation. *ACS Nano* **2016**, *10*, 2128–2137.

(284) Zhao, W.; Ribeiro, R. M.; Toh, M.; Carvalho, A.; Kloc, C.; Castro Neto, A. H.; Eda, G.

Origin of Indirect Optical Transitions in Few-Layer MoS_2, WS_2, and WSe_2. *Nano Lett.* **2013**, *13*, 5627–5634.

(285) El-Mahalawy, S. H.; Evans, B. L. The Thermal Expansion of 2H-MoS_2, 2H-$MoSe_2$ and 2H-WSe_2 between 20 and 800 °C. *J. Appl. Crystallogr.* **1976**, *9*, 403–406.

(286) El-Kareh, B. *Fundamentals of Semiconductor Processing Technology*; Springer, 1995.

(287) de Ligny, D.; Richet, P. High-Temperature Heat Capacity and Thermal Expansion of $SrTiO_3$ and $SrZrO_3$ Perovskites. *Phys. Rev. B* **1996**, *53*, 3013–3022.

(288) Kibsgaard, J.; Clausen, B. S.; Topsøe, H.; Lægsgaard, E.; Lauritsen, J. V.; Besenbacher, F. Scanning Tunneling Microscopy Studies of TiO_2-Supported Hydrotreating Catalysts: Anisotropic Particle Shapes by Edge-Specific MoS_2-Support Bonding. *J. Catal.* **2009**, *263*, 98–103.

(289) Narasimhan, S. Elastic Stress Domains and the Herringbone Reconstruction on Au(111). *Phys. Rev. Lett.* **1992**, *69*, 1564–1568.

(290) Brunen, J.; Zegenhagen, J. Investigation of the $SrTiO_3$(110) Surface by Means of LEED, Scanning Tunneling Microscopy and Auger Spectroscopy. *Surf. Sci.* **1997**, *389*, 349–365.

(291) Sheng, Y.; Xu, W.; Wang, X.; He, Z.; Rong, Y.; Warner, J. H. Mixed Multilayered Vertical Heterostructures Utilizing Strained Monolayer WS_2. *Nanoscale* **2016**, *8*, 2639–2647.

(292) Qin, P.; Fang, G.; Ke, W.; Cheng, F.; Zheng, Q.; Wan, J.; Lei, H.; Zhao, X. *In Situ* Growth of Double-Layer MoO_3/MoS_2 Film from MoS_2 for Hole-Transport Layers in Organic Solar Cell. *J. Mater. Chem. A* **2014**, *2*, 2742–2756.

(293) Jiang, L.; Zhang, S.; Kulinich, S. A.; Song, X.; Zhu, J.; Wang, X.; Zeng, H. Optimizing Hybridization of 1T and 2H Phases in MoS_2 Monolayers to Improve Capacitances of Supercapacitors. *Mater. Res. Lett.* **2015**, *3*, 177–183.

(294) Kumar, P.; Singh, M.; Sharma, R. K.; Reddy, G. B. A Study on Role of Partial Pressure in Controlled Synthesis of Core-Shell MoO_2/MoS_2 Nanoflakes. *Mater. Chem. Phys.* **2016**, *178*, 6–11.

(295) Sun, Y.; Hu, X.; Luo, W.; Huang, Y. Ultrafine MoO_2 Nanoparticles Embedded in a Carbon Matrix as a High-Capacity and Long-Life Anode for Lithium-Ion Batteries. *J. Mater. Chem.* **2012**, *22*, 425–431.

(296) Jin, Y.; Shen, P. K. Nanoflower-Like Metallic Conductive MoO_2 as a High-Performance Non-Precious Metal Electrocatalyst for the Hydrogen Evolution Reaction. *J. Mater. Chem. A* **2015**, *3*, 20080–20085.

(297) Shi, Y.; Huang, J.-K.; Jin, L.; Hsu, Y.-T.; Yu, S. F.; Li, L.-J.; Yang, H. Y. Selective Decoration of Au Nanoparticles on Monolayer MoS_2 Single Crystals. *Sci. Rep.* **2013**, *3*, 1839.

(298) Ehre, D.; Cohen, H.; Lyahovitskaya, V.; Lubomirsky, I. X-Ray Photoelectron Spectroscopy of Amorphous and Quasiamorphous Phases of $BaTiO_3$ and $SrTiO_3$. *Phys. Rev. B* **2008**, *77*, 184106.

(299) Peng, J.; Zhou, Y.; Wang, H.; Zhou, H.; Cai, S. Hydrothermal Synthesis and Formation

Mechanism of Photocatalytically Active $SrTiO_3$ Nanocrystals Using Anatase TiO_2 with Different Facets as a Precursor. *CrystEngComm* **2015**, *17*, 1805–1812.

(300) Psiuk, B.; Szade, J.; Szot, K. $SrTiO_3$ Surface Modification upon Low Energy Ar^+ Bombardment Studied by XPS. *Vacuum* **2016**, *131*, 14–21.

(301) Pondick, J. V.; Woods, J. M.; Xing, J.; Zhou, Y.; Cha, J. J. Stepwise Sulfurization from MoO_3 to MoS_2 via Chemical Vapor Deposition. *ACS Appl. Nano Mater.* **2018**, *1*, 5655–5661.

(302) Wagner, C. D. *Practical Surface Analysis, Auger and X-Ray Photoelectron Spectroscopy*, 2nd ed.; Briggs, D., Seah, M. P., Eds.; John Wiley & Sons: New York, 1990.

(303) Li, H.; Zhang, Q.; Yap, C. C. R.; Tay, B. K.; Edwin, T. H. T.; Olivier, A.; Baillargeat, D. From Bulk to Monolayer MoS_2: Evolution of Raman Scattering. *Adv. Funct. Mater.* **2012**, *22*, 1385–1390.

(304) Molina, L. M.; Hammer, B. Active Role of Oxide Support during CO Oxidation at Au/MgO. *Phys. Rev. Lett.* **2003**, *90*, 206102.

(305) Fu, Q.; Saltsburg, H.; Flytzani-Stephanopoulos, M. Active Nonmetallic Au and Pt Species on Ceria-Based Water-Gas Shift Catalysts. *Science* **2003**, *301*, 935–938.

(306) Liu, X. Y.; Wang, A.; Zhang, T.; Mou, C. Catalysis by Gold: New Insights into the Support Effect. *Nano Today* **2013**, *8*, 403–416.

(307) Si, R.; Flytzani-Stephanopoulos, M. Shape and Crystal-Plane Effects of Nanoscale Ceria on the Activity of Au-CeO_2 Catalysts for the Water−Gas Shift Reaction. *Angew. Chemie Int. Ed.* **2008**, *47*, 2884–2887.

(308) Ta, N.; Liu, J.; Chenna, S.; Crozier, P. A.; Li, Y.; Chen, A.; Shen, W. Stabilized Gold Nanoparticles on Ceria Nanorods by Strong Interfacial Anchoring. *J. Am. Chem. Soc.* **2012**, *134*, 20585−20588.

(309) Kelly, P. F. *Properties of Materials*; CRC Press, 2014.

(310) Bernard, O.; Andrieux, M.; Poissonnet, S.; Huntz, A. M. Mechanical Behaviour of Ferroelectric Films on Perovskite Substrate. *J. Eur. Ceram. Soc.* **2004**, *24*, 763–773.

(311) Wachtman, J. B.; Wheat, M. L.; Marzullo, S. A Method for Determining the Elastic Constants of a Cubic Crystal from Velocity Measurements in a Single Arbitrary Direction; Application to $SrTiO_3$. *J. Res. Natl. Bur. Stand. Sect. A* **1963**, *67A*, 193–209.

(312) McKeown Walker, S.; Bruno, F. Y.; Wang, Z.; de la Torre, A.; Riccó, S.; Tamai, A.; Kim, T. K.; Hoesch, M.; Shi, M.; Bahramy, M. S.; et al. Carrier-Density Control of the $SrTiO_3$(001) Surface 2D Electron Gas Studied by ARPES. *Adv. Mater.* **2015**, *27*, 3894–3899.

(313) Wang, Z.; McKeown Walker, S.; Tamai, A.; Wang, Y.; Ristic, Z.; Bruno, F. Y.; de la Torre, A.; Riccò, S.; Plumb, N. C.; Shi, M.; et al. Tailoring the Nature and Strength of Electron-Phonon Interactions in the $SrTiO_3$(001) 2D Electron Liquid. *Nat. Mater.* **2016**, *15*, 835–839.

(314) Sivaramakrishnan, S.; Wen, J.; Scarpelli, M. E.; Pierce, B. J.; Zuo, J.-M. Equilibrium Shapes and Triple Line Energy of Epitaxial Gold Nanocrystals Supported on TiO_2(110).

Phys. Rev. B **2010**, *82*, 195421.

(315) Lopez, N.; Nørskov, J. K.; Janssens, T. V. W.; Carlsson, A.; Puig-Molina, A.; Clausen, B. S.; Grunwaldt, J. D. The Adhesion and Shape of Nanosized Au Particles in a Au/TiO_2 Catalyst. *J. Catal.* **2004**, *225*, 86–94.

(316) Marks, L. D.; Peng, L. Nanoparticle Shape, Thermodynamics and Kinetics. *J. Phys. Condens. Matter* **2016**, *28*, 53001.

(317) Medeiros-Ribeiro, G.; Bratkovski, A. M.; Kamins, T. I.; Ohlberg, D. A. A.; Williams, R. S. Shape Transition of Germanium Nanocrystals on a Silicon (001) Surface from Pyramids to Domes. *Science* **1998**, *279*, 353–355.

(318) Müller, P.; Kern, R. Equilibrium Nano-Shape Changes Induced by Epitaxial Stress (Generalised Wulf–Kaishew Theorem). *Surf. Sci.* **2000**, *457*, 229–253.

(319) Shchukin, V. A.; Bimberg, D. Spontaneous Ordering of Nanostructures on Crystal Surfaces. *Rev. Mod. Phys.* **2002**, *71*, 1125–1171.

(320) Grigoriev, I. S.; Meilikhov, E. Z.; Radzig, A. A. *Handbook of Physical Quantities*; CRC Press, 1996.

(321) Müller, P.; Kern, R. Equilibrium Shape of Epitaxially Strained Crystals (Volmer−Weber Case). *J. Cryst. Growth* **1998**, *193*, 257–270.

(322) Müller, P.; Kern, R. Some Aspects of Coherent Epitaxial Deposits. *Microsc. Microanal. Microstruct.* **1997**, *8*, 229–238.

(323) Hammar, M.; LeGoues, F. K.; Tersoff, J.; Reuter, M. C.; Tromp, R. M. *In Situ* Ultrahigh Vacuum Transmission Electron Microscopy Studies of Hetero-Epitaxial Growth I. Si(001)/Ge. *Surf. Sci.* **1996**, *349*, 129–144.

(324) Ahmadi, M.; Behafarid, F.; Cuenya, B. R. Size-Dependent Adhesion Energy of Shape-Selected Pd and Pt Nanoparticles. *Nanoscale* **2016**, *8*, 11635–11641.

(325) Zhang, Z.; Li, L.; Yang, J. C. Adhesion of Pt Nanoparticles Supported on γ-Al_2O_3 Single Crystal. *J. Phys. Chem. C* **2013**, *117*, 21407–21412.

(326) Silly, F.; Castell, M. R. Encapsulated Pd Nanocrystals Supported by Nanoline-Structured $SrTiO_3$(001). *J. Phys. Chem. B* **2005**, *109*, 12316–12319.

(327) Liu, X.; Liu, M. H.; Luo, Y. C.; Mou, C. Y.; Lin, S. D.; Cheng, H.; Chen, J. M.; Lee, J. F.; Lin, T. S. Strong Metal−Support Interactions between Gold Nanoparticles and ZnO Nanorods in CO Oxidation. *J. Am. Chem. Soc.* **2012**, *134*, 10251–10258.

(328) Bennett, R. A.; Pang, C. L.; Perkins, N.; Smith, R. D.; Morrall, P.; Kvon, R. I.; Bowker, M. Surface Structures in the SMSI State; Pd on (1 × 2) Reconstructed TiO_2(110). *J. Phys. Chem. B* **2002**, *106*, 4688–4696.

(329) Gubó, R.; Yim, C. M.; Allan, M.; Pang, C. L.; Berkó, A.; Thornton, G. Variation of SMSI with the Au:Pd Ratio of Bimetallic Nanoparticles on TiO_2(110). *Top. Catal.* **2018**, *61*, 308–317.

(330) Wu, C.; Marshall, M. S. J.; Castell, M. R. Surface Structures of Ultrathin TiO_x Films on Au(111). *J. Phys. Chem. C* **2011**, *115*, 8643–8652.

(331) Vitos, L.; Ruban, A. V.; Skriver, H. L.; Kollár, J. The Surface Energy of Metals. *Surf. Sci.* **1998**, *411*, 186–202.

(332) Kuwauchi, Y.; Yoshida, H.; Akita, T.; Haruta, M.; Takeda, S. Intrinsic Catalytic Structure of Gold Nanoparticles Supported on TiO_2. *Angew. Chemie Int. Ed.* **2012**, *51*, 7729–7733.

(333) Gao, W.; Choi, A. S.; Zuo, J.-M. Interaction of Nanometer-Sized Gold Nanocrystals with Rutile (110) Surface Steps Revealed at Atomic Resolution. *Surf. Sci.* **2014**, *625*, 16–22.

(334) Gao, W.; Sivaramakrishnan, S.; Wen, J.; Zuo, J.-M. Direct Observation of Interfacial Au Atoms on TiO_2 in Three Dimensions. *Nano Lett.* **2015**, *15*, 2548–2554.

(335) Castro, T.; Reifenberger, R. Size-Dependent Melting Temperature of Individual Nanometer-Sized Metallic Clusters. *Phys. Rev. B* **1990**, *42*, 8548–8556.

(336) Schmid, G.; Corain, B. Nanoparticulated Gold: Syntheses, Structures, Electronics, and Reactivities. *Eur. J. Inorg. Chem.* **2003**, No. 17, 3081–3098.

(337) Wei, S.; Fu, X.-P.; Wang, W.-W.; Jin, Z.; Song, Q.-S.; Jia, C.-J. Au/TiO_2 Catalysts for CO Oxidation: Effect of Gold State to Reactivity. *J. Phys. Chem. C* **2018**, *122*, 4928–4936.

(338) Bando, H.; Aiura, Y.; Haruyama, Y.; Shimizu, T.; Nishihara, Y. Structure and Electronic States on Reduced $SrTiO_3$(110) Surface Observed by Scanning Tunneling Microscopy and Spectroscopy. *J. Vac. Sci. Technol. B* **1995**, *13*, 1150–1154.

(339) Gunhold, A.; Beuermann, L.; Gömann, K.; Borchardt, G.; Kempter, V.; Maus-Friedrichs, W.; Piskunov, S.; Kotomin, E. A.; Dorfman, S. Study of the Electronic and Atomic Structure of Thermally Treated $SrTiO_3$(110) Surfaces. *Surf. Interface Anal.* **2003**, *35*, 998–1003.

(340) Gunhold, A.; Gömann, K.; Beuermann, L.; Kempter, V.; Borchardt, G.; Maus-Friedrichs, W. Changes in the Surface Topography and Electronic Structure of $SrTiO_3$(110) Single Crystals Heated Under Oxidizing and Reducing Conditions. *Surf. Sci.* **2004**, *566–568*, 105–110.

(341) Matsumoto, T.; Tanaka, H.; Kouguchi, K.; Kawai, T.; Kawai, S. A Scanning Tunneling Microscopy Study of Laser Molecular Beam Epitaxy on $SrTiO_3$(100) Surface. *Surf. Sci.* **1994**, *312*, 21–30.

(342) Tanaka, H.; Matsumoto, T.; Kawai, T.; Kawai, S. Interaction of Oxygen Vacancies with O_2 on a Reduced $SrTiO_3$(100)$\sqrt{5} \times \sqrt{5}$-R26.6° Surface Observed by STM. *Surf. Sci.* **1994**, *318*, 29–38.

(343) Jiang, Q.; Zegenhagen, J. $SrTiO_3$(001)-*c*(6 × 2): A Long-Range, Atomically Ordered Surface Stable in Oxygen and Ambient Air. *Surf. Sci.* **1996**, *367*, L42–L46.

(344) Erdman, N.; Poeppelmeier, K. R.; Asta, M.; Warschkow, O.; Ellis, D. E.; Marks, L. D. The Structure and Chemistry of the TiO_2-Rich Surface of $SrTiO_3$(001). *Nature* **2002**, *419*, 55–58.

(345) Newell, D. T. The Surface Structure and Reconstructions of $SrTiO_3$(001) (Ph.D. Thesis), University of Oxford, 2007.